

Alma Mater Studiorum - Università di Bologna

**DOTTORATO DI RICERCA IN**

**Meccanica e scienze avanzate dell'ingegneria**

Ciclo 33°

**Settore Concorsuale: 09/C1**

**Settore Scientifico Disciplinare: ING-IND/08**

**Numerical Assessment of the Water Injection Application  
to GDI Engines**

**Presentata da: Matteo Ricci**

**Coordinatore Dottorato**

**Supervisore**

**Chiar.mo Prof. Ing. Marco Carricato**

**Chiar.mo Prof. Ing. Gian Marco Bianchi**

**Esame Finale anno 2021**

# Abstract

A possible future scenario for the water injection application has been explored as an advanced strategy for modern GDI engines. The aim is to verify whether the PWI (Port Water Injection) and DWI (Direct Water Injection) architectures can replace current fuel enrichment strategies to limit turbine inlet temperatures (TiT) and knock engine attitude. In this way, it might be possible to extend the stoichiometric mixture condition over the entire engine map, meeting possible future restrictions in the use of AES (Auxiliary Emission Strategies) and future emission limitations.

The research was first addressed through a comprehensive assessment of the state-of-the-art of the technology and the main effects of the chemical-physical water properties. Then, detailed chemical kinetics simulations were performed in order to compute the effects of water injection on the laminar flame speed, the laminar flame thickness and the ignition delayed time and to develop database of such parameters to be used real-time during CFD simulations. The latter represents an important methodology step for accurate numerical combustion simulations.

The water injection was then analysed in detail for a PWI system, through an experimental campaign for macroscopic and microscopic injector characterization inside a test chamber. The collected data were used to perform a numerical validation of the spray models, obtaining an excellent matching in terms of particle size and droplet velocity distributions.

Finally, a wide range of three-dimensional CFD simulations of a virtual high-bmep engine were realized and compared, exploring also different engine designs varying the compression ratio and the stroke to bore ratio. The simulations were performed both with and without water injection (fuel-only mode configuration), with different mixture strategies, and for PWI and DWI systems under non-reacting and reacting flow conditions, varying a series of parameters such as: the injection pressure, the SOI/EOI and the injected water mass. The aim was to verify the possible performance gain by using WI (Water Injection) keeping the knock engine attitude and the exhaust gas temperature below the imposed thresholds, achieving the best configurations for each architecture. In research, in order to pursue water consumption minimization, only the configurations achieving a minimum of 90% of water evaporated were considered as those suitable for reacting flow simulations.

According to the latter, it was found that thanks to the introduction of water, for both PWI and DWI systems, it could be possible to obtain an increase of the target performance and an optimization of the *bsfc* (Break Specific Fuel Consumption), lowering the engine knock risk at the same time, while the TiT target has been achieved hardly only for one DWI configuration.



# List of Contents

List of Figures .....	7
List of Tables .....	13
Introduction .....	15
Chapter 1: Global Engine Scenario .....	17
1.1 Introduction.....	17
1.2 Emissions Standards Issued in Europe .....	18
1.3 Homologation Driving Cycles.....	20
1.4 Auxiliary Strategies .....	23
1.5 ICE Future Trends .....	24
1.6 Engine Technologies Description.....	25
1.6.1 GDI Lean Combustion .....	26
1.6.2 Miller and Atkinson Cycles .....	27
1.6.3 Variable Compression Ratio .....	28
1.6.4 Cylinder Deactivation .....	28
1.6.5 Exhaust Gas Recirculation .....	28
1.6.6 Multistage Air Charging .....	29
Chapter 2: Water Injection Application to Engines: State of the Art .....	31
2.1 Literature Review .....	31
2.1.1 HCCI Engines .....	31
2.1.2 Spark Ignited Engines .....	32
2.1.3 Diesel Engines .....	34
2.2 Spark Ignition Engine Water Injector Layouts .....	35
2.2.1 Intake Line Injection .....	36
2.2.2 Port Water Injection .....	37
2.2.3 Direct Water Injection .....	37
2.3 Water Sources .....	39
2.3.1 Air Conditioning Systems.....	40
2.3.2 Exhaust Gases Recovery System.....	40
2.3.3 Surface Water Recovery System .....	41
2.4 Conclusions.....	42
Chapter 3: Water Properties .....	44
3.1 Water Physical Properties: Effects on Jet Atomization, Droplet Breakup and Evaporation .....	44
3.1.1 Jet and Droplet Breakup: Analytical Analysis .....	46

3.1.2 Mass Evaporation Rate: Analytical Analysis .....	51
3.2 Water Cooling Effects: Preliminary Analysis.....	55
3.3 Humidity Effects on Water Injection: Brief Analysis.....	58
3.4 Brief Review of Chemical Water Effects on Laminar Flame Speed and Ignition Delayed Time .....	61
3.5 Summary.....	62
Chapter 4: Numerical Methodologies .....	64
4.1 Spray Modelling.....	64
4.2 Atomization Modelling .....	66
4.3 Secondary Break-Up Modelling.....	67
4.4 Particle Interaction Modelling.....	68
4.5 Spray-Wall Interaction Modelling.....	69
4.6 Reaction Rate Modelling .....	70
4.6.1 Ignition Model .....	70
4.6.2 Combustion Model.....	72
4.7 Thermal Wall Function Modelling .....	74
4.8 Turbulence Modelling.....	75
4.9 Numerical Methods.....	76
Chapter 5: Water Effects on Combustion Process: Chemical Kinetics Calculations.....	77
5.1 Choice of the Fuel Surrogate .....	77
5.2 Chemical Water Effect on Laminar Flame Speed and Thickness.....	78
5.2.1 Baseline Correlation Laws for Laminar Flame Speed and Thickness.....	78
5.2.2 Characteristics of the Chemical Simulations .....	79
5.2.3 Chemical Kinetics Mechanism and Validation.....	80
5.2.4 Thermodynamic and Mixture Conditions Tested .....	81
5.2.5 LFS and LFT Chemical Simulation Results.....	82
5.3 Chemical Water Effect on the Ignition Delay Time .....	86
5.3.1 Baseline Correlation Laws for Ignition Delayed Time.....	86
5.3.2 Chemical Kinetics Mechanism and Validation for the Ignition Delayed Time.....	87
5.3.3 Thermodynamic and Mixture Conditions Tested .....	88
5.3.4 Results of the Kinetic Chemical Simulations.....	88
5.4 Summary.....	92
Chapter 6: Experimental Characterization of a Low-Pressure Water Injector.....	93
6.1 Hydraulic Characterization .....	93
6.2 Imaging Characterization.....	100
6.3 Experimental PDA Results of the Water Injection System .....	101
6.4 Summary.....	105

Chapter 7: PWI Numerical Validation.....	106
7.1 CFD Spray Validation against Experimental Data: CASE 1.....	106
7.1.1 Numerical Validation Results of the PWI System.....	107
7.2 CFD Spray Validation against Experimental Data: CASE 2.....	111
7.2.1 Numerical Validation Results of the PWI System.....	113
7.3 Summary.....	117
Chapter 8: GDI Engine Simulations under Non-Reacting Flow Conditions .....	118
8.1 Engine Specifications.....	119
8.2 Simulation Set-Up.....	121
8.3 Simulations results without Water Injection.....	123
8.4 Summary.....	132
Chapter 9: Port Water Injection Simulations under Non-Reacting Flow Conditions .....	134
9.1 Port Water Injection Features and Configurations tested .....	134
9.2 Simulation Results for PWI 10 bar Strategies.....	137
9.2.1 Mixture Quality Effects.....	137
9.2.2 Fluid-dynamic Analysis .....	139
9.2.3 Thermodynamic Analysis.....	142
9.3 Simulation Results for PWI 20 bar Strategies.....	145
9.4 Results comparison among PWI strategies at 10 bar and 20 bar.....	147
9.5 Relative Humidity Effects on PWI Performance.....	149
9.6 Evaluation of the Main Effects of Higher S/B Ratio on PWI Strategy.....	151
9.7 Summary.....	155
Chapter 10: Direct Water Injection Simulations under Non-Reacting Flow Conditions .....	156
10.1 Direct Water Injection Features .....	156
10.2 Definition of the DWI Injection Centre.....	157
10.2.1 Mixture Distribution Analysis .....	158
10.2.2 Thermodynamic Effect .....	160
10.2.3 Fluid-dynamic Analysis .....	161
10.3 Simulation Results of the DWI System for different Water Injection Strategies at 50 bar and 150 bar .....	162
10.3.1 Mixture Distribution Analysis .....	163
10.3.2 Thermodynamic Analysis.....	165
10.3.3 Fluid-dynamic Analysis .....	167
10.4 Comparison between PWI and DWI best Configurations and Rich Mixture Strategies.....	168
10.5 Evaluation of the Main Effects of Higher Compression Ratio on PWI and DWI Strategies.....	172
10.5.1 Higher Compression Ratio Geometries Design .....	172

10.5.2 Simulation Results in Non-Reacting Flow Conditions for Higher Compression Ratio .....	173
10.6 Summary.....	174
Chapter 11: PWI and DWI Engine Applications under Reacting Flow Conditions.....	176
11.1 Combustion Simulation Set-up.....	176
11.2 Criteria and Aim of Combustion Simulation Analysis .....	177
11.3 Combustion Simulation without Water Injection .....	180
11.4 Combustion Simulation with Water Injection .....	184
11.4.1 Water Injection Combustion Results - CR 9.5.....	185
11.4.2 Water Injection Combustion Results for Higher Compression Ratio .....	189
11.4.3 Effects of Stroke to Bore Ratio Increase from 1.01 to 1.13 on Best PWI CR 10.5 Strategy.....	191
11.5 Summary.....	195
Chapter 12: Conclusion and Future Direction .....	199
Acknowledgments.....	200
References.....	201

# List of Figures

Figure 1. Trends in EU-28 emissions for road transport sector (% of 2000 levels) [1] .....	17
Figure 2. Contribution to EU-28 emissions for the main source sectors in 2017 [2] .....	18
Figure 3. Euro emission limits [3] .....	19
Figure 4. CO <sub>2</sub> regulation trends [3] .....	19
Figure 5. Discrepancy between laboratory and real data emissions EURO 5 and 6 for different passenger cars [4] .....	20
Figure 6. NEDC and WLTC homologation cycles [4] .....	21
Figure 7. Emission Cycles comparison [5].....	22
Figure 8. CO emission increase due to the richer mixture for component protection [7].....	24
Figure 9. ICE possible future trend [7].....	25
Figure 10. Stratified fuel techniques [10].....	27
Figure 11. Miller and Atkinson cycles [9].....	27
Figure 12. Schematic representation of a LP-EGR circuit (left) and a HP-EGR circuit (right) [21].....	29
Figure 13. Water Injector Locations [52].....	35
Figure 14. PWI close to intake valve [52] .....	36
Figure 15. DWI stratified solution [59] .....	39
Figure 16. AC Water recovery system [69].....	40
Figure 17. Exhaust Water Recovery system [69].....	41
Figure 18. Water Surface Recovery system [69] .....	42
Figure 19. Water versus iso-octane fluid properties.....	45
Figure 20. Classification of modes of disintegration [73].....	47
Figure 21. Ohnesorge-Reynolds diagram with expected primary breakup regions for iso-octane and water for various injection pressure [72] .....	47
Figure 22. Droplet break-up regime .....	49
Figure 23. Water and iso-octane We comparison as a temperature (on the left) and relative velocity (on the right) function.....	50
Figure 24. Water and iso-octane We breakup time comparison, assuming constant reference conditions in terms of SMD and $U_r$ .....	51
Figure 25. Variation of temperature and gas concentration during droplet evaporation [73] .....	52
Figure 26. Drop evaporation time: water and iso-octane comparison .....	54
Figure 27. Heat capacity ratio example for different mixture condition in a GDI turbocharged engine .....	55
Figure 28. Maximum cooling effect for PWI-like condition system .....	56
Figure 29. Water LHV as a function of pressure.....	57
Figure 30. Theoretical cooling effect for different pressure conditions and s values.....	58
Figure 31. Air relative humidity variation between ambient air and PWI injection point for three temperature levels .....	60
Figure 32. Maximum s value before reaching saturation point for different ambient RHU.....	60
Figure 33. LFS water effect using the ETRF reaction scheme by Seidel [88] .....	61
Figure 34. Water effects on IDT [89] .....	62

Figure 35. Atomization model representation .....	67
Figure 36. Regime map of the spray-wall interaction according to Kuhnke [90].....	69
Figure 37. ECFM3Z scheme .....	72
Figure 38. Thermal wall function comparison in a low-bmep engine case.....	75
Figure 39. Comparison between PoliMI and PoliMI-reduced mechanisms with experimental data [] for the prediction of LFS of PF87 at P=20 bar, T=353 K [123] .....	81
Figure 40. Comparison between PoliMI and LLN against experimental [124] LFS data for TAE7000 surrogate at T=358 K, P =1 bar.....	81
Figure 41. TAE 7000 undiluted mixture: effect of different engine-like thermophysical conditions and equivalence ratio on LFS.....	82
Figure 42. Water effect on LFS: P = 50 bar, T = 600 K, EGR 5% .....	83
Figure 43. Water effect on LFS: P = 90 bar, T = 700 K, EGR 5%, focus on $\Phi$ variation .....	83
Figure 44. Water effect on LFS: P = 50 bar, $\Phi=1$ , EGR 5%, focus on T variation .....	83
Figure 45. Water effect on LFS: T = 700 K, $\Phi=1$ , EGR 5%, focus on P variation .....	84
Figure 46. Water and EGR effect comparison on LFS.....	84
Figure 47. Water effect on LFT calculated with Blint's correlation[120].....	85
Figure 48. pure Water and pure EGR effects on LFT calculated with Blint's correlation [120].....	85
Figure 49. Ignition delay time of surr_A for different equivalence ratios and temperatures at P=50 bar .....	87
Figure 50. Ignition delay time of surr_A for different EGR mass fractions and temperatures at P=20 bar .....	87
Figure 51. TAE7000 IDT: effect of pressure, temperature and mixture without diluents .....	89
Figure 52. EGR and Water dilution effects on IDT for $\Phi=1$ .....	89
Figure 53. IDT: EGR and water effects at $\Phi =1.0$ , P = 75 bar, T=1100 K.....	89
Figure 54. IDT: EGR and water effects at $\Phi =1.0$ , P = 75 bar, T=950 K.....	90
Figure 55. IDT: EGR and water effects at $\Phi =1.0$ , P = 75 bar, T=650 K.....	90
Figure 56. IDT: EGR and water effects at $\Phi =0.5$ , P = 75 bar, T=650 K.....	90
Figure 57. Pure Water and EGR effect on IDT at $\Phi=1$ , P= 75 bar and T= 950 K .....	91
Figure 58. Pure Water and EGR effect on IDT at $\Phi=1$ P= 75 bar and T= 650 K .....	91
Figure 59. Schematic representation of a momentum flux device [133].....	94
Figure 60. Flow nozzle conditions: ideal vs real distributions .....	95
Figure 61. Experimental facility layout.....	97
Figure 62. Momentum Flux for $P_{inj}$ 4, 6, 8 bar, $T_{fluid}$ 25°C and BP 1 bar.....	98
Figure 63. Momentum Flux signal filtered, $P_{inj}$ 8 bar, $T_{fluid}$ 25°C and BP 1 bar .....	98
Figure 64. Mean Momentum Flux $P_{inj}$ 4, 6, 8 bar, $T_{fluid}$ 25°C and BP 1 bar .....	99
Figure 65. ROI for injection pressure of 8 bar, 25°C and BP 1 bar.....	99
Figure 66. Mean Rate of Injection, $P_{inj}$ 4, 6, 8 bar, $T_{fluid}$ 25°C and BP 1 bar .....	99
Figure 67. PDA layout .....	100
Figure 68. Example of raw PDA data @30 mm .....	102
Figure 69. Number of drops and SMD distributions @30 mm.....	103
Figure 70. Mean SMD @50 mm .....	103
Figure 71. Number of drops and SMD recorded @30 mm and @50 mm, $P_{inj}$ 8 bar, $T_{fluid}$ 25°C .....	104
Figure 72. Droplet velocity distributions @30 mm .....	104
Figure 73. PDF @30 mm for different injection pressure .....	105
Figure 74. Droplet $D_{32}$ : CFD vs Experimental results for $P_{inj}$ 4 bar at 30 mm and 50 mm .....	108

Figure 75. Droplet $D_{32}$ : CFD vs Experimental results for $P_{inj}$ 8 bar at 30 mm and 50 mm .....	108
Figure 76. Droplet $D_{32}$ : CFD vs Experimental results for $P_{inj}$ 4 and 8 bar .....	109
Figure 77. Water mass evaporation, $P_{inj}$ 4 bar and 8 bar .....	109
Figure 78. We number of the droplet for $P_{inj}$ 4 bar (left) and 8 bar (right) .....	109
Figure 79. Droplet Velocity: CFD vs Experimental results for $P_{inj}$ 4 bar at 30 mm and 50 mm .....	110
Figure 80. Droplet Velocity: CFD vs Experimental results for $P_{inj}$ 8 bar at 30 mm and 50 mm .....	110
Figure 81. Injector plumes representation [136] .....	112
Figure 82. Injector holes distribution and diameters [136].....	112
Figure 83. Rosin-Rammler distribution for $P_{inj}$ 9 bar: SMD 90 $\mu\text{m}$ , $d_{10}$ 51 $\mu\text{m}$ .....	112
Figure 84. Experimental spray imaging visualisation [136] .....	113
Figure 85. Representation of the double spray cone .....	113
Figure 86. CFD vs Experimental $d_{32}$ validation @30 mm and @60 mm .....	114
Figure 87. Focus on $d_{32}$ differences on PDA planes between CFD and Experimental results .....	114
Figure 88. Drops We distribution .....	115
Figure 89. Drops Temperature distribution.....	115
Figure 90. Rosin-Rammler distribution for $P_{inj}$ 9 bar: SMD 60 $\mu\text{m}$ $d_{10}$ 35 $\mu\text{m}$ .....	116
Figure 91. CFD vs Experimental $d_{32}$ validation @30 mm and @60 mm (4 bar on the top, 8 bar on the bottom).....	116
Figure 92. Spray penetration validation .....	117
Figure 93. Virtual engine configuration.....	119
Figure 94. Fuel Spray layout .....	119
Figure 95. Fuel injection profiles .....	120
Figure 96. Inlet and exhaust valve lifts .....	121
Figure 97. Engine spatial discretization .....	122
Figure 98. Cylinder air mass evolution (half geometry) .....	124
Figure 99. In-cylinder Tumble ratio: intake stroke (left), compression stroke (right).....	124
Figure 100. Tumble vortex formation .....	125
Figure 101. In-cylinder cross Tumble.....	126
Figure 102. In-cylinder swirl .....	126
Figure 103. Turbulent intensity during the compression stroke .....	126
Figure 104. Turbulent intensity distribution at 710 CA deg., $\lambda$ 1.0 .....	127
Figure 105. Mean In-Cylinder mixture distribution close to TDC.....	127
Figure 106. In-Cylinder mixture standard deviation close to TDC.....	128
Figure 107. Mixture index distribution under spark plug (sphere radius 10 mm) close to TDC .....	128
Figure 108. Mixture index standard deviation under spark plug (sphere radius 10 mm) close to TDC.....	128
Figure 109. Equivalence ration distribution @710 CA deg., $\lambda$ 0.75 (top left), $\lambda$ 0.85 (top right), $\lambda$ 1.0 (bottom) .....	129
Figure 110. EGR distribution @710 CA deg., $\lambda$ 0.75 (top left), $\lambda$ 0.85 (top right), $\lambda$ 1.0 (bottom) .....	130
Figure 111. Wallfilm generation: percentage w.r.t the total fuel mass injected .....	131
Figure 112. Fuel evaporation rate .....	131
Figure 113. Mean In-cylinder temperature .....	131
Figure 114. GDI Spray evolution .....	132
Figure 115. Virtual engine PWI configuration .....	135

Figure 116. PWI Spray targeting .....	135
Figure 117. PWI droplets passing through the intake valve curtain area on the exhaust side .....	137
Figure 118. In-Cylinder STD mixture distribution for different PWI strategies .....	138
Figure 119. Spark plug mixture index distribution for different PWI strategies .....	138
Figure 120. Spark plug STD mixture distribution for different PWI strategies .....	138
Figure 121. Percentage of water mass close to spark plug .....	139
Figure 122. PWI effect on tumble ratio during intake stroke (on the left) and compression stroke (on the right) .....	140
Figure 123. PWI effect on in-cylinder mean turbulent intensity .....	140
Figure 124. Tumble and Fuel-Water Spray interaction .....	141
Figure 125. PWI effect on turbulent intensity close to the spark plug .....	141
Figure 126. Turbulence field at 700 CA deg., PWI 10 bar, s 0.3 SOI 293 .....	142
Figure 127. Temperature variation w.r.t $\lambda$ 1.0 case – $\lambda$ 0.75 $\lambda$ 0.85 and PWI 10 bar strategies comparison	143
Figure 128. PWI 10 bar system: water evaporation rate .....	143
Figure 129. PWI 10 bar: Water-fuel liquid reaming in spray cloud .....	144
Figure 130. PWI 10 bar: Water wallfilm formation .....	144
Figure 131. Wallfilm formation areas on intake walls: s 02 SOI 363 (on the left) and s 02 SOI 293 (on the right) .....	145
Figure 132. PWI cooling efficiency for the least advanced SOI .....	145
Figure 133. Temperature variation w.r.t $\lambda$ 1.0 case – $\lambda$ 0.75 $\lambda$ 0.85 and PWI 20 bar strategies comparison	146
Figure 134. PWI 20 bar system: water evaporation rate .....	146
Figure 135. PWI 20 bar: water-fuel liquid reaming in spray cloud .....	146
Figure 136. PWI 20 bar: In-Cylinder water wallfilm formation .....	147
Figure 137. Temperature variation w.r.t $\lambda$ 1.0 case – $\lambda$ 0.75 $\lambda$ 0.85 and PWI 10 bar - 20 bar strategies, s 0.2 .....	147
Figure 138. PWI 10 bar - 20 bar systems: water evaporation rate .....	148
Figure 139. PWI 10 bar -20 bar: Water-fuel liquid reaming in spray cloud .....	148
Figure 140. PWI 10 bar - 20 bar: In-Cylinder Water wallfilm formation .....	148
Figure 141. PWI 10 bar - 20 bar cooling efficiency .....	149
Figure 142. Temperature difference at TDC w.r.t $\lambda$ 1.0 only-fuel case, for different RHU values .....	150
Figure 143. Percentage of evaporated water: comparison between DRY air and different RHU values .....	150
Figure 144. Percentage of water wallfilm: comparison between DRY air and different RHU values .....	150
Figure 145. PWI strategy: stroke/bore ratio effect on temperature reduction .....	152
Figure 146. Heat transfer comparison between S/B 1.01 and S/B 1.13 .....	152
Figure 147. PWI strategy: bore/stroke ratio effects on Tumble ratio (intake stroke) .....	153
Figure 148. PWI strategy: stroke/bore ratio effects on Tumble ratio (compression stroke) .....	153
Figure 149. PWI strategy: stroke/bore ratio effects on turbulent intensity .....	153
Figure 150. Tumble motion residual at 700 CA deg., S/B 1.01 (on the left) and S/B 1.13 (on the right) .....	154
Figure 151. Turbulence kinetic energy at 700 CA deg., S/B 1.01 (on the left) and S/B 1.13 (on the right) ..	154
Figure 152. DWI engine design .....	156
Figure 153. DWI Spray targeting .....	157
Figure 154. Mean In-Cylinder quality mixture .....	158
Figure 155. In-Cylinder STD mixture distribution .....	159

Figure 156. Mean quality mixture close to sprak plug .....	159
Figure 157. STD mixture distribution close to spark plug.....	159
Figure 158. Cylinder temperature variation w.r.t $\lambda$ 1.0 case – Injection law centre comparison.....	160
Figure 159.Evaporation rate: Injection law centre comparison.....	160
Figure 160.Water wall film: Injection law centre comparison .....	161
Figure 161. Effect of injection law on Tumble Ratio: Intake stroke .....	161
Figure 162. Effect of injection law on Tumble Ratio: Compression stroke .....	162
Figure 163. Effect of injection law on In-cylinder turbulent intensity.....	162
Figure 164.DWI strategy: in-cylinder mixture quality index.....	164
Figure 165. DWI strategy: mixture quality index close to spark plug.....	164
Figure 166. DWI strategy: DWI strategy: in-cylinder mixture index STD .....	164
Figure 167. DWI strategy: mixture index STD close to spark plug .....	165
Figure 168. Percentage of water mass close to spark plug .....	165
Figure 169. DWI strategies: temperature variation at TDC.....	166
Figure 170.DWI best strategies: cooling efficiency .....	166
Figure 171. DWI strategies: water evaporation rates .....	166
Figure 172. DWI strategies: wallfilm formation .....	167
Figure 173. DWI strategies: Tumble motion, intake stroke (on the left) and compression stroke (on the right) .....	167
Figure 174.DWI strategies: In-cylinder mean turbulent intensity.....	168
Figure 175. DWI strategies: Mean turbulent intensity close to spark plug.....	168
Figure 176. Temperature variation at TDC: PWI, DWI, rich mixture comparison .....	169
Figure 177. Cooling efficiency at TDC: PWI and DWI comparison.....	170
Figure 178. Evaporation rate: PWI and DWI comparison.....	170
Figure 179. Percentage of water mass under the spark plug: PWI and DWI comparison .....	170
Figure 180. PWI and DWI strategies: mixture index STD close to spark plug .....	171
Figure 181. PWI and DWI strategies: Tumble motion comparison .....	171
Figure 182. DWI strategy: in-cylinder turbulent intensity comparison.....	171
Figure 183. On the top, PWI CR 9.5 (left) PWI CR 10.5 (right), on the bottom DWI CR 9.5 (left) DWI CR 10.5 (right).....	172
Figure 184. PWI vs DWI strategies: compression ratio effect on temperature reduction at TDC .....	173
Figure 185. PWI vs DWI strategies: compression ratio effect on Tumble ratio .....	173
Figure 186. In-cylinder turbulent intensity of W1-W7 and rich fuel strategies in non-reacting conditions at 700 CA deg.....	179
Figure 187. Temperature reduction at TDC of W1-W7 and rich fuel strategies in non-reacting conditions	179
Figure 188. Mixture distribution close to spark plug of W1-W7 and rich fuel strategies in non-reacting conditions .....	180
Figure 189. MAPO vs MFB50 only-fuel combustion cases .....	181
Figure 190. MAPO vs exhaust temperature only-fuel combustion cases .....	181
Figure 191. Combustion heat release, only-fuel combustion cases, SA 706 CA deg.....	181
Figure 192. Pressure sensor, only-fuel combustion cases, SA 706 CA deg. ....	182
Figure 193. Mixture auto-ignition region at 736 CA deg. for the case $\lambda$ 1.0 with SA 706 CA deg.....	182

Figure 194. Normalized IMPEH vs MFB50 crank angle (on the left) and vs SA (on the right) for fuel-only simulations .....	183
Figure 195. Laminar flame speed evolution: fuel-only simulations .....	183
Figure 196. Combustion flame propagation at 720 CA deg. and 725 CA deg., $\lambda$ 0.75 (top), $\lambda$ 0.85 (centre) and $\lambda$ 1.0 (bottom), SA 706 CA deg.....	184
Figure 197. Normalized IMPEH vs MFB50 crank angle (on the left) and SA (on the right): PWI, DWI and fuel-only strategies .....	186
Figure 198. MAPO vs MFB50: PWI, DWI and fuel-only strategies.....	187
Figure 199. MAPO vs exhaust gas temperature: PWI, DWI and fuel-only strategies .....	187
Figure 200. MFB10-MFB50 vs MFB50: PWI, DWI and fuel-only strategies.....	187
Figure 201. MFB50-MFB90 vs MFB50: PWI, DWI and fuel-only strategies.....	188
Figure 202. Unburnt temperature: PWI, DWI and fuel-only strategies .....	188
Figure 203. Flame front propagation $\lambda$ 1.0 SA 706 CA deg. without water (left), PWI s 0.3 (right) .....	188
Figure 204. Normalized IMPEH vs MFB50 crank angle (on the left) and SA (on the right): CR 9.5 and 10.5	189
Figure 205. MAPO vs MFB50: PWI, DWI and fuel-only strategies, CR 9.5 and 10.5 .....	190
Figure 206. MAPO vs exhaust gas temperature: PWI, DWI and fuel-only strategies, CR 9.5 and 10.5 .....	190
Figure 207. MFB10-MFB50 vs MFB50: PWI, DWI and fuel-only strategies, CR 9.5 and 10.5.....	190
Figure 208. MFB50-MFB90 vs MFB50: PWI, DWI and fuel-only strategies, CR 9.5 and 10.5.....	191
Figure 209. In-Cylinder turbulence kinetic energy at SA 706 CA deg. ....	191
Figure 210. Normalized IMPEH vs MFB50 crank angle (on the left) and SA (on the right): PWI S/B 1.01 and 1.13 .....	192
Figure 211. MAPO vs MFB50: fuel-only strategies and PWI S/B 1.01 and 1.13 .....	193
Figure 212. MAPO vs exhaust gas temperature: fuel-only strategies and PWI S/B 1.01 and 1.13 .....	193
Figure 213. MFB10-MFB50 vs MFB50: fuel-only strategies and PWI S/B 1.01 and 1.13 .....	193
Figure 214. MFB50-MFB90 vs MFB50: fuel-only strategies and PWI S/B 1.01 and 1.13 .....	194
Figure 215. Flame surface and turbulence kinetic energy on the flame front: comparison between PWI S/B 1.01 and S/B 1.13 cases for SA 706 CA deg. ....	194
Figure 216. Heat transfer comparison between PWI S/B 1.01 and S/B 1.13 cases for SA 706 CA deg.....	195
Figure 217. Knock Safe SA for all the cases tested .....	195
Figure 218. Normalized IMPEH at Knock Safe SA for all the cases tested.....	196
Figure 219. Exhaust gas temperature at 800 CA deg. ATDC, at Knock Safe SA, for all case tested .....	196
Figure 220. MFB50 at Knock Safe SA for all the cases tested.....	196

# List of Tables

Table 1. Main differences between NEDC and WLTP cycles .....	21
Table 2. Main SI technologies [9] .....	26
Table 3. Fluid properties at 25°C and 1 bar .....	44
Table 4. Atomization breakup time and drop SMD, based on Reitz work[75].....	48
Table 5. Composition of the analysed surrogate.....	77
Table 6. Chemical kinetics mechanisms .....	80
Table 7. Breakpoints used for generating the dataset of LFS.....	82
Table 8. Breakpoints used for generating the dataset of IDT.....	88
Table 9. Test Conditions .....	96
Table 10. Injector Layout .....	102
Table 11. Injection test conditions .....	102
Table 12. Instrumentation used for PDA tests .....	102
Table 13. Main injector settings .....	107
Table 14. Spray Models adopted.....	107
Table 15. Injector features and test conditions [136] .....	111
Table 16. GDI fuel injector features .....	120
Table 17. Engine features .....	120
Table 18. Engine working conditions.....	121
Table 19. Simulation duration and model adopted.....	122
Table 20. GDI and PWI injector features .....	135
Table 21. PWI system: analysed cases.....	136
Table 22. PWI system: fuel and water mass injected.....	137
Table 23. GDI and DWI injector features.....	157
Table 24. DWI injection law centre tested .....	158
Table 25. DWI configurations tested.....	163
Table 26. Fuel and water mass introduced for the DWI strategies.....	163
Table 27. Combustion simulation set-up and models.....	177
Table 28. List of water injection cases examined in reacting flow conditions .....	178
Table 29. Fuel and water mass injected .....	178
Table 30. Injection strategies .....	179



# Introduction

Climate change and gaseous emissions environmental impact are two of the most critical issues that world population is currently facing. The road transportation sector is found to be one of the most contributors to those.

On April 17th 2019, the European Parliament and the Council issued the Regulation (EU) 2019/631 introducing CO<sub>2</sub> emission performance standards for new passenger cars and new vans for 2025 and 2030. Car engine are responsible of around 12% of the total EU emission of carbon dioxide in atmosphere. In addition, from 2021, phased in from 2020, the EU fleet-wide average emission target for new cars will be 95 g CO<sub>2</sub>/km and a penalty fee of €95 every g/km for exceeding this limit. This CO<sub>2</sub> concentration released to atmosphere corresponds to a fuel consumption of around 4.1 l/100 km of gasoline. In this scenario, the demand to reduce even all the other pollutants has introduced a more stringent homologation cycle, the dynamic RDE cycle, which is now mandatory for all newly type-approved passenger car models, covering higher engine load and speed for different driving conditions.

For these reasons, nowadays engineers aim to design engines with lower fuel consumption and emissions, in order to cope with the continuous updating of the international emission regulations. This has led to a review of the engine working conditions across the overall operating map and the adoption of different Auxiliary Emission Strategies (AES).

The development of technologies aimed to increase engine efficiency are the current guidelines for new engine concept design and one of the main current topics is the replacement or reduction of the fuel enrichment under specific engine conditions. Currently the application of fuel enrichment strategy is used for component protection (i.e., Turbine Inlet Temperature control) thanks to the evaporation of fuel and the following reduction of the in-cylinder fresh charge temperature. Moreover, the same strategy is used to suppress abnormal combustion events. The boost pressure and the high downsizing level that characterize modern engines, necessary to ensure high efficiency and high power, have led to the increase of the in-cylinder pressure and temperature, promoting the knock onset/development and the raise of turbine inlet temperature (TiT), especially at medium/high load conditions. Among them, the full power condition represents the most demanding engine points.

However, the use of a rich mixture strategy results in a dramatic increase of raw emissions, especially CO emissions, because they cannot be handled by the three ways catalyst (TWC), so new solutions need to be pursued to cope with new emission standard.

In this scenario the water injection technology represents a possible solution to meet the demand for high power and low emissions in the development of future engines. The aim is to replace the fuel enrichment with water injection, exploiting its high latent vaporization heat reducing the maximum temperatures in the combustion chamber. Water injection can therefore be a valid technology to analyse and optimize to preserve the engine from knock and exhaust gas temperatures too high for the turbine materials. Moreover, this technology can be combined with those already known and currently used in the most advanced engines, such as the use of over-expansion cycles (Miller or Atkinson), cooled EGR, advanced turbochargers, new ignition systems, variable compression ratio and the search for alternative fuels.

However, it must be considered that the injection of water changes both the thermodynamic (due to the temperature reduction) and the chemical behaviour of the mixture. Therefore, it is necessary to carefully evaluate these two effects that could also mitigate the potential benefits of water injection or even lead the engine to worse working conditions.

The objective of this doctoral thesis is to assess, for a high-bmep GDI engine, both PWI (Port Water Injection) and DWI (Direct Water Injection) architectures from a thermo-fluid dynamics point of view also under

reacting flow conditions, through three-dimensional CFD (Computational Fluid Dynamic) simulations. One of the main scientific contribution consists in the development of a complete methodology, especially from a chemical point of view, for the simulation and analysis of PWI and DWI systems. Through detailed chemical kinetics simulations, new databases have been extracted to take into account the effects of the injected water, separated from the EGR, in the calculation of the laminar speed, the flame thickness and the auto-ignition time. In addition, for the PWI technology, which might be the most promising technology for a rapid placing on the market, experimental tests, conducted during the internship abroad, have been performed for the complete characterization of the spray and the validation of numerical spray models. The main CFD approach used in the simulations is the RANS (Reynolds-averaged Navier–Stokes), together with the ECFM-3Z combustion model for reacting flow conditions.

The analysis were performed considering the real short-term applicability of both PWI and DWI technologies, as injection pressure and water consumption, highlighting the advantages and disadvantages of both architectures, imposing specific performance and safe condition targets in order to identify the best feasible strategies.

A brief summary of the main topics that will be presented in this thesis is here provided as an introductory guide to the thesis, underlining the contribution of each chapter.

Chapter 1 provides an overview of the global scenario within which combustion engines are developing, taking into account the new pollution regulations and the most advanced solutions currently considered for the engine design. Chapter 2 is dedicated to the state of the art of the water injection technology and it reviews the scientific literature in order to emphasize on which issues the scientific community has put more effort until now. To understand the fundamental thermodynamic effects of water and spray dynamics, Chapter 3 describes the physical properties of water compared with those of fuel, defining the cooling efficiency parameter, useful for the detailed analysis of simulations. Chapter 4 and 5 are dedicated to the methodology used for the CFD simulations development. The first one describes the main models adopted underlining where some modifications have been made over the basic models, while Chapter 5 is reserved to the analysis of the chemical effects of water on the laminar speed, the flame thickness and the auto-ignition times through detailed chemical kinetics simulations and the creation of new databases. An experimental campaign was carried out for the microscopic and macroscopic characterization of a PWI injector, whose data are shown in Chapter 6. Thanks to these results, it was possible to perform a numerical validation of the spray at low injection pressure, by calibrating the spray model parameters. The validation was also repeated using a literature test case. Finally, starting from Chapter 8, the GDI engine under examination and its different geometric configurations are presented. At first the engine is examined without the injection of water, with different fuel mixing strategies in order to highlight the main fluid-dynamic engine features and the cooling target. Chapters 9 and 10 are dedicated to the simulations with PWI and DWI architectures respectively, under non-reacting flow conditions, varying a series of parameters such as: injection pressure, SOI/EOI and injected water mass. The best configurations, both PWI and DWI are then analysed under reacting flow conditions in Chapter 11, verifying the possible performance gain, keeping the MAPO index and the exhaust gas temperature below the maximum imposed thresholds. The conclusions and possible future directions are described in the last Chapter 12.

# Chapter 1: Global Engine Scenario

## 1.1 Introduction

Over the last decades, all the air quality reports have shown a significant reduction of the pollutant emission increase in all major sectors: industry, energy production, transport and agriculture [1]. As an example, Figure 1 shows the trend of major transport emissions up to 2017 in Europe. Despite transported passengers and freight volumes have been gradually increasing, the percentage of pollutants has been drastically reduced. However, the countermeasures are not enough to fully limit the negative effects on the environment and human health. Therefore, the European Union, together with other states around the world, are constantly trying to impose new emission reduction targets.

Air pollution is currently the most important risk to human health, and it is perceived as the second biggest environmental concern for Europeans, after climate change (European Commission, 2017). As a result, there is growing political, media and public interest in air quality issues and increased public support for actions. This includes ongoing citizen science initiatives for air quality monitoring and initiatives targeting public awareness and behavioural changes. This has led to growing support and demand for measures that improve air quality.

In addition to human health, which is of primary importance, air pollution also has a negative impact on climate change and the ecosystem in general. This kind of problems are addressed mainly through the measurement of the annual average temperature increase in the atmosphere and oceans and the concentration of carbon dioxide in the air, as an indicator of the greenhouse effects.

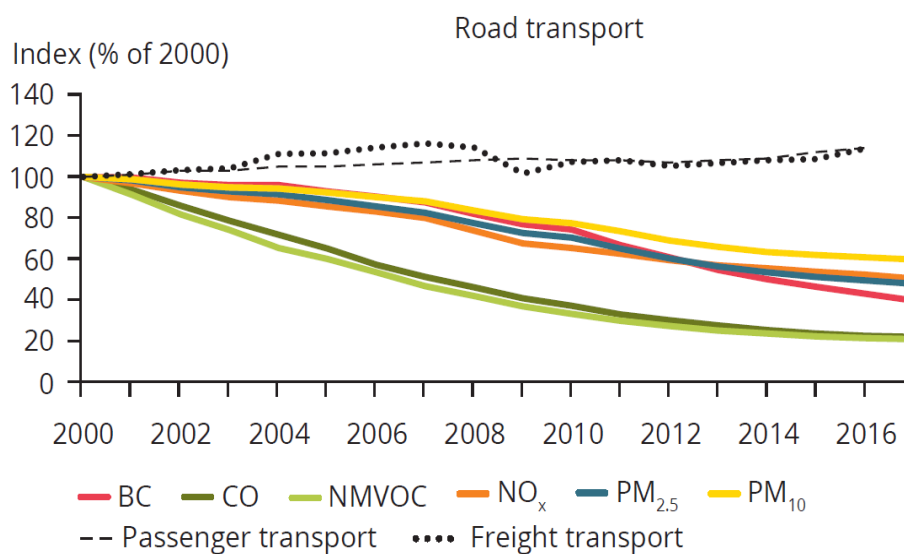


Figure 1. Trends in EU-28 emissions for road transport sector (% of 2000 levels) [1]

A more detail analysis, Figure 2, has been reported: the road transport sector is one of the major contributor of carbon dioxide (CO<sub>2</sub>) (which is indeed a greenhouse gas and not a pollutant), nitrogen oxides (NO<sub>x</sub>) and particulate matters (PM<sub>2.5</sub> and PM<sub>10</sub>). The sector contribution to NO<sub>x</sub> and PM is of particular concern in the urban environment because of the large numbers of people directly exposed.

Vehicle emissions for European passenger cars have been regulated by means of the Euro emission standards since 1992 [2]. Further tightening it was introduced by regulation on carbon dioxide emission because of the contribution to the greenhouse effect. Thanks to the implementation of subsequent European Union Commission directives, relevant reductions of pollutants carbon monoxide (CO), unburned hydrocarbons (HC), NO<sub>x</sub>, PM and particle number (PN) have been achieved along years up to nowadays. As a consequence, the automotive industry has been compelled to develop auxiliary emission control devices (AEC) and strategies for their cars, to ensure a noticeable reduction in pollutant emissions and greenhouse gases (i.e., CO<sub>2</sub>).

While this may appear as a restriction in the development of engines, it lays the foundations for constant product innovation, helping companies to invest in research and development by always looking for new solutions. In the transition to Euro 6, for instance, the gasoline direct injection (GDI) downsized turbo-engines, which have been conceived to drop the engine specific fuel consumption to contribute to accommodate the CO<sub>2</sub> limits, have seen the introduction of particulate filters and the improvement of the injection technologies since they are more prone to particulate engine out emissions than PFI.

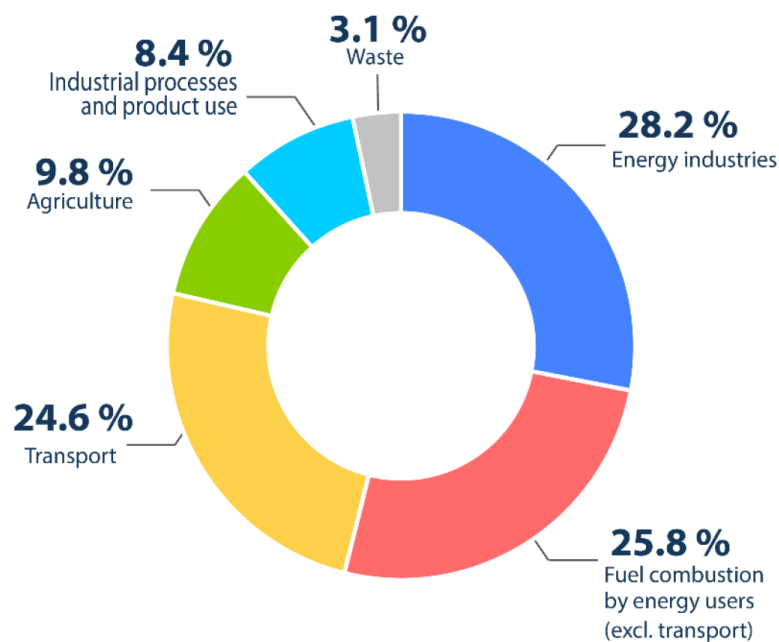


Figure 2. Contribution to EU-28 emissions for the main source sectors in 2017 [2]

## 1.2 Emissions Standards Issued in Europe

The emissions produced by cars and their connection with environmental pollution have been recognized as an important issue since the 1950s. Since then, the link between pollutant emissions of CO, HC, NO<sub>x</sub> and PM and photochemical smog has been highlighted: pollutants are not only dangerous for human health directly but also indirectly, as they play an important role in the generation of some precursors for the formation of PM<sub>2.5</sub> and ozone in the atmosphere, two serious dangerous pollutants for human's health and environment.

It was not until 1970 that the matter was addressed with regulatory action at the European level. Directive 70/220/EEC established emission limits for CO and HC from gasoline-powered vehicles. The landmark directive was amended several times over the following decades to extend its scope. Emission limits for NO<sub>x</sub> were introduced in 1977 (Directive 77/102/EEC), amendments to also cover the gaseous pollutants of diesel vehicles were passed in 1983 (Directive 88/436/EEC), and a particulate mass (PM) emissions limit was introduced for diesel vehicles in 1988 (Directive 88/436/EEC). In 1992, the introduction of what is known today as Euro 1 (Directive 91/441/EEC) marked a new regulatory era for pollution control. Since then, the European Union has moved quickly to further tighten emission limits in the Euro 2 (Directive 96/69/EC), Euro 3 and 4 (Directive 98/69/EC), and Euro 5 and 6 (Regulation 715/2007) standards (Figure 3). Data from remote sensing, a technique for measuring emissions in real driving conditions, comprising hundreds of thousands of light-duty vehicles (LDVs) [3], suggested that Euro standards have been ineffective in reducing the real-world pollutant emissions from vehicles. For example, from 2000 to 2016 (from Euro 3 to Euro 6) the nominal NO<sub>x</sub> limits set by the diesel Euro standards have been reduced by 84%. However, NO<sub>x</sub> emissions from transport have gone down only 32% in the same period.

Country	Topic	2015	2016	2017	2018	2019	2020	2021	2022	2023	2024	2025		
EU	Limits	Euro 6b			Euro 6d temp		Euro 6d		?	? Euro 7				
	CO <sub>2</sub>	130 g/km CO <sub>2</sub>					95 g/km CO <sub>2</sub>							-15%
	Tech. Reg	UN-ECE Reg. 83			EU 2017/1151 (WLTP)									
	EVAP							Euro 6d-temp-EVAP						
	RDE	Monitor			NO <sub>x</sub> 2.1, PN 1.		RDE CF NO <sub>x</sub> 1.43, CF PN 1.5							
	ISC							New procedure incl. RDE, EVAP, -7°C						

Figure 3. Euro emission limits [3]

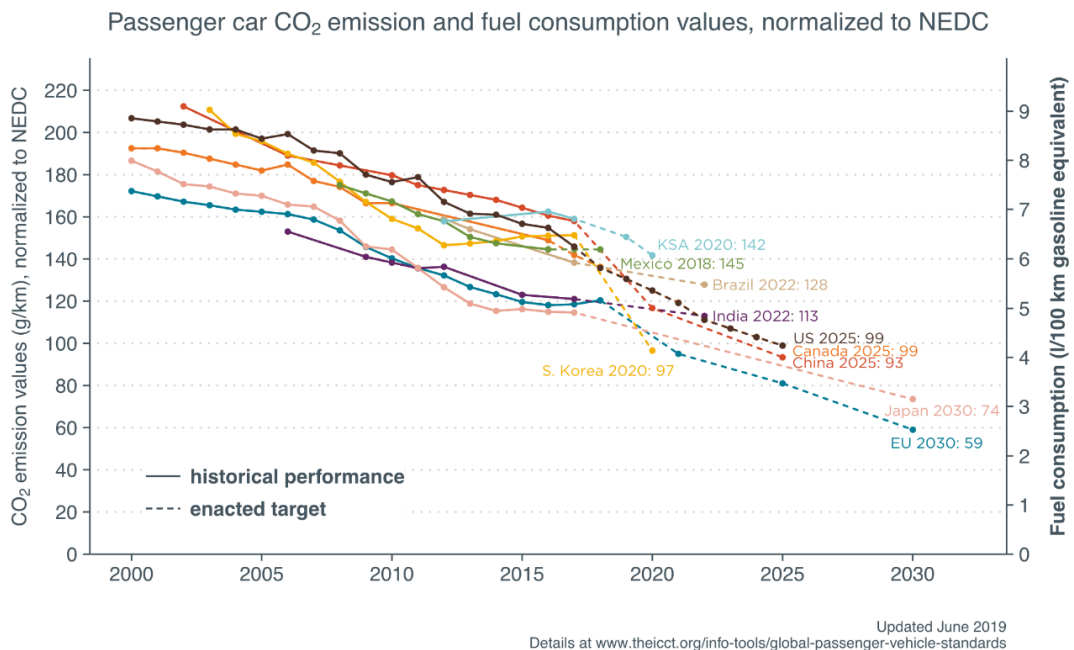


Figure 4. CO<sub>2</sub> regulation trends [3]

Recently, special attention has also been given to carbon dioxide emissions from vehicles. CO<sub>2</sub> is not classified as a real pollutant in the strict sense of the term, but as a determining factor for the greenhouse effect. Carbon dioxide is an unavoidable product of the hydrocarbon fuel combustion and the more is the CO<sub>2</sub> concentration in the exhaust gases the more is the combustion efficiency. The current regulations do not enforce a CO<sub>2</sub> concentration limit to allow the vehicle sale. They require that automotive manufacturers pay a fee when the prescribed threshold (expressed in gCO<sub>2</sub>/km) is exceeded. From 2021 the new regulations will enforce a limit of 95 gCO<sub>2</sub>/km and a penalty fee of €95 every g/km exceeding that limit. Similar trends are also expected for other countries as showed in Figure 4 [3]. Because of these economic penalties, some car manufacturers were forced to withdraw certain engines or even car models from the market, as happened recently at Suzuki with the Jimmy model, whose sales volume were high but the price to pay for exceeding CO<sub>2</sub> emissions did not make it anymore economically affordable.

For this reason, any technology capable of increasing engine efficiency, saving fuel, will increasingly become a crucial point during the development phase of an engine.

### 1.3 Homologation Driving Cycles

In the previous paragraphs an overview on the regulations of the automotive pollutant emission has been presented: now the focus is on the method used to check if the vehicles fulfil these limits. The NEDC (New European Driving Cycle) homologation driving cycle, designed in the 1980s, was used to measure the pollutant emissions of a vehicle and fuel economy up to 2016, performed on a roller test bench. However, this cycle was found to be obsolete and not in line with real data. As proof of this, Figure 5 shows a German study [4] on Nitrogen Oxide emissions (NO<sub>x</sub>) from various car models. It can easily be seen that despite the reduction of mg/km with the Euro 6 standard, there is still a large discrepancy between the emissions evaluated in the laboratory through the NEDC homologation test and the real ones.

The new testing procedure WLTP (world harmonized light-duty vehicles test procedure), which replaces the old lab test NEDC, is based on new test conditions that attempts to reproduce real-world circumstances,

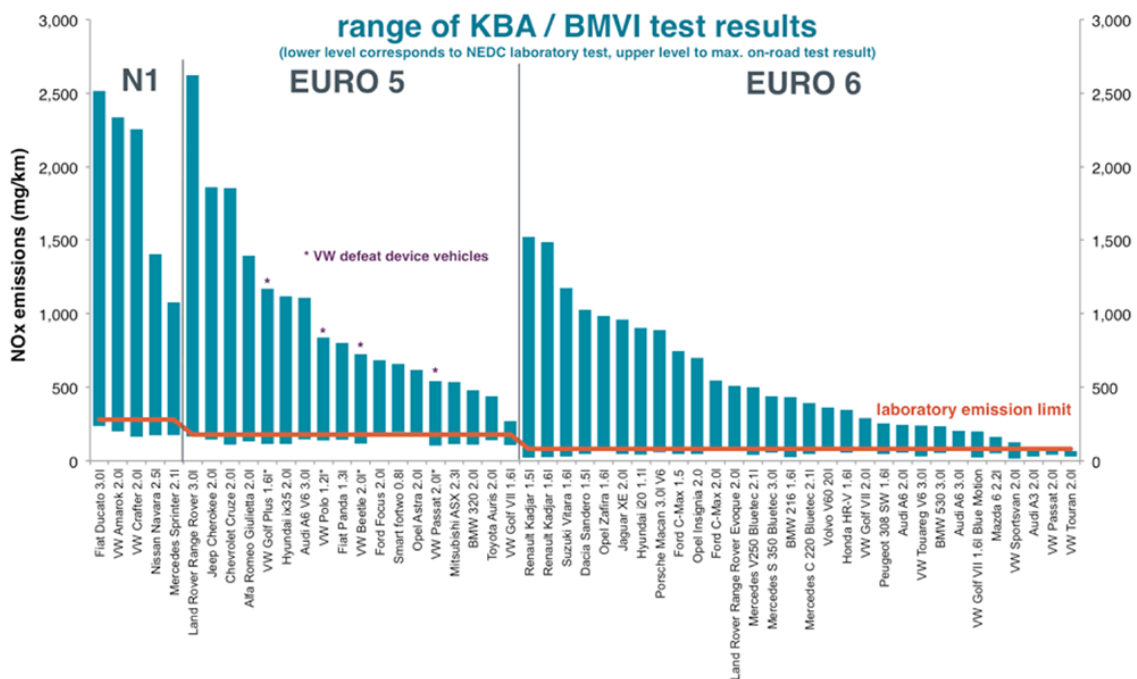


Figure 5. Discrepancy between laboratory and real data emissions EURO 5 and 6 for different passenger cars [4]

which means that the values determined will also have a greater relevance on reality. Among the main changes there are significantly stricter and aggressive test conditions at higher vehicle speeds together with a substantially longer test duration (30 instead of 20 minutes). To obtain a more precise determination of emissions, the new test procedure includes not only standard equipment, as was previously the case, but also all special and auxiliary equipment options of a vehicle to better assess vehicle's consumptions and emissions. In Table 1 and Figure 6, the two homologation cycles NEDC and WLTP are compared.

Despite the great accuracy, deviations are of course also possible with this test procedure. Everyday fuel consumptions and emissions continue to be subjected to the different conditions of topography, climate and personal driving technique. The traffic situation and the use of devices such as the air conditioning system are of further influence on the vehicle emissions. For these reasons, in addition to WLTP, the new RDE cycle (Real Driving Emissions) will also be compulsory for vehicle homologation in the EU, through the use of PEMS

Table 1. Main differences between NEDC and WLTP cycles

Parameter	WLTP	NEDC
Starting temperature	cold	cold
Cycle time	1,800 s	1,180 s
Endurance	242 s	267 s
Stop share	13.4 %	22.6 %
Distance	23,262	10,931
Maximum speed	131.3 km/h	120 km/h
Average velocity	46.5 km/h	33.35 km/h
Temperature	23 °C	25+/-5 °C

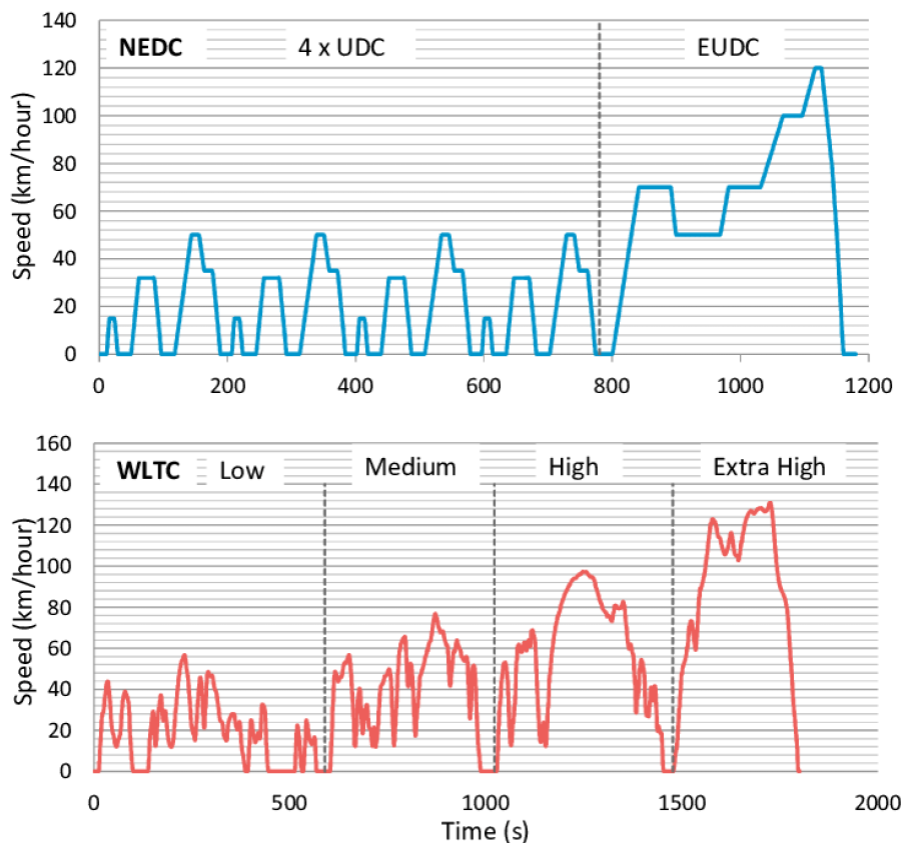


Figure 6. NEDC and WLTC homologation cycles [4]

(Portable Emission Measuring Systems). The latter are complex equipment that integrate advanced gas analysers, exhaust mass flow meters, weather station, Global Positioning System (GPS) and a connection to the vehicle network.

In these RDE tests, the pollutant emissions, such as particulate matter and nitrogen oxides, are measured directly on the road. RDE cycles, unlike standard test cycles (NEDC, WLTC etc.) consist of aggressive, real-life dynamic driving events. A comparison of the main emission cycles, including a possible RDE cycle, are presented in Figure 7 [5]. Clearly, the engine operating conditions are more severe in a dynamic RDE cycle as pointed by the higher engine load and speed covered. This method determines the average emission values that can be expected during everyday driving. The route comprises three sections: urban (approx. 34% of total distance), countryside (approx. 33%) and motorway (approx. 33%). The vehicle must remain at an altitude of between zero and 700 meters above sea level and the ambient temperature between +3°C and +30°C.

The most challenging part of RDE cycle for both spark ignited and Diesel engines is the fact that engine operation may likely included full power or at least very high engine speeds and loads. As a matter of fact, some strategies applied (or not applied), used in the engine map up to now, may be required to be completely revised. In particular, in the case of GDI turbo-engines, the next paragraph enters into the detail of EU commission policy assessment of calibration and engine strategies during the whole homologation test cycle procedures, including the RED part and how they may affect heavily the engine design.

The implementation of the RDE cycle is scheduled in a two-step process:

- (I) From September 2019: mandatory for all newly registered passenger car models: NO<sub>x</sub> emissions may exceed in laboratory conditions by max. 2.1 times (conformity factor (CF)) the measured value according to NEDC cycle and a CF 1.5 for PN (Particular Number), to ensure a technological transition;
- (II) From 1 January 2020, mandatory for all newly type-approved passenger car models with a conformity factor equal to 1.5 (taking into account a measuring tolerance of 0.5).

Restrictions on pollutant emissions from vehicles will therefore become increasingly restrictive, prompting engineers to design more efficient engine and new pollutant reduction systems, acting both inside the cylinder and using innovative after-treatment devices.

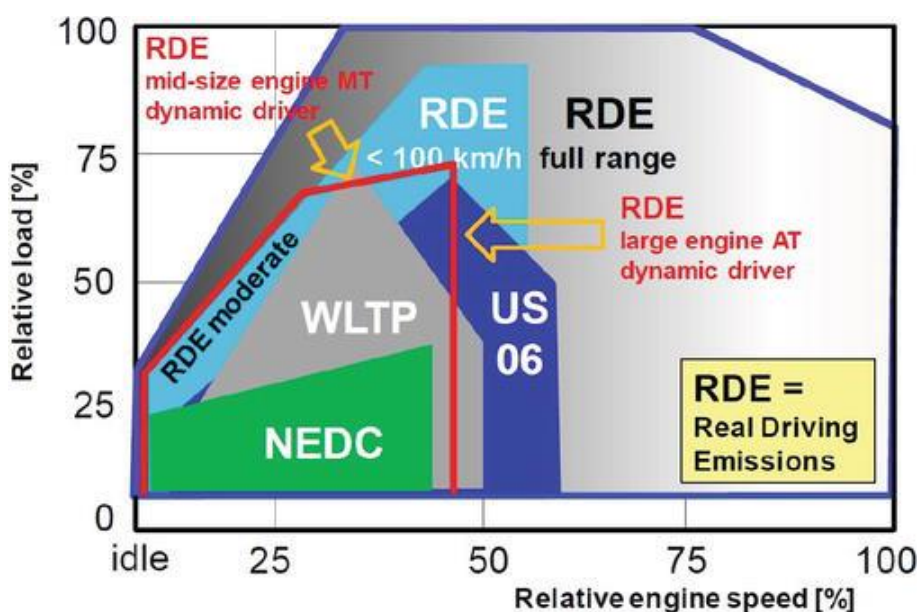


Figure 7. Emission Cycles comparison [5]

## 1.4 Auxiliary Strategies

The European legislation also defines the concept of auxiliary strategies for the control of pollutants, obliging manufacturers to declare any devices implemented for the emission reduction. Specifically, they are divided into three categories.

1. defeat system: any element of design which senses temperature, vehicle speed, engine speed (RPM), transmission gear or any other parameter for the purpose of activating, modulating, delaying or deactivating the operation of any part of the emission control system, that reduces the effectiveness;
2. base emission strategy (BES): means an emission strategy that is active throughout the speed and load operating range of the vehicle unless an auxiliary emission strategy is activated;
3. auxiliary emission strategy (AES): means an emission strategy that becomes active and replaces or modifies a BES for a specific purpose and in response to a specific set of ambient or operating conditions and only remains operational as long as those conditions exist.

In particular, the first category, i.e. the alteration of emission data, is strictly prohibited. The other two categories are instead allowed if they are declared.

With the already known road map for the reduction of the Conformity Factors (CF) for NO<sub>x</sub> and PN between RDE and WLTP values, it is very likely that also CO emissions from S.I. engines under RDE conditions will undergo conformity factor compliance by future integration of the emission legislation. As a matter of fact, the EU Commission notice, issued in January 2017 [6], represents a clear evidence that a new acceptance policy regarding the component protection has been introduced, as that for fuel enrichment. Thus, all those Auxiliary Emission Strategies (AES) that are found to increase emissions might not be authorized in the next future. One of the main examples of auxiliary strategy concerns the use of a rich mixture in the cylinder, under certain operating conditions, in order to thermally preserve some components, in particular the turbine, and reduce the engine knock attitude thanks to the cooling evaporation process. As far as the fuel enrichment for turbine protection is concerned in S.I. engines, the two main disadvantages of using this strategy are the use of more fuel with a consequent decrease in engine efficiency and a higher production of carbon monoxide (CO), due to incomplete oxidation reactions. Figure 8 shows an example of CO emission variation in the RDE cycle due to the use of a rich mixture for thermal component protection [7]. It can be seen that there is a maximum increase of about 600% towards the end of the cycle which cannot be handled by the three ways catalyst (TWC), thus exceeding the possible limits imposed by future legislations, which will tend to impose a CF equal to 1 for all pollutants.

According to the perspective of large CO emissions increase by the use of fuel enrichment and to the above-mentioned EU Commission notice, the development of S.I. engines operating at lambda 1.0 in the overall map is forced and recommended. This new scenario makes the adoption of the water injection very attractive as one of the possible and effective solutions (together with Miller cycle, Advanced Turbocharging and Turbine Technology, Variable Compression Ratio, etc.) to make SI engine operations at lambda 1.0 possible while still fulfilling TiT limits.

This is the primary motivation that led to a deeper knowledge and assessment of the water injection technology in internal combustion engines as a valid and attractive alternative to the mixture enrichment. Many studies have been conducted so far as it will be reported in the next chapter, analysing the state of the art of this technology. Moreover, in the present thesis more emphasis is given to the study of configurations applicable in the short term, with a low economic impact (comparable to PFI systems), trying to minimize the amount of water introduced through the optimization of the evaporation process (at least 90%).

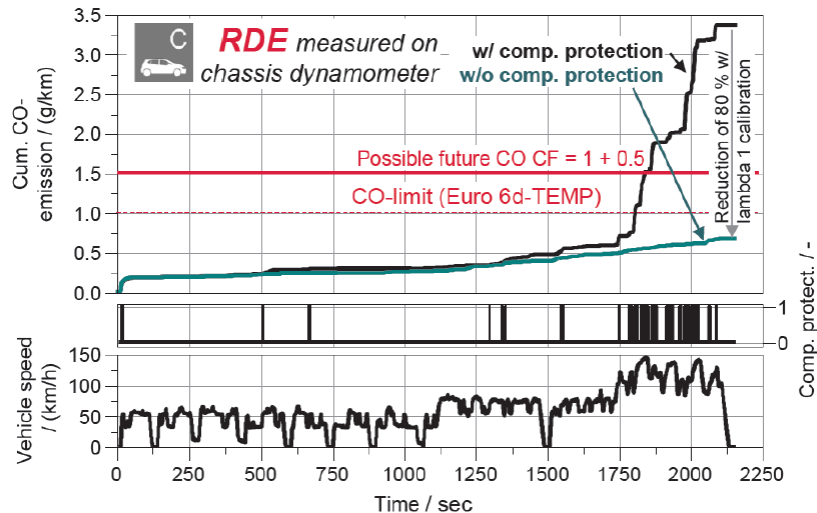


Figure 8. CO emission increase due to the richer mixture for component protection [7]

## 1.5 ICE Future Trends

Before focusing on next generation of ICE SI engines technologies, a very brief overview is provided on the ICE future trends. The recent scandals in the automotive world, concerning polluting emissions, have highlighted the real difficulties of this sector in making an effective contribution to reducing environmental pollution. For this reason, the electrification of transport systems has experienced strong growth, considering them one of the best ways to cope with legislative restrictions and as an effective way of reducing and relocating emissions away from cities. Despite the real impact that internal combustion engines have on air pollution, public opinion seems to blame them, not caring how and what resources energy is used to recharge the batteries of electric vehicles, or how these are disposed of.

It must be highlighted that it is clear that renewable and clean energy sources will be the base for the energy productions in the next future and that electricity will be the primary energy which will be available. This is a ground point since hydrogen-based energy and synthetic fuels will need electricity for their production. Without discussing about infrastructure, renewable energy storage, battery disposal or second life and life cycle assessments, it is very likely that the future mobility will be characterized by a mix of solutions [8], involving battery (BEV, HEV, P-HEV), fuel cell electric vehicles (FCEVs) and conventional vehicles or hybrid electric (Plug-In) vehicles fuelled with synthetic fuels, depending on the consumer acceptance (e.g. cost, fashion, etc), the country considered, the specific application (urban mobility, commuting, heavy duty, etc) and how the mobility will be redesigned. Forecast on the future powertrain it is very difficult because it depends on many parameters like the real transition to renewables (i.e., the sharing of renewable is expected to increase up to 80% to 2050). Despite the expected, albeit moderate, increase in fully electric engines considered to be zero emissions (which indeed depends on the actual sharing of renewables), it is clear that their total expansions will not be able in the short term (2035-2040), to fully replace the internal combustion engines fuelled with hydrocarbons, at least in the commercial transport sector, due to the weight and cost of batteries. Application of fuel cells in these sectors is nowadays on-going since the volume requirements for the hydrogen storage can be affordable in heavy duty vehicles including trucks. In the short-term future, combustion engines, running on petroleum-based liquid fuels, will largely continue to power transport of the world's goods and services and a transition from the gasoline or diesel ICE to a full gasoline/diesel hybrid can significantly reduce emissions. A Mazda forecast would confirm this outlook as shown in Figure 9 [7].

It has been estimated [5] that, thanks to future technologies, fuel consumption could even be halved compared to today and consequently CO<sub>2</sub> emissions.

# IMPORTANCE OF REDUCING CO<sub>2</sub> FROM COMBUSTION ENGINES

THE COMBUSTION ENGINE WILL HELP POWER THE MAJORITY OF VEHICLES GLOBALLY FOR MANY YEARS TO COME AND CAN MAKE THE BIGGEST CONTRIBUTION TO CO<sub>2</sub> REDUCTION

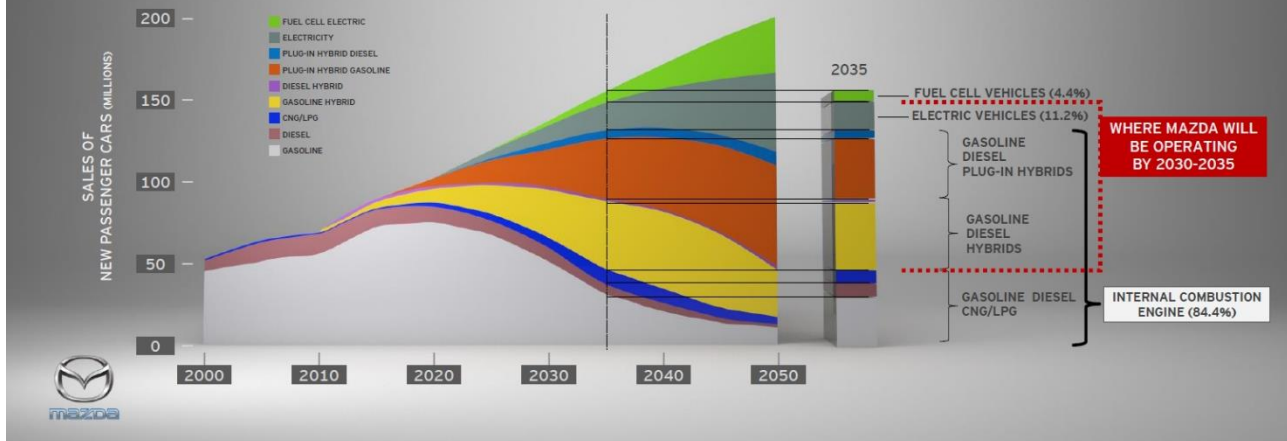


Figure 9. ICE possible future trend [7]

The new after-treatment systems and strategies will allow a reduction of all pollutant emissions reaching the so-called 'zero impact emission vehicle': pollutants will be so low as to be difficult to measure and their real impact on the environment will be negligible.

In the medium to long term the objective is also to design new fuel/engine systems for performance optimization. Single- and dual-fuel technologies, such as homogeneous charge compression ignition (HCCI), premixed controlled compression ignition (PCCI), and reactivity-controlled compression ignition (RCCI) offer significant promise for improving efficiency and reducing unwanted exhaust emissions

Beyond that, it must be considered that the transition to fully renewable energy source does not mean the transition to BEV or fuel cells based powertrain, because of concerns on their full scale applicability (battery/hydrogen volumetric energy density that limits the cruise range, infrastructure availability, safety issue for H<sub>2</sub> application, etc)[8]. The future might include the transition to hybrid-vehicle which will be equipped with advanced ICE fuelled by biofuel or synthetic fuels (including H<sub>2</sub>) produced taking advantage from the renewable energy.

Therefore, despite the difficulties in the forecast, in the short term ICE combustion systems need to be developed and made even more efficient, with a constant development of new technologies to increase efficiency, studying the engine in all its parts: combustion, exhaust treatment systems, control systems and hybridisation.

With this scenario it can be easily understood that internal combustion engines are still far from being replaced by other systems and that their development is still long. Water injection is certainly one of the many strategies that can be studied and optimized to meet the demand of tomorrow's engines in order to reduce emissions and increase performance.

## 1.6 Engine Technologies Description

Modern automotive engines have been pushed to high level of downsizing to comply with more stringent emission legislations and fuel economy general concerns achieved thanks to lower frictions, with a more efficient combustion system, thermo-fluid dynamic and mechanical design. For the sake of completeness, it

must be underlined that the downswing trend is currently revised toward what is called “right-sizing” that means that the engine fluid-dynamics design is developed specifically for a kind class of engines without pushing further to stronger downsizing, and focusing to better efficiency by looking to optimization of the stroke to bore diameter. Moreover, a broader range of operating conditions is pushing the latest engines, towards very high Brake Mean Effective Pressure (*bmep*), whose safe working conditions must be insured. In order to comply with the international legislations, to contrast global pollution, and at the same time to meet the end user's demand for higher performance, various technologies have been used on spark ignition engines. In Table 2 is reported a summary of the main solutions adopted, divided according to whether they are applied on the combustion system or on the intake system. In the following paragraphs the main characteristics of these technologies will be briefly described, leaving a deep analysis for the application of water injection [9].

Table 2. Main SI technologies [9]

Engine subsystem	Technologies
Combustion system	GDI lean combustion
	Miller/Atkinson Cycle
	Variable compression ratio
	Water injection
	Cylinder deactivation
Air system	External EGR
	Multistage Air charge

### 1.6.1 GDI Lean Combustion

Lean combustion, with a stratified charge, is a strategy that significantly increases engine efficiency. The aim is to create a slightly rich mixture under the spark plug, in order to start combustion in an optimal way, and to have a leaner and leaner mixture moving away from the ignition zone towards the peripheral areas of the combustion chamber [10]. The spray is injected into the cylinder later around 60° before the top dead centre (TDC), towards the end of the compression phase.

The stratification can be achieved through three main injection strategy techniques as reported in Figure 10:

1. wall guided: designing appropriate walls of the combustion chamber and piston, to obtain a deviation of the spray jet such as to create a richer mixture under the spark plug;
2. air guided: through the exploitation of air motion (swirl, tumble, squish) for the convective transport of drops and vapours under spark plug, through intake ducts and chamber geometry optimization in terms of stroke/bore ratio;
3. spray guided: through a correct positioning of the injector near the spark plug in order to exploit the momentum of the drops.

usually these strategies are combined with each other in order to achieve the best possible result. With a stratified lean combustion (e.g.  $\lambda$  1.4) the combustion process is no longer influenced by the overall mixture ratio (as in homogeneously charged engines), but only by the local mixture quality. The engine load can therefore be controlled by varying the amount of fuel injected, eliminating pumping losses. In addition, heat dispersion from cylinder is reduced as excess air creates an insulating layer on the wall, increasing engine efficiency. This leads to a reduction of fuel consumption up to 10-20 % compared to the traditional homogeneously charged engine, as showed in [11], where a lean burn combustion concept that uses spray guided lean stratified operation was tested, showing remarkable BSFC improvements: a reduction of 14% over NEDC cycle and 12% over WLTC.

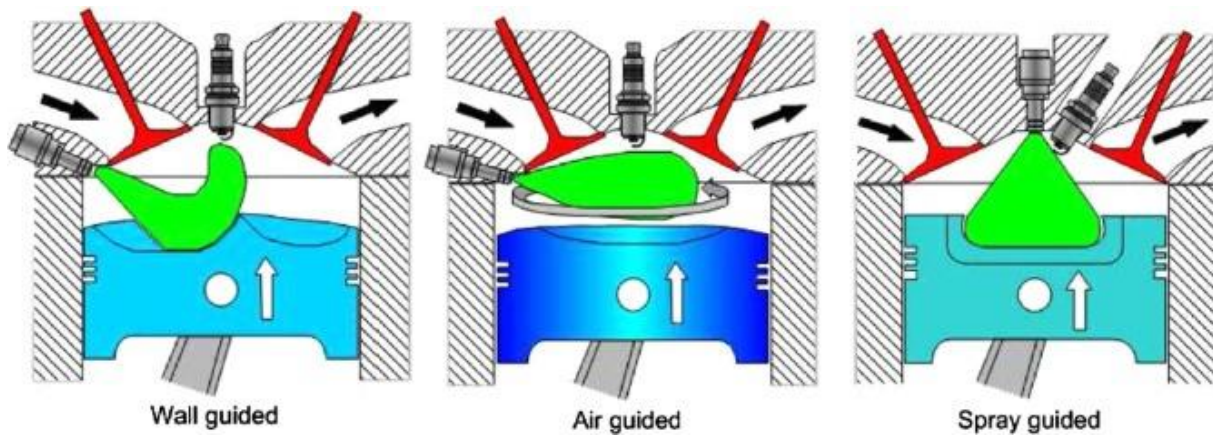


Figure 10. Stratified fuel techniques [10]

### 1.6.2 Miller and Atkinson Cycles

The Miller and Atkinson cycles consist of the early and later closure of the intake valves, as shown in Figure 11 [9]. The Miller and Atkinson cycles are realized through a variable control of the valve timing (VVT) [12,13], that it can be implemented mechanically by modifying the camshaft (different cam profiles), hydraulically, electro-mechanically or pneumatically. The Atkinson cycle was originally realized by a different crank train, which involved a system redesign that produced an increase of the expansion stroke.

In both cycles the objective is to obtain a longer expansion stroke than the compression stroke, but with the penalty of a lower mass trapped inside the cylinder. With the Miller cycle the early closure does not allow a complete filling of the cylinder, which involves an expansion of the fluid from IVC to BDC (Bottom Dead Centre). On the other hand, with the Atkinson cycle, the movement of the piston towards the TDC pushes the air back into the intake duct, reducing the residual air quantity present at IVC (Inlet Valve Closed). In both cases there are advantages in terms of pumping losses and a decrease in pressure and temperature in the cylinder, which affect the entire combustion process.

To recover some performance losses, due to a reduced air trapped, these strategies are usually coupled with a turbocharger with high boost pressures to increase the charge density. Indeed, the compensation of power and torque in a natural aspirated engine by an increased displacement would lead to more friction losses.

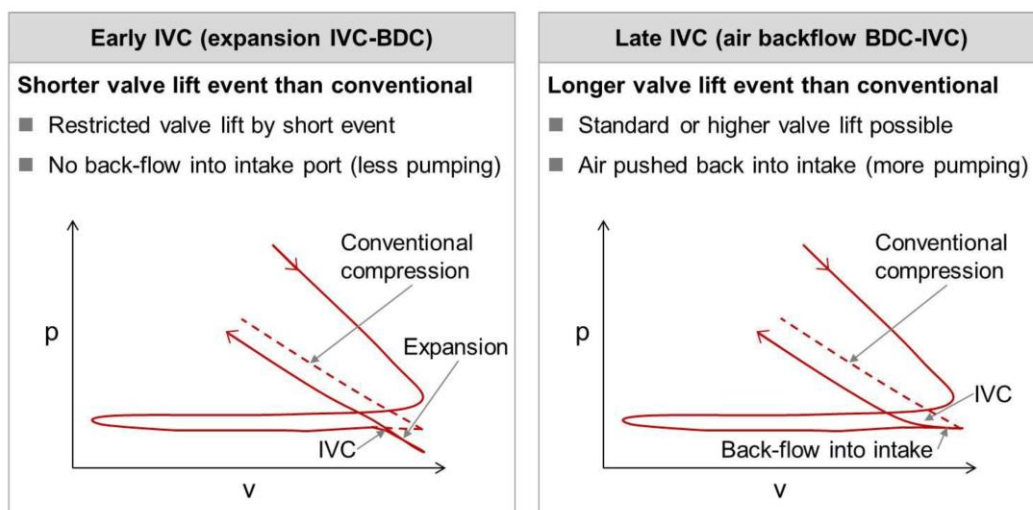


Figure 11. Miller and Atkinson cycles [9]

### **1.6.3 Variable Compression Ratio**

The purpose of a variable compression ratio engine is to increase performance, efficiency and emissions at the same time [14-16]. It is well known that the development of engines towards a downsizing approach has led to an increase in the compression ratio precisely to increase engine efficiency. The main problems of a high compression ratio are the higher temperatures and pressures which develop in the combustion chamber, which can lead the engine to knock events, especially when the driver requires power at low engine speed. VCR strategy consists in using a high compression ratio at partial loads to optimize the fuel consumption, and a lower compression ratio at higher loads to comply with power demand, resulting globally in a more efficient combustion over a wide range of loads and speeds, as well as a number of other benefits such as low frequency noise, reduced cold start emissions and minimum friction losses.

VCR systems can significantly contribute to the aim of lower fuel consumption of advanced, high performance internal combustion engines, being able to integrate other strategies described in this chapter.

### **1.6.4 Cylinder Deactivation**

Cylinder deactivation can be considered as an additional (temporary) engine downsizing technique, which produces a significant reduction in pumping losses as well as an overall reduction in the global heat exchanged through the walls at low loads and rpm [17,18]. There are different systems for deactivating the cylinders. The most common is to apply this strategy to a specific cylinder, cutting off the fuel supply and disabling all moving parts, such as intake and exhaust valves, reducing the engine frictions. Valve deactivation is made available with various mechanical options such as switchable bucket tappets, switchable finger followers or fully variable mechanical/electrohydraulic valve train systems based on detent cam gears. To ensure that the engine continues to run smoothly enough, only certain cylinders are deactivated in accordance with the ignition sequence.

Depending on the strategy adopted, either fresh air or combustion products may be trapped inside the combustion chamber. In the latter case, the heat generated by the exhaust gases make the cylinder cool down more slowly, producing higher pressure rises during the compression phase which can lead to an irregularity in the overall operation and friction losses increase. Therefore, this strategy must be maintained for a longer period of time to ensure optimal benefit in terms of fuel consumption. However, thanks to modern engine cooling systems and the blow-by effect, about ten revolutions are required to make the pressure fluctuations in the cylinder, due to the closed-valve compression and expansion phases, comparable to those of a fresh mixture.

An example of the use of this technology is given in [18], where an electronic cylinder deactivation system was used in a 4 Cyl 1.4L TC GDI engine, obtaining In the NEDC cycle, a fuel consumption improvement up to 7%.

### **1.6.5 Exhaust Gas Recirculation**

The use of EGR (Exhaust Gas Recirculation) makes it possible to combine the effects of the downsized engines to save fuel, mitigate the knock onset, control the cylinder temperature and reduce NO<sub>x</sub> emission. EGR, combined with downsizing and turbochargers, has proved to be one of the most promising technologies for gasoline engines in the recent years [19]. The exhaust gases act as inert gases that take heat from the combustion chamber, reducing the maximum temperatures of the system, helping also to improve the part load efficiency thanks to de-throttling [20]. The addition of exhausted gases, in fact, pushes to keep the throttle valve further open to ensure the same power target, decreasing pressure drops in the intake duct.

Lowering temperatures in the combustion chamber also reduces the heat rejected from the surfaces, with a conversion of the energy into work in the most efficient way during the expansion phase.

Basically, there are two types of EGR systems:

- Internal EGR: the exhaust gases are forced to move in the cylinder by overlapping the opening time of the intake and exhaust valves, where the amount of EGR trapped inside the combustion chamber depends on factors such as the valve timing, engine speed, and differential pressure;
- External EGR: exhaust gases are recirculated back into the intake manifold by using an external duct and an additional valve (EGR valve). The system is mainly designed as High Pressure EGR (HP-EGR) or Low Pressure (LP-EGR) system (also present in combined version), as showed in Figure 12 [21].

As an example, in [22] the authors, thanks to the use of an LP-EGR system, report a reduction in fuel consumption at partial loads between 1% and 4%, without affecting the PN-emission, by shifting the 50% MFB50 to the optimum in knock limited engine operating points.

One of the limiting factors in the use of EGR is that excessive dilution can lead to problems of combustion stability, condensation and lower power.

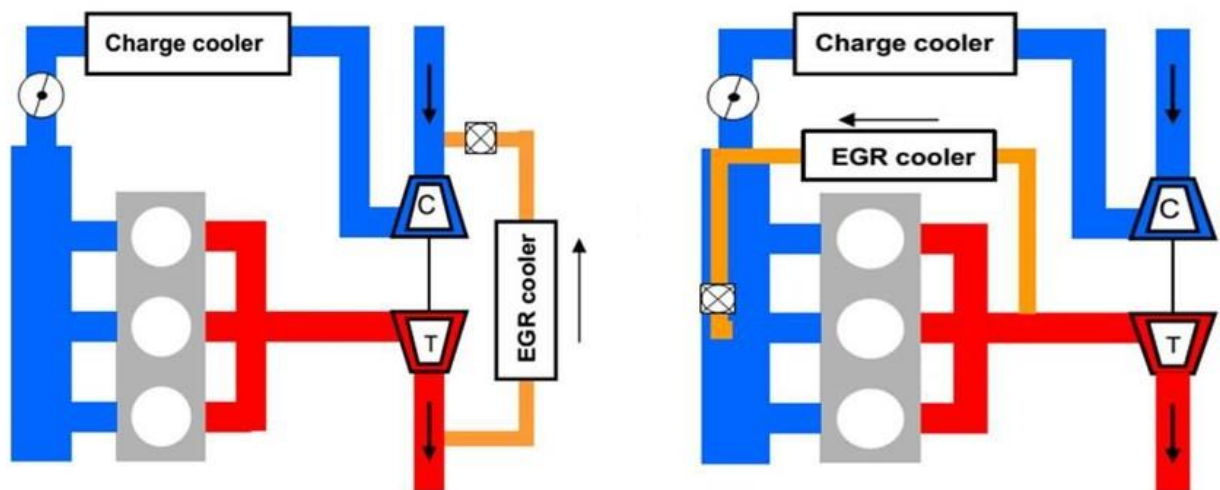


Figure 12. Schematic representation of a LP-EGR circuit (left) and a HP-EGR circuit (right) [21]

### 1.6.6 Multistage Air Charging

The most effective method to increase the power of an engine is certainly to compress the air in order to increase the amount of oxygen available for combustion [23]. As mentioned in the previous paragraphs, this technology is also crucial for some strategies such as the adoption of EGR and the Miller/Atkinson cycles, to avoid a great loss of performance. Alongside common turbochargers, which are particularly critical at low engine speed, technologies such as VGT (Variable Geometry Turbocharger) and, the most advanced, multi-stage compressors have been developed to improve the driving experience and efficiency of these systems. As far as the multi-stage compressors are concerned, there are two main solutions:

1. 2-stage turbochargers;
2. mechanical supercharger or electric turbocharger in addition to the first turbocharger stage.

In general, a multi-stage turbocharger brings the following advantages:

- a significantly higher boost pressure level, enabling the achievement of very high mean effective pressure values;

- an improved charging efficiency, even at unchanged charge pressure, since the efficiencies of compressor and turbine decrease with an increasing pressure ratio in a single stage. Additionally, the total efficiency can be further increased with an intercooler;
- wider compressor and turbine maps, improving the possibilities to adapt their working conditions to the desired engine operating point.

The main drawbacks are due to the cost and packaging of the system and the added complexity for the engine control.

# Chapter 2: Water Injection Application to Engines: State of the Art

This chapter summarizes the state of the art related to the water injection technology applied to internal combustion engine. The revision is divided into three main parts:

1. a literature presentation with the aim of understanding where the scientific research is converging and which are the main parameters to consider;
2. a list of the main layouts and designs used to inject water into the engines;
3. a presentation of the technologies available today for the water recovery and consumption minimization

Through these three points the aim is to give a clear idea of the development that the water injection technology has experienced so far. In the conclusion paragraph it also summarized the main scientific contribution of this thesis project, specifying the reason why it differs from the state of the art.

## 2.1 Literature Review

The application of the mixture water injection mixture cooling (hereafter referred to as “WI”) cooling is not a novelty in ICEs, and the first successful use of WI for suppressing combustion knock can be traced back to the early 1930s [24]. During World War II, similar use of WI was made in the operation of high output power aircraft engines [25,26], and additional studies were conducted until the 1980s [27,28].

Because of the more and more rigorous CO<sub>2</sub> and pollutant emissions regulations, the WI technique has again been investigated to explore its potential benefits on both the SI (spark ignition) and CI (compression ignition) engines [29,30].

Below some references are quoted being divided between HCCI, spark ignition and diesel engine applications. It should be noted that the focus of the presentation of the state of the art is that to highlight the worth important motivations and the solutions studied and tested by the different authors. Moreover, since this thesis is mostly focused on the application to gasoline engines, deeper details will be provided on the application to this combustion system.

### 2.1.1 HCCI Engines

The application of the water injection to internal combustion engines became of interest again at the end of the 90's, in particular for HCCI combustion systems. These types of gasoline engines would join SI and CI combustion system working principle and they operate with a homogeneous air-fuel mixture heated and compressed inside the cylinder to reach the auto-ignition condition near the TDC. They are characterised by high efficiency and low NO<sub>x</sub> emissions. However, one of their most limiting factor in terms of maximum operating load is the control of the ignition time over a wide load and speed range and the high HC emissions.

Since they do not have direct control of the ignition timing, they may face heavy issues increasing the load in terms of heat release sharpness, mechanical loads, and cycle-to-cycle variability. The main techniques to limit the combustion rate involve the use of extremely lean mixtures ( $\lambda$  larger than 3) and/or the use of very high external EGR rates. A third alternative explored by several authors was to exploit water injection. In [31] the authors experimentally studied how a water-fuel mass ratio up to 3, affected the ignition timing and the HCCI combustion process, with three different fuels: iso-octane, ethanol and natural gas, both on an aspirated and supercharged engine, with different intake temperatures. The results showed how water could slow down and control the combustion in an HCCI engine. The main parameter governing the process was the air temperature: the higher was the inlet temperature the greater was the effect of water evaporation. The authors concluded that the water injection could be used to increase the upper load limit of HCCI system, as the cooling effect from the water slowed down the combustion rate and reduced peak pressure and  $\text{NO}_x$  but not the CO, that slightly increased in all tests.

### 2.1.2 Spark Ignited Engines

Lanzafame [32] experimentally tested the use of the water injection in a CFR single-cylinder engine, replacing the use of primary anti-knock additives, in order to reduce the knock engine attitude and to increase the compression ratio for a more efficient combustion system. Water was supplied by a continuous injection system (high pressure pump), under the pressure of 1 MPa, located in the intake manifold, just before the inlet valve. The results showed a significant increase of the knock resistance. As a matter of fact, the equivalent RON move from 70 to 94 and MON from 64 to 90. A reduction of about 50% of  $\text{NO}_x$  and an increase of 20% of HC was also detected with a water-to-fuel mass ratio between 1 and 1.25.

Later, the same authors investigated the effect of the water on a similar engine but with two different injection techniques [33]: continuous injection and pulsed injection, with a maximum water-to-fuel mass ratio of 2. In both cases it was possible to notice the effect of cooling due to water evaporation, which induced a combustion slowing and an increase in the octane number, almost linearly with the mass of water injected. However, the use of the pulsed injection resulted in a more pronounced reduction of  $\text{NO}_x$  and a less noticeable increment of HC emission. This phenomenon was attributed to a better atomization and a more efficient water evaporation, thus allowing to create a more homogeneous distribution of the water.

Nande et al. [34] performed experiments by considering a PWI configuration into a research hydrogen four valve engine operating with the charge stratification. Its performance was limited by regulatory limits on  $\text{NO}_x$ , whose engine out concentration was above the imposed limits because of the excessive in-cylinder temperature and the lean mixture adopted. The Start of Injection (SOI) timing was varied from 140 ca deg. before the top dead centre (BTDC) to 20 ca deg. BTDC. Spark sweeps were performed and all tests were conducted at wide open throttle (WOT). The authors found that the water injection proved to be a more effective technique for  $\text{NO}_x$  reduction compared to delaying the spark timing. In fact, both at low and high loads, lower efficiency penalties and larger reductions in  $\text{NO}_x$  emissions were obtained by using the water injection.

A similar study was carried out by Younkings et al. in [35] who investigated the effects of the water injection on a hydrogen-powered engine through a Direct Water Injection (DWI) system. The system was effective at reducing  $\text{NO}_x$  emissions: 21 mg/cycle and 35 mg/cycle of water injected were found to reduce  $\text{NO}_x$  by 93% and by 95%, respectively, albeit with an increase in fuel consumption of 8%.

A PWI system operating with an injection pressure of 4 bar was investigated by Iacobacchi et al. in [36] on a downsized PFI twin-cylinder turbocharged spark ignition engine at high load condition (15.5 bar IMEP) within the engine speed range from 3500 to 4500rpm. The water was injected at the same time with the gasoline, with a water-to-fuel ratio between 0.2 and 0.3. The combustion phasing was advanced up to an optimal condition without knock occurrence, resulting in an increase of IMEP up to 7.3% at 3500 rpm, with respect

to the reference gasoline case without water injection. Another very important result achieved was the reduction of Turbine Inlet Temperature (TiT) from 25°C to 50°C thanks to the water evaporation and the induced mixture cooling. However, these results were achieved only by advancing the spark advance (SA): even with the maximum water-to-fuel ratio of 0.3 explored, leaving the SA unchanged, an increase in turbine inlet temperature was recorded due to slower combustion during the expansion phase.

Since now it must be pointed out that the slower flame speed, because of the water dilution, may counterbalance the mixture cooling effect and therefore it must be properly accounted for in the CFD simulation methodology.

In recent years the development of the computational analysis has allowed CFD to become an effective tool for the study and optimization of water injection in engines, thus increasing the number of publications. In [37] the authors studied, through CFD (Computational Fluid Dynamics) and a multi-cycle approach, a turbo-charged GDI engine (maximum BMEP of 20 bar) with port water injection (PWI), investigating different water injection timing, different water spray Sauter Mean Diameter (SMD) (90, 70 and 50  $\mu\text{m}$ ) and spray targeting. They highlighted how the primary atomization quality, which ultimately depends on the nozzle design and the injection pressure, together with the installation position, were key parameters to optimize the system in terms of combustion control and knock suppression. The best results were obtained for the highest injection pressure that carried the water spray SMD down to 50  $\mu\text{m}$ , and a water injector location very close to the intake valves, resulting in lower wall film formation and lower peak temperature.

Water injection can be efficiently coupled with other existing strategies to reduce fuel consumption, emissions and TiT as shown by Hoppe et al. [38]. They examined the operation of a DWI engine by varying the compression ratio and the Miller cam timing, on a very wide engine map, identifying, the right amount of water to be injected at each operating point. The experimental data showed that the potential of water injection to reduce the fuel consumption increased by increasing the load demand, from about 2% with 1L/100km of water consumption on the NEDC cycle, to about 4% with 2L/100km of water consumption on the WLTC cycle.

Different injection mixtures were tested by means of 3D-CFD by Breda et al. [39] on a turbocharged GDI engine. Water, water/methanol emulsion and methanol were port-fuel injected to replace mixture enrichment while preserving, if not improving, the engine indicated mean effective pressure and knock-safe operation limit. Leaving the SA (Spark Advance) unchanged, the best results in terms of the specific fuel consumption and IMEP were obtained with the 75% methanol mixture (MW75): -13% and +1% respectively. On the contrary, advancing the ignition timing, within the knock limits, the best overall results were verified by injecting only water, despite an increase of the temperature at EVO of about 40 °C.

The impact of PWI and DWI strategies on knock mitigation and over-fuelling limitation was also analysed by Lecompte et al [40], respectively in two operating conditions: 2000 rpm with 17bar of IMEP and 4000 rpm with 20 bar of IMEP, in conjunction with the use of external EGR. They illustrated how EGR mainly played an important role on wall losses, whereas water had more impact on combustion phasing. A global efficiency close to 40% was reached at 2000 rpm at 17bar IMEP with DWI, claiming that DWI was the most efficient way to inject water for gasoline engine applications.

The authors in [41] studied a single hole PWI system, with an injection pressure of 5 bar, applied to a GDI supercharged engine at full load, high and low rpm. They compared the cooling effects between an enriched fuel mixture without water dilution and a stoichiometric mixture with different amount of water injected depending on the operating points. The results showed that for WI case, with the suit injection strategy, the *bsfc* (brake specific fuel consumption) improved between -2 and -22% depending on the engine point, highlighting how the evaluation of the percentage of the evaporated water was an important parameter not only for quantifying the cooling effect but also for avoiding an accumulation of liquid film on cylinder's walls. They also showed that water spray liquid droplets could enter better inside the cylinder if the injector was

placed near the inlet valves. In addition, it was identified an optimum injection timing (around 100 CA deg. before intake valve open) to lower the charge temperature before the start of combustion depending on the engine speed (due to the very different flow velocities in the intake port) and the physical time allowed for water to enter the cylinder which, in turn, depends on the water injector location and injection pressure.

Mauss et al. in [42] carried out an in-depth analysis of the effect of water on spark ignition engine, with special attention to knock occurrence, isolating the physical and chemical effects of the water properties, in order to understand which was the most influencing one on the auto-ignition events. The analysis was performed using a detailed ethanol toluene reference fuel reaction scheme, representing a typical European gasoline fuel with a RON/MON of 94.5/88.8. The effect of water on the laminar speed reduction was found to have the largest impact on KLSA (knock limit spark advance), while the variation of the IDT (ignition delayed time) was less affected by the presence of water, as long as the temperatures were below 900 K.

In the work of Teodosio et al. [43] different techniques to reduce the Brake Specific Fuel Consumption (BSFC) were tested on a downsized, turbocharged, spark-ignition and Variable Valve Actuation (VVA) engine. The solutions proposed and analysed through 1D simulations were: Variable Compression Ratio (VCR), port Water Injection (WI) and external cooled Exhaust Gas Recirculation (EGR). WI proved a higher effectiveness at medium-high load, mainly thanks to its knock suppression capability. Cooled EGR demonstrated to be preferable at low load, reducing the pumping work, while for high Compression Ratio (CR), if coupled to the WI, was always beneficial. The combination of the above techniques provided BSFC reductions of 6.9%, 5.2%, and 9.0% at low, medium, and high loads, respectively.

In [44] the effect of water in a four-stroke, four-valve, wall-guided GDI engine was considered, testing different water DWI injectors, spray patterns and orientations through 3D simulations. The analysis was conducted under full-load conditions with a constant engine speed of 2000 rpm and with a 6-hole water injector at 50 bar. From the results it was found that the water spray pattern with a regular hexagon shape (with regard to a plane placed at 30 mm below the injector tip) and an injector orientation of 25° produced higher IMEP with lower NO<sub>x</sub> and soot emissions.

The authors in [45] stated that for the gasoline engines under examination there was an optimal DWI injection timing and moving forward or backward could cause a severe detrimental effect on MFB50, enlightening the combustion. The optimum timing was found to be independent from the intake valve lift law, the load, and the amount of water injected. However, it was found that the optimal injection timing of water shifted to earlier timings with increasing engine speed. In addition, the compression ratio also had a non-negligible effect on the injection timing and the reason, according to the authors, could be attributed to the higher thermodynamic conditions in terms of pressure and temperature, which reduced spray penetration that shifted the trade-off for the optimal injection timing to slightly earlier SOI.

3D-CFD simulations of mixture formation, in-cylinder flow conditions and water distributions for two different operating points (part load and maximum power), was investigated by Vacca et al in [46]. The data illustrated that the PWI architecture should not be thought as a secondary solution to DWI. By optimizing the indirect injection strategy, excellent results comparable to those of DWI, in terms of exhaust gas temperature reduction, could be achieved with the same amount of the water-fuel ratio, with the advantage of avoiding oil contamination. Both the solutions were able to reduce of about 25°C the turbine inlet temperature compared with a  $\lambda$  0.85 strategy, without water injection, keeping the components in a safer condition.

### **2.1.3 Diesel Engines**

Water-diesel emulsion has also been extensively tested in the past with the main objective of replacing or reducing the use of EGR. The aim is to provide a minimum amount of water in the right place in the combustion chamber, in post-flame areas, where high temperatures last longer and where NO<sub>x</sub> formation is

higher. The extensive experimental campaign reported by [47], underlined the effectiveness of water injection also in reducing soot. The micro-explosions of the water droplets led to a better dispersion of the fuel in the chamber, expanding the volume of the spray. It was finally found that the EGR-water combination with high injection pressure was the best strategy to have the lowest emissions and optimized combustions in the cylinder.

Rahaman et al. [48] investigated the effects of the water injection on a small, automotive HSDI diesel engine with Variable Geometry Turbocharger, with a water flow rate between 3 and 21 kg/h, corresponding to a water/fuel ration up to 4. Moreover, they compared the emission results with those obtained with low-pressure dry Exhaust Gas Recirculation (LP EGR), using a cooler to maintain the EGR temperature under 50 °C. The water was injected together with a pressurized air in order to obtain a fine mist. They noticed a significant reduction of the NO<sub>x</sub> and a slight increase of the specific consumption by using only WI, but a combination of EGR and WI allowed the NO<sub>x</sub> emissions levels to be reduced similar to only-EGR systems. However, with water injection, the PM emissions did not rise.

With a specially designed injection nozzle, Wirbeleit et al. [49] applied a stratified fuel/water injection on a single-cylinder heavy duty diesel engine. In the 13-mode ECE test, they obtained a NO<sub>x</sub> reduction of 55% for the same PM and BSFC with the application of stratified fuel/water injection combined with EGR. However, the disadvantages were the greater complexity and higher cost of the injection nozzle.

Tanner et al. [50] compared several WI techniques including the injection of water via separate injectors, emulsified, and stratified. CFD simulations, on a large-bore diesel engine, showed both the stratified and the emulsified injections yielded best NO<sub>x</sub> reductions per injected water mass for the same power outputs, and an identical peak cylinder pressure.

Kegl et al. [51] conducted experiments on different WI methods (multipoint injection into the manifold, single-point injection before and after the compressor and fuel/water emulsion injection into the cylinder) on a four-cylinder truck diesel engine. Comparative results, with the same water/diesel volume ratio ranging from 0 to 20%, showed that water/diesel emulsion was the most proper approach to decrease NO<sub>x</sub> and PM simultaneously, without worsening the fuel consumption. The single-point injection after the compressor experienced the worse potential in NO<sub>x</sub> reductions compared with the other two WI locations.

## 2.2 Spark Ignition Engine Water Injector Layouts

The main objective of the water injection technologies is to achieve the highest mixture cooling efficiency trying to minimize the amount of water used.

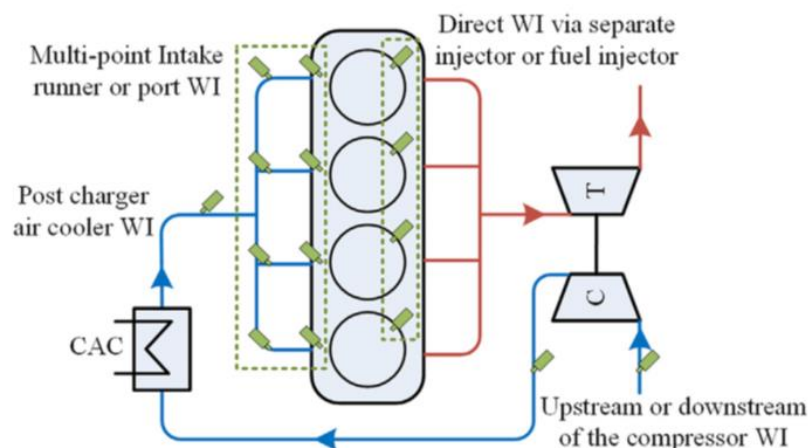


Figure 13. Water Injector Locations [52]



Figure 14. PWI close to intake valve [52]

There are several possibilities to introduce the water into the cylinder, each with its own advantages and disadvantages, especially when applied to different types of engines. In general, water injection can be realized through three methods (Figure 13):

1. Single point WI upstream or downstream of the compressor or post charge air cooler;
2. Multipoint WI into the intake runner or intake port;
3. Direct WI into the cylinder via a separate injector or the same injectors fuel.

### 2.2.1 Intake Line Injection

For supercharged engines, water can be injected directly upstream or downstream of the compressor, or downstream of the intercooler, which is commonly known as intake air humidification or fumigation [53]. In order to evaluate the different installation possibilities, some guidelines should be considered, such as the maximum permitted amount of humidity in the air, optimization of the water evaporation, ease of installation and maintenance. Fast water evaporation is important to avoid the formation of water liquid film and accumulation inside the intake line. Another important aspect is to make sure that there is an equal distribution of water vapour in each cylinder, in order to avoid cyclic dispersion and abnormal emissions, to eliminate possibilities of cylinder liner corrosion problems and contaminations of the lubrication oil. Since the temperature before the compressor is close to the ambient one, this could greatly reduce the evaporation capacity of the water droplets, despite the low pressure. The droplets therefore tend to remain in suspension in the air and evaporate inside the compressor itself, reducing the air temperature and increasing its efficiency. However, the presence of drops should be avoided, or at least reduce their diameter as much as possible. These droplets can seriously damage the structure of the compressor. However, with a reliable system design, this injection point would allow a good mixing between air and water before entering the intake duct.

Using an injection point after the compressor, even if the pressure is higher, it would have the advantage of a much higher air temperature, often higher than the boiling point in those thermodynamic conditions. Thanks to the temperature reduction made by the water, it is possible to reduce the sizing of the intercooler, in terms of amount of cooling fluid and/or dimensions. Under some conditions, it may even be possible to remove the intercooler, relying totally on the water evaporation [54,55].

Therefore, this injection point should be used only for a small amount of water or in addition to other injection strategies described below.

With those characteristics, the intake air humidification is especially attractive for engines operating on heavy fuel where the use of EGR is difficult and expensive. In addition, intake air humidification is more easily integrated on large marine engines due to the wider installation room, low engine and compressor speeds, steady operating conditions and easy water supply.

Another problem with injecting water too far upstream is the possibility that the air will reheat when it flows through the intake line before it reaches the cylinder, minimizing the benefit of evaporation.

### **2.2.2 Port Water Injection**

The intake runners and intake ports are two alternative locations for the water injector. The main advantage is the easy implementation, similar to a PFI (Port Fuel Injection) system. In general, the gasoline port fuel injectors or UREA injectors can be directly used for the PWI application with small modifications [56]. The latter feature brings a very high probability that the PWI may be preferred to DWI for the short-term series production thanks to the low pressure (5-20 bar) design that is simpler, cheaper and more corrosion resistant. In PWI configuration the amount of the water injected can be directly controlled by injectors located in each intake port, to ensure an excellent distribution inside each cylinder. Even in this case, the thermodynamic conditions of the air in the intake ducts are not the most suitable for the water evaporation. For this reason, the system must be carefully studied to maximise the interaction of the water liquid drops with the air stream in order to reduce their diameter as much as possible, and to target the water liquid spray inside the cylinder minimizing the evaporation in the intake ports. In addition, unlike in the case of fuel, the water evaporation is dependent on the humidity conditions of the intake air. For highly boosted engines with a highly efficient charge air cooler, the cooled fresh charge may be very close to 100% relative humidity [57] depending on the ambient air humidity. Under this condition, the water injected in the intake runner/port evaporates very slowly and saturation limits may be reached. On the contrary, the liquid water that enter the cylinder can evaporate much faster during the compression stroke as the in-cylinder temperature rise. It must be noted that in-cylinder conditions never face the risk of condensation of the water evaporated.

The location and targeting of the water injector are also very important. Experimental and numerical analysis of the liquid water distributions indicate that the installation of the water injector very close to the inlet valves, can mimic a “quasi-direct” WI if compared with the installation far upstream in the intake runners (Figure 14). Wall film formation (that reduces charge cooling and premature vaporization outside the cylinder) are the main causes for the lower efficiency of the intake runner installation, which drops substantial gains in terms of combustion control and knock suppression. Generally, the main drawback of a PWI system with respect to other possible solution (DWI) is the higher water consumption to achieve the same cooling target because part of the cooling effect is lost due to the heat transfer through the intake port walls.

### **2.2.3 Direct Water Injection**

Water can also be injected directly into the cylinder through an injector specially designed for water or in combined fuel/water operation layout. The main advantage of the DWI is the flexibility that this system brings with it in a GDI-like manner (Gasoline Direct Injection). The amount and distribution of the vaporized water inside the cylinder can be optimized by a precise choice of the injection timing, to maximize the interaction with the charge motions and to induce high water concentrations in specific combustion chamber locations. Drawbacks are also obvious, such as the cost of a high-pressure injection system, packaging, robustness and reliability.

The WI during the intake stroke and compression stroke may have different effects on the engine volumetric efficiency, in-cylinder evaporation and mixture evolution. In general, water should be injected to ensure that there is no water spray impingement and no water liquid film on cylinder walls and that evaporation is completed before the end of the compression stroke. However, inappropriate WI timing and spray targeting, with respect to GDI may determine local flame quench, contamination of the lubrication oil and the increase of both the cycle-to-cycle variability and emissions [58].

As far as the GDI engines are concerned, the installation of a dedicated water injector on the cylinder head may consume a considerable fraction of the package volume available. A more feasible solution may be the combination of port fuel injection and direct water injection or emulsion water injection.

Furthermore, from a system perspective, there is one big disadvantage for DWI with separate injectors: when the water injection is not in operation no water flows inside the injector and it cannot be cooled. Since the water injector may not be operated for many engine cycles, it is clear that the water injector cannot remain uncooled in order to avoid thermal damage. This issue is not really solved at the moment, unless conceiving the injection of small amount of water at a given frequency.

A possible DWI implementation is the use of a direct injection with stratified charge (fuel/water) as shown in Figure 15. The water is injected into the system in sequence with respect to the fuel inside the same injector, for this reason the timing is dependent on the fuel injection and water/fuel ratio. With this operation the water can be inserted directly close to the flame, exploiting its high enthalpy of vaporization right in the hottest point of the system, avoiding contact with the walls and the formation of liquid film. This solution is particularly effective for diesel engines thanks to a strong reduction of nitrogen oxide emissions. This arrangement can also minimize the negative impact on overall engine reliability, compared with a poorly placed nozzle which may over-cool the combustion chamber and lead to ignition delay and incomplete combustion [59,60]. However, additional cost on modification of the injector make this system less popular compared to other WI systems.

A further solution is to use a water/fuel emulsion with the addition of emulsifiers. The presence of a surfactant (or emulsifier), which is a typical chemical additive attracting the immiscible liquids, plays an important role in forming a stable emulsion. In addition, different types and percentages of chemical additives determines the type of emulsion. With larger amounts of surfactant, normally up to 10%, micro-emulsion can be generated compared to the normal emulsion with up to 2% of surfactant [61,62]. Thus, microemulsion has a much smaller dispersed water droplets with a diameter size ranging from 5–20 nm compared to 1–10  $\mu\text{m}$  of the normal emulsion. Regarding the engine power and emission performances, Ithnin et al. [62] indicated that not much difference can be observed with those two types of emulsion fuels. Even though the micro-emulsion has more stable thermodynamic properties, the high cost of micro-emulsion restricts its commercialization. The main disadvantage of using fuel emulsion technology is the limitation of the amount of water that can be added to the system [63]. For fuels emulsified with water, there is always an inherent risk that an excess of water may be injected into the cylinder either too early or too late in the combustion process. This can cause cooling of the entire cylinder and lead to increased ignition delay, engine noise and retarded combustion. In addition, an increased engine operation cost, like a more extended and developed distribution network of fuel/water emulsion or a complex on-board emulsion production system equipped on the engine, should be evaluated seriously. For the gasoline engine, the technology of pre-mixed macro emulsions of water and gasoline is proposed and investigated in [64]. In this system, water is metered into a mixing chamber filled by the pre-pressurized fuel flow of 4–5 bar [65,66]. Thus, short-term time-resistant emulsions can be obtained, and emulsifying additive is avoided. Pumped by the high-pressure pump, stabilized emulsions flow through the fuel supply system to the fuel injectors. With no modification of the cylinder head, this implementation is relatively easy to integrate into an existing engine. Since water is directly injected into the combustion chamber with fuel, chamber-wall wetting can be minimized, which shows great potential for the future gasoline water injection.

For a complete overview of possible installations, a further injection strategy is mentioned, that has not been much developed, regarding the location of the injector downstream of the exhaust valve, exploiting the exhaust gas enthalpy for the water evaporation. This solution was mainly tested in Diesel engines [67]. The steam generated in this way re-enters inside the cylinder, diluting the charge in a similar way to EGR, and to supply some species useful for the soot oxidation during its thermal dissociation.

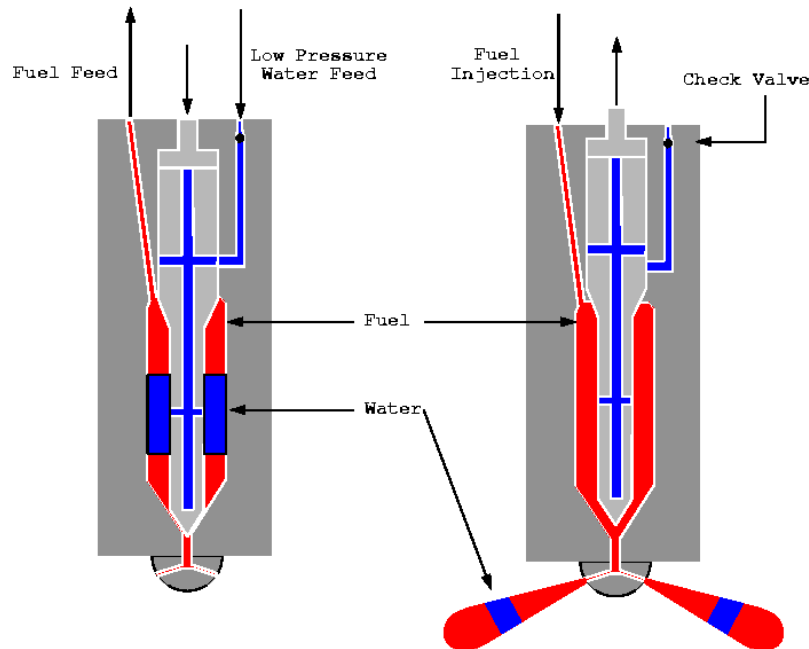


Figure 15. DWI stratified solution [59]

The purpose of using this strategy is to limit the temperature drop, however this solution tends to increase the combustion duration and lower in-cylinder mean pressure, leading in Diesel engine to higher rates of cylinder pressure rise and increased combustion noise.

Moreover, some others water-mixture can be used. For example, water injection systems typically use a mixture of water and alcohol (approximately up to 50/50), with trace amounts of water-soluble oil. The water provides the primary cooling effect due to its great density and high heat absorption properties. The alcohol is burnable, and also serves as antifreeze for the water. The purpose of the oil is to prevent corrosion of water injection and fuel system components. The alcohol mixed into the injection solution is often methanol (CH<sub>3</sub>OH), and the system is also known as methanol-water injection (MW50). The methanol in the mixture, which is characterized by higher octane number and laminar flame speed than that of pure gasoline, burns increasing the resistance to knock of the fuel-air mixture, and thanks to the higher energy density per oxidizer unit it improves performance output. The net result is equivalent to have a higher-octane number fuel that will support much larger compression ratios before knock onset. Moreover, the higher methanol volatility can improve the evaporation mixture in low rpm and part load operating conditions, where the reduced charge temperature and turbulence intensity prevent a complete evaporation of the pure-water injection.

## 2.3 Water Sources

The application of the water injection to internal combustion engines can have a short-term development especially for PWI systems. However, it is also important to take into account all the problems associated with this technology, including tank refilling, which is likely to be between 5 and 15 L, and the cost of water.

It is therefore necessary to consider what options currently exist for water supply and recovery, in addition to manual water filling. Now the most three promising architectures, already developed by automotive companies [68,69], are here described.

### 2.3.1 Air Conditioning Systems

Air conditioning is a good candidate to supply enough water to the engine, without any problem on the water quality or pH that other water recovery solutions encounter: when ambient air enters the AC module it is cooled down usually below its dew point. The resulting condensation of air humidity forms a liquid layer. However, the major drawback of this solution is that it only works when the air conditioning is activated. Therefore, for cold ambient conditions, water supply cannot rely only on this strategy. However, BMW [69] enabled a system with a water tank linked both to AC and manual filling (Figure 16). The condensate generated inside the AC unit is conveyed to a 5L tank, which can also be filled manually. The water is put under pressure by a first pump and filtered in order to protect the valves and the fuel supply system from possible contamination. The injection line is then separated into two parts, one directed to a PWI system and one to a DWI system, passing through a high-pressure pump. Depending on the operating point, the two injectors can operate separately or together. For example, direct water injection is activated at high loads and high speed, the most critical condition for turbine inlet temperature control, while PWI is used, with different percentages of water, throughout the map for medium/high loads. Moreover, this layout uses a rail before the DWI injector in order to obtain both a damping of the pressure waves in the line and a fast system response. To avoid water freezing, the tank is equipped with a heater that brings the temperature from  $-10^{\circ}\text{C}$  to  $70^{\circ}\text{C}$  in about 3 minutes, also to prevent bio-contamination caused by algae growth. Even the engine cooling system could act as a source of heat to warm up the water tank.

The performance of the AC system depends largely on ambient conditions and relative humidity. In summer the amount of condensate may be largely sufficient to meet the needs of the engine. In winter, even if the outside air temperature is lower, it may not be sufficient, making manual filling indispensable.

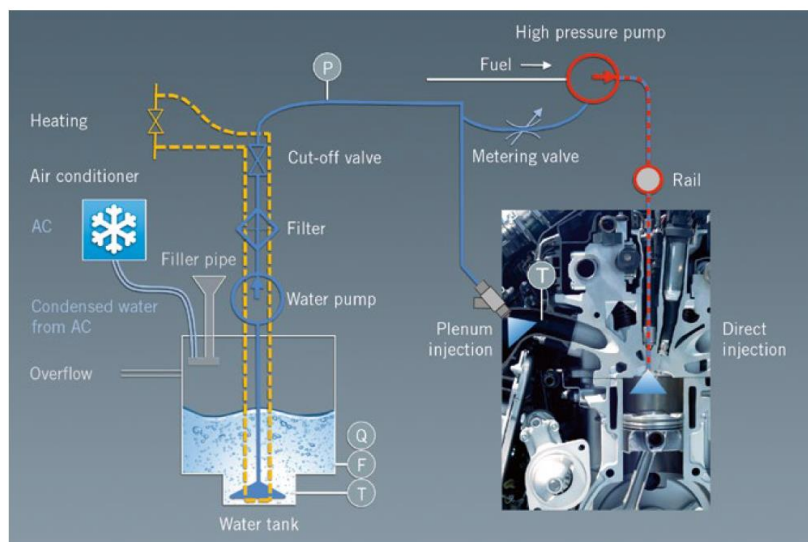


Figure 16. AC Water recovery system [69]

### 2.3.2 Exhaust Gases Recovery System

The exhaust gases are the main source of water, about 13% of the gases for an engine running under stoichiometric mixture conditions. In [69] the authors also mentioned the possibility to re-inject the

condensing water present in the exhaust gas into the intake duct. From a theoretical point of view, for that specific engine, the amount of water present in the exhaust gas would be sufficient to lower NO<sub>x</sub> emission without an additional water supply system. An example of this application is given in Figure 17.

However, the energy content in the water vapour can be so high that might over-load the recovery system. Usually the outlet gas temperatures range from a minimum of 150 °C to 700 °C in WOT. For this reason, water recovery with this technology is limited at medium-low load operating points: at high load this would require too much enthalpy to be removed from the exhaust gases.

The amount of water recovered depends on the degree of cooling obtained: around 40-50°C is about 35%. Contrary to the AC strategy, a decrease in the outdoor temperature is helpful in this case. The recovery unit can be placed at the silencer, preparing the line for both high and low water temperature recovery circuit. However, the main drawback is the too low pH.

Another interesting technical feasibility of the exhaust water recovery (EWR) system is described in the article of Sun et al. [70]. Water injection experiments were conducted at a full load condition (5000 rpm/18.1 bar BMEP) and a high load condition (3000 rpm/14.0 bar BMEP) on a turbocharged gasoline direct injection (GDI) engine. Water recovery testing was performed both after the exhaust gas recirculation (EGR) cooler and after the charge air cooler (CAC) at a high load (3000 rpm/14.0 bar BMEP), as well as a part load (2080 rpm/6.8 bar BMEP) condition, at temperatures of about 10-15 °C below the dew point of the flow stream. Three types of water separation designs were tested: a passive cyclone separator (CS), a passive membrane separator (MEM), and an active separator (AS), simulating their effectiveness on FTP, WLTP and US06 driving cycles. The results showed that both post EGR cooler and post CAC were possible effective locations for the installation of a EWR. The CS and AS system were able to reach 94% of water recover, performing better than MEM (50% of recovery), but with a lower final water quality.

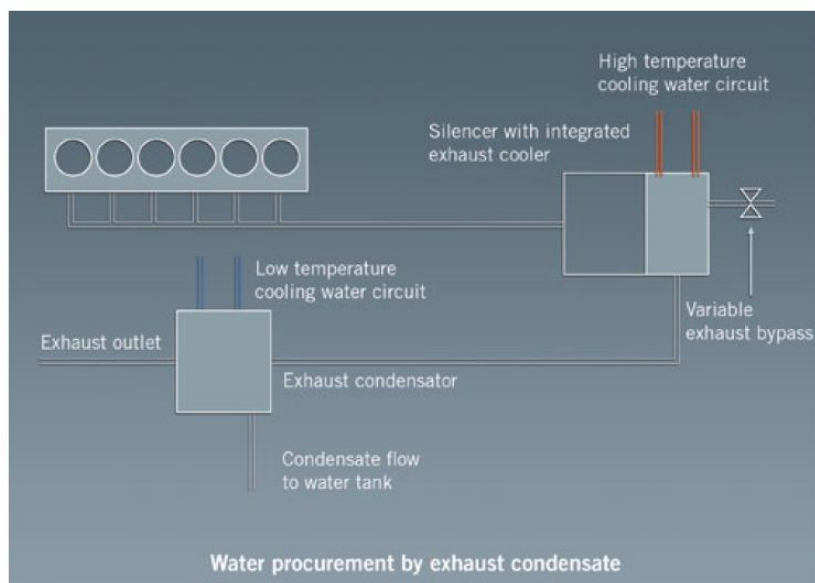


Figure 17. Exhaust Water Recovery system [69]

### 2.3.3 Surface Water Recovery System

The recovery of surface water incorporates all approaches to collect and store rainwater by the cars bodywork. The main issue of surface water usage is an uncontrolled load of debris, particles and other contamination, requiring very high level of quality sensors and water aftertreatment devices. For these reasons, a two-chamber arrangement is necessary for collecting surface water, in order to prevent chemical contamination (Figure 18). The water collected from the bodyshell surfaces flows through a filter to the

header tank, where it can drain to a discharge line if the quality is unsatisfactory or chemical contamination is detected. Otherwise, the water is carried by a connecting line and open valve to the main reservoir, if the level in the reservoir permits refilling. The filter can be flushed at regular intervals, or when it becomes clogged. The main reservoir also incorporates a drain valve that regularly lets off some water when enough is available. This is a way of expelling deposits and dirt particles that settle to the bottom of the reservoir.

Water quality is a parameter to be monitored carefully. The least complex case is the manual filling. In this case the quality control would be guaranteed at source, through the use of demineralized or distilled water, in order to prevent the formation of limescale in the injection circuit. The pH should not be too low in order to avoid corrosion problems in the line. This is in fact the main problem in the use of exhaust gases as a recovery system, whose water tends to be acidic with pH values below 5.

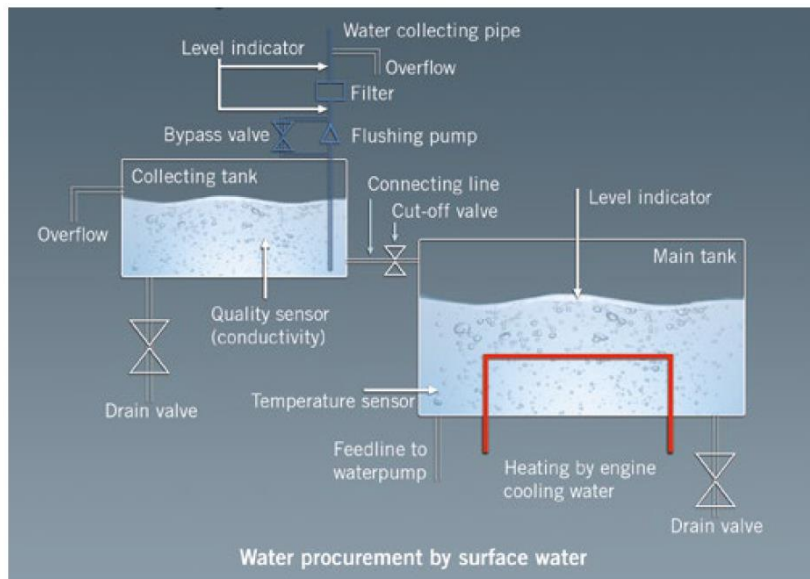


Figure 18. Water Surface Recovery system [69]

## 2.4 Conclusions

This chapter has highlighted the main features of the water injection applied to internal combustion engines and a literature review. However, as it can be seen there is no single direction of development and water injection design that assures optimal results. First, there are no strong motivations to focus on PWI systems rather than DWI. Both architectures have advantages and disadvantages, and the selection of one of those two depends not only on the type of engine but also on the main purpose of their use. In fact, it has been pointed out that the same architecture can perform in a different way depending on the choice of the installation point and the injection features such as injected mass, injection pressure and SOI/EOI.

The scientific contribution of the present doctoral thesis is the comprehensive approach to thermo-physical and chemical effects of water, in order to identify a CFD simulation and analysis methodology with which to extract guidelines for the implementation of PWI and DWI architectures in GDI engines in the next future. Another key aspect lies in the attention to the water consumption and the negative effects of the remaining water droplets. For this reason, it has been investigated the water percentage that must evaporate inside the cylinder before ignition. The target was set at 90%, thus ensuring a low impact on the formation of liquid film, which could become a dangerous risk for the safe and reliable operation of these systems.

In addition, it has been decided to give more space, both experimentally and through preliminary analysis, to the PWI technology, which is expected to be the most promising one in the short term because of the much lower cost and complexity..

For this reason, it will be presented a PWI validation activity in order to find the best model set-up able to represent the real water spray evolution inside the cylinder. In addition, in the last part of the thesis, also the DWI architecture will be analysed and compared with the PWI architecture, trying to highlight their advantages and disadvantages.

# Chapter 3: Water Properties

In order to optimize the water injection application in internal combustion engines, it is necessary to fully understand the physical phenomena that may influence their operation.

This chapter will highlight the main physical properties of the water and the differences between commercial gasoline or a reference primary hydrocarbon fuel like iso-octane with respect to:

1. Atomization and droplet breakup
2. Evaporation: cooling effect and saturation limits because of humidity

The discussion of the effect of the water on the combustion in terms of laminar flame speed and autoignition times will be undertaken later in Chapter 5.

Table 3 lists the main properties at 25°C and ambient pressure of water, iso-octane and a common RON95 gasoline [71]. It is evident that the water differs greatly in all properties compared to the other two fluids, and each of these properties has specific effects as will be shown shortly. In particular, in the following analysis the differences between water and iso-octane will be analysed. Iso-octane, according to several works [71,72], has been chosen as a representative fluid to show the macro differences between water and fuels for SI engines. In fact, iso-octane exhibits repeatable and defined properties unlike gasoline which is indeed a blend. In Figure 19 are illustrated all the fundamental properties of the two fluids as a function of temperature.

Table 3. Fluid properties at 25°C and 1 bar

	Water	Iso-octane	Gasoline (RON95)
Surface tension [N/m]	72.71e-3	18.32e-3	19.80e-3
LHV [kJ/kg]	2257.00	307.00	397.00
Vapour pressure [kPa]	2.34	5.30	5.90
Viscosity [mPa·s]	0.88	0.47	0.50
Density [kg/m <sup>3</sup> ]	999.00	690.00	750.00

## 3.1 Water Physical Properties: Effects on Jet Atomization, Droplet Breakup and Evaporation

The different physical properties of the water lead to different atomization dynamics and spray breakup compared to a common gasoline, leading to different spray mixture development.

The performance of any injector depends primarily on its injector features, fluid physical properties and gas thermodynamic conditions. In general, the properties of the liquid phase that most influence the characteristics of the spray, in terms of drop size and flow rate, are: viscosity, surface tension and density. Viscosity plays a very important role in the injection process, as it not only affects the droplet breaking dynamics but also the nozzle flow rate and spray pattern. The viscosity determines the liquid jet internal shear stress that may contribute to its disintegration together with the aerodynamic instabilities.

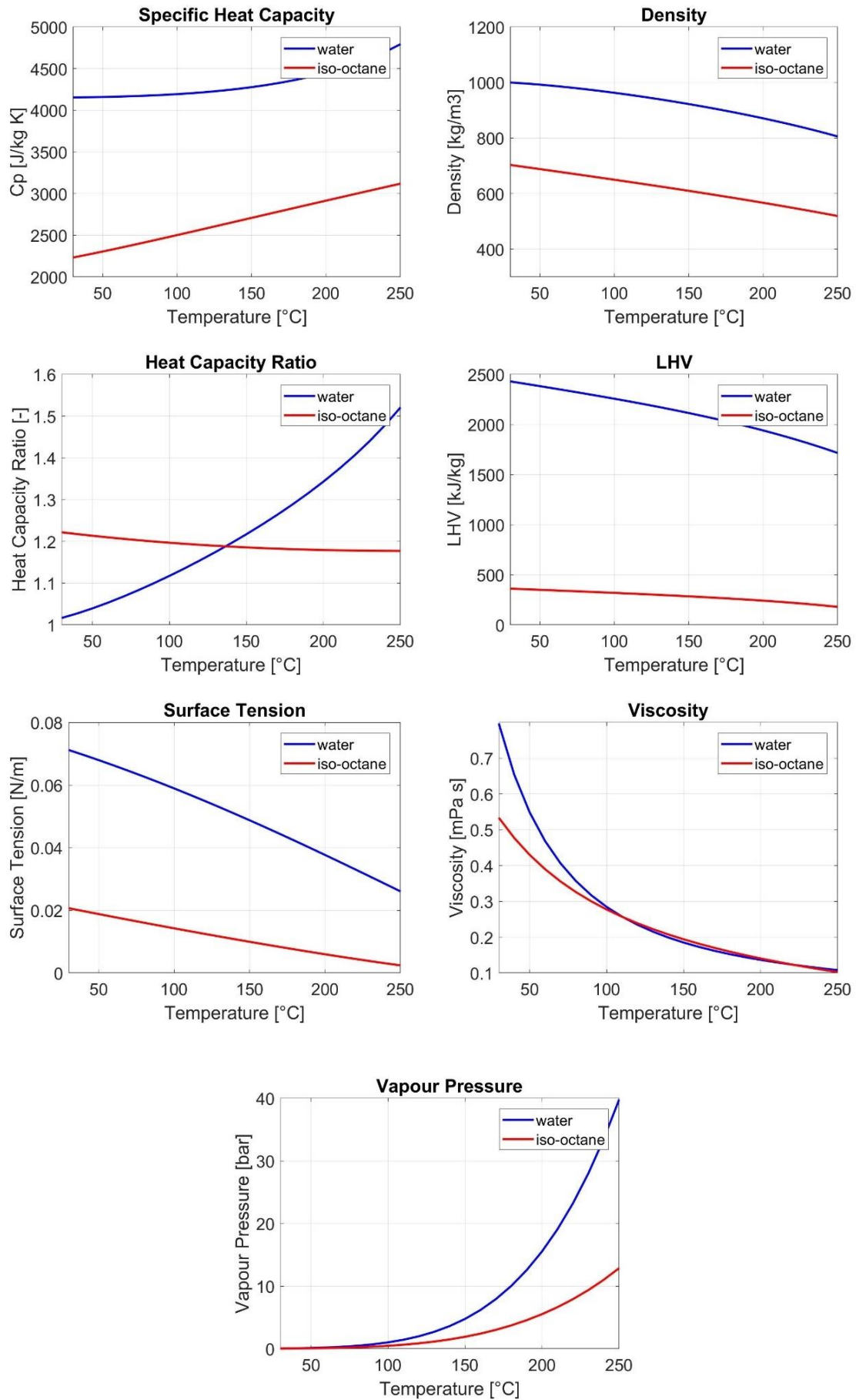


Figure 19. Water versus iso-octane fluid properties

In particular, an increase of the viscosity results in the reduction of the Reynolds jet number, and in turn, damping the instability effects on the surface of the liquid and therefore its rupture.

From Figure 19 it can be seen that the viscosity decreases with temperature in an exponential way. This is the reason why often the injectors are heated in order to reduce pumping power but also to improve atomization. The most interesting feature is that for low temperatures (below 100 °C) the differences between the two fluids tend to amplify, up to 40% higher values for water in the typical engine thermodynamic operating conditions.

The surface tension represents the intermolecular surface attraction force and therefore the resistance to breakup. The minimum amount of energy required for atomization is equal to the surface tension multiplied by the surface of the liquid, cylindrical if referred to the column of liquid flowing out from the injector or spherical if referred to a drop. Figure 19 shows clearly how the surface tension decreases with the temperature almost linearly, and that the values of water always remains above that of iso-octane (and also to that of a common gasoline). Considering the typical temperature of a turbocharged engine intake runner after the intercooler, i.e, about 40-50 °C, the value of the superficial tension is about 3.5 times larger than that of the iso-octane, resulting in much greater difficulty in the atomization and spray breakup.

Finally, the higher water density increases the effective hydraulic flow rate and can improve the spray penetration of the jet into the intake duct or cylinder, because of the higher momentum. Greater penetration may have both positive and negative effects. For example, by pushing the water towards the more peripheral areas of the cylinder, a more homogeneous mixing with the air can be obtained. On the other hand, greater penetration can also lead to liquid film formation on the combustion chamber or intake port walls, with undoubted disadvantages in terms of performance, cooling efficiency and risk of lubricant contamination.

### 3.1.1 Jet and Droplet Breakup: Analytical Analysis

Going into details about liquid jet atomization, it possible to distinguish four regimes according to the liquid Weber number and Ohnesorge numbers [73,74]:

$$We_L = \frac{U_L^2 d_o \rho_L}{\sigma_L} \quad (1)$$

$$Oh = We_L^{0.5} \left( \frac{U_L d_o \rho_L}{\mu_L} \right)^{-1} = We_L^{0.5} Re_L^{-1} \quad (2)$$

where  $U_L$  is the liquid jet velocity,  $d_o$  is the jet liquid diameter,  $\rho_L$  the liquid density,  $\sigma_L$  the superficial tension,  $\mu_L$  the dynamic viscosity and  $Re_L$  the liquid Reynold number. So, the Weber number is the ratio between inertial and surface tension forces, while the Oh number, also called “stability number”, represents the ratio between the viscous and inertia forces. According to the Reitz work [75], the liquid jet atomization regimes are (Figure 20):

1. Rayleigh jet breakup. This is caused by the growth of small axisymmetric oscillations of the jet surface, induced by surface tension. In order to have a collapse of the liquid jet, the wavelength must be greater than its circumferential: the drop diameters are nearly twice the diameter of the undisturbed jet.
2. First wind-induced breakup. The surface tension effect is now augmented by the relative velocity between the jet and the ambient gas, which produces a static pressure distribution across the jet, with disturbance present on the liquid jet surface that are mostly rotationally, thereby accelerating the breakup process. As in regime 1, breakup occurs many jet diameters downstream of the nozzle. Drop diameters are about the same as the jet diameter.

3. Second wind-induced breakup. Drops are produced by the unstable growth of short wavelength surface waves on the jet surface caused by the relative motion of the jet and the ambient gas. This wave growth is opposed by surface tension. Breakup occurs several diameters downstream of the nozzle exit. Average drop diameters are much less than the jet diameter.
4. Atomization. The jet disrupts completely at the nozzle exit: for high-velocity jets it is now generally believed that the action of the liquid jet turbulence and cavitation are the primary causes of atomization, by ruffling the surface of the jet thus making it more susceptible to aerodynamic effects. Average drop diameters are much less than the jet diameter.

As far as the water injection is concerned, it must be noted that PWI system working below 20 bar of injection pressure are expected to operate according to the first/second wind induced regime while DWI system working above 50 bar of injection pressure are expected to operate according to the second wind induced and the atomization regimes, depending on the injection pressure [72].

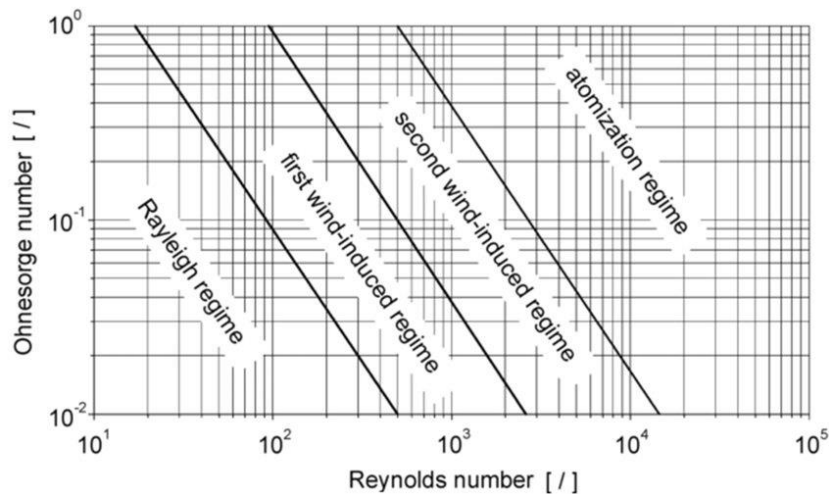


Figure 20. Classification of modes of disintegration [73]

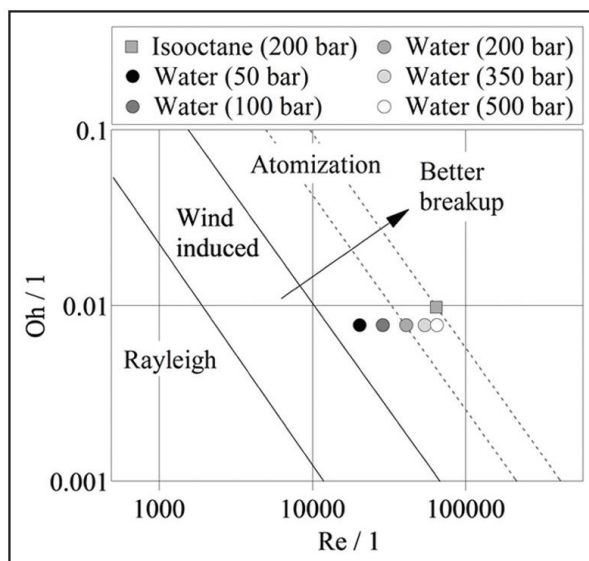


Figure 21. Ohnesorge-Reynolds diagram with expected primary breakup regions for iso-octane and water for various injection pressure [72]

Generally, the atomization of water liquid jet is less favourable than that of isooctane (commercial gasoline) because of its physical properties. As reported in [72] (Figure 21), the higher viscosity and surface tension of water compared to isooctane are such that to have the same jet breakup regime in a GDI injection system at 200 bar (atomization regime), a pressure of 500 bar with water would be required.

Empirical correlations for the estimation of the length breakup in the turbulent flow region have been developed by several workers, for example, Grant and Middleman [76] suggested the following empirical relationship:

$$L = 8.51d_0We^{0.32} \quad (3)$$

while Baron's [77] correlation of Miesse's [78] water data give

$$L = 538d_0We^{0.5}Re^{-0.625} \quad (4)$$

in which it is clear that under the same thermodynamic and flow conditions, the water exhibits much longer break-up length than iso-octane (and gasoline in general).

Reitz [75] also proposed two expressions for the calculation of the jet atomization time and for the average size of the first generated drops:

$$t_b = 5 \left( \frac{\rho_L}{\rho_A} \right)^{0.5} \left( \frac{1}{Re_L We_L} \right)^{0.2} \frac{d_0}{U_0} \quad (5)$$

$$SMD = 0.15 \left( \frac{\rho_L}{\rho_A} \right)^{0.1} \left( \frac{1}{We_A} \right)^{0.2} d_0 \quad (6)$$

Taking into account real intake port conditions, it is possible to obtain the results showed in Table 4. The data indicate that water has about three times lower atomization capacity than iso-octane. This will result in a longer jet penetration length and a higher probability of impact to the wall inside the engine.

Table 4. Atomization breakup time and drop SMD, based on Reitz work [75]

<b>P<sub>inj</sub> = 10 bar, T=40 °C, U<sub>air</sub> = 100 m/s, P<sub>a</sub> = 2 bar</b>		
	<b>Water</b>	<b>Iso-octane</b>
<b>t<sub>b</sub> [s]</b>	4.1 10 <sup>-4</sup>	1.6 10 <sup>-4</sup>
<b>SMD [μm]</b>	45	31

As far as the breakup of the droplet formed by jet atomization or previous atomization event is concerned, similarly different regimes can be defined according to the droplet Weber number  $We_d$  defined as:

$$We_d = \frac{U_r^2 D \rho_d}{\sigma_d} \quad (7)$$

where  $U_r$  is the relative gas-droplet velocity,  $D$  the droplet diameter,  $\rho_d$  the droplet density and  $\sigma_d$  the superficial tension.

In general, the breakup of a drop in an air flow stream is obtained when the aerodynamic forces are equal to the surface tension forces, which can be described through the equation:

$$C_D \frac{\pi D^2}{4} 0.5 \rho_A U_r^2 = \pi D \sigma_d \quad (8)$$

where  $\rho_A$  is the air density,  $C_D$  the drag coefficient. Rearranging the terms, it gives:

$$\left(\frac{\rho_A U_r^2 D}{\sigma_d}\right)_{crit} = We_{crit} = \frac{8}{C_D} \quad (9)$$

and the subscript *crit* denotes that a critical condition has been reached. From the previous equations it is possible to obtain the maximum droplet diameter, before breakup, for a given relative velocity:

$$D_{max} = \frac{8\sigma_d}{C_D \rho_A U_r^2} \quad (10)$$

or the relative velocity at which the drop will disrupt:

$$U_{Rcrit} = \left(\frac{8\sigma_d}{C_D \rho_A D}\right)^{0.5} \quad (11)$$

For the droplet breakup condition, Hinze [79] estimated a critical value of the Weber number equal to 22 in case of a freely falling drop, and a value of 12 for a drop subjected to a strong gas flow stream. Under engine fuel injection conditions, the latter value, i.e., 12, is taken as the threshold below that drop breakup does not occur.

To take into account the effect of viscosity, Hinze developed an expression of the following form:

$$We_{crit} = We_{crit}[1 + f(Oh_d)] \quad (12)$$

where  $Oh_d$  is the Ohnesorge droplet number defined as:

$$Oh_d = \frac{\mu_d}{(\rho_d \sigma_d D)^{0.5}} \quad (13)$$

representing the ratio between viscosity and interfacial surface tension forces of the droplet.

In addition, the experimental work of Faeth [80] led to the development of a regime map based on droplet  $We$  and  $Oh$  numbers, showing that the real effect of viscosity on regime break up become relevant only for high  $Oh$  values (high viscosity) above 0.01, while comparing water and n-heptane, that could be taken in this case as representative of gasoline, only the  $We$  number is necessary to determine the droplet break up regime (Figure 22).

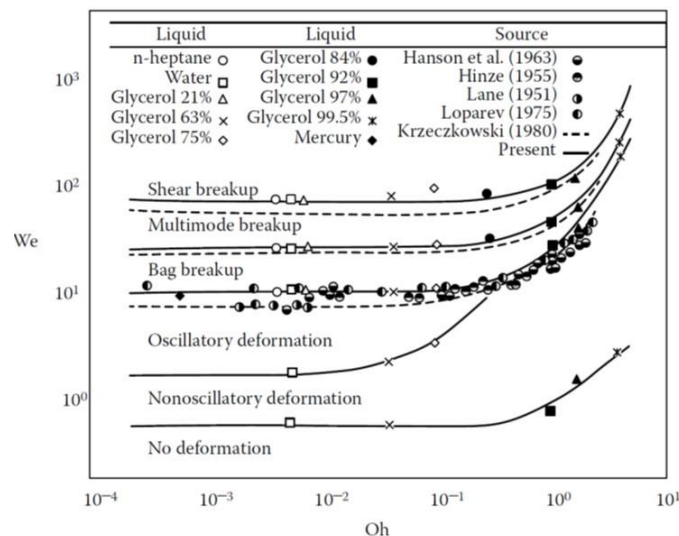


Figure 22. Droplet break-up regime

Obviously, the process of droplet breakup is not instantaneous, but it takes a certain amount of time. Many analytical models have been developed over time to assess the average life of a drop before all breakup modes are achieved. As an example, the work of Pilch and Erdman [81], who proposed a correlation that estimates the break-up non-dimensional time of a drop as a function of Weber's number, is reported here as follows:

$$\begin{aligned}
 t_b &= 6(We - 12)^{-0.25} & 12 < We < 18 \\
 t_b &= 2.45(We - 12)^{0.25} & 18 < We < 45 \\
 t_b &= 14.1(We - 12)^{-0.25} & 45 < We < 351 \\
 t_b &= 0.766(We - 12)^{0.25} & 351 < We < 2670 \\
 t_b &= 0.766 & 2670 < We < 10^5
 \end{aligned} \tag{14}$$

where  $t_b$  is the non-dimensional time at which the breakup mode has completed.

Through the study of fluid properties and the introduction of parameters for the analysis of the drop breakup performed so far, it is possible to compare the general break-up dynamics of a drop of water and iso-octane. Assuming the following conditions of a general port fuel/water injection case:

- Droplet-air steam relative velocity  $U_r = 100$  [m/s]
- Droplet Sauter Mean Diameter = 100 [μm] for water and 70 [μm] for iso-octane
- Intake runner pressure  $P_{intake} = 2$  [bar]

this gives the  $We$  numbers as a function of the temperature reported in Figure 23.

Figure 23 shows the different behaviours between water and iso-octane whose differences tend to widen as the temperature of the fluid (and therefore of the environment) increases, due to surface tension variation. Considering a fluid temperature of 40°C, typical for an injection in the intake runners and ports, and varying the relative speed between gas and liquid phase, it is to note again the greater difficulty that water faces in producing smaller droplets (Figure 23 on the right). To reach the critical breakup condition ( $We=12$ ) a relative speed almost double than that of iso-octane is required for the water. If the relative speed does not exceed 55 m/s no breakup will occur.

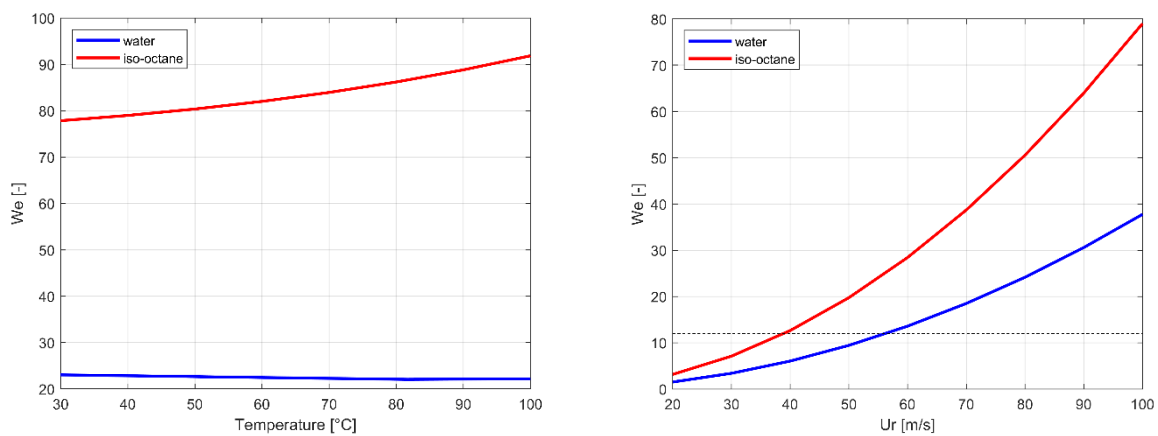


Figure 23. Water and iso-octane  $We$  comparison as a temperature (on the left) and relative velocity (on the right) function

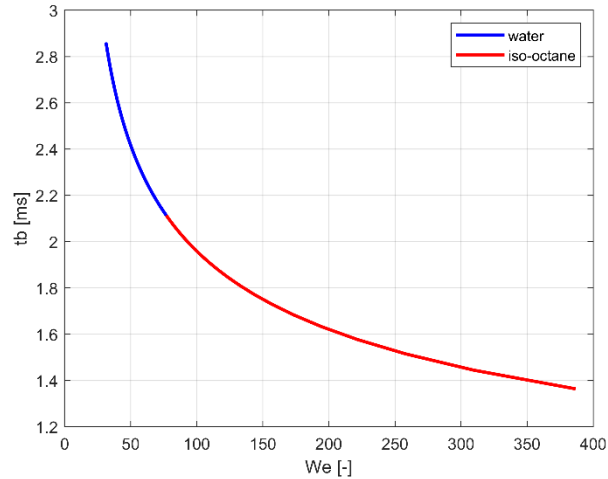


Figure 24. Water and iso-octane  $We$  breakup time comparison, assuming constant reference conditions in terms of SMD and  $U_r$

Finally, it is also interesting to compare the time taken by the drop to undergo all the breaking processes up to the last one (Eq.(14)), for the same temperature range seen previously (from 30°C to 100°C), assuming constant reference conditions in terms of SMD and  $U_r$ . The trend, illustrated in Figure 24, is a decreasing exponential, in which the iso-octane, due to the higher  $We$  number, shows lower characteristic times. For both fluids, the presence of turbulence inside the air flow stream will produce oscillations on the external surface of the drops with a characteristic frequency, which in case of resonance, will help in the breaking drop process, decreasing the characteristic times  $t_b$ .

### 3.1.2 Mass Evaporation Rate: Analytical Analysis

The drop evaporation in a spray cloud includes various phenomena of transport through its surface. Specifically, there is an exchange of heat by conduction and convection from the surrounding environment to the drop and a transfer of steam by convection and diffusion in the opposite direction. The evaporation rate of the drop depends mainly on the transport properties, pressure and temperature of the gas, relative velocity, volatility and characteristic diameter (SMD). The size of the drop, in terms of SMD, influences not only the heat transfer due to different surface/volume ratios, but the larger is the drop the longer it takes to reach the temperature equilibrium condition on the surface. The mass and energy exchange processes are also strongly affected by the Reynold number of the drop, whose value varies over time because neither the speed nor the size of the drop remains constant.

The goal is now to analytically compare the evaporation rate of a water drop with that of the iso-octane for different physical conditions. The study is of particular importance because it allows to estimate a priori the time-life of a drop which, for engine applications, means to understand the probability that the drop evaporates before entering the cylinder. The analysis starts from a simplified condition, where the drop is in a quiet environment, then, through appropriate modifications, the study will move to the evaluation in flow stream conditions. Here only the main steps are reported, all the mathematical details can be found in [73]. The analysis assumes the following assumptions:

- spherical drop;
- the liquid is pure and has a defined boiling point;
- negligible radiant heat transfer.

The diagram of the evaporating drop is shown in the Figure 25. Under common engine port injection temperature conditions, the vapour concentration on the liquid surface is low and little mass transfer occurs

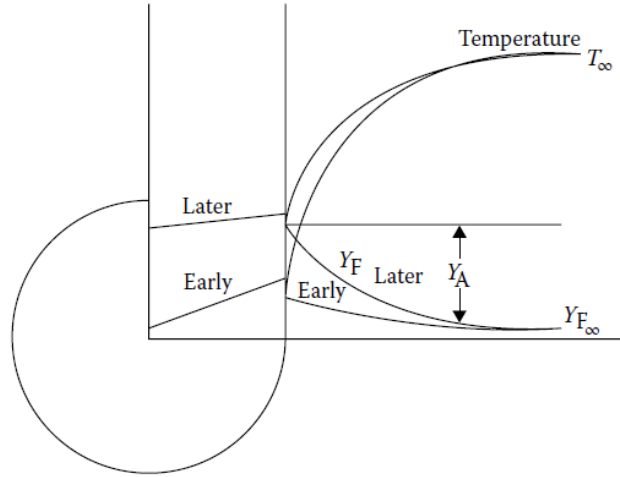


Figure 25. Variation of temperature and gas concentration during droplet evaporation [73]

in this first phase (early phase). Subsequently the drop removed heat from the gas environment, assuming a non-uniform temperature distribution due to its low thermal conductivity: colder in the centre and warmer outside. As the temperature of the drop increases, the vapour formed on the external surface causes a decrease in the heat transfer, making the temperature inside the drop more uniform.

Neglecting the thermal diffusion and assuming that the driving force for species diffusion is the concentration gradient in the radial direction, the following expression can be written for an evaporating drop:

$$\frac{dY_F}{dr} = -\frac{RT}{D_c P} (m_F Y_A) \quad (15)$$

where  $Y_F$  is the fuel mass fraction,  $Y_A$  the air mass fraction,  $m_F$  the diffusion mass rate per unit area,  $D_c$  the diffusion coefficient,  $P$  gas pressure,  $r$  the droplet radius ( $r=0$  at the centre of drop and  $r=r_s$  at drop surface). From continuity conservation, the diffusion mass rate at the drop surface is given by:

$$m_{F_s} = 4\pi r_s^2 \dot{m}_F = m_F 4\pi r_s^2 \quad (16)$$

$$\frac{dY_F}{dr} = -\frac{RT}{D_c P} (m_{F_s} Y_A) \left( \frac{r_s^2}{r^2} \right) \quad (17)$$

or, since  $Y_A = 1 - Y_F$ ,

$$\frac{dY_F}{dr} = -\frac{RT}{D_c P} (m_{F_s} (1 - Y_F)) \left( \frac{r_s^2}{r^2} \right) \quad (18)$$

Rearranging and integrating the Eq.(18) between the surface and the far ambient condition and considering that the ambient gas mass flux is zero at the liquid surface [82], it is possible to achieve the following mass evaporation rate expression:

$$\dot{m}_F = 4\pi r_s \rho D_c \ln(1 - Y_{F_s}) \quad (19)$$

The quantity  $\rho \cdot D_c$  can be replaced with  $(k/c_p)_g$ , assuming a Lewis number equal to one, where  $k$  and  $c_p$  are the mean thermal conductivity and specific heat, respectively. Defining the mass transfer number as:

$$B_M = \frac{Y_{Fs}}{1 - Y_{Fs}} \quad (20)$$

then,

$$\ln(1 - Y_{Fs}) = -\ln(1 + B_M) \quad (21)$$

and the final formulation is:

$$\dot{m}_F = 2\pi r_s D_s \left( \frac{k}{c_p} \right)_g \ln(1 + B_M) \quad (22)$$

This is the basic equation for the drop evaporation rate. Its accuracy is very dependent on the choice of properties values. According to Hubbard et al. [83], best results are obtained using the one-third rule of Sparrow and Gregg [84], where average properties are evaluated at the following reference temperature and composition:

$$T_r = T_s + \frac{T_\infty - T_s}{3} \quad (23)$$

$$Y_{Fr} = Y_{Fs} + \frac{Y_{F\infty} - Y_{Fs}}{3} \quad (24)$$

where  $T$  is the temperature,  $Y_f$  is the vapor mass fraction, and subscripts  $r$ ,  $s$ , and  $\infty$  refer to reference, surface, and ambient conditions. If  $Y_{F\infty}$  is assumed to be zero, Eq. (24) becomes:

$$Y_{Fr} = \frac{2}{3} Y_{Fs} \quad (25)$$

and

$$Y_{Ar} = 1 - \frac{2}{3} Y_{Fs} \quad (26)$$

Eq.(23)-(26) are used to calculate the reference values of the relevant physical properties of the vapor–air mixture that constitutes the environment of an evaporating drop. For example, the reference specific heat at constant pressure and thermal conductivity are obtained as:

$$c_{pg} = Y_{Ar}(c_{pA}@T_r) + Y_{Fr}(c_{pv}@T_r) \quad (27)$$

$$k_g = Y_{Ar}(k_A@T_r) + Y_{Fr}(k_v@T_r) \quad (28)$$

In a similar way it is also possible to define a heat transfer number through the surface of the drop:

$$B_T = \frac{c_{pg}(T_\infty - T_g)}{L} \quad (29)$$

where  $L$  is the vaporization heat at surface temperature  $T_s$ . The number  $B_T$  denotes the ratio of the available enthalpy in the surrounding gas to the heat required for liquid evaporation. It represents the driving force for the evaporation process and the heat transfer rates can be evaluated as:

$$\dot{m}_F = 2\pi r_s D_s \left( \frac{k}{c_p} \right)_g \ln(1 + B_T) \quad (30)$$

Under steady-state conditions  $B_M=B_T$  and both Eq.(22) and Eq.(30) can be used.

When the drop and the air are in relative motion, the evaporation rate increases due to the convective effect and the average life of the drop decreases. Ranz and Marshall [85] proposed a correction factor for the evaluation of the evaporation rate on the drop surface within a gaseous stream:

$$1 + 0.3Re_D^{0.5}Pr_g^{0.33} \quad (31)$$

The combination of Eq.(30) and Eq.(31) yields the following expression for the drop evaporation rate in forced convection:

$$\dot{m}_F = 2\pi r_s D_s \left( \frac{k}{c_p} \right)_g \ln(1 + B_T)(1 + 0.3Re_D^{0.5}Pr_g^{0.33}) \quad (32)$$

This equation gives the instantaneous evaporation rate for a drop of diameter  $D$ . To obtain the average evaporation rate, the constant should be reduced from 2 to 1.33. Substituting also  $D = 0.667D_0$  and  $Pr_g = 0.7$  it gives:

$$\dot{m}_F = 1.33\pi r_s D_0 \left( \frac{k}{c_p} \right)_g \ln(1 + B_T)(1 + 0.22Re_{D_0}^{0.5}) \quad (33)$$

and

$$t_e = \frac{\rho_F D_0^2}{8 \left( \frac{k}{c_p} \right)_g \ln(1 + B_T)(1 + 0.22Re_{D_0}^{0.5})} \quad (34)$$

where  $D_0$  represents the initial drop diameter and  $t_e$  is the total time required to fully evaporate the drop.

Figure 26 shows the ratio between the evaporation time of a drop of water and iso-octane, in three typical thermodynamic conditions of the intake duct for PWI and PFI systems, using the equations seen so far, in which an air speed of 100 m/s has been assumed. Although the results are purely indicative, as correlations can introduce wide margins of error, the tendency of water to exhibit slower evaporation rates is clear.

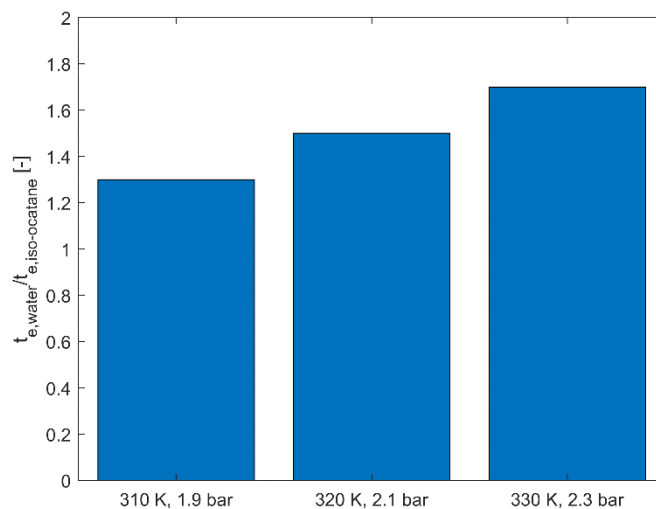


Figure 26. Drop evaporation time: water and iso-octane comparison

In conclusion, all the previous analytical considerations show that water spray evaporation rate are much lower than iso-octane (i.e., gasoline spray) at same conditions. That is an important issue since on one hand it means that water spray evaporation rate is lower than iso-octane and wall impingement will be more likely. On the other hand, this feature may be desirable since, as already discussed, in PWI configuration water spray should be targeted to evaporate inside the cylinder to promote the evaporation rate. As a matter of fact, the previous preliminary assessment highlights the importance to promote evaporation with injection ad-hoc strategy and injection system specification (Injector HFR and operating injection pressure, nozzle hole diameter) for both PWI and DWI configurations. It is clear that PWI would require a more intense optimization of the injection systems despite the much lower cost and the minor installation constraints.

### 3.2 Water Cooling Effects: Preliminary Analysis

After the previous discussion where some conclusions were drawn on the water properties effect on atomization, spray breakup and evaporation, a forecast can be provided on the conditions and parameters that play a role, or are expected to play a role, in the mixture cooling because of the water evaporation.

The cooling of the charge achieved by the water injection is due by three effects, having a different weight. The first one concerns with the very high LHV (latent heat of vaporization), which allows heat to be subtracted from the surrounding gas during the liquid to vapour phase change. As far as the water LHV is concerned, it is clear from Figure 19 and Table 3 that this is significantly higher than isooctane and gasoline regardless the temperature. For example, considering air temperature condition of 50 °C, similar to that in the intake duct of a turbocharged engine, LHV is about six times that of gasoline. Moreover, it is important to notice that LHV decreases with increasing air pressure and temperature, making it necessary to carefully optimize the water injection mass and timing in order to achieve the maximum mixture cooling. Theoretically, if only the effect of the LHV is considered, PWI systems would have a much higher charge cooling potential than DWI systems where temperatures and pressures are much higher. Unfortunately, the problem of the air saturation due to humidity, the greater possibility of liquid film formation on the walls and the larger evaporation duration due to the low temperatures, makes DWI a better option from a thermodynamic point of view and it requires a careful design of the PWI system which otherwise may perform inefficiently.

The second cooling effect of the mixture is linked to the specific heat of the water vapour. It is important to note that the presence of water in the cylinder contributes to raising the specific heat of the whole mixture, leading to a reduction of the heat capacity ratio and therefore of the polytropic compression index. This contributes to bring down the mean cylinder temperature and pressure at TDC.

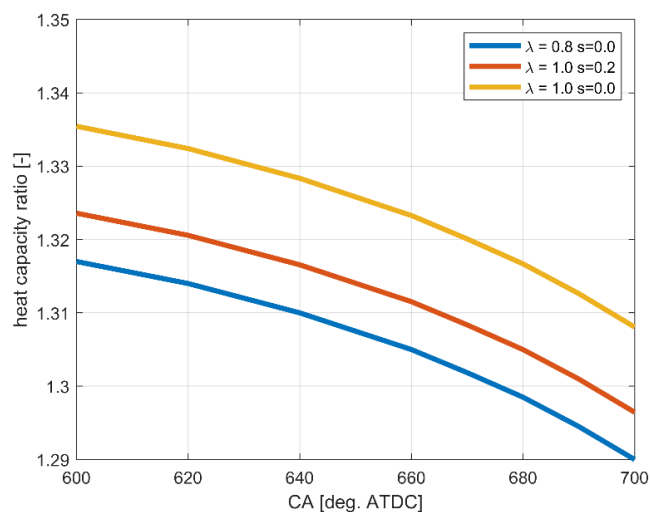


Figure 27. Heat capacity ratio example for different mixture condition in a GDI turbocharged engine

In general, this final effect depends also to water injector strategy adopted, because the temperature reduction in turn could rise again the heat capacity ratio.

Figure 27 shows three trends of the specific heat ratio during the combustion phase of a typical GDI turbocharged engine: one in the case of a rich mixture and two under stoichiometric conditions with and without the addition of water. Under the same mixture conditions, water actually tends to decrease the specific heat ratio, however, it can be seen that in the example considered a water/fuel ratio of 0.2 is not sufficient to achieve the same effect as  $\lambda$  0.8 strategy.

Finally, the water vapour behaves as an inert diluter in a similar way as EGR does (EGR which contains water indeed), absorbing heat from the surrounding environment and lowering the temperature. However, this effect is less effective because the amount of water mass injected is very small compared to that of the mixture, typically between 1% and 4%, without considering the mass of EGR.

In order to discover the potential of water injection applied to internal combustion engines, it becomes interesting to understand which is the maximum theoretical cooling effect achievable by the evaporation of the water for PWI and DWI systems.

Through a simple energy balance between the species present in the system, air, fuel and water, it is possible to derive the charge temperature variation due to the evaporation of the water:

$$\Delta T_{th} = \frac{s LHV + Q_{wall}}{\lambda \alpha_{st} c_{p,charge}} \quad (35)$$

where  $Q_{wall}$  is the wall energy transfer,  $\alpha_{st}$  the air/fuel stoichiometric ratio,  $c_{p,charge}$  the mean charge specific heat and  $s$  is the water/fuel mass ratio under stoichiometric mixture condition. Assuming that:

- the system is adiabatic;
- the mixture is stoichiometric;
- the heat capacity considered is that of the air;
- all the water droplets evaporate instantaneously.

for a PWI strategy, considering an air pressure of 2 bar and temperature of 50°C, the maximum theoretical cooling effect is illustrated in Figure 28.

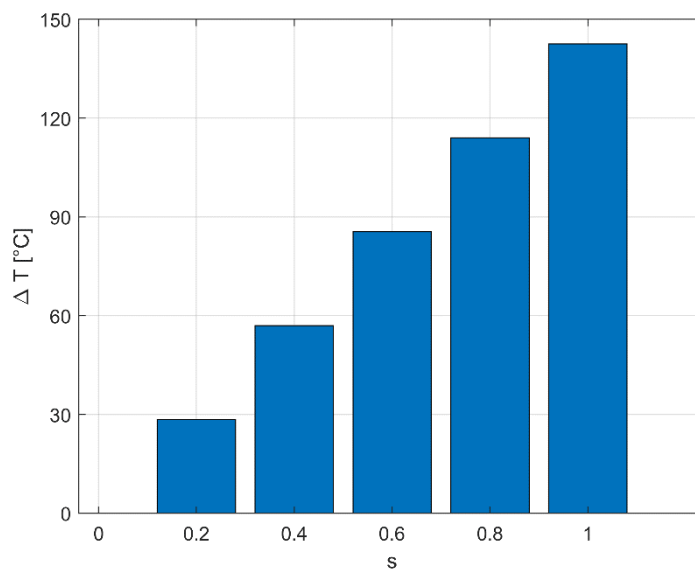


Figure 28. Maximum cooling effect for PWI-like condition system

The theoretical results show great reduction of the mixture temperature increasing the water/fuel ratio, even reaching about 150 °C for  $s$  equal 1. However, this result differs greatly from the actual cooling capacity of the water for the following reasons:

- Not all the water droplets will be able to evaporate in the air. Some of them will form a layer of liquid wall film. This effect is particularly present in a PWI systems, where an optimization of all the injector parameters, in particular spray angles and targeting, are necessary to limit the phenomenon;
- The water does not evaporate instantly: according to the local evaporation rate, it goes through different thermodynamic conditions in the system that reduce the water LHV, as reported in Figure 29, where the LHV is plotted against pressure. In a GDI engine at full load, the in-cylinder mean pressure at the end of the compression stroke may reach 45 bar, this means that the last evaporating droplets during the final part of the compression stroke may face a reduction of the LHV (cooling effect) of about 25%;
- the evaporation rate also depends on the humidity of the air stream. If local saturation conditions occur, evaporation is inhibited;
- locally the effect of high LHV let the surrounding media, close to evaporated zones, facing a huge temperature reduction, preventing, as a result, the evaporation of further water droplets, due to the decrease of the local saturation pressure.

This means that the actual mixture temperature reduction achievable is expected to be much smaller than the theoretical one. Assuming ambient conditions at higher pressures, as in the case of a DWI strategy, it is possible to compare, according to the water/fuel ratio and under the same hypotheses mentioned above, how the maximum theoretical cooling of the charge varies. Figure 30 shows that there is a cooling difference of about 4 °C between 2 and 60 bar, for  $s$  equal to 0.2. This difference reaches even more than 40 °C for the highest  $s$  value, mainly due to the decrease of LHV with the pressure.

Even under these conditions, equivalent to a direct water injection system, the water does not evaporate instantaneously, but some drops may form wall film and/or contaminate the lubrication oil, thus losing effectiveness in cooling, especially for part-load engine working points.

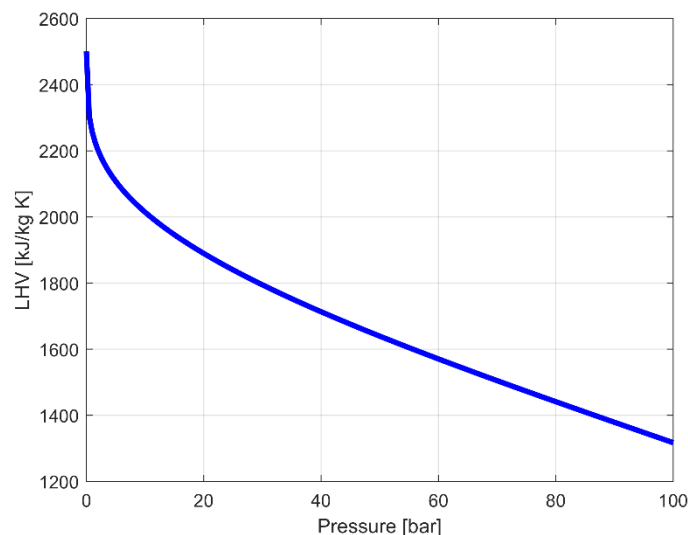


Figure 29. Water LHV as a function of pressure

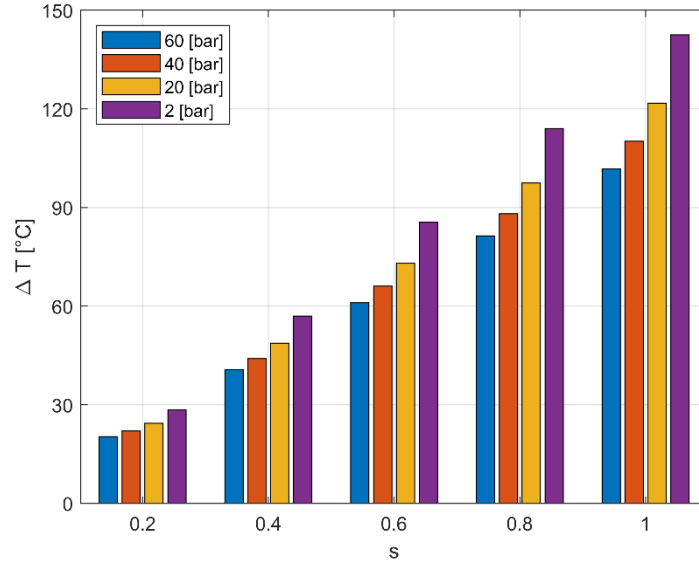


Figure 30. Theoretical cooling effect for different pressure conditions and s values

It is therefore important to define a cooling efficiency, with which the different water injection strategies will be compared during the fluid dynamic simulations:

$$\eta = \frac{\Delta T_{th}}{\Delta T_{real}} \quad (36)$$

i.e. the ratio between the theoretical temperature reduction, defined by Eq.(35), and the real temperature variation of the system at the top dead centre.

### 3.3 Humidity Effects on Water Injection: Brief Analysis

Usually CFD simulations neglect the air relative humidity (RHU), considering it as dry. However, unlike fuel, water evaporation is dependent on the humidity conditions of the air. For highly boosted engines with a highly efficient charge air cooler, the cooled fresh charge may be at or near 100% relative humidity.

In this paragraph is intended to investigate the possible effect that water vapor can have on the water injection strategy. In particular this section aims to assess the mass of water that can be injected until local saturation is reached, for different relative humidity.

Regarding the cooling humidity effects, some CFD simulations considering different RHU values have been performed for the baseline engine adopting PWI architecture and the main results will be shown in Chapter 9, concerning CFD simulations for non-reacting flows. Here it is reported a quick recap of relative humidity main concepts and the leading equations in the definition of the evaporative process of the water.

The maximum amount of steam that can be present in a gaseous mixture depends on its vapor pressure and therefore on local temperature conditions. As the temperature decreases, the amount of vapor admissible in the gas decreases until condensation is reached when the gas is 100% saturated [86]. This is important not only because of the negative consequences in the generation of liquid water inside the intake line, but also because of the change in the composition of the gas mixture.

Considering the pseudocritical thermodynamic coordinates of the dry air and of the saturated water vapor, it can be deduced that both can be considered perfect gases in automotive field of application. Thus, the mass of dry air is considered constant, while the mass of vapor can change, as stated before. This fact explains why in the main CFD codes the specific quantities are not referred to the mass of the mixture, but to the

mass of dry air. In CFD simulations of Internal Combustion Engines (ICE) the gas phase of the mixture is usually considered a mixture of two ideal gases because the vapor has a very small partial pressure. The composition of the gas phase may vary due to the evaporation or the condensation of water.

For the calculation of the water saturation pressure reference is made to Buck's expression [87]:

$$p_{SAT}(T) = 0.61121 \cdot \exp\left(\left(18.678 - \frac{T}{234.5}\right)\left(\frac{T}{257.14 + T}\right)\right) \quad (37)$$

where  $T$  is the mixture temperature in Celsius degrees and  $p_{SAT}$  is the computed saturation pressure in kPa. This equation validity is limited to the range above zero Celsius degrees, which is the only one of interest for engine applications.

From the Dalton Law, the total pressure  $p_{TOT}$  of the mixture is:

$$p_{TOT} = p_A + p_V \quad (38)$$

where  $p_A$  is the partial pressure of the dry air and  $p_V$  is the partial pressure of water vapor. The mixture title  $X$  is defined as the ratio between the evaporated water mass in the mixture  $m_V$  and the dry air mass  $m_A$ :

$$X = \frac{m_V}{m_A} \quad (39)$$

The hygrometric degree  $\Phi$  is the ratio between the local vapor pressure  $p_V$  and the saturation pressure  $p_{SAT}$ :

$$\Phi = \frac{p_V}{p_{SAT}} \quad (40)$$

The hygrometric degree is defined in the range 0-1, where 0 corresponds to dry air and 1 to the saturation condition. The relative humidity RHU is defined as the hygrometric degree  $\Phi$  multiplied by one hundred:

$$RHU = \Phi \cdot 100 \quad (41)$$

Thus, the range of RHU is between 0 and 100. If RHU = 70%, it means that the mixture contains a water vapor equal to 70% of what would bring it to saturation. It quantifies how close the mixture is to saturation: it does not quantitatively indicate how much water in the vapor state is present in the mixture. It possible to link the hygrometric degree to the mixture title:

$$X = 0.622 \cdot \frac{\Phi \cdot p_{SAT}}{p_{TOT} - \Phi \cdot p_{SAT}} \quad (42)$$

or:

$$X = 0.622 \cdot \frac{p_V}{p_A} \quad (43)$$

Then, it is also possible to compute the hygrometric degree knowing the  $X$  value:

$$\Phi = \frac{X}{X + 0.622} \cdot \frac{p_{TOT}}{p_{SAT}} \quad (44)$$

The maximum partial pressure  $p_V$  that can be reached by the water vapor in the mixture is the saturation pressure  $p_{SAT}$ : water vaporization takes place as long as the partial vapor pressure is less than the saturation

pressure. As the temperature increases, the relative humidity decreases, then the mass of water that can evaporate increases and the saturation condition moves away.

Through the above equations it is possible to evaluate analytically the maximum water injected mass before reaching saturation. The analysis has been carried out for different relative humidity values and for three levels of ambient temperature (0°C, 20°C, 40°C). Inside the cylinder the saturation condition is never reached, not even locally. For this reason, the study is referred to the thermodynamic conditions of the air in the intake duct and the mass of water injected by the PWI. The fuel mass considered for s calculation is 84 mg, the same used for stoichiometric mixture condition in the CFD simulations of Chapter 9, where all engine details will be presented. The aim here is only to focus on humidity thermodynamic effects.

Figure 31 compares the relative humidity of the external air with that at the injection point (SOI) after the intercooler. The interesting fact is that the RHU decreases substantially because the air, passing through the compressor and the intercooler, is globally heated raising the saturation pressure. Starting for example from a high RHU of 85%, typical during rainy days, the relative humidity in the intake duct is 50%, leaving a greater margin for the evaporation of the injected water before condensing.

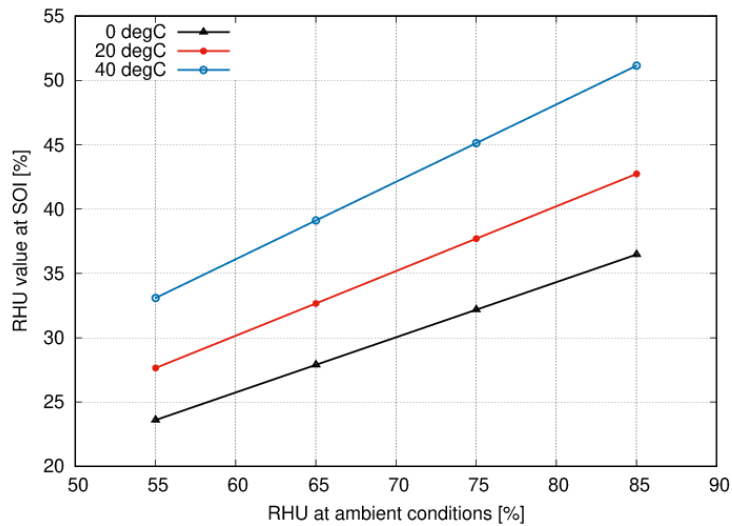


Figure 31. Air relative humidity variation between ambient air and PWI injection point for three temperature levels

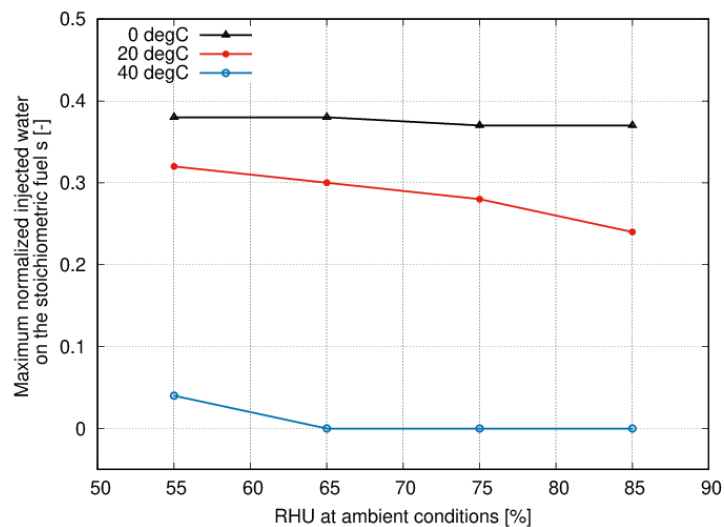


Figure 32. Maximum s value before reaching saturation point for different ambient RHU

Figure 32 indicates that the  $s$  parameter can vary from a minimum of 0 to a maximum of 0.38 before reaching saturation. Moreover, only at 0 °C the injectable quantity remains constant as the external relative humidity increases: on the contrary for higher air temperatures in the intake duct (40°C), typical in current turbo-engines, starting from ambient RHU values of 65% the saturation is reached before injecting. It is to say that in PWI systems with relative humidity and temperature values typical of European countries, it has been seen that saturation in the intake port is reached for a mean value of parameter  $s$  close to 0.38 at 0°C, and close to 0.30 at 20 °C: beyond those values there is no more evaporation in the intake port and the risk of condensation is very high.

However, it should be highlighted that one of the main objectives that must be guaranteed, during the injector design of PWI simulations, is to shift the evaporation of the water inside the cylinder rather than in the intake duct or port. This is achieved thanks to an appropriate optimization study of the PWI system in terms of spray targeting and injection timing. In this way it will be possible not only to maximize the cooling efficiency but also to eliminate the condensation problem in the intake duct, as the water droplets tend to evaporate in the cylinder. Since conditions of 100% relative humidity never occur inside the cylinder, the ambient RHU value is almost negligible.

The effect of relative humidity on the cooling capacity of the engine at the end of the compression stroke will be verified in Chapter 9, with appropriate fluid-dynamic simulations where the engine examined will be presented. In fact, the water vapor present in the air, being already in the vapor state, can have an impact only as an addition of diluent in the cylinder, modifying the heat capacity ratio.

### 3.4 Brief Review of Chemical Water Effects on Laminar Flame Speed and Ignition Delayed Time

Besides its effect on the physical phenomena that characterize the operation of the engine, the water chemical properties play a significant role. In particular they involve a variation of the laminar speed of flame and mixture auto-ignition times. In general water induces an effect both positive and negative. On the one hand it tends to increase the mixture auto-ignition times and therefore to reduce the detonation attitude of the engine, on the other hand it involves a slowing down of the chemical kinetics reducing the laminar flame speed and therefore the combustion rate.

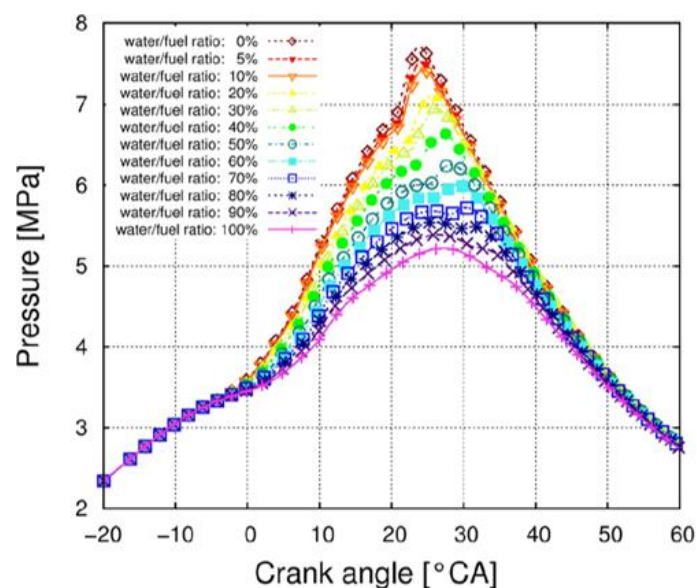


Figure 33. LFS water effect using the ETRF reaction scheme by Seidel [88]

In literature the experimental data on LFS (Laminar Flame Speed) and IDT (Ignition Delayed Time) with added water are rather limited. However, the topic has been treated by several authors through the use of chemical kinetics schemes in order to obtain LFS and IDT values under different thermodynamic and mixture conditions.

Mauss et al. [88] show through the use of the ETRF reaction scheme of Seidel, the laminar speed slowing down for different water to fuel ratios (Figure 33) and temperatures with pressure fixed at 40 bar. The slowdown is approximately linear to the increase of the water-fuel ratio, finding a similar effect on the combustion process in the engine simulation.

Because of this strong influence of water mass fraction on the laminar flame speed, it is mandatory to check the amount of water formed near the spark plug during the first stages of ignition. Although the overall amount of water injected is low, the accumulation under the spark plug might be considerable and this could compromise the speed and stability of the flame front, making combustion inefficient.

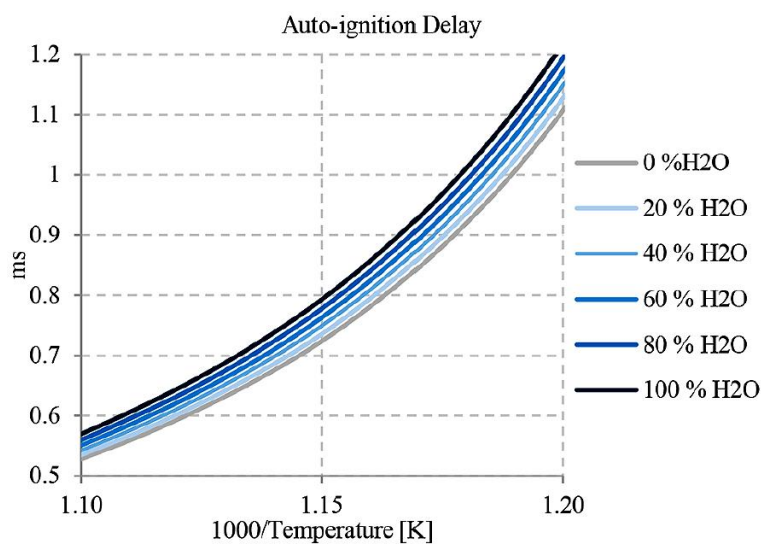


Figure 34. Water effects on IDT [89]

In order to assess the anti-knock attitude of water it is necessary to rely on auto-ignition times, calculated taking into account the addition of water diluent in the mechanisms of chemical kinetics. In [89] the authors used DARS software following a careful selection of the surrogate and validation of the mechanisms of reactions, to evaluate these chemical effects due to the presence of water in a constant volume reactor. Figure 34 shows how IDT is actually positively affected by increasing the percentage of water introduced compared to fuel under stoichiometric conditions.

Chapter 5 will assess in detail the effects of water on the laminar flame speed, the flame thickness and the auto-ignition times, through the use of numerical models based on kinetic chemical theory, which are all fundamental parameters to obtain reliable results from 3D combustion simulations. Thanks to these kinetic calculations it will be possible to obtain new databases for both LSF and IDT, for the evaluation of the chemical effects of water on a representative surrogate of common gasoline. The new databases can therefore be used at runtime during simulations or to extract new and more reliable correlations.

### 3.5 Summary

In this chapter the properties of water have been highlighted and compared with those of isooctane (representative specie to analyse the macro differences between water and gasoline). The water showed a lower attitude to evaporation and breakup of the drops. This is mainly attributable to the higher surface

tension and viscosity. The former involves a higher binding energy that must be overcome in order to atomize the spray jet and the following droplets, presenting a higher overall vapor pressure. The tendency is to have larger droplets, with an unfavourable surface/volume ratio for the evaporation. Moreover, the viscosity influences the propagation/damping of the perturbations on the surface of the jet/drops. Since water has a higher viscosity, especially below 50°C (typical temperature for PWI systems), surface rupture tends to be inhibited and so the generation of smaller droplets

It has also been shown how difficult it is to obtain critical  $We$  numbers comparable to those of common fuels. In order to have the same atomization regime as for iso-octane injection at 200 bar, 500 bar with water would be required.

In addition, the higher density of the water affects the penetration of the jet. Water injection increases the probability that the jet will hit the walls of the cylinder or intake duct, creating wallfilm and decreasing the cooling capacity. This is an important feature that must be taken into account during the definition of the main injector settings, like position and orientation.

From a theoretical point of view the temperature variation generated by water evaporation is very high thanks to the greater LHV with regard to gasoline: it increases with  $s$  and decreases with pressure (LHV decreases with pressure). Under the typical thermodynamic conditions of a PWI, a theoretical cooling capacity of 150 °C of the fresh charge could be reached. However, this does not happen because by increasing the injected water the losses due to wallfilm generation, local saturation conditions and the decrease of LHV with pressure increase exponentially. This has been summarized in the definition of cooling efficiency, a parameter that will be used in CFD simulation analysis to compare the different water injection strategies.

Finally, it has been introduced the concept of air humidity and the effects that different relative humidity values have on the maximum amount of injectable water without incurring into condensation problems, whose main effect on engine will be highlighted in Chapter 9, dedicated to non-reacting simulations with PWI architecture.

This preliminary study on the properties of water lays the necessary foundations to understand the most complex phenomena related to the engine, which will be analysed in the following chapters both from an experimental point of view, on the tests performed with PWI injector, and numerical in non-reacting and reacting flow conditions.

# Chapter 4: Numerical Methodologies

This chapter briefly presents the main numerical models adopted for the execution of three-dimensional numerical simulations. The solver used for the fluid-dynamic analysis is AvL-Fire. Specifically, it will be introduced the models and the fundamental parameters related to spray, combustion process and fluid dynamics (wall and heat exchange laws), underlining modification from the default settings or precise model implemented in the code. The main contribution provided to the methodology of engine simulation with water injection through opportune chemical kinetics calculations, will be examined in the next chapter: chemical effects of the water on the laminar flame speed, flame thickness and auto-ignition times, will be extract as fundamental data to consider during the simulations in order to assure a correct representation of the phenomena.

## 4.1 Spray Modelling

In general, the study of the injector spray can be carried out through an Eulerian or an Lagrangian approach. Both exhibit advantages and shortcomings: at the end, the Lagrangian approach is currently the most widely used for reciprocating internal combustion engine spray simulations.

In a Lagrangian framework, particle-like elements, known as ‘parcels’ (group of identical non-interacting droplets all having same properties like velocity, density, etc), are inserted into the gas continuum domain at given initial conditions of diameter, velocity and directions. The state of each parcel is updated according to the selected set of models, solving ordinary differential equations for the trajectory, momentum, heat and mass conservation of each parcel. The main equation describing the trajectory and speed of a parcel (momentum conservation equation) can be written as [90]:

$$m_d \frac{du_{id}}{dt} = F_{idr} + F_{ig} + F_{ip} + F_{ivm} + F_{ib} \quad (45)$$

where drag forces ( $F_{idr}$ ), buoyancy forces ( $F_{ig}$ ), pressure forces ( $F_{ip}$ ), virtual mass forces for the acceleration/deceleration of the medium surrounding the drops ( $F_{ivm}$ ) and external forces like magnetic one ( $F_{ib}$ ) are considered to evaluate the dynamic state of each parcel. Each of these forces are described by proper models (more details in [90]) which bring the Eq.(45) in the form of:

$$\frac{du_{id}}{dt} = \frac{3}{4} C_D \frac{\rho_g}{\rho_d} \frac{1}{D_d} |u_g - u_d| (u_{ig} - u_{id}) + \left(1 - \frac{\rho_g}{\rho_d}\right) g_i \quad (46)$$

which can be integrated to get the particle velocity  $u_{id}$ . The instantaneous particle position vector can be determined by integrating:

$$\frac{dx_{id}}{dt} = u_{id} \quad (47)$$

As far as parcel evaporation is concerned, the heat and mass transfer processes are described by Spalding model, originally derived by Dukowicz [91]. Essentially it is based on the following assumptions:

- Spherical symmetry;
- Quasi steady gas-film around the droplet;
- Uniform droplet temperature along the drop diameter;
- Uniform physical properties of the surrounding fluid;
- Liquid – Vapor thermal equilibrium on the droplet surface.

With the assumption of uniform droplet temperature, the rate of droplet temperature change is determined by the energy balance equation, which states that the energy conducted to the droplet either heats up the droplet or supplies heat for vaporization:

$$m_d c_{pd} \frac{dT_d}{dt} = L \frac{dm_d}{dt} + \dot{Q} \quad (48)$$

The convective heat flux  $Q$  exchanged between the gas and the droplet surface is:

$$\dot{Q} = \alpha A_s (T_\infty - T_s) \quad (49)$$

where  $\alpha$  is the convective heat transfer coefficient through the film surrounding the droplet in the absence of mass-transfer,  $A_s$  is the droplet surface area,  $T_s$  the surface droplet temperature and  $T_\infty$  is the local domain fluid temperature.

Now it is possible to reformulate the Eq.(48) in a different form, pointing the variation of the droplet ratio over time  $dr_d/dt$ :

$$m_d c_{pd} \frac{dT_d}{dt} - L \rho_d \pi D_d^2 \frac{dr_d}{dt} = \pi D_d^2 \dot{q}_s \quad (50)$$

The term  $dr_d/dt$  is determined explicitly by the Frossling correlation [92] and the right term of the Eq.(50) by the Ranz and Marshall correlation [85], with the introduction of the Nusselt number ( $Nu$ ):

$$\dot{q}_s = \lambda Nu (T_\infty - T_s) \quad (51)$$

and

$$Nu = 2 + 0.6 Re_d^{1/2} Pr^{1/3} \quad (52)$$

Here, the Reynolds ( $Re$ ) and Prandtl ( $Pr$ ) numbers are evaluated from the usual expressions seen before in Chapter 3. The reference temperature for evaluating transport properties like vapor viscosity, specific heat, thermal conductivity etc. is the average temperature between the local domain fluid temperature and the droplet surface temperature:

$$\bar{T} = \frac{T_{\infty} - T_s}{2} \quad (53)$$

It must be underlined that the Lagrangian solution of parcel governing equation induces inaccuracy in the mass and momentum liquid-gas depending on the local control volume size (mesh element size), which is used for the solution of the governing equation of the continuum phase basically decoupled from that of the continuum gas phase. In the present simulations,  $2^{/3}$  rule interpolation of the continuum phase velocity and density at parcel location has been adopted in order to reduce the grid dependency effect of the solution of spray momentum and mass transfer.

## 4.2 Atomization Modelling

The atomization model adopted is a modification of that proposed by Brusiani, Bianchi and Tiberi [93] which was an evolution of the Huh and Gosman model [94]. The model has been user-coded into Fire code. A brief description is here provided with emphasis on the modification with respect to the original model. Adopting the so called 'Blob Injection Approach' as proposed by Reitz [95], the liquid jet is simulated through a train of blob parcels issuing the nozzle. The injected parcel has an initial diameter  $D_{in}$  corresponding to the effective diameter of the injector nozzle. The Blobs (parcels) forming the liquid core are subjected to the atomization until their diameter  $D$  remains larger than a threshold  $D_T$  value, usually taken as the 0.8 time the initial parcel diameter.

The atomization process of the Blobs representing the liquid jet core, until the threshold is reached, is given by the following erosion rate:

$$\frac{dD}{dt} = -C_1 \frac{L_A}{\tau_A} \quad (54)$$

Unlike the original model, the atomization length scale  $L_A$  and the atomization time scale  $\tau_A$  are assumed to depend by liquid jet turbulence. The turbulence timescale is calculated as proposed in [94], as a function of the nozzle turbulence (kinetic energy and integral length scale), nozzle liquid effective velocity  $U_{eff}$  and area contraction coefficient.  $C_1$  is an adjustable constant that in the present cases is set to 0.1. It must be underlined that the accuracy in the definition of the injection mass flow rate, as well as of the area contraction coefficient and reduction velocity coefficient, is mandatory also for an accurate performance of the atomization model.

Once the critical threshold diameter is reached during erosion, it is assumed that the liquid core erosion is completed and the eroded blob (parcel) is finally disintegrated to a much smaller diameter as a function of the liquid jet velocity in the nozzle. In order to do not use a monodisperse sizing, the ultimate blob disintegration is modelled in such a way that the diameter of the parcel  $D_{os}$ , after final atomization stage, is chosen from a  $\chi^2$  distribution with a Sauter Mean Diameter  $D_p$  defined as a function of the nozzle liquid effective velocity  $U_{eff}$ :

$$D_p = C_2 \cdot 157.93 \cdot (U_{eff})^{-0.474} \quad (55)$$

where  $C_2$  is an adjustable constant that in the present cases is set to 1.0.

It must be noted that the spray angle is superposed by injecting Blobs according to a randomly selected angle within the prescribed limits. Figure 35 offers a simple sketch of the main working principles of the atomization model and its coupling with the secondary break up model.

Finally, in PWI cases the spray modelling has been performed by switching off the atomization model since the latter it has been validated for injection pressure and nozzle shape typical of both GDI injector or Common Rail Diesel Injector.

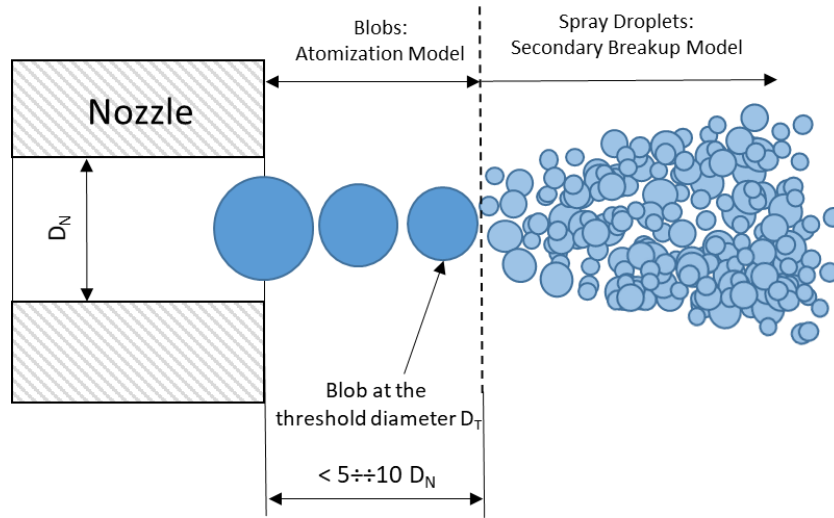


Figure 35. Atomization model representation

### 4.3 Secondary Break-Up Modelling

The secondary break-up model represents the conditions under which an additional splitting of the drops formed by atomization into smaller sizes can occur. Some models focus on aerodynamic interactions between droplets and surrounding gas, giving more importance to the relative velocity between the two phases, while others base their modelling on the generation of perturbations on the droplet surfaces and the wavelength that can trigger the break-up. Specifically, the break model adopted in the following simulations uses the correlation proposed by Hsiang and Faeth [96] and Pilch and Erdman [97]. The droplet breakup time  $t_b$  (i.e, the time required to get a diameter stable condition) is evaluated from a non-dimensional breakup time  $t_{bu}$  which is indeed a function of the droplet  $We_g$  number (i.e. breakup regime) assuming as a critical Weber number  $We_{g,cr} = 12$ :

$t_{bu} = 6.00 (We_g - 12)^{-0.25}$	$12 < We_g < 18$	
$t_{bu} = 2.45 (We_g - 12)^{+0.25}$	$18 < We_g < 45$	
$t_{bu} = 14.1 (We_g - 12)^{-0.25}$	$45 < We_g < 351$	(56)
$t_{bu} = 0.766 (We_g - 12)^{+0.25}$	$351 < We_g < 2760$	
$t_{bu} = 5.5$	$We_g > 2670$	

where the non-dimensional breakup time  $t_{bu}$  is also defined as:

$$t_{bu} = t_b \cdot \sqrt{\frac{\rho_g}{\rho_l}} \cdot \frac{U_{rel}}{d_d} \tag{57}$$

where  $\rho_g$  is the gas density,  $\rho_l$  is the droplet density,  $d_d$  the droplet diameter and  $U_{rel}$  the relative droplet to gas velocity. The correlations cover all the regimes from the 'Bag Regime' at low  $We_g$  to the 'stripping Regime' at very high  $We_g$  (i.e. close to 1000.0).

The model updates the droplet radius according to the current breakup time (breakup regime) and droplet current stable diameter:

$$d_{stable} = \frac{C_3 \cdot We_{cr} \sigma}{\rho_g U_{rel}^2} \quad (58)$$

where  $C_3$  is a model constant,  $We_{cr}$  is the critical Weber number,  $\sigma$  the surface tension. If droplet Weber number is below 12, breakup cannot occur and the droplet is stable (i.e., aerodynamic force can only deform the droplet and the droplet regime is the 'vibrational regime'). Model constant has been introduced in order to alleviate inaccuracy in the determination of the droplet-to-gas relative velocity because of the issue involved in the liquid-gas coupling in Lagrangian approach. The use of interpolation methods can alleviate those inaccuracies without eliminating them completely. Moreover, it must be underlined that, as a precise choice, adaptive mesh refinement or high reduction of mesh sizing have not been adopted since the grid size reduction may on one hand alleviate coupling inaccuracy between phases, but on the other hand it may face violation of void assumption used to make possible the decoupled solution of the dispersed phase governing equations from that of the continuum phase.

## 4.4 Particle Interaction Modelling

The parcel interaction models are based on statistical methods for the evaluation of the interaction between two or more parcels. The model chosen for the fluid dynamics simulation activities is the Schmidt model [98], because of its robustness and tuning parameters to modify its effect.

The collision is evaluated only if the droplets are in the same cell, considered to be uniformly distributed within it. The frequency of collision between two particles is modelled with a statistical approach as follows:

$$\nu = \frac{N_2 \pi}{V_{cell}} \frac{\pi}{4} (d_1 - d_2)^2 |u_1 - u_2| \quad (59)$$

where the subscript 1 and 2 refer to the properties of the two parcels,  $d$  is the diameter,  $N$  the number of particles,  $u$  the velocity and  $V$  the volume of the cell.

The probability  $P$  that a collector undergoes into  $n$  collisions follows a Poisson distribution:

$$\nu P_n = e^{-\bar{n}} \frac{\bar{n}^n}{n!} \quad (60)$$

with the mean value (number of expected collisions)  $n = \bar{n} \cdot \Delta t$ , where  $\Delta t$  is the computational time step. Thus, the probability of no collisions is  $P_0 = e^{-\bar{n}}$ . More details can be found in [90]. Still using a statistical approach, the interaction between the parcels may involve either a coalescence or a simple rebound. Furthermore, this model allows the choice of three tuning parameters:

1. Collision distance, parameter for defining the maximum distance of a collision event;
2. Mass Criterion for Split, for defining the mass threshold where parcel splitting takes place;
3. N° of split parcels, for the number of new parcels generated by the mass splitting.

Through the properties of the liquid phase and a series of random numbers it is statistically evaluated i) if the collision happens and ii) the number and type of collision (coalescence or impact with change of trajectory). For each *collector* particle,  $n$  droplets are removed from their associated parcel and the properties of the collector particles, diameter, velocity and temperature are appropriately modified due to conservation of mass, momentum and energy.

The Schmidt model is pretty the same as in O'Rourke, but the method of looping using a pre-sorting algorithm is much more efficient for most cases. The higher the average number of parcels per cell the greater the effect.

## 4.5 Spray-Wall Interaction Modelling

The model of Kuhnke [99] is an advanced wall interaction model, which in contrast to other models also takes into account the wall temperature  $T_w$  besides the impact parameter  $K$ . Depending on a dimensionless wall temperature

$$T^* = \frac{T_w}{T_s} \quad (61)$$

and a dimensionless droplet velocity

$$K = \frac{(\rho_d d_d)^{3/4} u_d^{5/4}}{\sigma_d^{1/2} \mu_d^{1/4}} \quad (62)$$

the Kuhnke model distinguishes between four regimes as showed in Figure 36. In Eq.(62) all the variables are referred to droplet properties:  $\rho$  the density,  $d$  the diameter,  $u$  the velocity,  $\mu$  the dynamic viscosity and  $\sigma$  the surface tension.

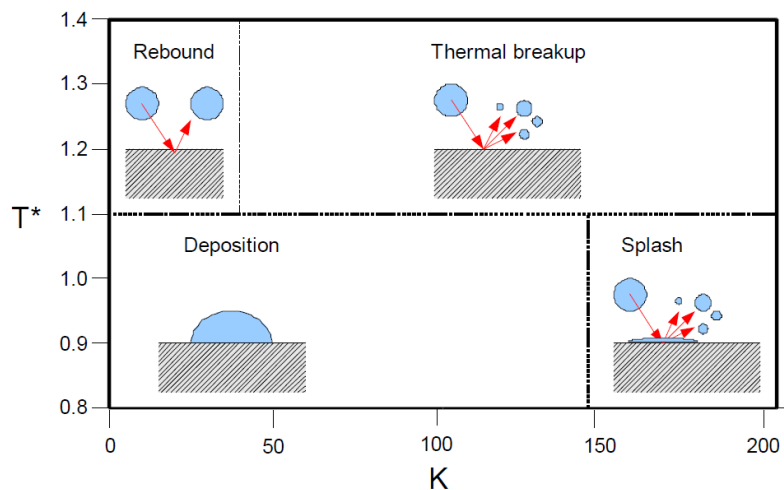


Figure 36. Regime map of the spray-wall interaction according to Kuhnke [90]

From Figure 36 it can be asses that the wall film is generated during the deposition and splash event only if  $T^*$  is lower than 1.1. In addition, a 'combined evaporation model', based on equilibrium conditions (physical and thermodynamic properties are always in equilibrium state) is used to evaluate the wallfilm evaporation process [90].

## 4.6 Reaction Rate Modelling

The determination of mean chemical reaction rates represents a central problem in the numerical simulation of chemical kinetic processes. This is because they appear to be highly non-linear functions of the local values of temperature and species concentrations.

Although it is desirable to use detailed reaction mechanisms, available computational resources are inadequate to manage thousands of elementary reactions with hundreds of participating species. This is due to the fact that for each species considered in the reaction mechanism, an additional conservation equation must be solved. From CFD numerical point of view, the combustion process simulation involves several models:

- The ignition model;
- The main premixed combustion model;
- Then auto-ignition and knock rate model;
- Look-up table Laminar Flame speed.

In the present paragraph the ignition and the main combustion models will be briefly presented since they were already available, and they were not specifically developed. In the next chapter, a methodology based on detailed chemistry calculation for look-up table creation, developed for laminar flame speed, laminar flame thickness and auto-ignition time, will be presented in detail since it represents a contribution to the simulation methodology, specifically developed in the present research for handling engine reacting flow simulation with water injection.

### 4.6.1 Ignition Model

The spark ignition model used in the present simulations is the Eulerian version of that proposed by Bianchi and Falfari [100] and it basically solves the energy and mass conservation equation of the initial flame kernel assumed to be spherical. The initial radius and temperature of the kernel after the breakdown phase are provided by a specific submodel according to the breakdown voltage and electrodes gap [101]. The breakdown energy  $E_{bd}$  available at electrodes during the breakdown phase operation is given by an empirical relation:

$$E_{bd} = \frac{V_{bd}^2}{C_{bd}^2 d_{gap}} \quad (63)$$

where  $C_{bd}$  is a model constant and the breakdown voltage  $V_{bd}$  in [kV] can be evaluated according to [102]:

$$V_{bd} = 4.3 + 136 \frac{P}{T_{unb}} + 324 \frac{P}{T_{unb}} d_{gap} \quad (64)$$

where  $P$  is the gas pressure in bar,  $T_{unb}$  is the fresh gas temperature in K,  $d_{gap}$  is the inter-electrodes distance in mm. The breakdown energy is released to the main CFD solver in the cells where the spark plug is located. At the end of plasma shock wave dynamics, the model starts to simulate the kernel expansion. Thus,

1. A spherical flame kernel of initial radius  $r_i$  and initial temperature  $T_i$  is deposited into the gas flow in the cell where spark plug lies;
2. The model by Song and Sunwoo [103] provides the initial kernel temperature  $T_i$  and radius  $r_i$  according to Kravchik's model [104]:

$$T_i = \left[ \frac{1}{k} \left( \frac{T_b}{T_{unb}} - 1 \right) + 1 \right] T_{unb} \quad (65)$$

$$r_i = \left[ \frac{k-1}{k} \cdot \frac{E_{bd}}{p \cdot d_{gap} \left( 1 - \frac{T_{unb}}{T_i} \right) \pi} \right] \quad (66)$$

The breakdown temperature  $T_b$  can be reasonably assumed to be 60000 K according to [104].

The flame kernel expansion velocity is based on Herweg and Maly model [105]. By the application of the mass conservation the kernel mean expansion velocity is evaluated:

$$\frac{dm}{dt} = \rho_{unb} \cdot s_{lam} \cdot (A \cdot \Xi) \quad (67)$$

where  $\rho_{unb}$  is the fresh gas density,  $A$  is the flame kernel surface assumed to be unaffected by turbulence,  $\Xi$  is the wrinkling coefficient of the flame surface introduced here for accounting for turbulence influence and  $s_{lam}$  the laminar flame speed.

Differentiating the Eq.(67) and applying the general gas law, one obtains the variation of the mean flame kernel radius over time:

$$\frac{dr}{dt} = \frac{\rho_{unb}}{\rho_k} s_{lam} \cdot \Xi - \left[ \frac{V}{A} \left( \frac{1}{T} \frac{dT}{dt} - \frac{1}{P} \frac{dP}{dt} \right) \right] \quad (68)$$

In the first phase the flame kernel expansion at high temperature is dominated by heat conduction from burned to fresh mixture. The temperature variation of the kernel is evaluated by solving the heat conduction equation for the space-dependent plasma temperature  $T_{pl}$  according to [105]. Once the flame kernel has reduced his temperature, the kernel temperature is estimated by applying an energy balance equation for the open system represented by the flame kernel under the following assumptions:

- The system is in thermodynamic equilibrium;
- The general gas law holds;
- The pressure is uniform in burnt and fresh gases.

The kernel can be convected because of the mixture flow close to electrodes and a specific submodel is used to account for wrinkling because of turbulence, which is experimentally found to affect the kernel burning rate since its early development, as shown by Herweg and Maly in their experiments [105]. The wrinkling factor  $\Xi$  is computed as [100]:

$$\frac{d\Xi}{dt} = P_1 \Xi - D \quad (69)$$

where the destruction term  $D$  is:

$$D = \left[ \frac{s_{lam}}{2} (\Xi - 1)^3 \nu_t^{-0.5} P_1^{1.5} \right]^{0.5} \quad (70)$$

and  $P_1$  is the flame surface production term and  $\nu_t$  the turbulent viscosity.

The coupling with the main combustion models occurs at flame kernel radius of 1.2 mm: at that moment, the main combustion model starts to operate after the flame surface density has been initialized according

to the final effective kernel area, whose value depends on the turbulence wrinkling. In order to guarantee grid independent solution of the ignition phase, a grid size of 0.5 mm has been ensured in a control volume of 5 mm around the spark plug.

#### 4.6.2 Combustion Model

The main combustion model used for premixed reacting flow combustion is the ECFM-3Z model in the standard implementation, available in the CFD code Fire. Only a brief summary of this model is here presented and further details on the ECFM-3Z model can be found in the Fire User Manual and [90].

The ECFM3Z is a combustion model based on a flame surface density transport equation and a mixing model that can describe inhomogeneous turbulent premixed and diffusion combustion. It allows to consider the wrinkling of the flame front surface by turbulent eddies.

According to the ECFM3Z zone splitting (Figure 37), each computational cell is divided into three mixing zones: the unmixed fuel zone (letter F in the figure), the mixed zone containing fuel, air and EGR (letter M), and the unmixed air + EGR zone (letter A)

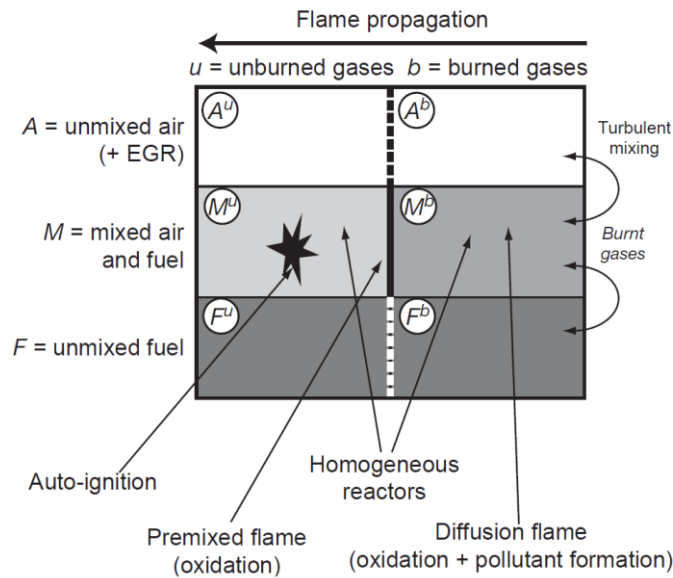


Figure 37. ECFM3Z scheme

The amount of unburned/burned gases in the mixed zone M is given by the progress variable  $\tilde{c}$  which is equal to zero when the burned gas mass is zero, and equal to one when the total mass contained in the mixed zone has been burned. Burned gases of region  $M_b$  have a temperature  $T_b$  while the gases of the five other regions have the same temperature  $T_u$

In the ECFM3Z model, a transport equation is solved for the Favre average mass densities of chemical species fuel,  $O_2$ ,  $N_2$ ,  $NO$ ,  $CO_2$ ,  $CO$ ,  $H_2$ ,  $H_2O$ ,  $O$ ,  $H$ ,  $N$ ,  $OH$  and soot inside the computational cell containing the three mixing zones. Therefore, when “burned gases” are mentioned they include the real burned gases in the mixed zone (zone  $M_b$ ) plus a part of the unmixed fuel (zone  $F_b$ ) and air (zone  $A_b$ ). These equations are classically modelled as:

$$\frac{\partial \bar{\rho} \hat{Y}_x}{\partial t} + \frac{\partial \bar{\rho} \hat{u}_i \hat{Y}_x}{\partial x_i} = \frac{\partial}{\partial x_i} \left( \left( \frac{\mu}{Sc} + \frac{\mu_t}{Sc_t} \right) \frac{\partial \hat{Y}_x}{\partial x_i} \right) + \dot{\omega}_x \quad (71)$$

where  $\mu$  and  $\mu_t$  are the laminar and turbulent viscosities respectively, and  $Sc$  and  $Sc_t$  are the laminar and turbulent Schmidt numbers.  $\bar{\omega}_x$  is the average combustion source term, and  $\hat{Y}_x$  is the average mass fraction of species  $x$ :

$$\hat{Y}_x = \frac{\bar{m}_x/V}{\bar{m}/V} = \frac{\bar{\rho}_x}{\bar{\rho}} \quad (72)$$

$V$  is the cell volume,  $\bar{\rho}$  is the mean density and  $\bar{m}$  is the cell mass. The fuel is divided in two parts: the fuel present in the fresh gases  $\hat{Y}_{fu}^u$  and the fuel present in the burned gases  $\hat{Y}_{fu}^b$ . This division is necessary to represent the fact that a part  $\hat{Y}_{fu}^u$  of the fuel will be consumed by auto-ignition or premixed flame, while the remaining fuel  $\hat{Y}_{fu}^b$  will be consumed by a diffusion flame:

$$\hat{Y}_{fu}^u = \frac{\bar{\rho}_{fu}^u}{\bar{\rho}} \quad (73)$$

$$\hat{Y}_{fu}^b = \frac{\bar{\rho}_{fu}^b}{\bar{\rho}} \quad (74)$$

A transport equation is used to compute  $\hat{Y}_{fu}^u$

$$\frac{\partial \bar{\rho} \hat{Y}_{fu}^u}{\partial t} + \frac{\partial \bar{\rho} \hat{u}_i \hat{Y}_{fu}^u}{\partial x_i} = \frac{\partial}{\partial x_i} \left( \left( \frac{\mu}{Sc} + \frac{\mu_t}{Sc_t} \right) \frac{\partial \hat{Y}_{fu}^u}{\partial x_i} \right) + \bar{\rho} \tilde{S}_{fu}^u + \bar{\omega}_{fu}^u \quad (75)$$

where  $\tilde{S}_{fu}^u$  is the source term quantifying the fuel evaporation in fresh gases.  $\bar{\omega}_{fu}^u$  is a source term taking auto-ignition, premixed flame and mixing between mixed unburned and mixed burnt areas into account, given by:

$$\bar{\omega}_{fu}^u = \bar{\rho}_{fu}^u S_{lam} \hat{Y}_{fu}^u \Sigma \quad (76)$$

where  $\Sigma$  is the flame surface density whose transport equation is:

$$\frac{\partial \Sigma}{\partial t} + \frac{\partial}{\partial x_j} (\bar{u}_j \Sigma) - \frac{\partial}{\partial x_j} \left( \frac{\nu_t}{Sc_t} \frac{\partial \Sigma}{\partial x_j} \right) = S_\Sigma = S_g - S_a + S_{LAM} \quad (77)$$

and  $S_\Sigma$  represent the source surface density term composed by the production of the flame surface by turbulent rate of strain  $S_g$ , the annihilation of flame surface due to reactants consumption  $S_a$  and the contribution of laminar combustion to the generation of flame surface density  $S_{LAM}$ . The main contributor  $S_g$ , which depends on a mean stretch rate parameter, is evaluated with the ITNFS function, used to account for turbulence interaction with the flame and flame quenching according to the local ratio of the integral length scale to the laminar flame thickness and to the local ratio of the turbulence fluctuations to the laminar flame speed. In the  $\Sigma$  transport equation and in the ITNFS function (and in the relation for the determination of the laminar flame thickness) the determination of the laminar flame speed is required.

Since it affects the burning rate and it determines the efficiency how turbulence vortex may stretch the flame front, it is mandatory to provide the most accurate determination for the laminar flame speed, especially when different amount of water dilution must be considered. To this purpose, as already mentioned, a detailed chemistry solver has been used for the determination of the laminar flame speed at different condition of unburnt gas equivalence ratio, pressure, temperature, EGR and injected water mass fraction. It

is to note that the contribution to the laminar flame speed of the water injected mass fraction has been separated from that of the water in the exhaust gases by introducing a specific passive scalar. The methodology is presented in the next chapter.

Further detail on ECFM3Z combustion model and all equations here reported can be found in [90].

## 4.7 Thermal Wall Function Modelling

One of the main physical processes affecting engine operation and exhaust emissions is the heat flux through the cylinder boundaries. For a proper estimation of the heat flux the simulations have relied on Han and Reitz model. Han and Reitz [106,107] suggested and tested a wall function that included the compressibility effect inside the boundary layer and a variable turbulent Prandtl number, as a function of the dimensionless wall distance, written as:

$$T^+ = - \int_{T_w}^{T_c} \frac{\rho c_p u_\tau}{q_w} dT = \frac{\rho_c c_p u_\tau T_c}{q_w} \ln\left(\frac{T_w}{T}\right) \quad (78)$$

and,

$$T^+ = 2.1 \cdot \ln(y^+) + 2.5 \quad (79)$$

where  $T^+$  is the non-dimensional temperature,  $y^+$  the non-dimensional distance,  $T_w$  the wall temperature,  $T_c$  the temperature in the first cell centroid,  $\rho_c$  the density in the first cell centroid,  $c_p$  the specific heat,  $q_w$  the heat flux and  $u_\tau$  the friction velocity is function of the turbulence kinetic energy  $k$ , given by:

$$u_\tau = C_\mu^{0.25} \cdot k^{0.5}, C_\mu = 0.085 \quad (80)$$

However, the correlations used to derive the turbulent Prandtl number profiles and so the  $T^+$  were extracted from incompressible flow experimental data, hence the final formulation was only partially non-isothermal. In order to deal with a more robust and accurate methodology for the assessment of the engine in-cylinder wall heat transfer, over the very large range of loads typical of both SI and CI engines currently under production, it would be important to rely on a more comprehensive fully non-isothermal wall function with a lower mesh sensitivity. The new thermal wall function presented in [108] lays the foundations for developing and testing a new fully compressible non-isothermal wall function. The main goal is to keep a general approach limiting the underlying hypothesis without relying only on the empirical correlations to track the temperature variation properties inside the boundary layer, usually adopted due to the lack of data for the compressible cases.

The importance of this approach is because the flow temperature variation during the engine cycle in the near wall layer is large and so the density variation next to the walls. Moreover, it depends on the operating point (*bmp*, in particular) considered which affects the near-wall flow conditions.

The wall function proposed in [108] is derived with the goal to predict the in-cylinder wall heat flux over a wide range of operating conditions, from idle to rated power. The proposed wall function, and the corresponding equation derivation steps have been compared with the most widely isothermal and non-isothermal wall functions used in the Internal Combustion Engine (ICE) in-cylinder flow simulations. Then it was applied to the case referred to GM Pancake Engine, representative of low *bmp* engine. The new proposed wall function was validated both on pressure trace and heat flux profiles showing better accuracy than the other wall functions, as showed in Figure 38 reporting only one thermocouple result as example. In addition, a mesh sensitivity analysis has been performed pointing out how the new model allows the heat flux to be almost independent from the grid size.

The mesh size is an important variable during an In-Cylinder simulation as proved by several authors that found different heat flux curves changing the grid dimension near the walls. For these reasons, it could be useful to remove this uncertainty variable thanks to an independent mesh model.

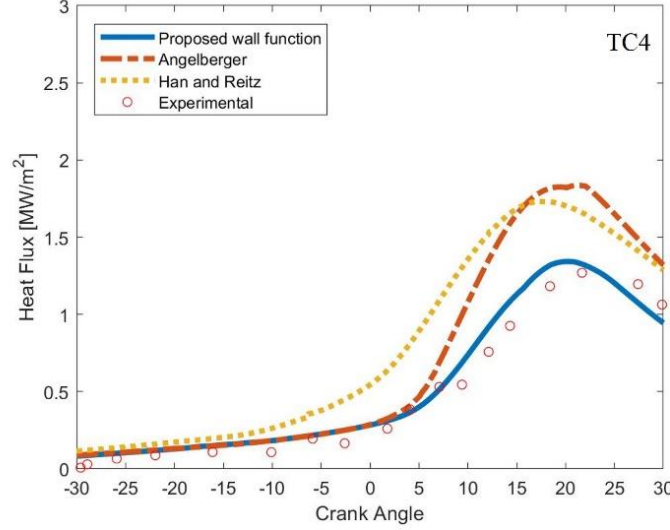


Figure 38. Thermal wall function comparison in a low-bmep engine case

The next application on a current high-power density production engine, characterized by thermocouple measures in the engine block and representative of large *bmep* conditions, might be the topic of the forthcoming research. For this reason, since the new proposed wall function is not yet validated for high loads, it was decided to use the Han and Reitz formulation, whose reliability, supported by a correct mesh representation, has been validated several times.

## 4.8 Turbulence Modelling

The  $k$ - $\zeta$ - $f$  RANS model, employed in the 3D CFD simulations of this work, relies on the elliptic relaxation concept providing a continuous modification of the homogeneous pressure-strain process as the wall is approached to satisfy the wall conditions, thus avoiding the need for any wall topology parameter. The variable  $\zeta$  represents the ratio  $\bar{v}^2/k$ , where  $\bar{v}^2$  is a scalar property in the Durbin's  $v_2 - f$  model [109], which reduces to the wall-normal stress in the near-wall region, and  $k$  is the turbulent kinetic energy. The set of equations are:

$$\frac{\partial k}{\partial t} + U_j \frac{\partial k}{\partial x_j} = (P - \varepsilon) + \frac{\partial}{\partial x_j} \left[ \left( \nu + \frac{\nu_t}{\sigma_t} \right) + \frac{\partial k}{\partial x_j} \right] \quad (81)$$

$$\frac{\partial \varepsilon}{\partial t} + U_j \frac{\partial \varepsilon}{\partial x_j} = \frac{(C_{\varepsilon 1} P - C_{\varepsilon 2} \varepsilon)}{T} + \frac{\partial}{\partial x_j} \left[ \left( \nu + \frac{\nu_t}{\sigma_\varepsilon} \right) + \frac{\partial \varepsilon}{\partial x_j} \right] \quad (82)$$

$$\frac{\partial \zeta}{\partial t} + U_j \frac{\partial \zeta}{\partial x_j} = f - \frac{\zeta}{k} P + \frac{\partial}{\partial x_j} \left[ \left( \nu + \frac{\nu_t}{\sigma_\zeta} \right) + \frac{\partial \zeta}{\partial x_j} \right] \quad (83)$$

$$L^2 \nabla^2 f - f = \frac{1}{T} \left( C_1 + C_2 \frac{P}{\varepsilon} \right) \left( \zeta - \frac{2}{3} \right) \quad (84)$$

with the wall boundary condition for  $f$ :  $f_{wall} = \lim_{y \rightarrow 0} (-2\nu\zeta/y^2)$ . Here  $T$  represents a switch between the turbulent time scale  $\tau = k/\varepsilon$  and the Kolmogorov time scale  $\tau_k = (\nu/\varepsilon)^{0.5}$ :

$$T = \max \left[ \frac{k}{\varepsilon}, C_\tau \left( \frac{\nu}{\varepsilon} \right)^{0.5} \right] \quad (85)$$

The corresponding length scale  $L$  is obtained as a switch between the turbulent and Kolmogorov length scales:

$$L = C_L \max \left[ \frac{k^{3/2}}{\varepsilon}, C_\eta \left( \frac{\nu^3}{\varepsilon} \right)^{0.25} \right] \quad (86)$$

Values of the coefficients appearing in the model equations can be found in [90].

## 4.9 Numerical Methods

The transient flow algebraic equations have been solved by using the PISO algorithm, along with the MARS scheme as second-order discretization scheme for mass, momentum and energy equations, achieving better accuracy, because it possesses the least sensitivity of solution accuracy to the mesh structure and skewness, while turbulence is resolved with a second order blended scheme. More detail can be found in [90].

# Chapter 5: Water Effects on Combustion Process: Chemical Kinetics Calculations

Among the main objectives of this thesis there is the evaluation of the effects of water on the combustion development and the engine knock attitude. In the present paragraph, the aim is to present the methodology used to consider the effect of the mixture index  $\lambda$ , thermodynamic conditions, EGR and water vapor on combustion properties, namely Laminar Flame Speed (LFS), Laminar Flame Thickness (LFT) and Ignition Delayed Time (IDT), at different local pressure and temperature conditions, representative of the unburnt mixture conditions during the compression and combustion processes in GDI engines. The aim is to extract specific database through chemical kinetics calculations for each combustion property, as a support of 3D numerical simulation, replacing the less accurate correlations available.

## 5.1 Choice of the Fuel Surrogate

The real gasoline fuels are complex blends composed by thousands of hydrocarbons but the number of the most relevant hydrocarbon groups present in real fuels can be reduced to six: n-alkanes, iso-alkanes, olefins, aromatics, cycloalkanes and oxygenated components. Even considering only the hydrocarbons of these groups, the computational effort would result in unaffordable simulation time and this is the reason why only some components are taken into account, generating surrogates that can mimic the real fuel behaviour. More precisely, the behaviour of a fuel can be divided into physical properties (distillation curve, vapor pressure curve, density, droplets break-up etc.) and chemical properties (auto-ignition delayed time, laminar flame speed, etc.). Depending on the characteristic to be represented, different hydrocarbon blends are selected. The most common surrogates are defined as Primary Reference Fuel (PRF), a mixture of iso-octane and n-heptane (for example PRF87) or an extended version containing also aromatics, the so-called Toluene Reference Fuel (TRF), by adding toluene to PRF, whose purposes are to replace the chemical properties of real fuel in term of combustion accuracy, for the representation of auto-ignition delayed time and laminar flame speed. Pitz et al. [110] recommend the addition of at least toluene to the mixture, as the toluene is the most abundant aromatic in the gasoline and it is characterized by a weak NTC behaviour. Moreover, modern real gasolines exhibit a fuel sensitivity that a conventional PRFs are incapable to correctly reproduce.

Table 5. Composition of the analysed surrogate

Surrogate	Composition	RON
TAE7000	<i>i</i> -C <sub>8</sub> H <sub>18</sub> (42.9%) <i>n</i> -C <sub>7</sub> H <sub>16</sub> (13.7%) C <sub>7</sub> H <sub>8</sub> (43.4%)	98

Furthermore, the continuous interest in bio-fuels has led to the investigation of PRF and TRF with the addition of ethanol (oxygenated component), which have an important antiknock property thanks to its high RON and MON values (116 and 101) and a negligible influence of laminar flame speed for values up to 15% (vol) [111]. Since the aim of the activity is to generate a database of LFS, LFT and IDT for the simulation of gasoline combustion, the analysis is mainly conducted on the fuel surrogate named *TAE7000*, whose composition is reported in Table 5, which was experimentally designed to provide similar values of reaction speed and auto-ignition time to a TOTAL commercial gasoline [112].

## 5.2 Chemical Water Effect on Laminar Flame Speed and Thickness

As already described in the previous chapter, common combustion methodologies, used for RANS simulations of internal combustion engines, require the knowledge of the laminar flame speed and its thickness. These are essential properties to calculate the reaction rate in most combustion models such as ECFM-3Z and G-Equation, which are based on flamelet approach.

State-of-the-art combustion models, however, mostly rely on experimental correlations for the LFS and LFT [113], which present several shortcomings with respect to the sensitivity to the chemical properties of the mixture, and do not keep into account the presence of water vapor as a diluent. Moreover, experimental measurements of the laminar flame speed are complex, and due to technological and physical issue (see Rallis et al. [114] for an in-depth survey) the measures are limited in pressure and temperature ranges of investigations, away from the engine's typical ones. This is the reason why several authors [115,116] have proposed to refer to databases of LFS and LFT generated by means of detailed chemical simulations, rather than to classical correlations. The generated datasets can be used in three-dimensional CFD simulations by direct interpolation [115] or by the use of new correlations fitting the new data [116]. In order to generate a database with all the possible combinations of chemical and physical properties, that can be reached during the simulation of ICE, including the presence of a given mass fraction of water vapor and exhaust gases, a very high number of detailed chemical kinetics simulations need to be performed.

### 5.2.1 Baseline Correlation Laws for Laminar Flame Speed and Thickness

Water is expected to have an effect comparable to that of EGR thus lowering the laminar speed and increasing the LFT. The LFS of a reacting mixture is defined in literature [117] as a function of the physical properties  $P$  (pressure) and  $T_u$  (temperature of the unburnt gas) and chemical characteristics  $\phi$  (equivalence ratio) and  $X_{EGR}$  (mass fraction of the diluent) of the fresh mixture with the following expression:

$$S_L = S_L^0 \left( \frac{T}{T_0} \right)^\alpha \left( \frac{P}{P_0} \right)^\beta \cdot (1 - k \cdot X_{EGR}) \quad (87)$$

$$S_L^0 = B_m - B_f(\phi - \phi_m)^2 \quad (88)$$

$$\alpha = \alpha_0 - \alpha_1(\phi - 1) \quad (89)$$

$$\beta = \beta_0 - \beta_1(\phi - 1) \quad (90)$$

where  $T_0$  is the reference unburnt gas temperature and  $P_0$  the reference pressure values at which  $s_{L0}$  was calculated (the values of  $T_0$  and  $P_0$  are usually taken at ambient conditions). The factor  $k \cdot X_{EGR}$  is a correction term introduced to account for the presence of EGR as inert ( $k$  has values found in literature between 1.7 and 2.3 [117]). The value  $\phi_m$  corresponds to the equivalence ratio at which the maximum LFS was found, while the other coefficients must be modified as a function of the chosen fuel and correlation (usually Metghalchi and Keck [117], Heywood [118], or Gulder [119]).

As far as LFT is concerned, among the several LFT literature meanings, many authors agree that the most one useful in combustion modelling is the thermal thickness [113], which is derived from the temperature profile inside the reaction zone defined as:

$$\delta_L^0 = \frac{T_2 - T_1}{\max\left(\left|\frac{dT}{dx}\right|\right)} \quad (91)$$

where  $T_2$  represents the temperature of the burnt gases and  $T_1$  is the temperature of the fresh mixture. A correlation based on scaling laws [120] was introduced to overcome the lack of experimental data regarding the LFT, as proposed in Eq.(9192), calculated with the properties of the fresh mixture, where  $\lambda$  is the thermal conductivity of the gas,  $\rho$  is its density,  $C_p$  the specific heat at constant pressure, and  $s_L$  is the LFS in that condition.

$$\delta_L^0 = \frac{\lambda}{\rho c_p s_L} \quad (92)$$

Blint in [120] corrected the previous correlation by introducing a correction factor based on the burnt gas temperature, leading to a new formulation:

$$\delta_L^{blint} = 0.626 \cdot \left(\frac{\lambda}{\rho c_p s_L}\right)_1 \cdot \frac{(\lambda/c_p)_2}{(\lambda/c_p)_1} \quad (93)$$

where subscript 1 indicates that the property refers to the fresh mixture, and subscript 2 is the condition of the burnt zone. Therefore, water induces a change in the laminar flame thickness due to both a change in the laminar speed and the mixture properties before and after the flame front.

## 5.2.2 Characteristics of the Chemical Simulations

The simulations, based on detailed chemistry approach, for the LFS and thickness were performed in a one-dimensional environment with successive mesh refinements. In this type of simulation, the flame is considered adiabatic, planar and stationary, invested by a fresh mixture current, whose speed corresponds to that of the displacement of the reaction zone. Since the simulation is performed for an unstrained steady flame, the displacement speed can be considered the reaction speed, and therefore, its value represents the LFS required for the combustion models [113].

The unburned mixture is formed by chemical species calculated on the basis of the equivalence ratio between fuel and air (formed only by  $O_2$  and  $N_2$ ) and the presence of EGR and water vapor. The composition of EGR is calculated based on a complete stoichiometric combustion, therefore from a combination of  $O_2$ ,  $N_2$ , and  $H_2O$  whose mass fractions only depend on the fuel formulation. The adopted methodology for the database generation and the chemical simulations is based on the work by Cazzoli et al. [115], which relies on the Cantera implementation in Python and requires to choose other two key aspects of the simulations:

- the chemical kinetics mechanism;
- the breakpoints for all the accounted variables.

### 5.2.3 Chemical Kinetics Mechanism and Validation

The air-fuel mixture within internal combustion engine experiences a wide range of pressure, temperature, and diluent distribution conditions, therefore it is of utmost importance that the chemical processes are well validated over these ranges. The selection of the chemical kinetics scheme must keep into account three parameters:

1. the presence of reactions for all the species of the chosen surrogate;
2. the number of species and reactions considered, under the point of view of the completeness of the mechanism;
3. the computing time required to run a simulation.

The quality of the numerical prediction depends on the employed kinetic reaction scheme. In literature several detailed, semi-detailed and skeletal chemical kinetics mechanisms are proposed, tailored for the resolution of LFS or IDT, or both, using a specific fuel or a mixture, and under different thermodynamic conditions.

Concerning the LFS evaluation, the reaction mechanisms considered are reported in Table 6: PoliMI red. [121], PoliMI [122] and LLN [123]. These mechanisms have been chosen because they were developed for simulating the reacting features of gasoline under both high and low temperature conditions.

Table 6. Chemical kinetics mechanisms

	Time/Sim	Species	Reactions
<b>POLIMI red. [121]</b>	REF	156	3465
<b>POLIMI [122]</b>	~6 x REF	451	8153
<b>LLNL [123]</b>	>20 x REF	1387	10481

However, in order to define the kinetic mechanism to be used for the whole LFS and thickness map, the calculation time was estimated as listed in Table 6. The computational cost was obtained with a benchmark performed on ten successive simulations on a computer with Intel Xeon Platinum with 3.0 GHz, 36 cores, 144 GB ram, Cantera version 2.3.0, and Python version 3.7.2. The time required for the computation is proportional to the number of species and reactions present in the chemical kinetics mechanism, but also to the physical and chemical properties of the simulated point, since the simulation might require more iterations to converge.

The reduced POLIMI mechanism, although it showed some interest for the undoubted lower calculation time, it was found to lose accuracy in the comparison between experimental and numerical laminar speed data in [123], for different fuel surrogates, as shown in Figure 39 for PRF87, where an increasing discrepancy was found as the equivalence ratio increases. As a result of these preliminary considerations, the PoliMI reduced scheme was excluded from further analysis. In addition, in order to reduce the time required to populate the dataset, an automatic reduction methodology defined as DRGEP (Directed Relation Graph with Error Propagation) with Sensitivity Analysis was implemented.

The validations of the PoliMI and LLNL chemical kinetics schemes, using surrogate *TAE7000*, have been performed by comparing the values of laminar flame speed with experimental data available from [124], for the adopted surrogate at 358 K and 1 bar. Figure 40 illustrates that the simulation results are in good agreement with experimental data both using PoliMi and LLNL along the entire equivalence ratio range. Considering the quality of the results and the computational cost, the PoliMi mechanism has been chosen in the end to extend the analysis to other conditions.

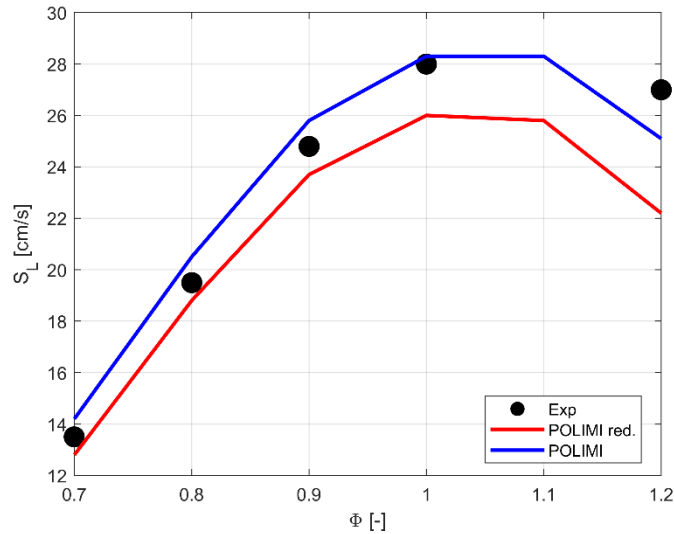


Figure 39. Comparison between PoliMI and PoliMI-reduced mechanisms with experimental data [123] for the prediction of LFS of PF87 at  $P=20$  bar,  $T=353$  K [123]

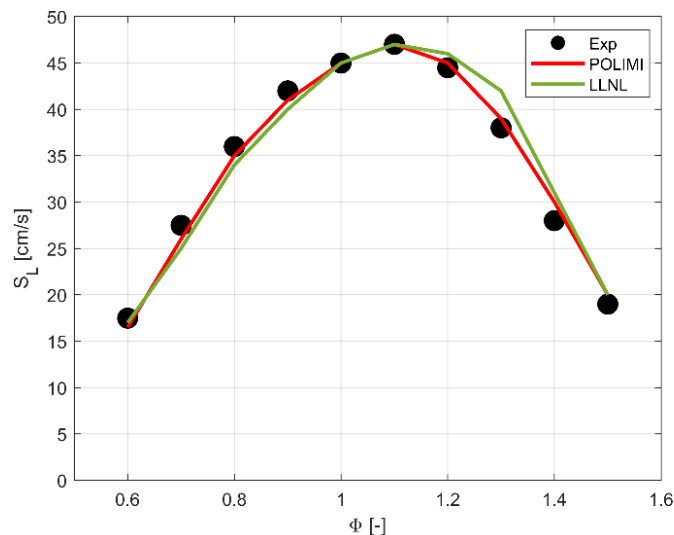


Figure 40. Comparison between PoliMI and LLN against experimental [124] LFS data for TAE7000 surrogate at  $T=358$  K,  $P=1$  bar

### 5.2.4 Thermodynamic and Mixture Conditions Tested

The database to be generated must include all the thermodynamic and mixing conditions faced by fresh mixture inside a high-bmep modern engine. The variables to be considered that influence the laminar speed of flame, are the temperature of the unburnt ( $T_{un}$ ), the pressure ( $P$ ), the equivalence ratio ( $\Phi$ ) and the mass of diluents ( $X_{EGR}$  and  $X_{water}$ ). In particular, the margins of the five variables examined have been taken wide enough to use the results for both low and high engine load simulations (Table 7). The number of breakpoints for each variable was chosen to adequately capture the main trends, with a focus on those regarding the mass fraction of each mixture component.

The water mass fraction of the mixture (i.e, this parameter is different from  $s$ , the non-dimensional water mass) is limited to 6% because it was reported in [115] that, during engine operations, it is not feasible to use a higher amount of water than of fuel at stoichiometric conditions, mainly because of the evaporation times of the liquid droplets.

Table 7. Breakpoints used for generating the dataset of LFS

	MIN	MAX	# Points
<b>P (bar)</b>	5	160	7
<b>T<sub>un</sub> (K)</b>	450	1100	14
<b>Φ (-)</b>	0.3	2.5	16
<b>X<sub>egr</sub> (%)</b>	0	30	5
<b>X<sub>water</sub> (%)</b>	0	6	4

Now that the surrogate, the chemical mechanism and the simulation conditions have been defined, some of the main results will be investigated in representative thermodynamic and mixing conditions inside the cylinder during the combustion and expansion phase, in order to illustrate the main water effect trends on LFS and LFT

### 5.2.5 LFS and LFT Chemical Simulation Results

As expected the LFS for an undiluted mixture shows a maximum around the stoichiometric equivalence ratio, the relative reduction for not too rich mixture is almost independent from the unburned pressure and temperature as showed in Figure 41, where on the y-axis is reported the  $S_L$  normalized against its maximum value and on x-axis the equivalence ratio.

In general, for a given equivalence ratio, unburned pressure and temperature, the addition of a diluent causes an overall reduction of the LFS. Figure 42 shows, for a representative engine-like conditions, that the LFS tends to slow down as the mass fraction of water present in the mixture increases, with a consequent slowing down of the whole combustion process. To better understand how the effect of water on the LFS evolves according to the mixture distribution, in Figure 43 the values are normalized with the maximum speed evaluated without water. The reduction of LFS tends to be greater for low  $\phi$  values: the leaner is the mixture, the greater is the slowdown caused by the presence of water.

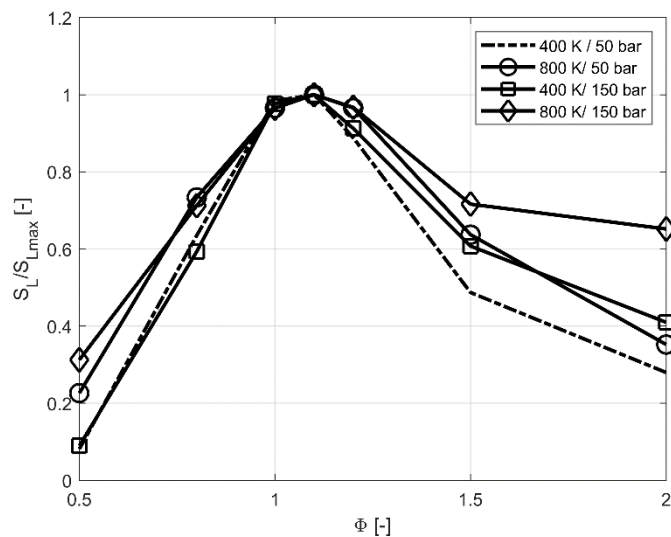


Figure 41. TAE 7000 undiluted mixture: effect of different engine-like thermophysical conditions and equivalence ratio on LFS

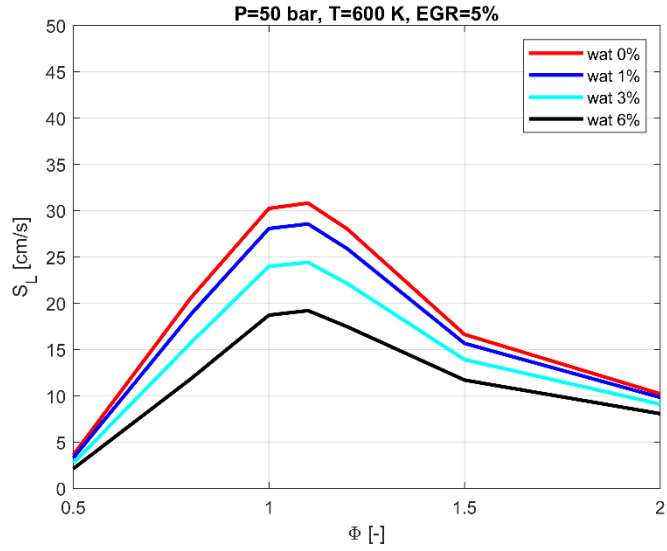


Figure 42. Water effect on LFS:  $P = 50$  bar,  $T = 600$  K, EGR 5%

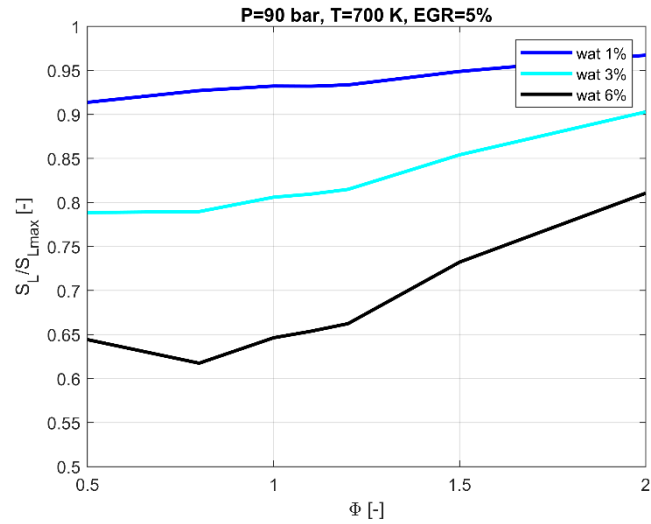


Figure 43. Water effect on LFS:  $P = 90$  bar,  $T = 700$  K, EGR 5%, focus on  $\Phi$  variation

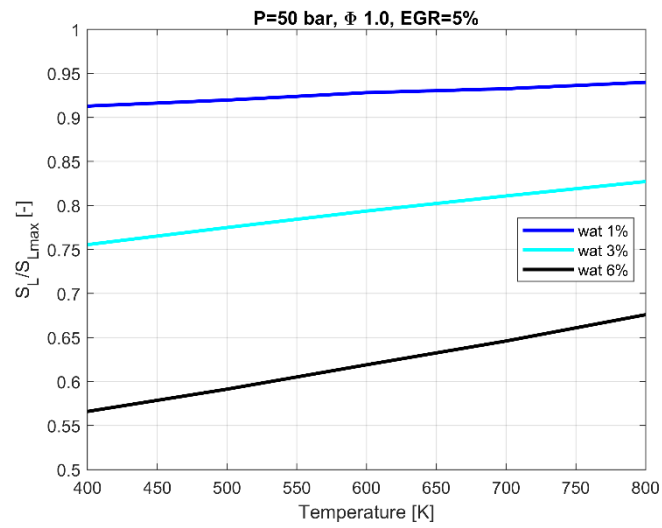


Figure 44. Water effect on LFS:  $P = 50$  bar,  $\Phi = 1$ , EGR 5%, focus on  $T$  variation

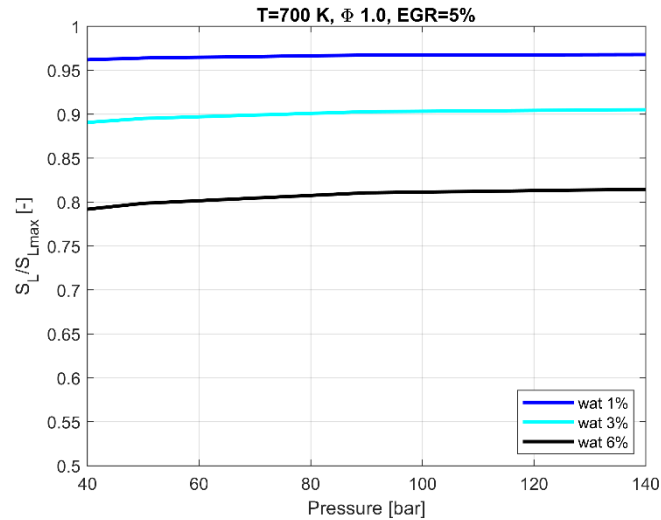


Figure 45. Water effect on LFS:  $T = 700 \text{ K}$ ,  $\Phi = 1$ , EGR 5%, focus on  $P$  variation

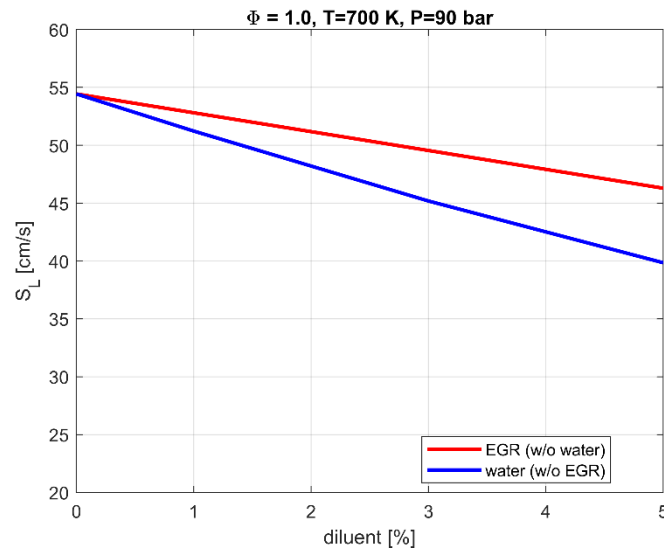


Figure 46. Water and EGR effect comparison on LFS

From Figure 44 it can be seen that the variation of temperatures, keeping the other variables constant, causes a stronger slowdown at low temperatures, with a more significant effect with the maximum percentage of water (6%). The black curve shows indeed a greater slope than the other cases. On the contrary, the pressure variation reported in Figure 45 is almost irrelevant.

As already described in the previous Chapter 3, water tends to have a more important impact on the laminar speed slowdown than EGR. Figure 46 shows the effects of different percentage of pure water diluent (without EGR) and pure EGR diluent (without water) on laminar flame speed. Even at 1% of diluents, water differs from the EGR profile showing a clear greater attitude to slow down the flame with a linear dependence. Despite they are both diluents and inert for the engine combustion process, the effect induced by the water and the EGR are quite different because of different chemical composition. This behaviour was found also in literature [125] and was represented by Cazzoli et al. [115] in a LFS correlation.

These water aspects are decisive for the combustion duration, especially in the first instants after ignition. For this reason, one of the objectives of fluid dynamics simulations will be to examine the amount of water vapor near the spark plug during the ignition, assessing immediately which configuration will tend to have a first slower combustion phase. Furthermore, longer combustion duration could involve higher exhaust gas

temperature during the expansion stroke exceeding the TiT limits. As a result, the combustion system has to be designed to counterbalance this effect.

In addition, the application of a flamelet combustion model, based on the flame surface density transport equation, requires not only the evaluation of the LFS but also of the LFT (Laminar Flame Thickness). This is relevant to consider the efficiency of the turbulent vortices to wrinkle the flame.

In Figure 47 is illustrated how the LFT is affected by the water for a given T, P and EGR parentage, evaluating the LFT with the Eq.(93). As the percentage of water in the mixture increases, the thickness of the flame is increased. From a theoretical point of view, a higher flame thickness leads to a lower interaction with turbulence vortices, because the capacity to corrugate the flame is weaker. As a result, this factor can also involve a reduced combustion speed.

Figure 48 reports the LFT versus equivalence ratio, showing the separate effects of water and EGR. For mixtures close to stoichiometric condition, low percentages of diluents (less than 1%) do not lead to a significant change in LFT between pure water and pure EGR.

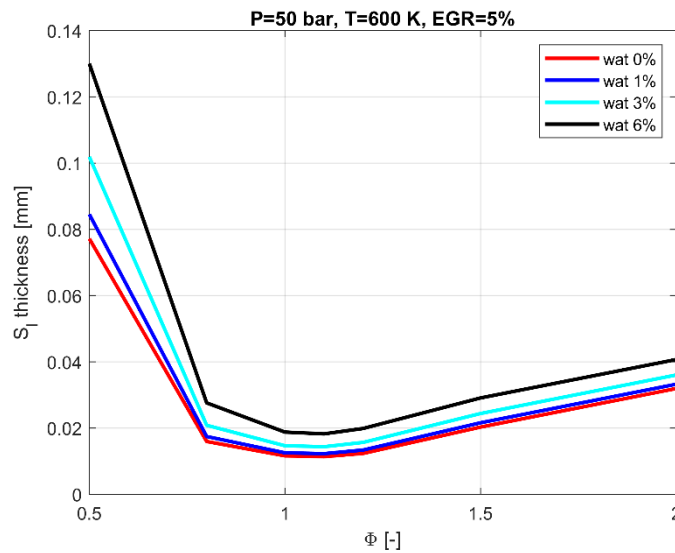


Figure 47. Water effect on LFT calculated with Blint's correlation[120]

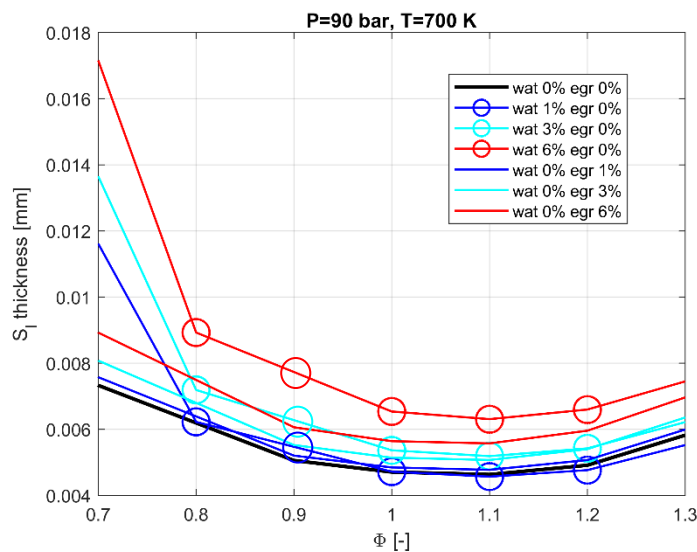


Figure 48. pure Water and pure EGR effects on LFT calculated with Blint's correlation [120]

However, as the diluent percentage increases, the flame tends to become thicker with a greater influence of water. This is due not only to the lower laminar flame speed in the presence of water vapor, but also to the variations in the local properties of the mixture in terms of specific heat and thermal conductivity. In addition, the greater effect of water seems to be more pronounced for leaner mixtures.

## 5.3 Chemical Water Effect on the Ignition Delay Time

As far as the auto-ignition time is concerned, this is determined experimentally from the instant when the mixture is spontaneously ignited without the auxiliary energy of an external ignition source. This can occur after the mixture has reached a threshold temperature called "auto-ignition temperature" which is not an intrinsic property of the mixture as it is mostly affected by the pressure and the vessel shape/pressure. Moreover in [126] the authors experimentally emphasized that the IDT was also associated with wave propagation inside the chamber due to flame instabilities.

As in the case of LFS, also the experimental determination of IDT is a rather difficult and expensive procedure, mostly performed under stoichiometric conditions by varying pressure and temperature.

Sometimes the diluent EGR is added in order to verify the autoignition delay time behaviour [127], but the addition of water vapor, not as part of the standard EGR but as a standalone specie, is usually not considered. For these reasons it is important to evaluate the of auto-ignition times with a similar approach as for LFS, in order to populate new lookup table under the typical conditions of GDI engines with the addition of the effects of dilution with water and EGR. Computational approach based on chemical kinetic calculations in a 0D model of an adiabatic reactor at constant volume was used in order to reproduce the experimental conditions of a shock tube, under imposed initial conditions.

### 5.3.1 Baseline Correlation Laws for Ignition Delayed Time

One of the first empirical correlation can be found in the work of Livengood and Wu [128], where the authors proposed a condition for which the auto-ignition starts by means of an induction time expression, as a function of cylinder pressure  $P$ , unburned temperature  $T_u$  and tuning constants ( $X_1$ ,  $X_2$  and  $X_3$ ) in order to fit the experimental data:

$$\tau = X_1 \cdot p^{-X_2} \cdot \exp\left(\frac{X_3}{T_u}\right) \quad (94)$$

where the ignition delay time,  $\tau$ , represents the time it takes to establish the amount of radicals and heat necessary for autoignition to take place for a fixed pressure and temperature. The main weak point of this formulation was the lack of accuracy in the negative coefficient region (NTC region) where the fuel experiences a decreasing ignition delay time by increasing temperature. This was source of inspiration for developing more reliable models, like that carried out by Del Vescovo et al, in [128]. They developed an Arrhenius-based power law correlation to predict ignition delays of PRF blends between PRF100 (iso-octane) and PRF0 (n-heptane) with particular emphasis in capturing the NTC region profile. The improvement was achieved by rework the Arrhenius starting function and substituting the constant parameter with coefficients that are function of temperature and PRF properties.

Despite the numerous attempts to define a reliable correlation law, as in the case of LFS, this can lead to major errors, especially when used in conditions far from experimental and with different fuel. This is the reason why also in this case it was preferred to rely on the generation of a new database for the TAE7000 surrogate, taking into account both the presence of water/EGR and the thermodynamic and mixing conditions that characterize the new modern high-bmep engines.

### 5.3.2 Chemical Kinetics Mechanism and Validation for the Ignition Delayed Time

The computational time required is considerably smaller than that of laminar flame speeds, so there is no need to research and test a reduced scheme: even in this case the kinetic scheme PoliMI has been used and validated.

Unlike LFS, for this type of surrogate, similar to the behaviour of a real gasoline, there are no experimental data with which to validate the chemical kinetics calculations for the extraction of IDT. For this reason it has been used another type of surrogate containing the same components of TAE7000 (*surr\_A* composition: 16.9% (vol.) n-heptane  $\text{NC}_7\text{H}_{16}$ , 62.9% iso-octane  $\text{IC}_8\text{H}_{18}$ , 20.2%(vol.) toluene  $\text{C}_7\text{H}_8$ ) whose data are available in literature [129].

Figure 49 shows the IDT versus the ratio  $1000/T$ . The simulations data report a good match between numerical and experimental data for temperatures higher than 900 K, while the chemical mechanism tends to underestimate the ignition delay time at lower temperatures, especially for the richer mixture.

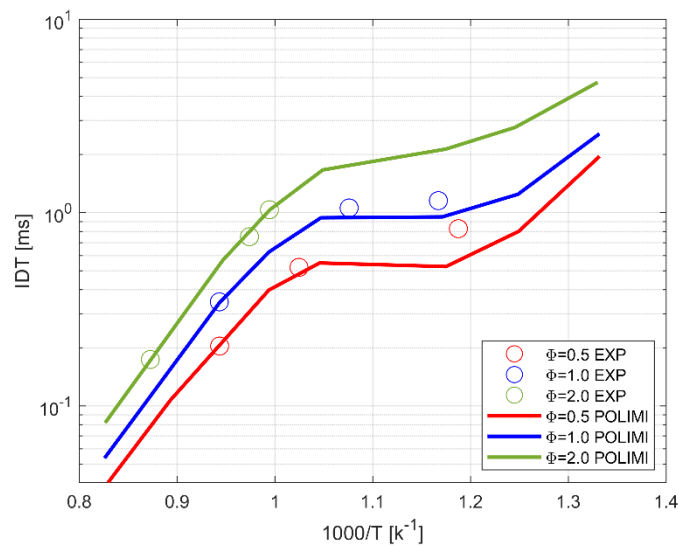


Figure 49. Ignition delay time of *surr\_A* for different equivalence ratios and temperatures at  $P=50$  bar

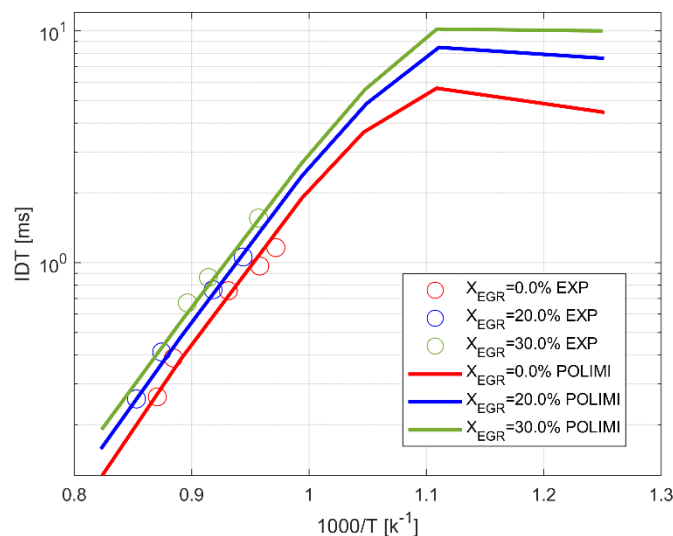


Figure 50. Ignition delay time of *surr\_A* for different EGR mass fractions and temperatures at  $P=20$  bar

The effect of water on IDT has never been measured experimentally by any author. The best way to test the effectiveness and sensitivity of the kinetic mechanism to a diluent is to add EGR, whose experimental data are available in [128]. The results, reported in Figure 50, compare the experimental and calculated values of ignition delay time for the *surr\_A* at  $P=20$  bar,  $\phi=1.0$  and different fractions of EGR (0%, 20%, 30%). The comparison between experimental data and the simulation results show a good agreement both in terms of absolute value and sensitivity to diluent addition.

### 5.3.3 Thermodynamic and Mixture Conditions Tested

Since the auto-ignition event triggers phenomena at higher temperature and pressure than normal combustion, it is necessary to take into account these thermodynamic conditions through an appropriate choice of breakpoints to simulate (Table 8). However, the size of the dataset has remained approximately unchanged since the number of points of the equivalence ratio has been reduced having, unlike the LFS, a much lower sensitivity.

Table 8. Breakpoints used for generating the dataset of IDT

	MIN	MAX	# Points
<b>P (bar)</b>	5	200	10
<b>T<sub>un</sub> (K)</b>	650	1200	20
<b>Φ (-)</b>	0.3	2.5	8
<b>X<sub>egr</sub> (%)</b>	0	30	5
<b>X<sub>water</sub> (%)</b>	0	6	4

### 5.3.4 Results of the Kinetic Chemical Simulations

For undiluted mixture, the IDT decreases with increasing pressure and temperature, as shown in Figure 51. It should also be noted that as the pressure increases, the slope change inside the NTC region becoming weaker, and thus the IDT values increase faster moving towards high temperature conditions. Figure 51 combines also the effects of temperature and equivalence ratio. It can be seen that the richer the mixture, the shorter the IDT, in agreement with the experimental value obtained by Gautier [130] for a generic gasoline fuel. The decreasing effect diminishes when the mixture gets rich and very rich ( $\phi=1.5-2$ ). It must be noted that this effect is relevant at high temperature, when the IDT is small.

Figure 52 shows the effects of adding diluents (EGR or water) on the IDT for stoichiometric mixture. Due to the very wide range of values that the IDT can assume in this temperature range, and the low amount of diluents involved, the differences can only be glimpsed. For this reason, three temperature values are analysed in detail with a multidimensional space: 650 K (low temperature), 950 K (mid temperature) and 1100 K (high temperature). For this comparison, a pressure of 75 bar is chosen since it is close to a possible mean pressure at the heaviest knock events in the engine simulation.

As expected, as the percentage of EGR or water increases the knock attitude tends to decrease significantly as showed in Figure 53-Figure 55, for the three temperature considered and for diluent mixture percentage up to 6% of pure water, pure EGR or both diluents.

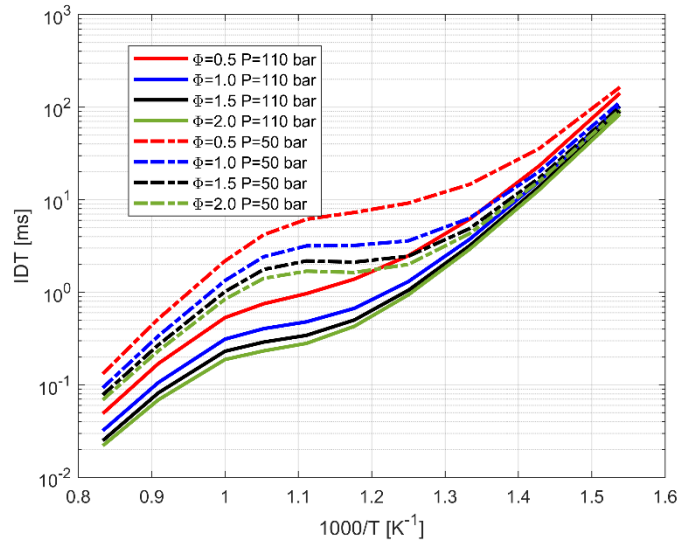


Figure 51. TAE7000 IDT: effect of pressure, temperature and mixture without diluents

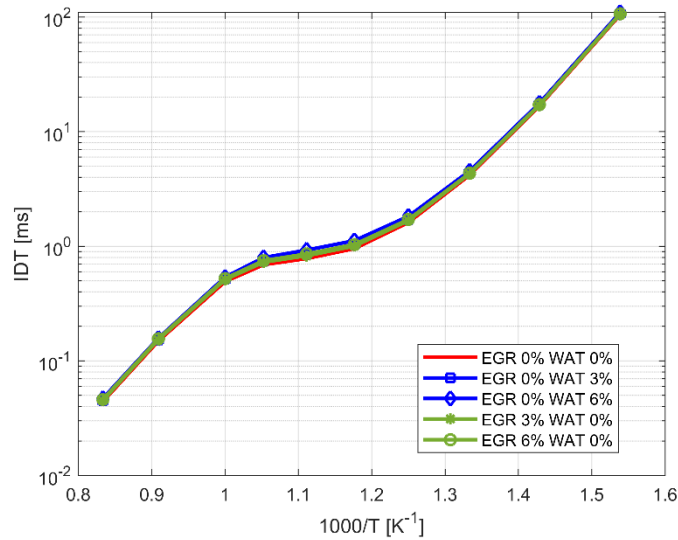


Figure 52. EGR and Water dilution effects on IDT for  $\Phi=1$

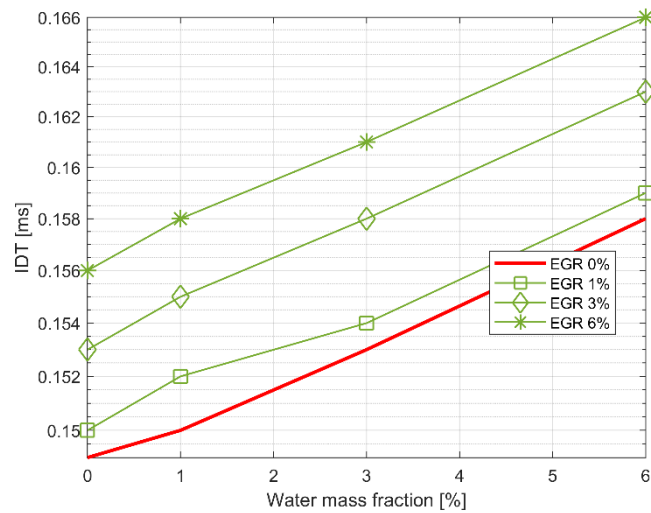


Figure 53. IDT: EGR and water effects at  $\Phi=1.0$ ,  $P=75$  bar,  $T=1100$  K

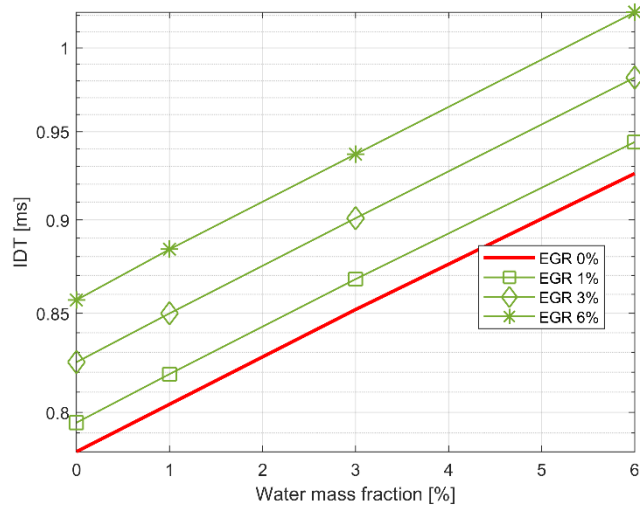


Figure 54. IDT: EGR and water effects at  $\Phi=1.0, P=75 \text{ bar}, T=950 \text{ K}$

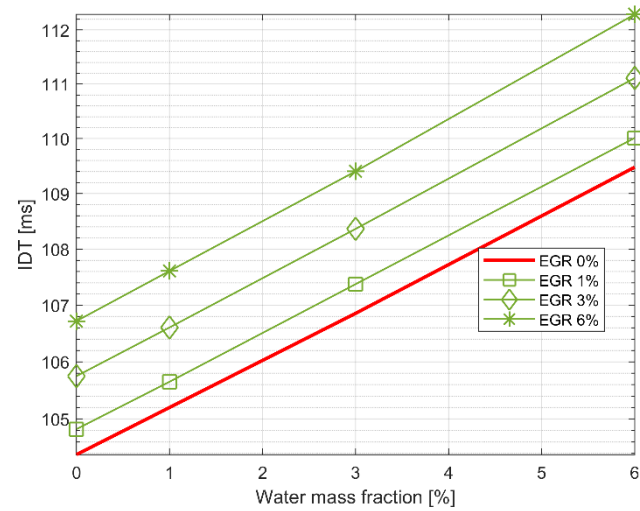


Figure 55. IDT: EGR and water effects at  $\Phi=1.0, P=75 \text{ bar}, T=650 \text{ K}$

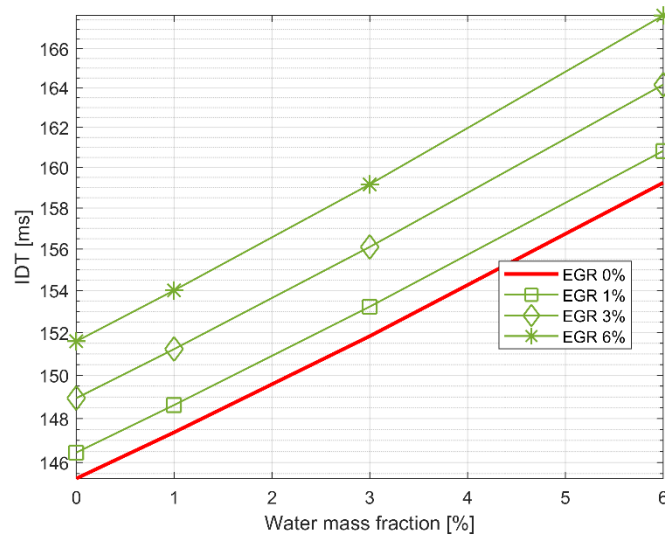


Figure 56. IDT: EGR and water effects at  $\Phi=0.5, P=75 \text{ bar}, T=650 \text{ K}$

At low temperature (650 K), the IDT can vary up to a maximum of 7 milliseconds compared to the undiluted case, while at 1100 K the variation is limited to about 1.5 milliseconds. Thus, from the previous graphs it can be deduced that the resistance due to water addition is higher at lower temperatures. This effect is positive in order to avoid the pre-ignition events that could occur during the compression stroke.

Observing the effect of the diluent, it is almost linear with its mass fraction independently from the thermo-physical conditions and diluent chemical composition. Moreover, for the clarity on the antiknock effect, it should be remembered that at 7000 rpm an increase of 1 milliseconds of auto-ignition time corresponds to 42 CA deg., which is a considerable value.

Furthermore, comparing Figure 55 and Figure 56, which take into account the same thermodynamic conditions, one can see that decreasing the equivalence ratio value from 1.0 (stoichiometric mixture) to 0.5 (lean mixture), the IDT enhancement due to the presence of EGR and/or water is greater. This confirms the great importance of analysing the local distribution of the fresh mixture inside the cylinder and close to the spark plug during the CFD simulations.

In order to highlight the separate diluents effects, Figure 57 and Figure 58 report the IDT variation of the pure diluents for different mass fractions and equivalence ratio at given pressure and temperature conditions. As one can see, the water influence is stronger than that played by the EGR as far as the reduction of the IDT is considered. However, the increase anti-knock attitude of the water is much more relevant at low temperature as highlighted before: at 950 K the maximum IDT increase (at 6% of diluent) with pure water is only 0.04 milliseconds with regards to pure EGR. The same trend has been observed for all the equivalence ratio, pressure and temperature combinations of the observed space.

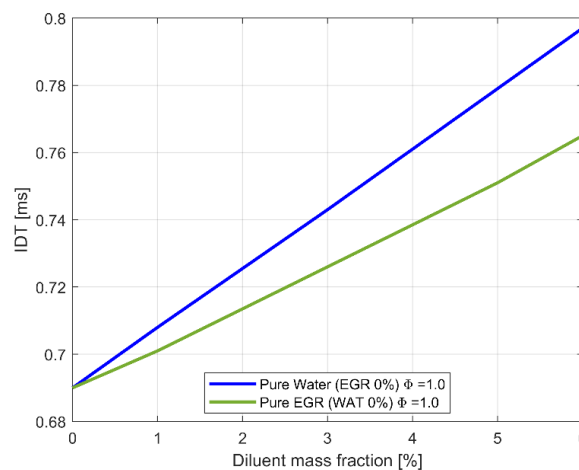


Figure 57. Pure Water and EGR effect on IDT at  $\Phi=1$ ,  $P= 75$  bar and  $T= 950$  K

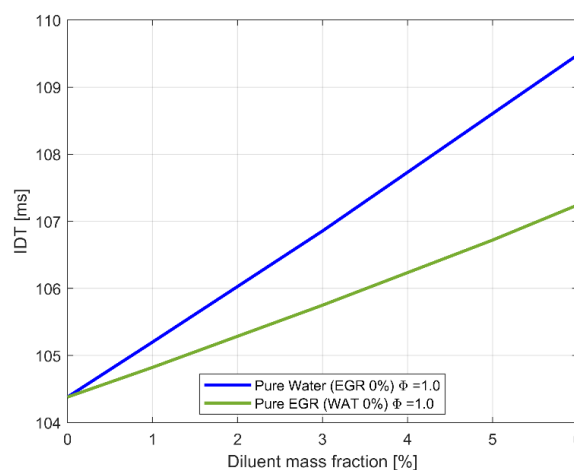


Figure 58. Pure Water and EGR effect on IDT at  $\Phi=1$   $P= 75$  bar and  $T= 650$  K

## 5.4 Summary

This chapter has presented in detail the main results of chemical kinetics simulations for the evaluation of the laminar speed, the flame thickness and the auto-ignition times for different thermodynamic and mixture conditions, typical of modern high bmep-engine. In particular, the effects of water have been highlighted, compared with those of EGR, making an important contribution to the correct simulation of combustion process of internal combustion engines with water injection.

For the analysis a surrogate that could best represent the behaviour of common gasoline was chosen: the TAE7000.

For the study of the laminar speeds, different kinetic mechanisms have been compared from the point of view of both accuracy and calculation time, whose final choice has fallen on the PoliMI. Water proved to have a more pronounced effect compared to EGR, decreasing the laminar speed regardless the equivalence ratio. The analysis has been extended also to the flame thickness, showing how for pure water or pure EGR greater than 1%, the water increases the flame thickness considerably, reducing the wrinkling capacity of the flame. Finally, the effect of water has been evaluated on auto-ignition time for the same surrogate. The validation was always carried out with the PoliMi mechanism but with a similar surrogate (Surr\_A), due to the absence of specific literature data. The water shows a higher anti-knock capacity than the EGR, especially at low temperatures.

Thanks to these data and the use of Machine Learning algorithms, for the minimization of errors, new correlations have been generated for LFS and IDT that take into account the presence of water as demonstrated in the articles [131]. However, in the simulations of this work the chemical kinetics data have been used to create new databases (look-up tables) that can be directly interrogated during the simulations in order to improve the accuracy of the combustion process.

# Chapter 6: Experimental Characterization of a Low-Pressure Water Injector

The objective of the experimental activity was to characterize the water spray of a PWI system, operating at relative injection pressure between 4 and 8 bar. Higher injection pressure investigation was not possible due to the safety limits of the installation.

The lack of data in literature and the need to properly initialize spray models under low pressure condition, at which atomization model are switched off, has made this type of experiment of relevant importance, for a correct representation of the spray through numerical analysis (CFD).

This paragraph briefly describes the fundamental procedures and techniques for the macroscopic and microscopic characterization of a typical injector used for UREA applications and perfectly suitable for Port Water Injection systems. The aim is to define some fundamental properties such as: mass flow rate, spray angle, spray penetration and characteristic diameters useful for numerical validations. This initially involves a hydraulic study of the system and then the use of specific techniques, such as imaging and PDA, to get a deeply knowledge of the spray development.

The experimental activity was conducted at CMT Termicos-Politecnico of Valencia laboratories during the stage abroad. The activity was limited to PW injector experimental characterization only because of the suspension of all activities due the pandemic emergency and related measures. A few months after the total closure of the facility, the working group belonging to the 'injection team' was able to carry out some of the pre-scheduled experiments about this injector for the last part regarding PDA analysis. The results sent to me, were sufficient both to have a very clear picture of its working conditions, through data post-processing, but above all to carry out the next part of numerical validation. Without this kind of information, it would be impossible to correctly calibrate the numerical models obtaining reliable results on engine simulations.

## 6.1 Hydraulic Characterization

As far as the characterization of an injector is concerned, the hydraulic characteristics in terms of momentum flux and rate of injection (mass flow rate) are of worth importance together with the widely and mostly common data on the spray droplet size and penetration. All these information are very important to properly initialize the three-dimensional CFD spray simulations.

The most common methods for calculating the mass flow rate of high-pressure injectors, such as those for diesel and GDI applications, are the Bosch and Zeuch methods [132,133]. For PWI applications, where the operating pressures are much lower, a different method is used: it is similar to what is performed for UWS (Urea Water Spray) systems and now it is briefly described.

The momentum flux method consists in the evaluation of the momentum of a liquid jet impacting on a surface. It is measured indirectly inside a constant volume vessel, usually filled with an inert gas such as nitrogen, where a liquid spray impacts orthogonally against a piezoelectric translator, which records the impact force, as showed in Figure 59. More precisely, a membrane pressure transducer is used instead of a force transducer to prevent the sensitive parts of the gauge from being directly exposed to the vessel

ambient. The transducer must have some characteristics such as fast dynamic response and a very high natural frequency in order to be unaffected by the injector frequency. Moreover, it should be very resistant since it may face high forces due to the liquid fuel spray impact versus the transducer plate, especially at the highest injection pressures.

Thanks to the addition of the piezoelectric transducer, it is possible to record the deformation experienced by the membrane, transforming it into an electrical signal and therefore into a force output. The piezoelectric transducer is preferred over other systems such as piezoresistive ones because of its improved dynamic behaviour and higher sensitivity.

Considering a fluid in a control volume  $V$  and surface  $S$ , as showed in Figure 59, the impact of the spray on the transducer plate is governed by the momentum conservation equation. Under the assumptions that:

- the gravity force is neglectable;
- the pressure  $P$  that acts on the target is uniform;
- the impact area is smaller than the frontal plate area;
- the flow direction of both the nitrogen entering the control volume, and fuel exiting it after impacting the sensor, are perpendicular to the spray axis: axial component of momentum flux, as well as the viscous stress, are null.

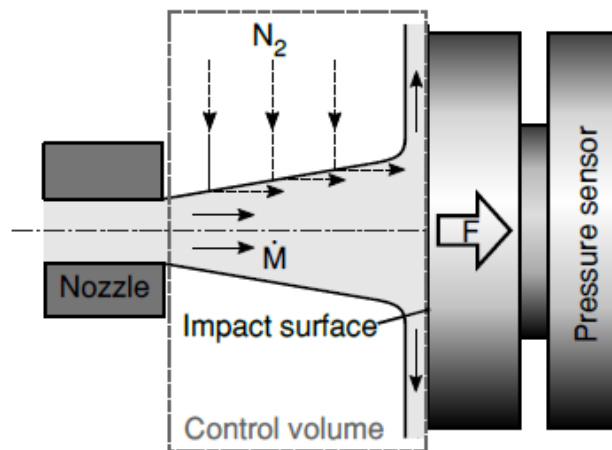


Figure 59. Schematic representation of a momentum flux device [133]

The force  $F$  produced by the spray on the impact surface can be written as:

$$F = \frac{\delta}{\delta t} \int_S \rho u \, dS + \dot{M} \quad (95)$$

where  $\rho$  and  $u$  are the local density and velocity, respectively, of the mixture passing through the control volume,  $S$  is the surface of the control volume, and  $\dot{M}$  represents the momentum flux at the outlet of the orifice, considered to be parallel to the nozzle axis. The first term on the right side of the equation represents the variation of momentum flux within the control volume. Thus, for steady state conditions, Eq.(95) can be simplified as:

$$F = \dot{M} \quad (96)$$

The injector tip is usually placed at a distance between 5 and 15 mm from the target plate. However, this does not affect the measurement as long as the transverse area of the jet remains much smaller than that of

the membrane, so that the jet is perpendicular to it. For this purpose, the target size can be increased taking into account that the addition of a mass leads to a decrease in the natural frequency of the sensor. Now it possible to extract the mass flow rate  $\dot{m}$  combining its definition with the momentum flux:

$$\dot{m} = A_{eff} \cdot \rho \cdot u_{eff} \quad (97)$$

$$\dot{M} = A_{eff} \cdot \rho \cdot u_{eff}^2 \quad (98)$$

For the calculation of the momentum flux and the mass flow rate it is important to consider that the velocity and density profiles and the actual area crossed by the fluid can deviate from the ideal conditions depending on the operating conditions of the injector and the geometry of the nozzle holes, as showed in Figure 60. For example, the presence of strong turbulence, slip condition and cavitation may alter the spray outflow from the nozzle holes, with a profile that is no longer uniform.

It is therefore necessary to introduce coefficients that take into account these deviations from ideal situations, such as:

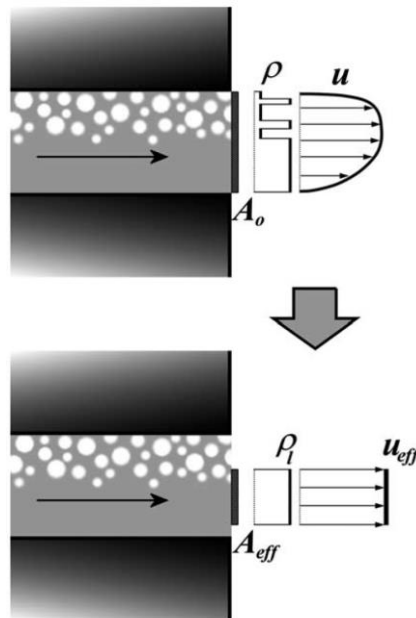


Figure 60. Flow nozzle conditions: ideal vs real distributions

- the velocity coefficient:

$$c_v = \frac{u_{eff}}{u_{th}} \quad (99)$$

- the area coefficient:

$$c_a = \frac{A_{eff}}{A_{th}} \quad (100)$$

- the discharge coefficient:

$$c_d = \frac{\dot{m}}{\dot{m}_{th}} \quad (101)$$

where the subscript *eff* and *th* mean effective and theoretic states respectively. So, it is possible to rewrite Eq.(97) and Eq.(98) as:

$$\dot{m} = A_{th} \cdot \rho \cdot u_{th} \cdot c_v \cdot c_a \quad (102)$$

$$\dot{M} = A_{th} \cdot \rho \cdot u_{th}^2 \cdot c_v^2 \cdot c_a \quad (103)$$

and combining them it is possible to obtain the final formula for the mass flow rate,

$$\dot{m} = \sqrt{C_a \cdot A_{th} \cdot \rho} \sqrt{\dot{M}} \quad (104)$$

Additionally, with the purpose of obtaining the exact total injected mass quantity, a gravimetric scale is used. The quantity of the water mass measured should correspond to the integral of the mass flow rate evaluated from the momentum flux in Eq.(104). Therefore, a correction factor will be used for adjusting the ROI (Rate Of Injection) curve calculated from the momentum flux in order to get the right water injected mass.

A listed in Table 9, the experimental campaign carried out on the examined injector has been very wide, including different injection pressures, chamber back pressures (named *BP* in this chapter) and fluid temperatures, for each of which a momentum flux and a mass flow rate have been extracted. Therefore, it is now reported an example that led to the mass flow rate extraction from a specific operating condition of the injector and a description of the experimental rig used.

The injector used is a dosing module from Bosch, with three nozzle holes each having a diameter of 135 microns. This type of injector is usually used for UWS applications, whose operating conditions in terms of injection pressure, pipe back pressure and mixing requirements are close to those of a typical PWI injector, operating in an pressure range between 4 and 9 bar (gauge). Table 9 shows the matrix of tests performed in the laboratory for the evaluation of momentum flux and ROI (Rate of Injection).

Table 9. Test Conditions

<b>Water Temperature</b>	25-60 [°C]
<b>Injection Pressure</b>	4 – 8 [barg]
<b>Back Pressure</b>	0.5 - 2.5 [bar]
<b>Energizing time</b>	4 [ms]
<b>Number of repetitions per test</b>	50
<b>Number or repetition</b>	2
<b>Injection frequency</b>	1 [Hz]

The measurements were made on a single nozzle hole, positioning its axis perpendicularly to the target which is the piezoelectric transducers and assuming the same behaviour for the other two holes. The hole is placed at 5 mm from the target in order to ensure the fulfilment of the fundamental hypotheses, previously mentioned. However, the measurements may not be affected by this distance with a wide tolerance (between 2 and 11 mm) depending on the operating condition and the type of injector, as reported in [134]. Once the injector has been installed inside the vessel and aligned with the transducer, it is connected to the signal generator which allows the control of the electrical impulse used to operate the needle lift by controlling timing and duration. A cooling/heating system, directly connected to the injector, was used to control the fluid temperature. Moreover, the pressure control of the working fluid (i.e, water) was enforced

by connecting the injector to a hydro-pneumatic pressurized system. The system has been previously calibrated to fulfil a maximum force standard deviation of 0.5%. A simple scheme of the entire test rig is shown in Figure 61.

Figure 62 shows the force signals measured by the instrumentation for three different relative injection pressures (4 bar, 6 bar and 8 bar) considering a constant back pressure (BP) of 1 bar and a fluid temperature of 25°C. These correspond to the same conditions used for the PDA spray imaging and for the CFD three-dimensional numerical validation of the spray models. Figure 62 clearly shows a background noise generated by some instabilities which introduces additional frequencies into the signal. Specifically, these disturbances are caused by all or a part of the followings:

- pressure waves inside and outside the injector induced by the opening of the needle (1000-4000 Hz) and related system perturbation;
- turbulence of the liquid jet both inside and outside (5000 Hz);
- mechanical vibrations due to the acceleration of the needle that can also activate the system's modal frequencies;
- acoustic waves (very weak);
- typical signal noise of the measuring system (minimized by a correct calibration).

Among all these disturbances it is proved that turbulence is the that one that most contributes to the noise of the recorded signal. For this reason, each measure, before being averaged, has been repeated twice with 50 injections for each repetition (100 injections in total at a rate of 1 injection event per second) and then a low pass filter has been applied. Figure 63 shows the final filtered signal obtained for the case at 8 bar of relative injection pressure, which may be considered as the most interesting and representative one for PWI applications.

The first important signal oscillation can be seen after the SOI (Start Of Injection) and it is due to the start of the liquid flow rate issuing from the injector.

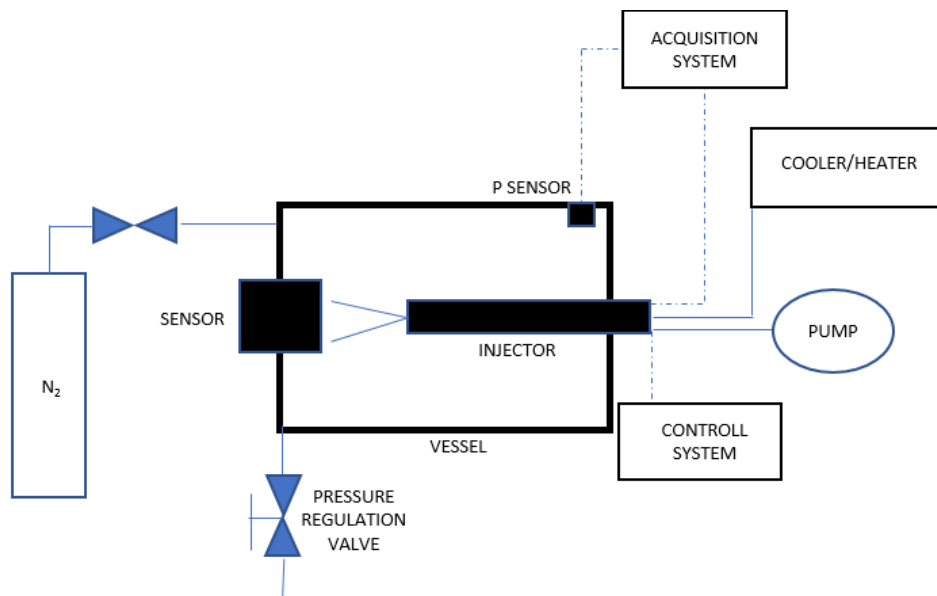


Figure 61. Experimental facility layout

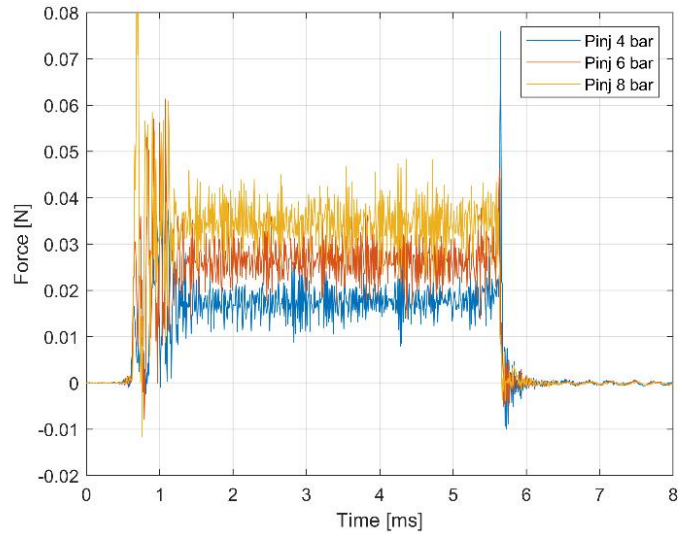


Figure 62. Momentum Flux for  $P_{inj}$  4, 6, 8 bar,  $T_{fluid}$  25°C and BP 1 bar

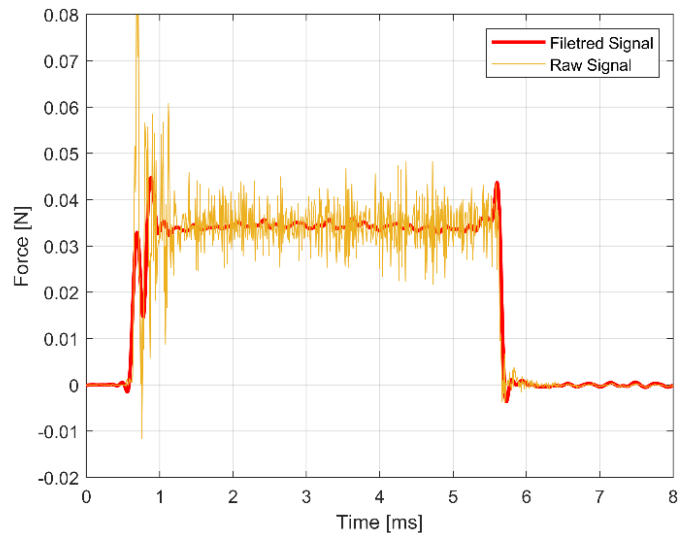


Figure 63. Momentum Flux signal filtered,  $P_{inj}$  8 bar,  $T_{fluid}$  25°C and BP 1 bar

It has been noticed how in the first instants the injector tends to generate ligaments and large drops, which increases the density of the spray and, therefore, the force impressed on the sensor. One can also notice a smaller oscillation of the signal when the needle is closing, due to the pressure instability inside the injector that is reflected back to the sensor. As far as the central phase of the signal is concerned, it can be seen that the initial higher instabilities, up to 1.2 ms, do not affect the main injection phase (between 1.2 ms and 5.5 ms), without generating greater signal disturbance waves in the filtered signal.

Figure 64 shows the average value of the momentum flux in the steady phase of the signal. As the pressure difference (difference between injection pressure and back pressure) rises, it increases linearly, being the force directly proportional to the pressure. Moreover, the experimental tests have shown that the effects of the fluid temperature between 25°C and 60°C are negligible on the momentum flux value, since they are far from those leading flash boiling conditions at the given back pressure.

The experimental results obtained from momentum flux were used for the calculation of the Rate Of Injected mass (ROI) as give by Eq. (104) and shown in Figure 65 for the case at 8 bar of relative injection pressure. During the test, the actual amount of the mass injected was also measured through a calibrated scale.

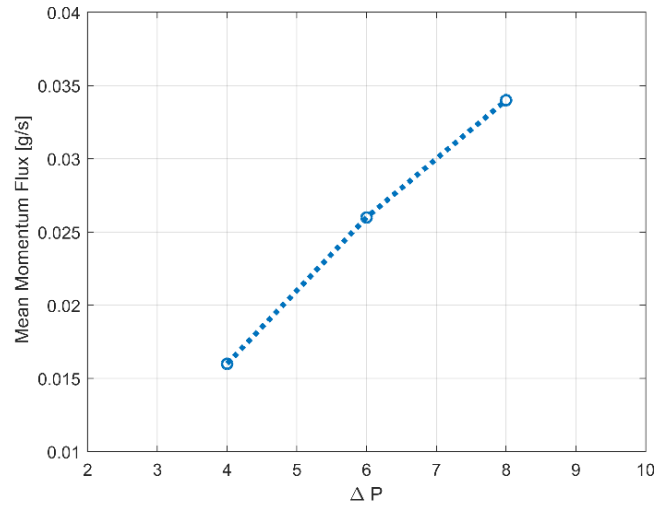


Figure 64. Mean Momentum Flux  $P_{inj}$  4, 6, 8 bar,  $T_{fluid}$  25°C and BP 1 bar

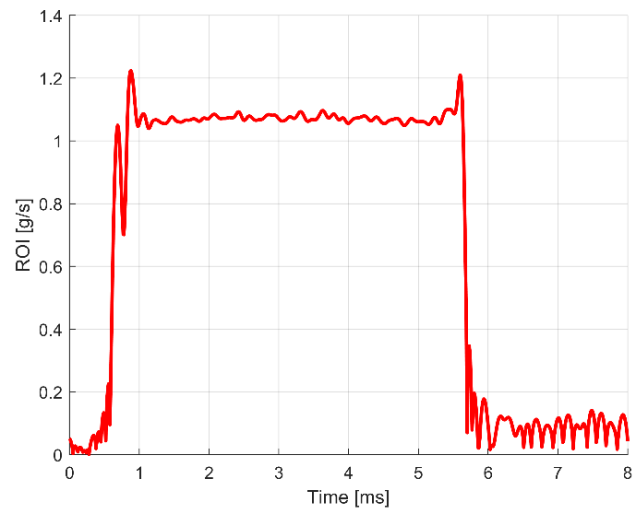


Figure 65. ROI for injection pressure of 8 bar, 25°C and BP 1 bar

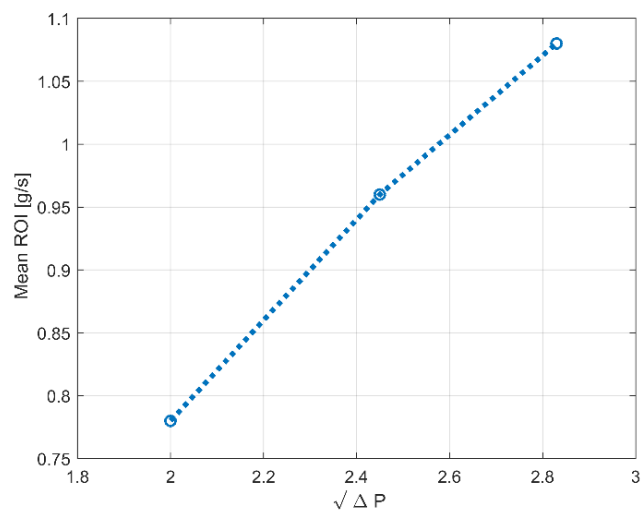


Figure 66. Mean Rate of Injection,  $P_{inj}$  4, 6, 8 bar,  $T_{fluid}$  25°C and BP 1 bar

The ROI curve derived from momentum flux was thus corrected so that the integral was equal to the measured water mass. However, the correction was rather small (about 1%) proving that the methodology is reliable and repeatable. Finally, the linear increase of the average mass flow rate as a function of the square root of the pressure difference is reported in Figure 66.

At this point, known the momentum flux and the ROI, the injector can be considered characterized from the hydraulic point of view.

## 6.2 Imaging Characterization

The measurement of the liquid spray sizing and penetration are rather complex to be performed, especially the former one. On the other hand, they remain fundamental to characterize the performance of a given injector and to validate CFD spray simulation. For a complete knowledge of the spray, three main complementary techniques can be used, each with its particular advantages and disadvantages [135]: Phase Doppler Anemometry (PDA), High Resolution Laser Backlight Imaging (HRLBI) and High-Speed Microscopic Visualization (HSMV).

The PDA is one of the most widely used techniques for the determination of droplet velocity and diameter, often applied to characterize engine fuel injectors. The system consists in measuring the light scattered within a control volume due to the passage of spray particles. Two laser beams are directed towards this control volume such that the frequency of the scatter measured by the receiver is proportional to the droplet velocity, while the phase shift recorded by two different detectors is proportional to the size.

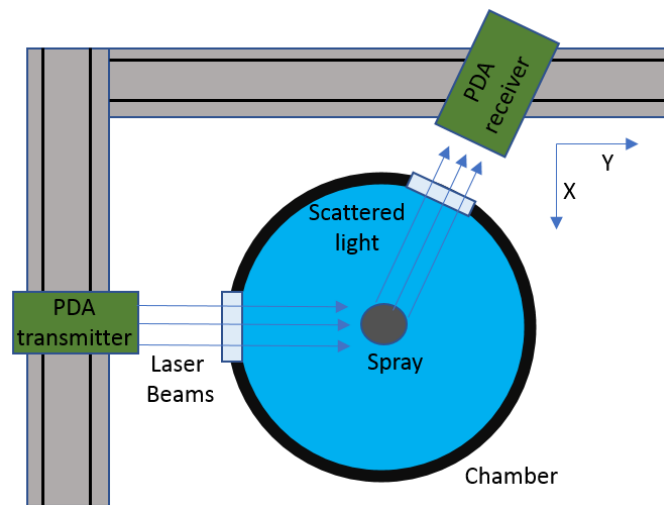


Figure 67. PDA layout

Figure 67 represents a scheme of the system. The PDA is performed on one or more planes at a certain distance along the injector axis (e.g. z axis) from the injector tip. Then the local measurements are performed along the other two directions (X-axis and Y-axis), with a certain sampling distance between one point and the other (example 1 mm). In this way the spray is characterized in terms of speed and diameter of the drops at a certain distance in both transverse and radial direction.

The HRLBI technique consists of interposing the spray between a light source and a high-resolution camera. In this way the light is reflected or diverted by the individual drops, substantially blocking their path towards the camera. The drops will then appear in the camera as black pixels, and their diameter can be accurately measured.

With an approach similar to HRLBI, the High-Speed Microscopic Visualization uses a camera with a much higher recording speed (even 150000 frames per second) but with a downsize of a lower image resolution.

In this way it is possible to determine the speed of the drops more precisely. Specifically, a LED characterized by a high-power pulse of light and frequency, with a parabolic reflector to collimate the light source and a Fresnel lens with a focal length close to the area of interest, is used. A diffuser creates a uniform back light. The high recording speed combined with the high frequency pulsed LED allows to capture images of the whole injection event, granting the opportunity to visualize and track the droplets during their time of residence inside the region of interest. The use of a LED (fast light-emitting diodes) provides significant improvement of the image quality since the pulse duration can be very short (nanoseconds) and the amount of light captured by each frame is thus governed by the pulse length of the LED and not by the exposure time of the camera.

In practice, from a physical point of view, these two optical techniques, for displaying sprays, use diffused back-illumination, where a light source is extinguished due to the optical depth ( $\tau$ ) of the spray. The extinction can be calculated for each frame using Beer-Lambert's law:

$$\frac{I - I_f}{I_0} = e^{-\tau} \quad (105)$$

where  $I$  is the pixel-wise intensity distribution of the current frame that considers attenuation from the spray,  $I_f$  accounts the light emitted by the flame for the same time step, and  $I_0$  is the reference image from the diffused source without attenuation. For non-reactive cases, the term  $I_f$  is zero.

The imaging processing for these two last techniques are very similar. The purpose is to separate the drops captured in the camera frames from the rest of the image. The procedure is divided into several steps:

- 1) imaging masking, consisting in post-processing the data provided in matrix form in order to eliminate unwanted elements from the image, such as the tip of the injector;
- 2) subtraction of the background ( $I_0$ ) of each image from the corresponding spray, thus creating an image in which the drops appear as grayscale points;
- 3) a binarization of the images, in order to separate the background and the unfocused spray from the rest of the drops that will be measured.

More detailed information about these optical techniques and picture manipulation can be found in [135]. The technique on which the experimental analysis will be focused is the first, concerning the PDA. Thanks to data obtained experimentally in the following paragraph, a CFD validation of the spray models will be carried out, also repeated and revalidated against a test case found in literature.

### 6.3 Experimental PDA Results of the Water Injection System

Some experimental results obtained with the first described technique, the PDA, for the characterization of a PWI injector within a constant volume chamber, ambient pressure and ambient temperature (25°C), are now presented. The short results that are now presented are only intended, as already explained at the beginning, to review in detail all the steps and which outputs offer a complete characterization of a water injector for PWI applications, whose experiment were carried out by CMT Termicos-Politecnico of Valencia laboratories after the end of pandemic emergency.

The main geometry features of the injector are listed in Table 10 (spray angles are kept confidential) and the operating conditions are reported in the following Table 11.

The PDA analysis was performed on three planes at a distance of 15, 30 and 50 mm from the injector tip, with respect to the centre of the spray plume along the transverse direction, as it was the one that found to have a higher droplet density in the preliminary tests. In Table 12 are listed the instrumentation used to perform the PDA analysis.

Table 10. Injector Layout

<b>Number of holes</b>	3
<b>D hole mean</b>	135 [ $\mu\text{m}$ ]
<b>Cooling</b>	Liquid cooled

Table 11. Injection test conditions

<b><math>P_{inj}</math></b>	4-6-8 [barg]
<b><math>t_{eng}</math></b>	5 [ms]
<b><math>T_{water}</math></b>	20 [ $^{\circ}\text{C}$ ]
<b><math>m_{inj}</math></b>	3.90 – 4.80 – 5.40 [mg]

Table 12. Instrumentation used for PDA tests

<b>Processor</b>	Dantec BSA P80
<b>Transmitter/Laser source</b>	FlowLite 60 mm
<b>Receiver</b>	HiDense 112 mm
<b>Beams diameter/spacing</b>	2.2 mm/38 mm
<b>Focal length (TX/RX)</b>	400 mm / 310 mm
<b>Velocity range</b>	-15.85 to 47.49 m/s
<b>Sizing range</b>	1-400 $\mu\text{m}$

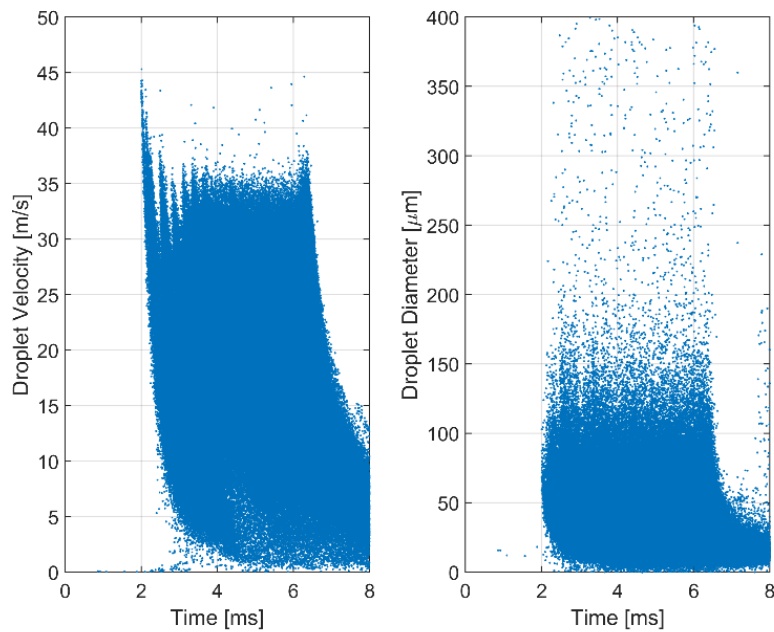


Figure 68. Example of raw PDA data @30 mm

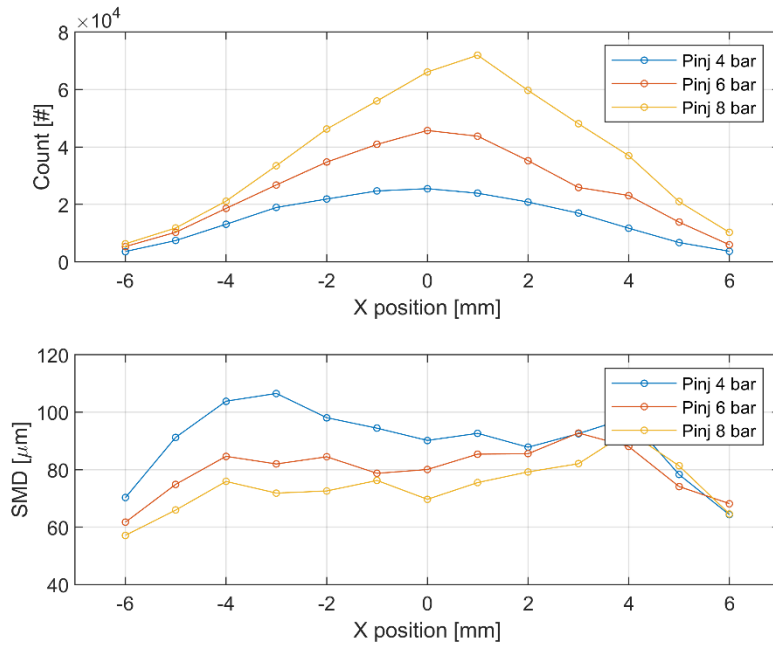


Figure 69. Number of drops and SMD distributions @30 mm

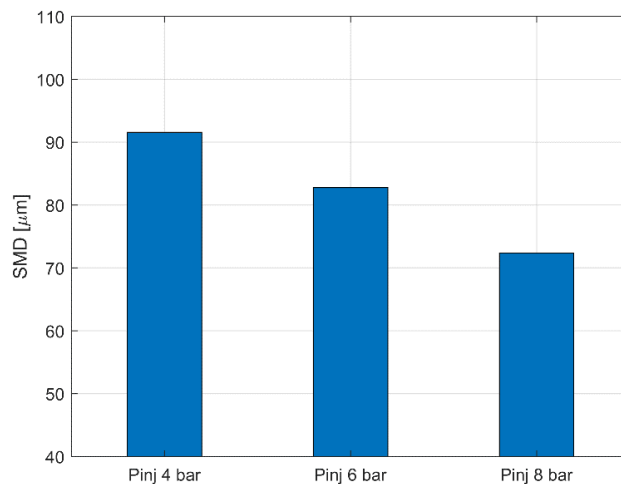


Figure 70. Mean SMD @50 mm

Figure 68 shows a PDA output concerning the time distribution of velocity and diameter of each drop recorded in a specific point of the plane at 30 mm. This type of output represents the raw output signal of the PDA. After establishing the time period in which the injection event can be considered stable, without the influence of the needle movement, the data are manipulated and averaged over time to obtain a single value for each sampling point along the transverse direction (X in this case). Figure 69 shows on the top the number of particles for each position for different injection pressures and on the bottom the corresponding average Sauter mean diameter (SMD). As expected, as the injection pressure increases, the greater velocity of the droplet and the greater turbulence of the jet flowing out from each hole promotes the liquid jet and the very first spray breakup by forming a greater number of droplets and a smaller diameter.

In addition, it also showed a bar chart (Figure 70) summarizing the mean SMD, compared to all sampling points, on the 50 mm plane. By doubling the injection pressure, it is possible to decrease the SMD of about 20 microns. From an engine point of view this means a much faster evaporation and a better homogenization

of the water droplets in the air, with a lower probability of creating wall film liquid areas because of wall impingement.

By comparing the same variables measured on different planes it is possible to get an overview of the real break-up dynamics undergone by the drops. In Figure 71 the data for injection pressure at 8 bar are shown, moving from 30 mm to 50 mm planes, when the spray is already dynamically developed. Globally, the SMD at 50 mm is slightly lower and this is due in particular to the droplets evaporation process rather than the secondary break up which, as will be demonstrated also through numerical simulation, does not occur under these operating conditions.

As far as the average speed of the drops for each single position is concerned, the Figure 72 shows a more uniform profile at low pressure and, as expected, a speed increase for higher injection pressure, almost linear to the square root ratio of the pressure jumps between the injector and the test chamber.

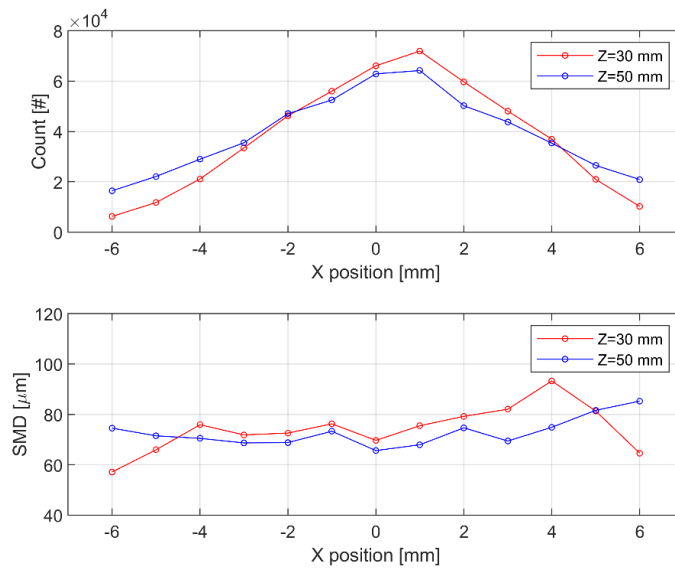


Figure 71. Number of drops and SMD recorded @30 mm and @50 mm,  $P_{inj}$  8 bar,  $T_{fluid}$  25°C

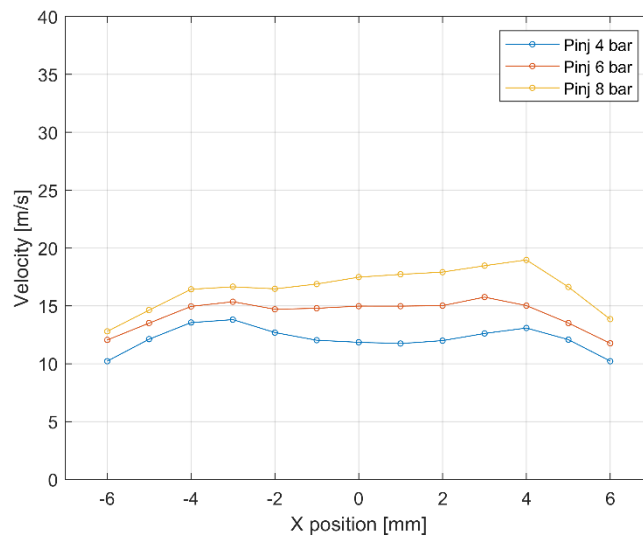


Figure 72. Droplet velocity distributions @30 mm

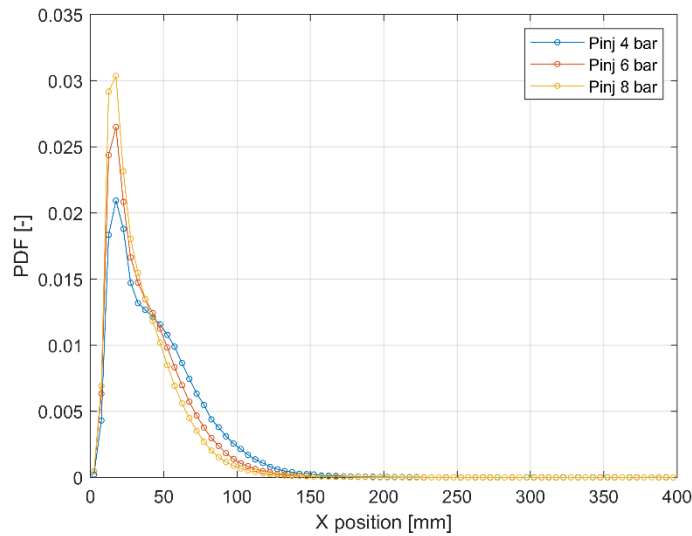


Figure 73. PDF @30 mm for different injection pressure

Finally, it is possible to extract the most important data for a correct setup of a CFD spray simulation: the Probability Distribution Function (PDF). In the Figure 73 are shown the PDFs for the analysed cases on the 30 mm plane, i.e. when the primary break-up phenomena can be considered completed. It was decided to use this 30 mm PDFs to verify also numerically that in the space between the 30 mm and 50 mm planes there was no significant change in the diameter of the drops.

## 6.4 Summary

In this chapter the hydraulic characterization of the water injector under examination was firstly presented by measuring the momentum flux. After describing the experimental procedure and the equations underlying this process, the most important data were extracted from the initial raw signal in order to evaluate the rate of injection.

As far as the microscopic characterization of the water injector spray is concerned, the post-processed data of the PDA technique, highlighted the effect of the injection pressure on the particle size, allowing a decrease of the SMD of 20 microns moving from 4 to 8 bar (relative injection pressure).

The main data collected from the experimental campaign will be used in the next chapter in order to find a reliable methodology to simulate the water spray development in engine simulations.

# Chapter 7: PWI Numerical Validation

One of the main uses of the experimental spray data is for the validation of fluid dynamic spray simulations in order to provide the initial conditions (i.e., mass flow rate) and the right tuning of the spray model setup constants. The characteristic spray parameters of interest for engine applications are the followings:

- a) The droplet size: the Sauter Mean Diameter (SMD or  $d_{32}$ ) and, some cases, the arithmetic spray diameter  $d_{10}$  are used to characterize the overall spray statistics and they are important since they affect the evaporation rate and the mixing with air. They can be referred to both to the overall spray or to local volumes where the measurements are taken;
- b) The droplet local velocity, which affects (together with the ambient density) spray penetration inside the intake runners/ports or the combustion chamber. The penetration of the spray is indeed responsible in gasoline engines for both the mixing capacity with air and the generation of wall film, while in diesel engines it governs the positioning of the diffusive flame. The availability of local velocity data recorded may help in evaluating possible errors in liquid-to-gas phase momentum coupling.

By using the CFD code AVL-FIRE, with the atomization and spray model setup previously presented in Chapter 4, different spray simulations representing the experimental spray characterization into vessel have been performed. The first numerical results presented (named CASE 1) are those for the comparison against experimental PDA data on 30 mm and 50 mm planes for two relative injection pressures 4 and 8 bar, whose details have been illustrated in the experimental activity of the previous Chapter 6.

A further CFD validation will be here presented with experimental literature data of a PWI injector (named CASE 2), tested in a constant volume chamber in condition similar to those of Chapter 6. Moreover, two different approaches for the representation of the spray in engine simulations will be described.

## 7.1 CFD Spray Validation against Experimental Data: CASE 1

The results of the CFD simulations will now be described and compared with the experimental data (Chapter 6), in order to calibrate the numerical models for a correct characterization of the spray. The simulations were performed for two relative injection pressures, at 4 bar and 8 bar. The data are recorded on two PDA planes: at 30 mm and 50 mm far from the injector tip.

In a different way from what will be described in the next paragraph, for these first validations all three injector holes have been simulated, whose geometrical design and all the experimental set-up have already been reported previously.

Thanks to the characteristic diameters data, the experimental  $d_{32}$  PDFs at 30 mm have been imposed for the initialization of the droplet's diameter, thus avoiding introducing a primary break-up model to describe the jet atomization.

In a similar way to the experiment, a cylindrical volume in ambient conditions (1 bar and 25°C), filled with nitrogen, was reproduced to perform the vessel spray test. The geometry, which represents the size of the test chamber, was discretized with a computational mesh composed of about 300k cells of hexahedral type,

with an average size of 1 mm and 0.5 mm in the hole directions. The refinements of the grid along the axis of the jets were necessary for a correct modelling of the interaction phenomena of the drops.

To guarantee a correct representativeness of the water spray, 1600 parcel/mg were used. For a PFI system (similar approach), the lower limit is usually about 800 parcel/mg, below which the loss of accuracy becomes too high. The choice of not exceeding the value of 1600 parcel/mg is for the high computational time, very sensitive to this parameter: as the number of parcels increases, also it increases the number of Lagrangian equations that the code must calculate. Moreover, this modelling is intended to be applied not only to a vessel test, relatively fast computationally, but also to a complete engine simulation.

In Table 13 are listed the simulated operating conditions and, in Table 14, the main models adopted and calibrated to perform this type of validation, whose details have been presented in Chapter 4.

Table 13. Main injector settings

Injection Pressure [bar]	Fluid Temperature [°C]	Injection Duration [ms]	Mass Injected [mg]
4	25	5	3.9
8	25	5	5.4

Table 14. Spray models adopted

<b>Evaporation Model</b>	Spalding
<b>Parcel Interaction Model</b>	Schimdt
<b>Primary Break-Up</b>	-
<b>Secondary Break-Up</b>	Proprietary model
<b>Drag Model</b>	Schimdt
<b>Turbulence Model</b>	K- $\zeta$ -f

### 7.1.1 Numerical Validation Results of the PWI System

Figure 74 and Figure 75 show the comparisons between the numerical and experimental SMD results on the two planes at 30 mm and 50 mm far from the injector tip along the X direction, for both the injection pressure examined. The comparison shows that simulations are able to reproduce, in a very faithful way, the characteristic size of the drops on both planes. In fact, it can be seen that the distribution of the SMD was captured not only around the centre of the PDA of the transverse position X, but also in the peripheral positions near the edge of the spray. The main small differences are attributable to the representativeness of the drops, which, although high, is not able to fully capture the stochastic experimental profile. However, the results have to be considered very satisfactory.

As also confirmed experimentally, the development of the spray does not undergo significant variations in terms of granulometry. The distribution along the transverse coordinate shows very similar profiles at 30 mm and 50 mm for the same injection pressure (Figure 76), meaning that no further break-up occurs after 30 mm from the tip. In a vessel spray test, the effects that can lead to a variation in particle size are mainly the evaporation of the drops and the secondary break-up, which confirm to be correctly calibrated.

With regard to evaporation, the fluid is injected at 25 °C. The latter condition is not suited for the water evaporation.

Figure 77 shows the percentage of the evaporated mass over the total injected mass for the two pressures considered. The values are negligible, and the minimum evaporated quantity can be attributable to the diffusion of the water in the gas, being far from the saturation condition.

As far as the second effect is concerned, the secondary break-up, it is interesting to evaluate the characteristic Weber number of the spray, for the two operating conditions. The images (Figure 78) show two frames of the spray simulations in which the  $We$  number is plotted ( $P_{inj}$  4 bar on the left and  $P_{inj}$  8 bar on the right). As previously seen, most break-up models provide a minimum critical  $We$  number of 12, below which the drops do not further split. Since water has a very large surface tension and the droplet relative velocities are very low here (low injections pressure), the  $We$  never exceeds the minimum threshold, leaving deactivated the secondary break-up model.

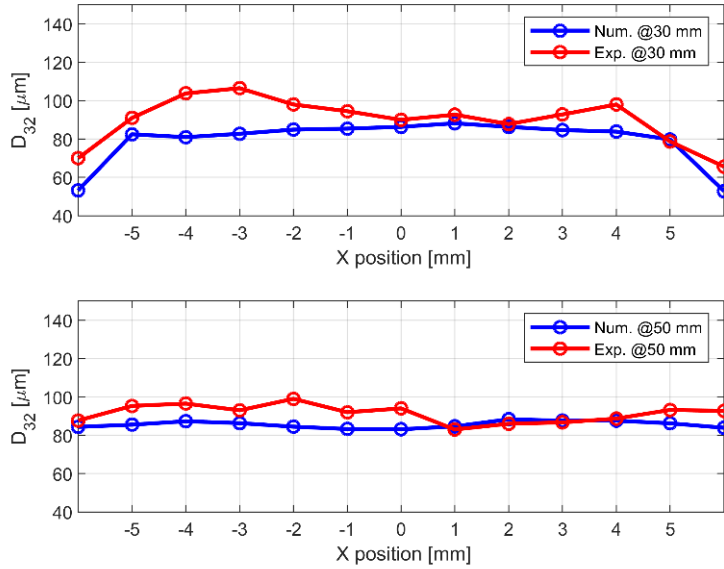


Figure 74. Droplet  $D_{32}$ : CFD vs Experimental results for  $P_{inj}$  4 bar at 30 mm and 50 mm

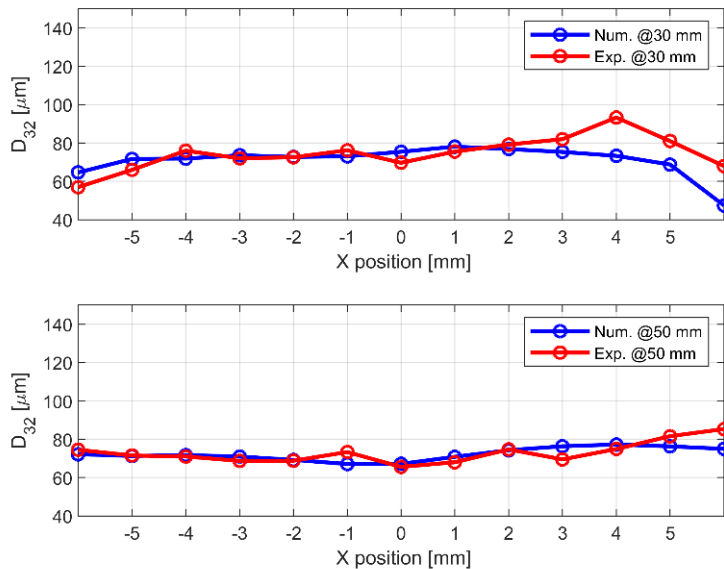


Figure 75. Droplet  $D_{32}$ : CFD vs Experimental results for  $P_{inj}$  8 bar at 30 mm and 50 mm

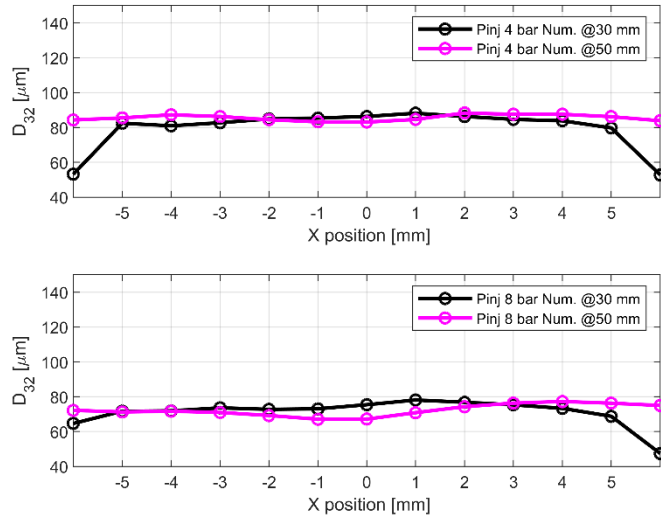


Figure 76. Droplet  $D_{32}$ : CFD vs Experimental results for  $P_{inj}$  4 and 8 bar

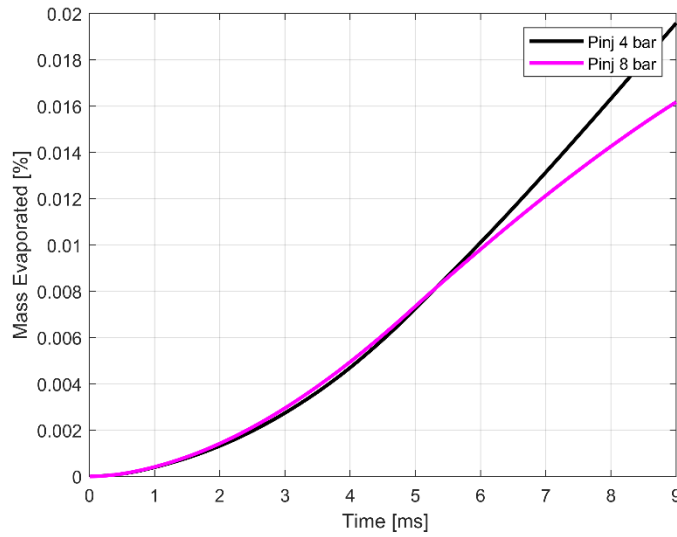


Figure 77. Water mass evaporation,  $P_{inj}$  4 bar and 8 bar

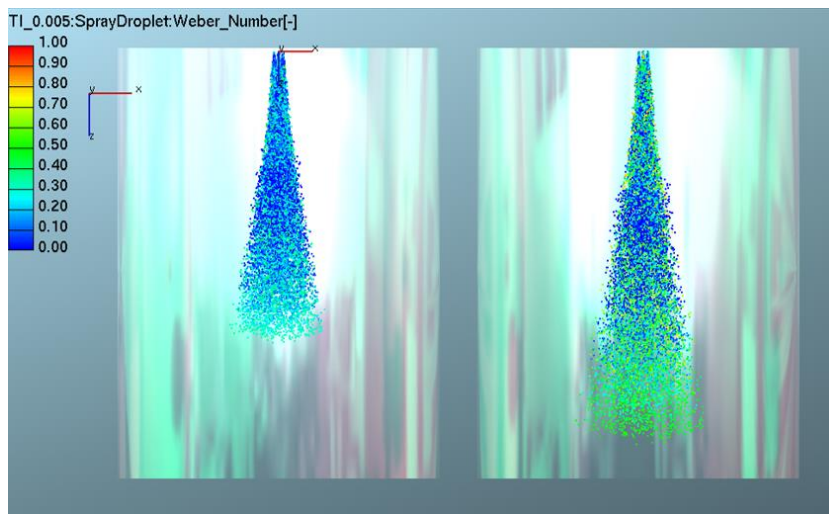


Figure 78. We number of the droplet for  $P_{inj}$  4 bar (left) and 8 bar (right)

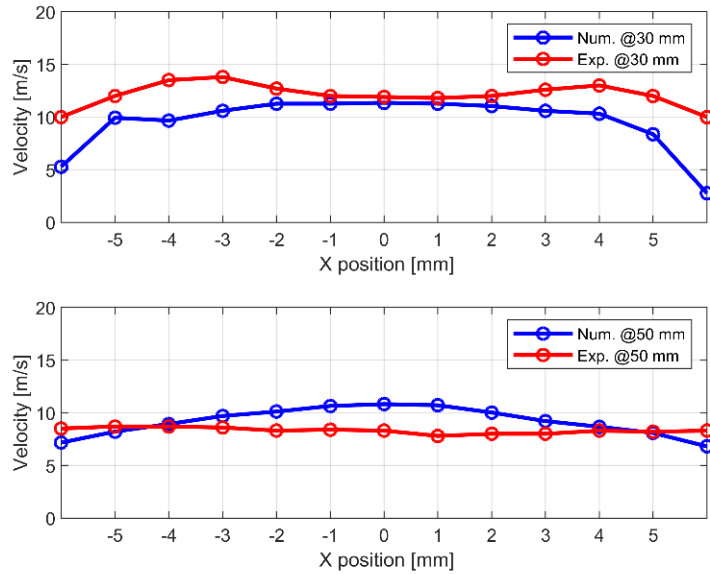


Figure 79. Droplet Velocity: CFD vs Experimental results for Pinj 4 bar at 30 mm and 50 mm

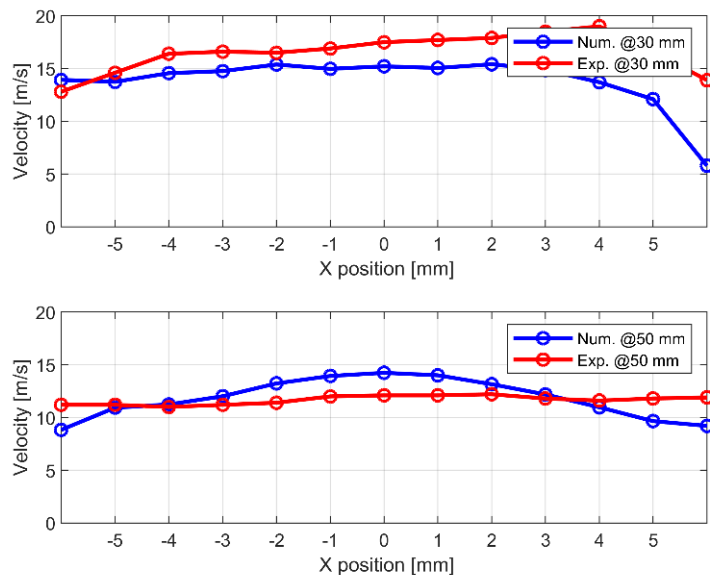


Figure 80. Droplet Velocity: CFD vs Experimental results for Pinj 8 bar at 30 mm and 50 mm

Finally, as one can see in Figure 79 and Figure 80, the predictions of the droplet velocity at measurement locations are good. Two very particular effects are captured:

- 1) On the 30 mm plane there is a tendency of the spray to slow down in the extreme zones of the plume, symmetrically at 4 bar and non-symmetrically at 8 bar. Both profiles are well-captured by CFD;
- 2) Moving towards the plane at 50 mm, for both pressures, the profiles tend to flatten in an evident way. This effect is also well represented numerically.

This means that both the initialization of the droplet speed and the drag model have been calibrated correctly. The numerical simulation not only succeeds in describing the global behaviour of the spray, but also its local differences and its variations during the temporal evolution, represented by the data on the two successive planes of the PDA.

## 7.2 CFD Spray Validation against Experimental Data: CASE 2

A literature PWI spray case (among the very few available) is now presented, where a PDA was performed in a similar way to what presented so far. However, it becomes interesting to analyse this case in detail for an additional phenomenon of coalescence, that has not emerged in the previous case presented.

The authors in [136] performed an experimental test under different operating conditions up to a pressure injection of 9 bar (relative), in order to define the spray characteristics within a constant volume chamber, containing nitrogen at ambient pressure. The CFD validation has been performed for the injection pressure of 9 bar (relative), being the most interesting for a real engine application of the PWI system.

For the macroscopic and microscopic description of the spray, a visualization technique using a high-speed camera and a PDA, both previously described, were used. Table 15 lists the geometrical features of the injector (PFI derivation) and the working points tested.

The two spray plumes are considered as symmetrical (Figure 81) and the injector is composed of two groups of holes, as shown in Figure 82. The PDA analysis were carried out only on one plume, on planes at 30 mm and 60 mm from the injector tip along Z direction, with the centre of the spray at  $Y=8$  mm and  $Y=16$  mm respectively.

As far as penetration is concerned, this was evaluated by the authors as the maximum distance between the injector tip and the spray edge. More details and other technical information about the instrumentation used for the set-up, can be found in the article [136].

Unfortunately, the authors do not specify all the geometry data required for a complete injector setup for CFD simulation purposes. The precise directionality in terms of injection angles, of each single hole, and the spray angle of the single plume have not been reported, for this reason some assumptions and evaluations will be presented shortly.

The article reports, from PDA results, the average SMD ( $90 \mu\text{m}$ ) and  $d_{10}$  ( $51 \mu\text{m}$ ) on a sample of 5000 drops at 30 mm from the injector tip: these data have been used to formulate a Rosin-Rammler distribution to impose at the exit of each hole. Figure 83 illustrates the cumulative distribution function for the 9 bar injection pressure case.

Unlike the methodology seen in the previous validation, in this case not all the injector holes have been represented numerically. It has been considered a single hole (symmetrical system) positioned in the central point of the Group1 (Figure 82), ensuring a good representativeness of the spray through the imposition of 1500 parcels per milligram of water injected. This hole has been aligned with respect to the centre of the PDA of the 30 mm plane.

Table 15. Injector features and test conditions [136]

<b>Number of holes [#]</b>	12
<b><math>D_{\text{hole}}</math> (averaged) [<math>\mu\text{m}</math>]</b>	138
<b>Spray Angle <math>\vartheta</math> [<math>^{\circ}</math>]</b>	20
<b><math>P_{\text{inj}}</math> [bar]</b>	9
<b><math>t_{\text{eng}}</math> [ms]</b>	2.795
<b><math>T_{\text{water}}</math> [<math>^{\circ}\text{C}</math>]</b>	20
<b><math>P_{\text{N2}}</math> [bar]</b>	1
<b><math>m_{\text{inj}}</math> [mg]</b>	13.7

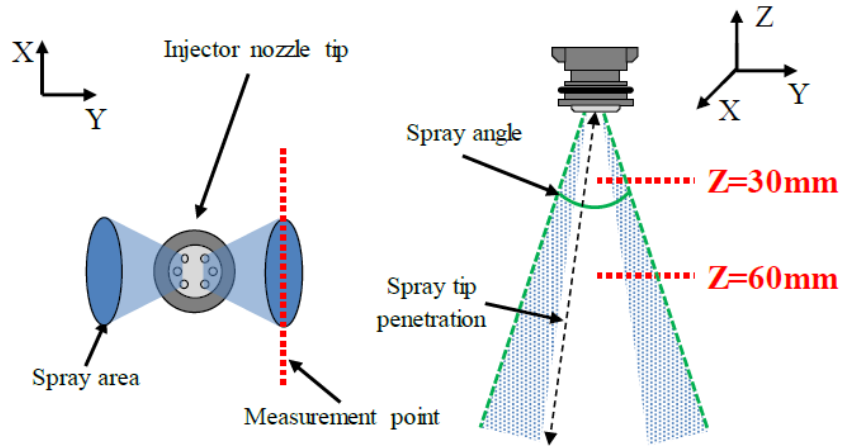


Figure 81. Injector plumes representation [136]

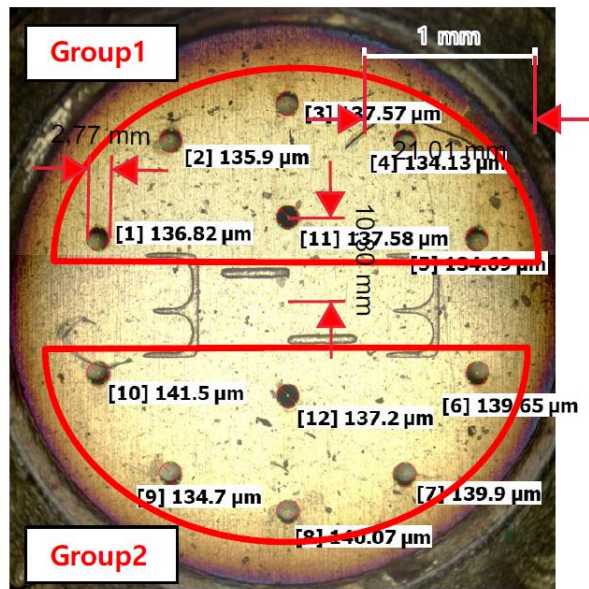


Figure 82. Injector holes distribution and diameters [136]

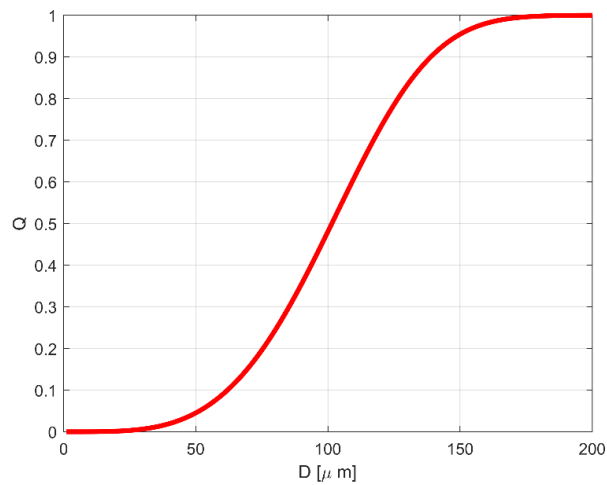


Figure 83. Rosin-Rammler distribution for  $P_{inj} 9 \text{ bar}$ :  $SMD 90 \mu\text{m}$ ,  $d_{10} 51 \mu\text{m}$

As mentioned above, no precise data are reported regarding the direction of each single hole, however, being a test in a stationary environment without any external disturbance, it is a good approximation taking the PDA centre as the actual geometric orientation of the holes. To fully define the injection, it is also necessary to impose the spray angle of the single plume. This data is not available, so a detail analysis of the high-speed imaging has been carried out in order to trace the average angle of the plume during its evolution (Figure 84).

Moreover, from the frame sequence, it can be noticed a higher concentration of drops in the centre of the plumes and a cloud of smaller droplets around the spray edges.

To transfer this phenomenon in the numerical simulation, it has been used a double spray angle (Figure 85): the inner one with an angle equal to  $13^\circ$  injecting 80% of the total mass and an outer one equal to  $18^\circ$ , to simulate the presence of the drops cloud, injecting the remaining 20%.

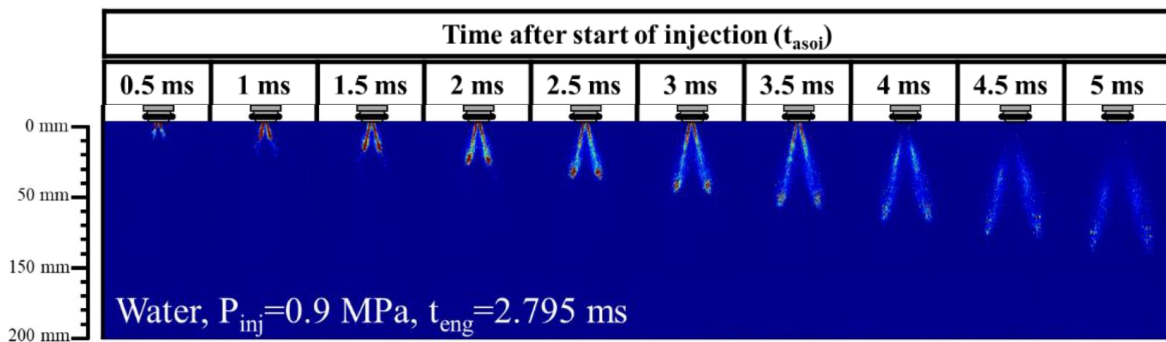


Figure 84. Experimental spray imaging visualisation [136]

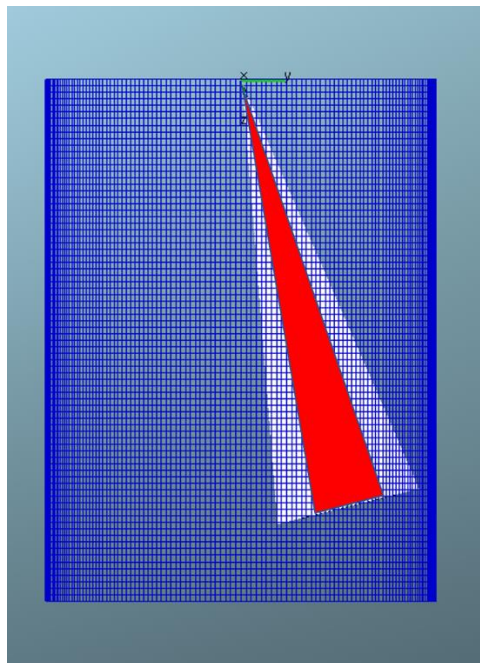


Figure 85. Representation of the double spray cone

### 7.2.1 Numerical Validation Results of the PWI System

Figure 86 shows the SMD distributions on the plane at 30 and 60 mm, compared with the PDA sampling data along the X-direction. It can be seen that on the 30 mm plane the two distributions show some differences in particular in the edge zones, despite the imposed PDF values come from SMD e  $d_{10}$  data on this plane. On

the 60 mm plane, the differences between the experimental and the simulation data become greater. It is evident how the PDA changes sensibly in the centre of the plume, while the CFD does not capture this detail. Comparing the results between planes, both numerically and experimentally (Figure 87), the differences appear clearer: basically, the profiles recorded by the simulation are the same at 30 mm and 60 mm denoting that the  $d_{32}$  has not changed.

Furthermore, the Weber number never exceeds the value 2, well below the critical value 12, above which the secondary break-up of the drops can occur. This seems to be consistent both with some preliminary theoretical considerations, seen in Chapter 3, and with the experimental results: the SMD tends to increase slightly, indicating that the drops do not experience further break-up. In addition, since the volume/surface ratio of the drops increases, the evaporation will tend to be reduced, also due to low test temperatures (Figure 89).

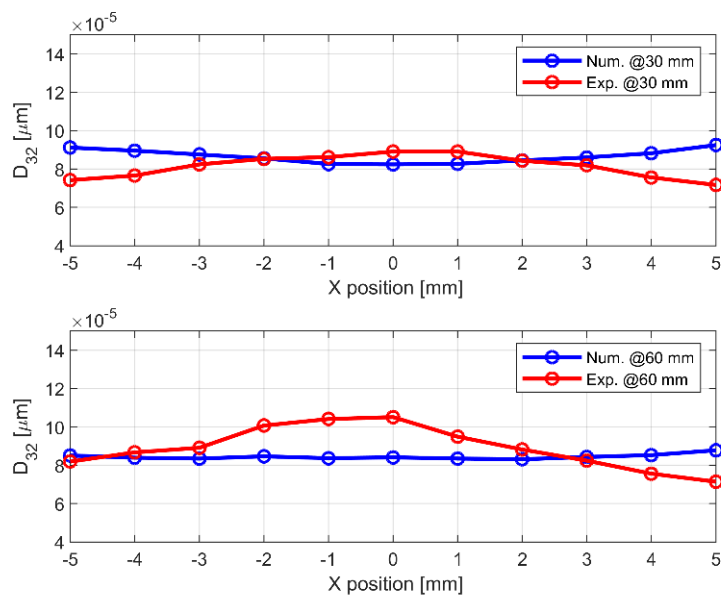


Figure 86. CFD vs Experimental  $d_{32}$  validation @30 mm and @60 mm

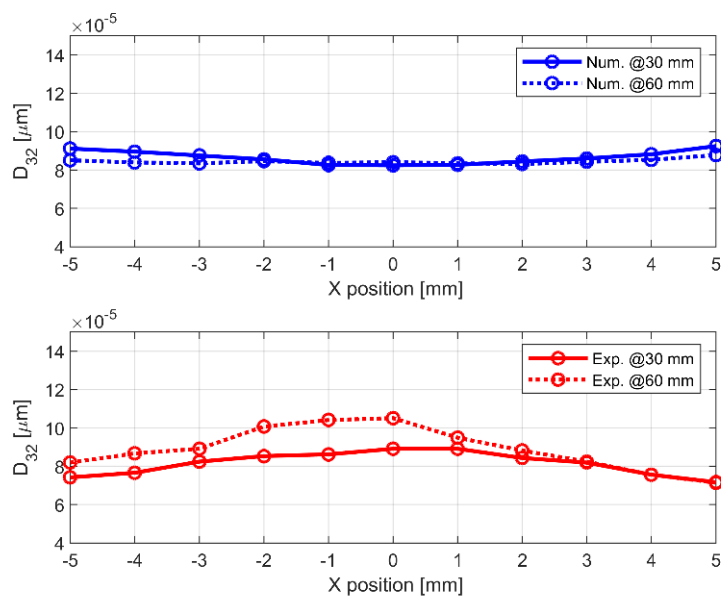


Figure 87. Focus on  $d_{32}$  differences on PDA planes between CFD and Experimental results

The SMD increase can be attributable to the phenomenon of coalescence, present in the centre of the plume where there is a higher initial concentration of drops, probably due to the number of holes. Several coalescence parameters related to the Schmidt model [98] (Chapter 4) have been investigated to test their effectiveness from a numerical point of view.

To make the model effective it was necessary to re-evaluated two parameters: the number of parcels introduced (spray representativeness), increased to 1800 parcel/mg, and the characteristic size of the cells, decreased to 0.3 mm along hole axis. Only in this way it was possible to increase the probability that two parcels were able to interact in the same cell. The first tests conducted, leaving these two features unchanged, indeed, did not present variations in the results despite the activation of the model. The increase in the number of parcels and cells involves a more significant computational time, but still sustainable for an application on a complete engine case.

By activating the coalescence model, it was necessary to create a new PDF with lower SMD (60  $\mu\text{m}$ ) and  $d_{10}$  (35  $\mu\text{m}$ ) values, such as to return to the target values on the 30 mm plane thanks to the interaction between the drops (Figure 90). Leaving the previous PDF, as a result of the coalescence phenomena that occur in the first section, at 30 mm it would have obtained characteristic diameters well above the experimental ones.

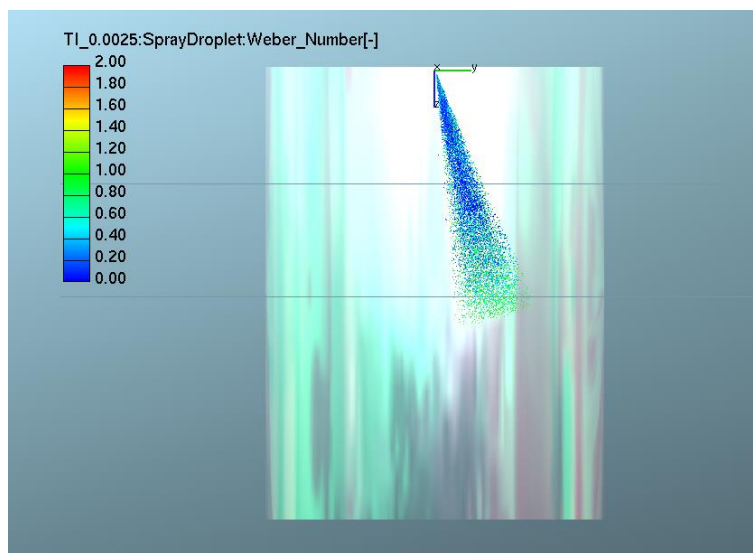


Figure 88. Drops We distribution

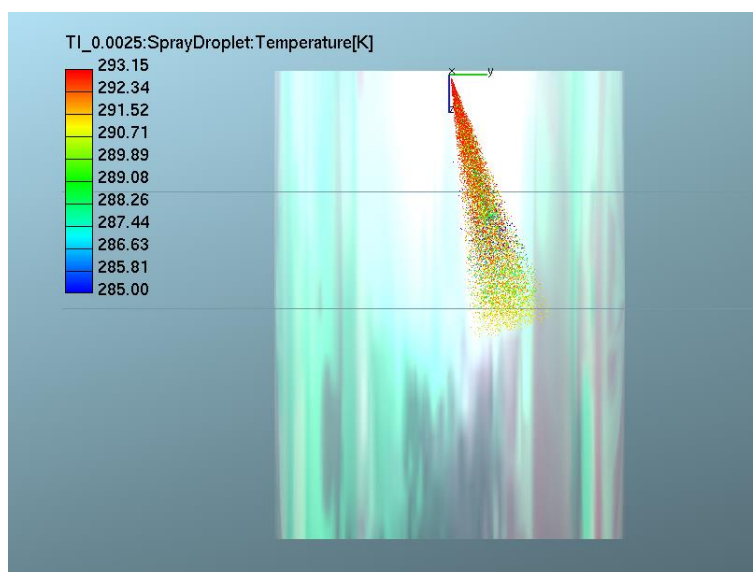


Figure 89. Drops Temperature distribution

Figure 91 shows again the distribution of the SMD on the two planes. Thanks to the activation and calibration of the particle interaction model, the numerical results are much more consistent with experimental data, especially on the first plane at 30 mm. There is a tendency to increase the SMD right towards the centre of the plume where is present a higher concentration of drops. On the 60 mm plane the global distribution is consistent with the experimental data even if locally there is a deviation between distributions ( $-2 < X < 2$ ). This is due to the low number of parcels remaining in this area, since many of these joined by coalescence already at 30 mm from the injector. The accuracy could be improved by increasing the parcel/mg ratio, but with an increasing computational resources demand. The reason why it was necessary to consider also the coalescence model could lie in the large number of injector holes. In this way it increases the probability that the jets can interact with each other, being enclosed in a very small space.

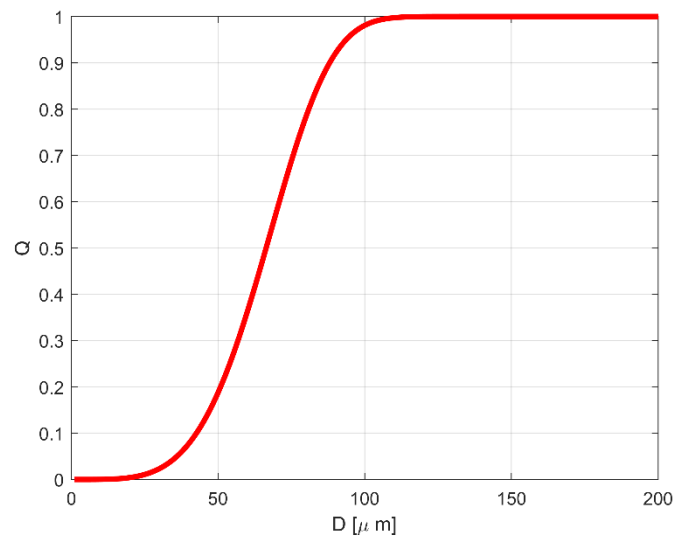


Figure 90. Rosin-Rammler distribution for  $P_{inj}$  9 bar: SMD  $60 \mu m$   $d_{10}$   $35 \mu m$

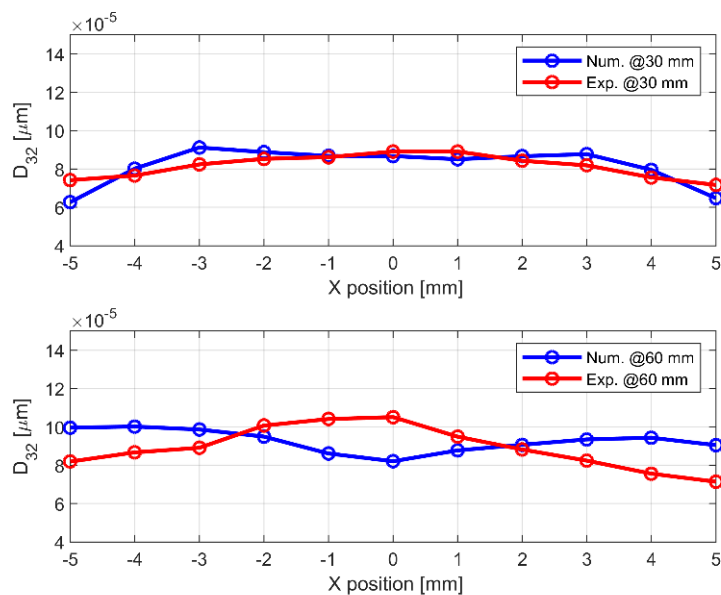


Figure 91. CFD vs Experimental  $d_{32}$  validation @30 mm and @60 mm (4 bar on the top, 8 bar on the bottom)

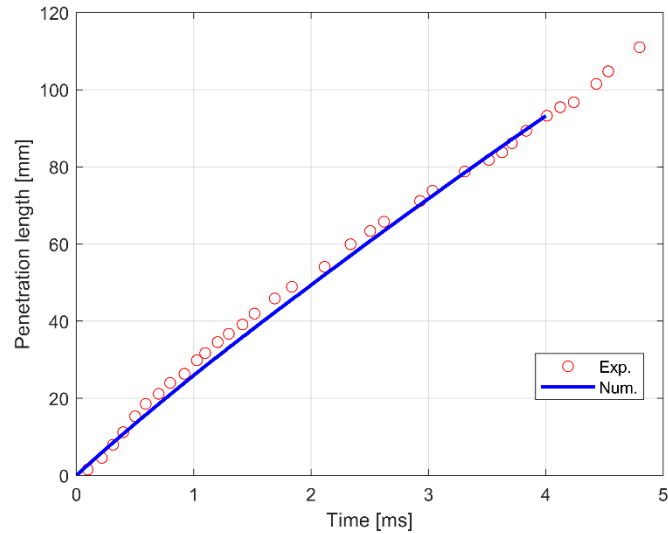


Figure 92. Spray penetration validation

Finally, Figure 92 depicts an excellent correlation for the spray penetration. The development of the spray inside the control volume is therefore ensured by a correct modelling of the speed and drag forces acting on the drops. This is a necessary feature in engine simulations to predict the position of the spray and its interaction with the walls of the intake duct.

### 7.3 Summary

In this chapter two experimental validations of water sprays for PWI applications have been performed. The first validation has been addressed starting from the experimental data collected and shown in Chapter 6, thanks to the use of the PDA technique. For both relative injection pressure tested, 4 and 8 bar, excellent results were obtained both in terms of particle size and speed distributions.

The second validation was conducted using data found in literature. The PWI injector was tested in a similar environment to the previous one, with injection pressure at 9 bar. This test highlighted the importance of the coalescence phenomenon, to correctly track the spray granulometry when the injector presents a large number of holes.

Overall, through the study of these two cases, it was possible to confirm the low attitude that the water droplets have in breaking, presenting  $We$  numbers well below 12.

Thanks to the results obtained, the spray models can be considered correctly calibrated and ready to be used in a complete engine simulation, where the phenomena related to the spray development have an important role for defining the water distribution inside the combustion chamber and the related effects.

# Chapter 8: GDI Engine Simulations under Non-Reacting Flow Conditions

Nowadays engineers aim to design engines with lower fuel consumption and emissions, in order to cope with the continuous updating of the international emission regulations. This has led to a review of the engine working conditions across the overall operating map and the adoption of different Auxiliary Emission Strategies (AES).

The boost pressure that characterize modern engines, necessary to ensure proper power levels, have increased the risk of engine knock, especially at medium/high load conditions. Currently, the main strategies adopted concern:

- fuel enrichment, with mixture index even of 0.75;
- ignition delay, reducing the Spark Advance well above TDC;
- fuel blends with higher knock resistance (RON).

The former exploits the evaporation of excess fuel to subtract latent vaporization heat from the air-fuel mixture by lowering the temperature. The main disadvantages are the additional fuel consumption and the increased pollutant emissions (CO in particular). The second, on the other hand aims to shift the combustion towards expansion by lowering the maximum temperatures in the cylinder. This, however, leads to a decline in torque and performance and an increase in exhaust gas temperature, putting the turbine components at risk.

Under the drive of the Europe Commission, engine working conditions are being pushed towards stoichiometric mixtures throughout the entire map to improve fuel economy, forcing new solutions for temperature limitations, such as the use of water injection. As already mentioned, the water injection can replace fuel enrichment not only to contain TiT (Turbine Inlet Temperature), but also to mitigate the onset of knock.

Up to now, more space has been given to the study of the water injection through PWI systems, also from an experimental point of view, because it is certainly the technology that today can be implemented in engines faster and with very low costs, comparable to those of PFI (Port Fuel Injection) systems. However, to have a wider view of the available technologies and their effects, both PWI and DWI configurations will be studied and compared numerically, applied on the same engine.

In this chapter the analysis will be carried out in a non-reacting environment without water injection, in order to assess the main working features of the baseline engine. The PWI and DWI systems and related methodologies will be presented in the next dedicated chapters with the objectives of verifying the possible advantages and disadvantages rising in the use of these two water architectures, leaving all the combustion analysis as the last examined topic.

After describing the main engine characteristics, with the aim of developing a reliable methodology for the study of the phenomena that characterize these type of simulations, the comparisons of the non-reacting fuel-only simulations with three different mixture strategies ( $\lambda$  0.75, 0.85 and 1.0) will be achieved in terms of charge motions, mixture distributions, evaporation rate, cooling temperature and cooling efficiency.

As for spray simulations, the numerical code used for this study is Avl-Fire v2020 (Chapter 4).

## 8.1 Engine Specifications

A high-bmep and high-power S.I. GDI turbo-charged engine has been virtually designed (Figure 93), which represents the reference system with three mixture strategies:  $\lambda$  0.75, 0.85 and 1.0. The  $\lambda$  0.75 and  $\lambda$  0.85 mixture strategies have been considered to lower cylinder temperature for TIT reduction and knock suppression. The fuel injector (Figure 94) is centrally located with a spray targeted to the spark plug for promoting combustion during cat-heating phase. The housing for the DWI injector in the combustion chamber has already been installed on the intake side, whose set-up will be presented in detail in Chapter 10.

In addition, a careful design of the intake duct has been carried out, both in terms of size and bend, in order to promote the formation of an intense in-cylinder Tumble motion.

The injector characteristics have been resumed in Table 16 and the fuel injection profile in Figure 95. Table 17 lists the main characteristics of the virtual high-bmep engine and in Table 18 are reported the operating condition examined. Further design variations such as compression ratio and S/B ratio have been tested with water configurations and they will be described in PWI Chapter 9 and DWI Chapter 10.

The operating point here simulated, maximum power (at very high bmep), represents the most demanding in term of mass and time available for injection and evaporation, where a careful evaluation of the water injection characteristics and optimization are required more than for other conditions.

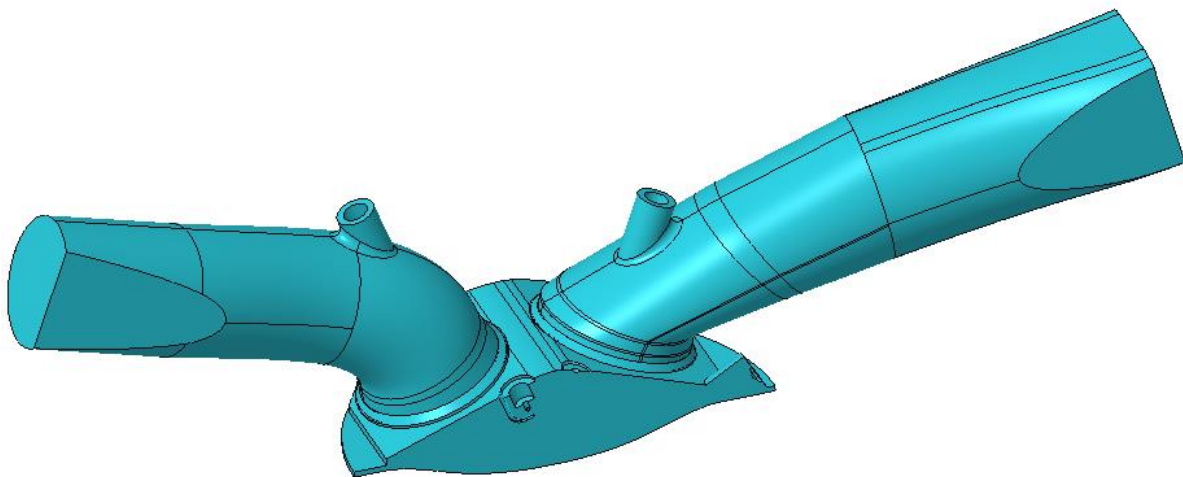


Figure 93. Virtual engine configuration

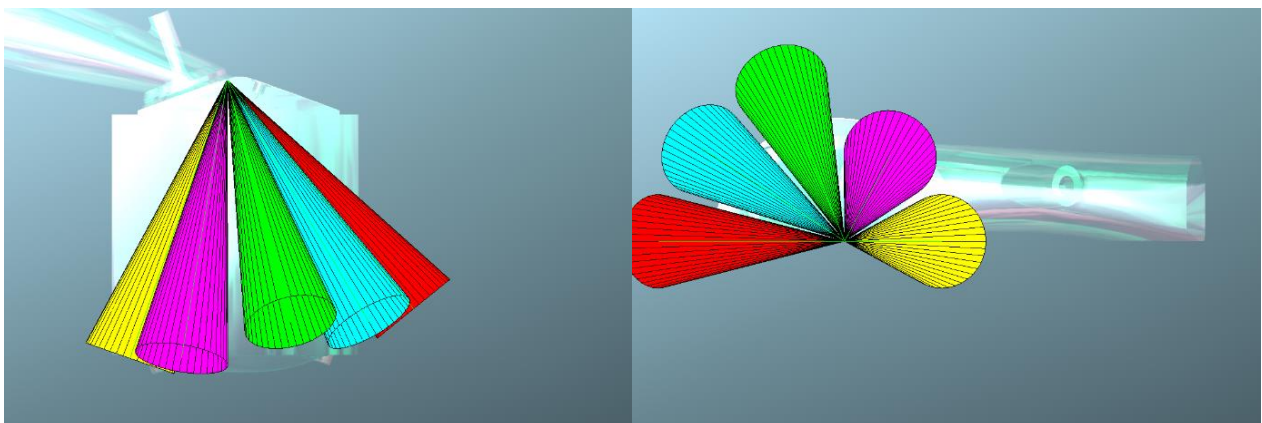


Figure 94. Fuel Spray layout

Table 16. GDI fuel injector features

	<b>GDI</b>
<b>Number of holes [-]</b>	8.0
<b>Injection pressure [bar]</b>	350.0
<b>Injection temperature [K]</b>	313.0
<b>HFR [cm<sup>3</sup>/s]</b>	20.0
<b>Hole geometric diameter [μm]</b>	188.0

Table 17. Engine features

<b>Unit Displacement [cm<sup>3</sup>]</b>	471.05
<b>Stroke S [mm]</b>	85.00
<b>Bore D [mm]</b>	84.00
<b>Conrod length [mm]</b>	165.60
<b>Number of valves</b>	4.00
<b>S/B [-]</b>	1.01
<b>Intake D<sub>v</sub>/D [-]</b>	0.36
<b>Exhaust D<sub>v</sub>/D [-]</b>	0.33
<b>Compression ratios</b>	9.50:1.00
<b>Squish Height [mm]</b>	1.10

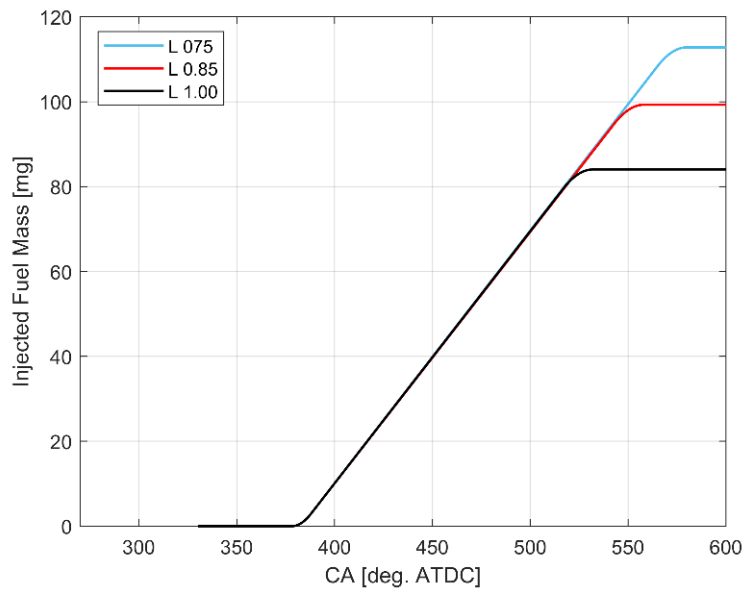


Figure 95. Fuel injection profiles

Table 18. Engine working conditions

<b>Engine speed [rpm]</b>	7000.0
<b>Engine load</b>	100.0%
<b>Mixture index (w/o water) [-]</b>	1.0
<b>Boost pressure [bar]</b>	2.7
<b>Max BMEP [bar]</b>	26.6
<b>Inlet valve opening [CA deg. ATDC] @0.2 mm</b>	362.0
<b>Inlet valve closing [CA deg. ATDC] @0.2 mm</b>	598.0
<b>Exhaust valve opening [CA deg. ATDC] @0.2 mm</b>	136.0
<b>Exhaust valve closing [CA deg. ATDC] @0.2 mm</b>	376.0

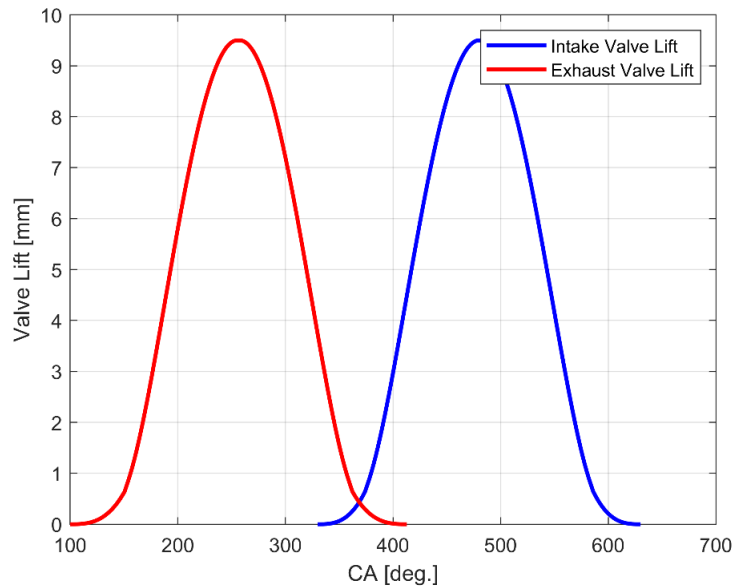


Figure 96. Inlet and exhaust valve lifts

## 8.2 Simulation Set-Up

In order to limit the computational time, the symmetry of the engine was exploited, keeping only half of the engine as a fluid-dynamic volume. The discretization was performed through hexahedral cells by carrying out appropriate local refinements, to obtain an adequate accuracy of the geometry representation and to better capture all the main phenomena that characterize this type of simulations (Figure 97). A smaller cell size was used in the valve curtain areas and in the lateral squish areas, both of which are fundamental for a correct representation of the charge motions inside the combustion chamber and for the evaluation of the trapped air. The total number of cells at the TDC is approximately 500,000.

The size of the grid close to the spray jets is designed to satisfy the hypothesis on which the Lagrangian model is based for the representation of the parcels: for this modelling it is always essential to guarantee a dispersed liquid phase inside the cell, i.e. a volumetric fraction occupied by the fluid lower than 10%. Interpolation of velocity and mass fraction at parcel location is used to alleviate grid dependency errors in Lagrangian spray simulations.

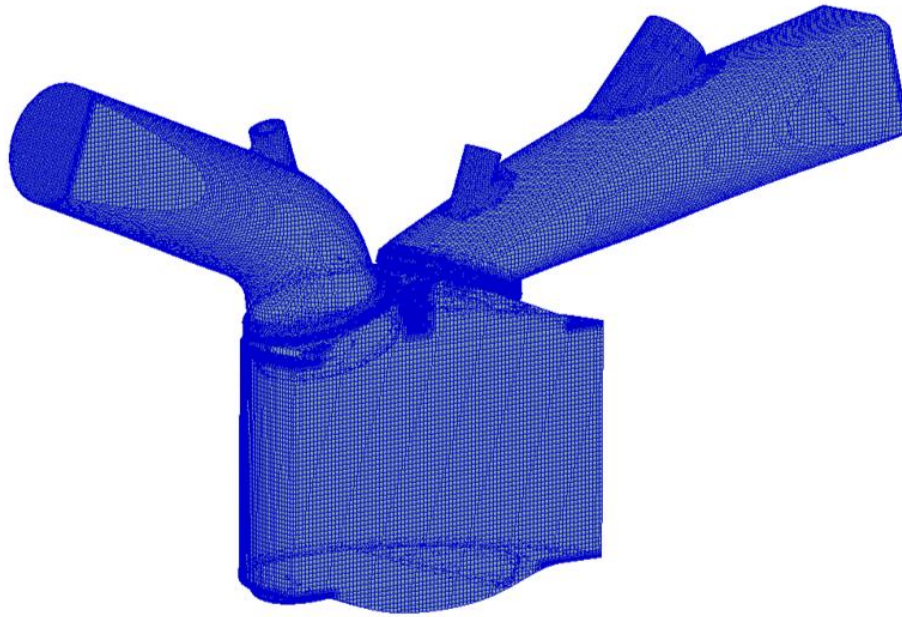


Figure 97. Engine spatial discretization

Table 19. Simulation duration and model adopted

<b>Start angle</b>	330 CA deg. ATDC
<b>End angle</b>	720 CA deg. ATDC
<b>Turbulence model</b>	K-z-f
<b>Wall heat model</b>	Hybrid wall treatment
<b>Law of the wall</b>	Standard + Han-Reitz
<b>Evaporation model</b>	Spalding
<b>Wallfilm evaporation model</b>	Combined
<b>Wallfilm entrainment model</b>	Schadel - Hanratty
<b>Wallfilm splashing model</b>	Kuhnke
<b>Atomization model</b>	Proprietary models
<b>Breakup model</b>	

The engine cycles examined here were first carried to convergence in terms of pressure fields, temperature and trapped mass through the multicycle methodology [137], which involves simulating a certain number of engine cycles, usually between 3 and 5, in order to stabilize the pressure oscillations that occur in the intake and exhaust ducts and the trapped mass (fuel, air, EGR and water). In this way it is also possible to eliminate the uncertainty error of the initial conditions, mainly dictated by the homogeneity of the imposed fields. The boundary conditions were obtained through a 1D calculations with OpenWam and the injected fuel is represented in 3D simulations with a multicomponent approach, whose mixture is formed by iso-octane (23%), n-decane (21.5%), n-octane (28.8%), n-hexane (17.4%) and ethanol (9.3%).

Differencing schemes are second order for mass, momentum and energy, while turbulence is resolved with a second order blended scheme. The solution is converged when the residual error for each equation is below the tolerance threshold of  $1e-4$ . The simulations are stopped once TDC is reached because no interest is given in the expansion phase in a non-reacting case.

Finally, to conclude the main simulation set-up, the models adopted for charge motion characterization, turbulence generation, heat exchange, atomization and break-up of the spray and spray-wall interaction are shown in Table 19, whose details have been reported in Chapter 4

### 8.3 Simulations results without Water Injection

First of all, simulations were carried out without water injection with three different mixture indices:  $\lambda$  0.75, 0.85 and 1.0 in order to provide references cases. The first two ones represent typical cases used in current engine maps to lower the temperatures in the combustion chamber, with the already known benefits in terms of TiT and likelihood of knock. These preliminary simulations are necessary to establish the baseline against which cases with water injection can be compared. The stoichiometric mixture case is run since it is the operating conditions which will be enforced by regulation and EU assessment policy in the near future. The same trapped air mass has been ensured in all the three simulations as shown in Figure 98 in order to provide a fair comparison in the next. Some preliminary analysis of the considered engine fluid dynamics features in the three cases are now presented.

As showed in Figure 99, the engine has been designed with an intake port capable to provide a very high tumble ratio (TR), 2.3 at IVC (598 CA deg.), in order support the high bmep target. Figure 100 shows the evolution of the intake flow on a plane passing through the intake valve and port with emphasis on the tumble formation. The position of the main tumble vortex generated in the combustion chamber and its evolution inside the cylinder are such that at IVC an high-angular momentum and large-mean flow structure is formed and well bounded within the cylinder. Those features determine the high level of turbulence recorded close to TDC thanks to high efficiency of the tumble breakdown. As far as the generation of the other two in-cylinder flow motions are concerned, omega swirl (it must be noted that omega swirl rely only on half part of the combustion chamber because of symmetry flow conditions) and cross tumble, their effects are minimal: the interaction of the air motion with the piston does not involve a significant formation of secondary motions inside the cylinder (Figure 101 -Figure 102).

The charge motion and the following turbulence generation are very important parameters to analyse and optimize before combustion also in the view to use a diluent like the water, that is expected to slow the flame speed. The flame propagation speed is strongly influenced by the mixture index, turbulence and the presence of diluents such as EGR or water. In particular, if they are analysed near the spark plug, they can be used to estimate the early flame speed during the phase from ignition crank angle to the angle when the 10% of the mixture burns (MFB10). For these reasons, a more detailed focus is placed on these three quantities: turbulence, mixture distribution and EGR.

As far as the turbulence is concerned, it is plotted in Figure 103 as turbulent intensity ( $u'/v_p$ ):

$$T = \frac{u'}{v_p} = \frac{\sqrt{\frac{2}{3}k}}{v_p} \quad (106)$$

where  $u'$  is the turbulent velocity and  $v_p$  is the averaged piston speed. The turbulence is described here through the definition of turbulent intensity  $T$ , being a parameter of engineering interest linking the turbulence to engine speed. Even in this case, the variations between the three mixtures are minimal, especially between 690 CA deg. and 710 CA deg. (possible angular range for spark ignition).

It is important to note that at the end of the compression phase the turbulence intensity  $T$  can exceed 1. This indicates that the average turbulence level generated in the cylinder is very high. Moreover, the average  $T$  value in the cylinder tends to remain high up to the TDC, indicating an excellent propensity of the system to

keep the flame front accelerated during combustion. This is certainly an important aspect to exploit and ensure even during water injection to counterbalance the negative effects of water on combustion speed.

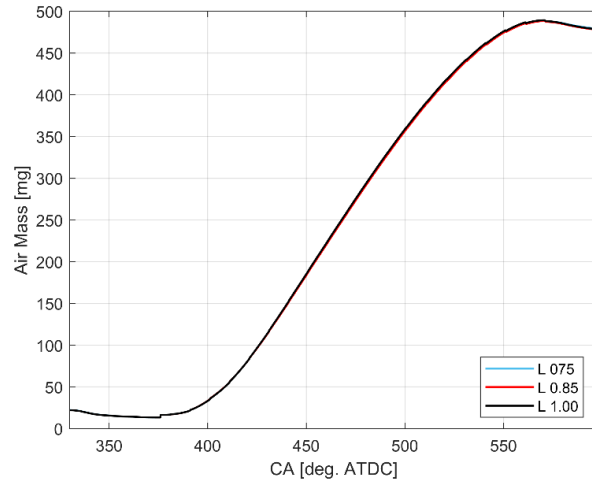


Figure 98. Cylinder air mass evolution (half geometry)

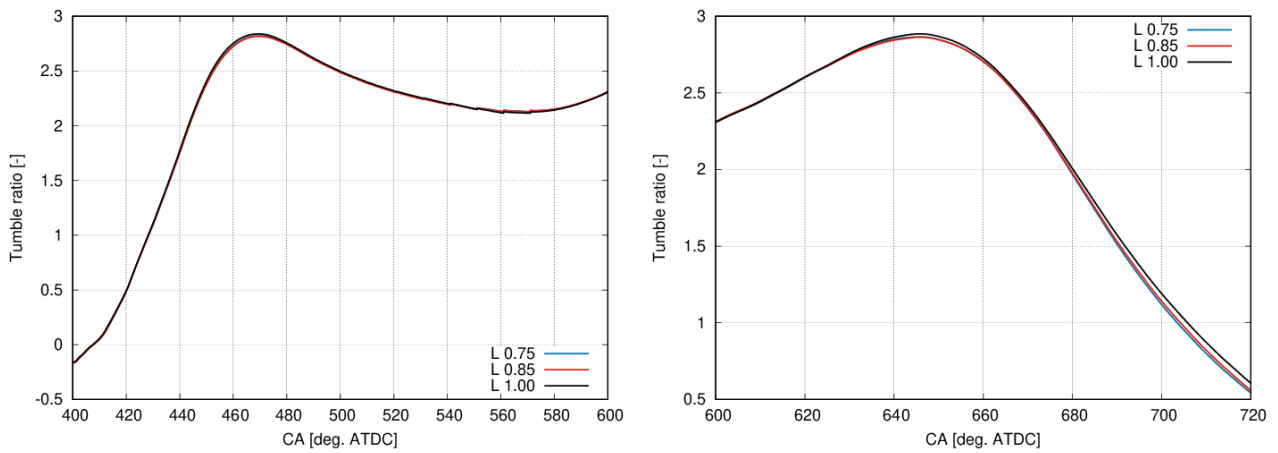


Figure 99. In-cylinder Tumble ratio: intake stroke (left), compression stroke (right)

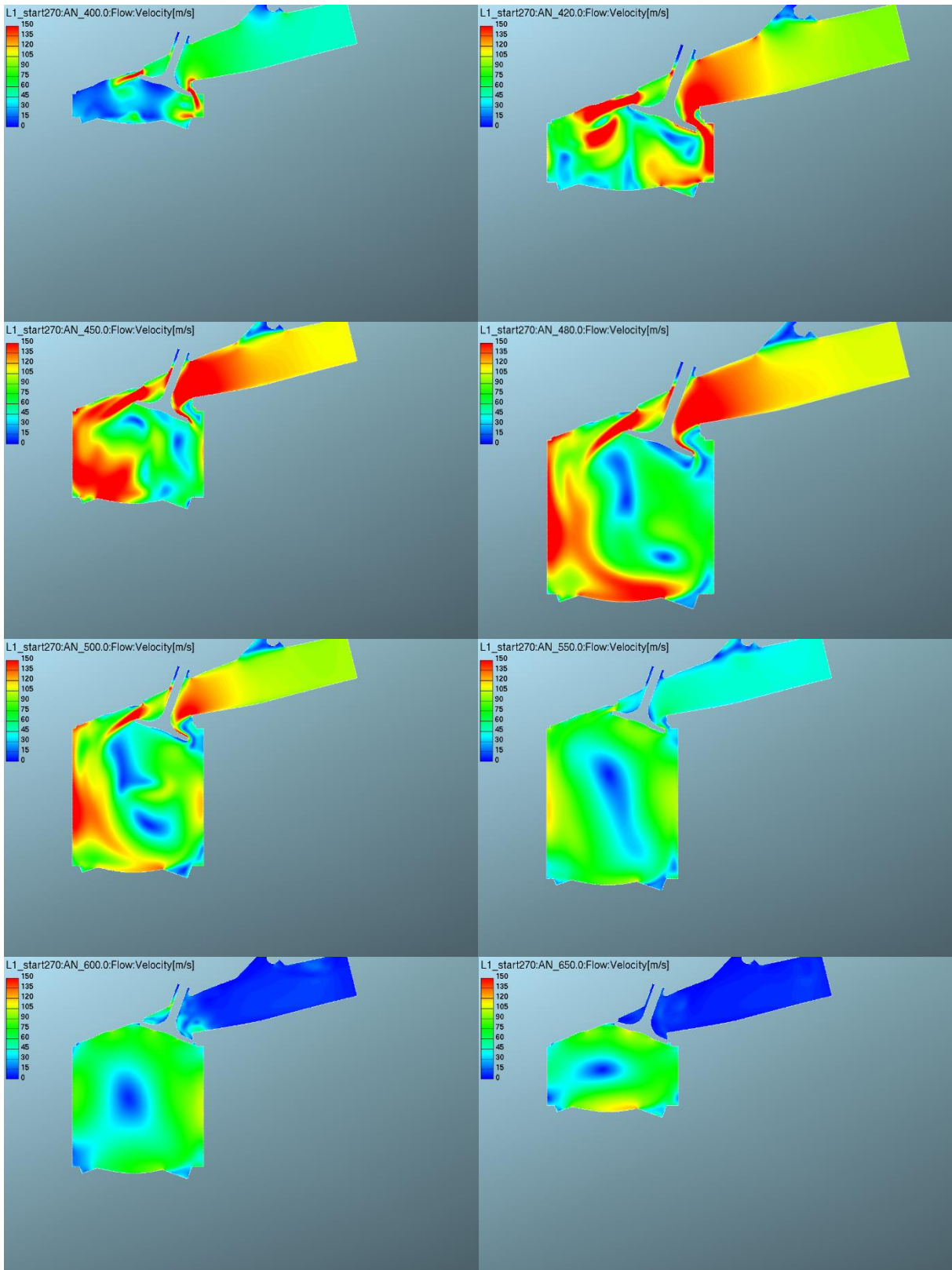


Figure 100. Tumble vortex formation

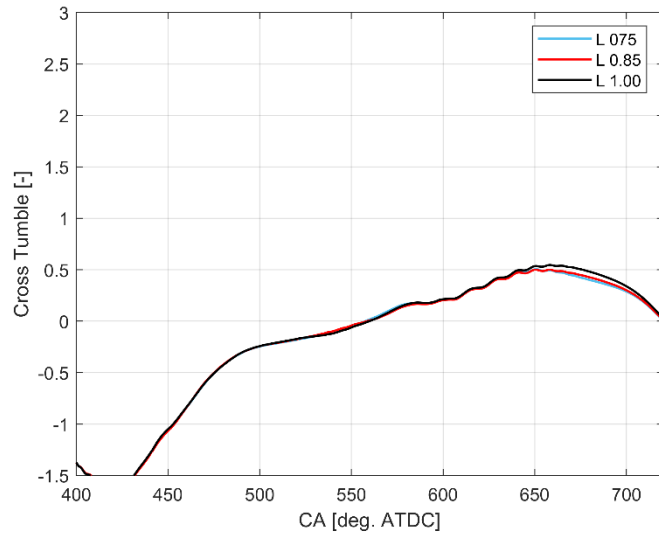


Figure 101. In-cylinder cross Tumble

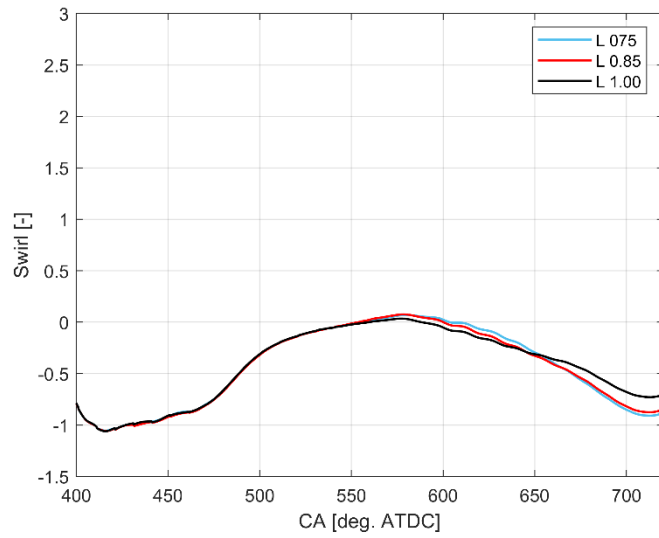


Figure 102. In-cylinder swirl

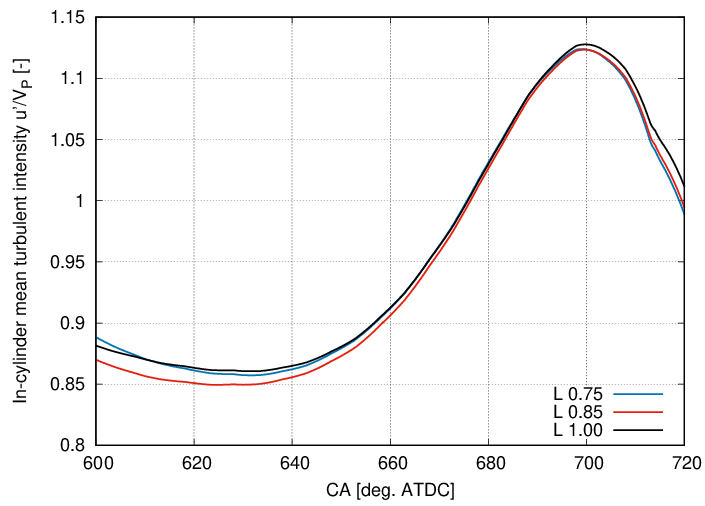


Figure 103. Turbulent intensity during the compression stroke

For an even more detailed analysis of the first combustion phase, just after ignition, it is necessary to explore the generation of turbulence near the spark plug. As example, Figure 104 shows the turbulence intensity for the stoichiometric case ( $\lambda = 1.0$ ), at 710 CA deg., highlighting a very large area with high turbulence values, ensuring an excellent corrugation of the flame front and a higher combustion speed. From this image it can also be deduced that, under the same mixture conditions, the flame could be initially pushed under the inlet valve rather than the exhaust valve. It will be interesting to check, during combustion simulations, whether this leads to auto-ignition events just under the exhaust valve, due to a non-optimal flame front propagation.

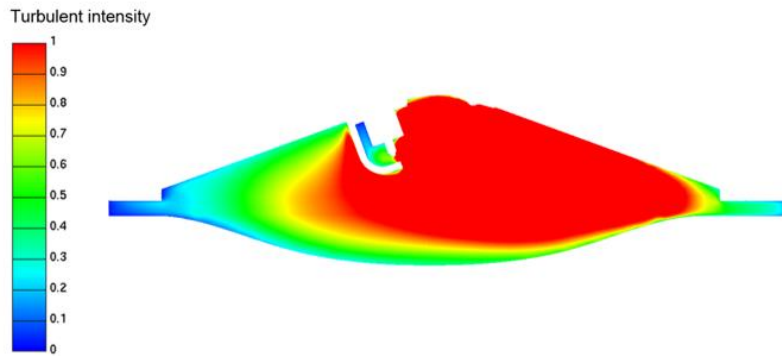


Figure 104. Turbulent intensity distribution at 710 CA deg.,  $\lambda = 1.0$

In Figure 105 the mean in-cylinder mixture index trends versus different crank angle (representing potential spark ignition crank angles) have been reported, while in Figure 106 the standard deviation for the same trends under the hypothesis of Gaussian distribution are visible. Standard deviation (STD) is an important parameter that allows to provide indication how large can be the cycle to cycle variation because of the mixture spatial distribution. It is to note that there is a good distribution of the mixture index in the overall cylinder and the standard deviation reduces moving toward TDC. The average lambda value in the cylinder remains constant in all three cases after 680 CA deg., meaning that no further fuel evaporation occurs. The same trends but close to the spark plug location, in a volume inside an ideal sphere centered in the nominal spark plug point with a radius of 10 mm, have been reported in Figure 107 -Figure 108. The STD of the mixture index distribution is lower close to spark plug than that computed in the overall combustion chamber. The mixture index values are close to the target for all cases, but from 690 CA deg. ATDC they tend to be slightly richer. The local value of lambda close to spark plug influences the laminar flame speed at combustion start, while its distribution, for a fixed operating condition, may alter the flame propagation sweeping the different spark advances.

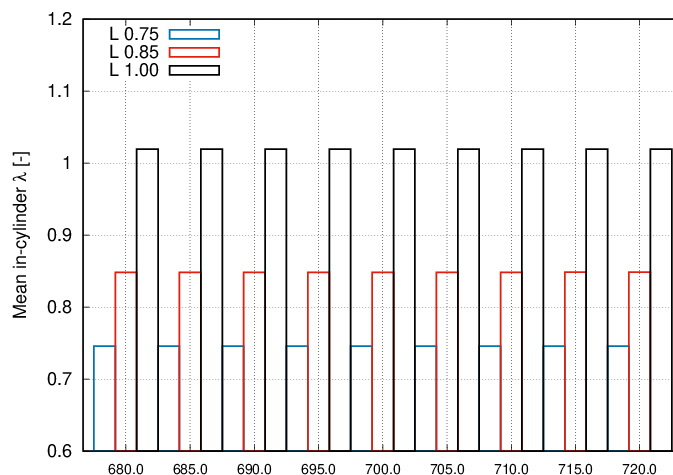


Figure 105. Mean In-Cylinder mixture distribution close to TDC

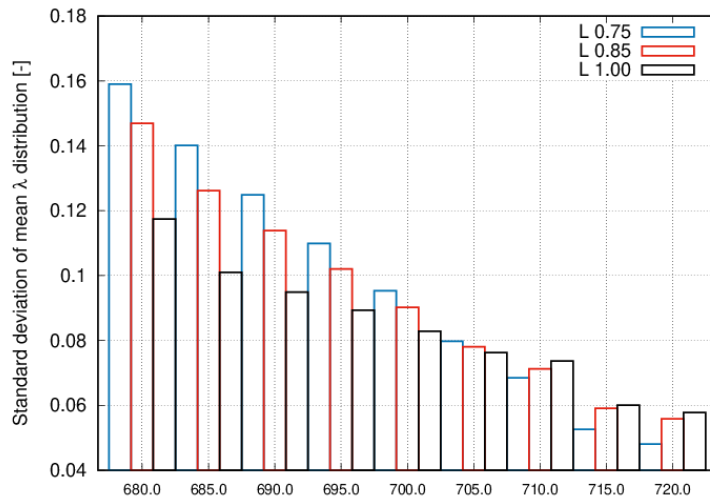


Figure 106. In-Cylinder mixture standard deviation close to TDC

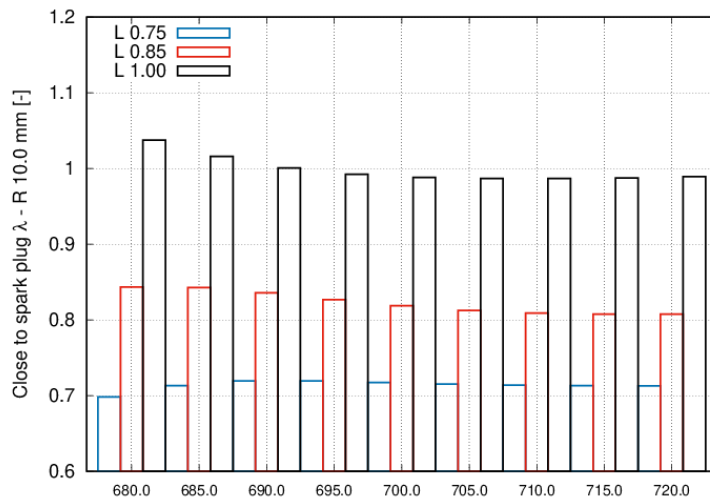


Figure 107. Mixture index distribution under spark plug (sphere radius 10 mm) close to TDC

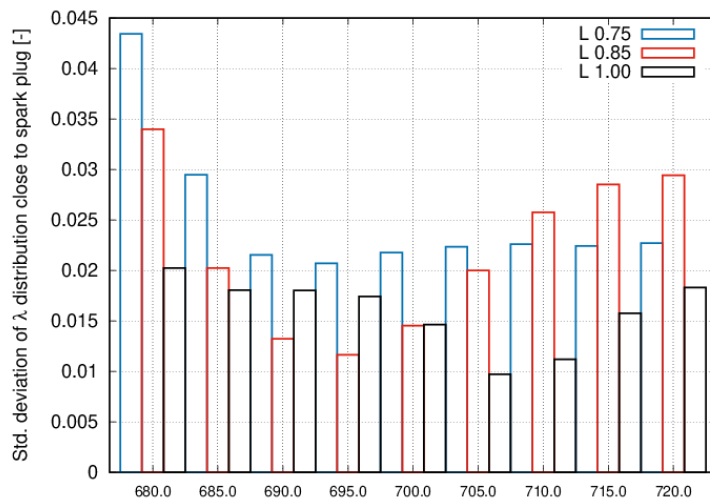


Figure 108. Mixture index standard deviation under spark plug (sphere radius 10 mm) close to TDC

It is important to remember that, as previously mentioned, the mixture index standard deviation can be an indicator of the mixture cycle repeatability, and therefore of the knock likelihood or performance variations for very different local mixture values. Engine multi-cycle simulations involving a RANS turbulence modelling approach, as in this case, do not, by their nature, simulate the cyclic variability, being the turbulence quantities averaged over time. Only through an LES approach it would be possible to assess the cyclic variability of an engine in a right way, but with a computational resource effort still far from industrial applicability. Despite the fact that a RANS CFD simulation can not return direct information on the cycle to cycle variation, it may provide a qualitative indication of it, since the cycle to cycle variation of a given parameter will be likely linked to the its spatial variation.

In Figure 109 are also showed the three-dimensional fuel distributions (equivalence ratio) of the mixture indexes analysed, at 710 CA deg.. The  $\lambda$  0.75 case presents locally richer areas under spark plug and in peripheral zones, therefore the combustion speeds might be slowed down and shifted towards expansion once reached these areas. This could lead to exhaust gases with higher average temperatures at EVO, partly mitigating the cooling benefit of fuel evaporation.

It is very important since now to highlight that the exhaust gases temperature comes from the balance between the mixture temperature at compression stroke end (which may be affected by cooling strategy adopted like fuel enrichment, water injection or water expanded cycle) and the combustion duration which is in general slowed down by cooling strategies.

As last comment on fuel distribution, the same squish zone, on the exhaust side near the symmetry boundary, seems to be common in all cases for fuel accumulation, probably due to the same charge motion in the cylinder that drags the fuel in that zone.

The engine operating point used for this study, high load and speed, is characterized by a low exhaust gas residual mass (EGR) in the cylinder at IVC (Figure 110): 4.2% for the  $\lambda$  0.75 case and 5.1% for the  $\lambda$  0.85 and  $\lambda$  1.0 cases. The differences are slightly amplified if it is considered the remaining EGR percentage under spark plug at 710 CA deg.: about 3.8 % ( $\lambda$  0.75), 4.7 % ( $\lambda$  0.85) and 5.0 % ( $\lambda$  1.0). Even if the richest mixture case has a slightly lower EGR mass fraction under the spark plug, this will not be the determining factor for a faster flame development, as will be shown in the combustion simulations.

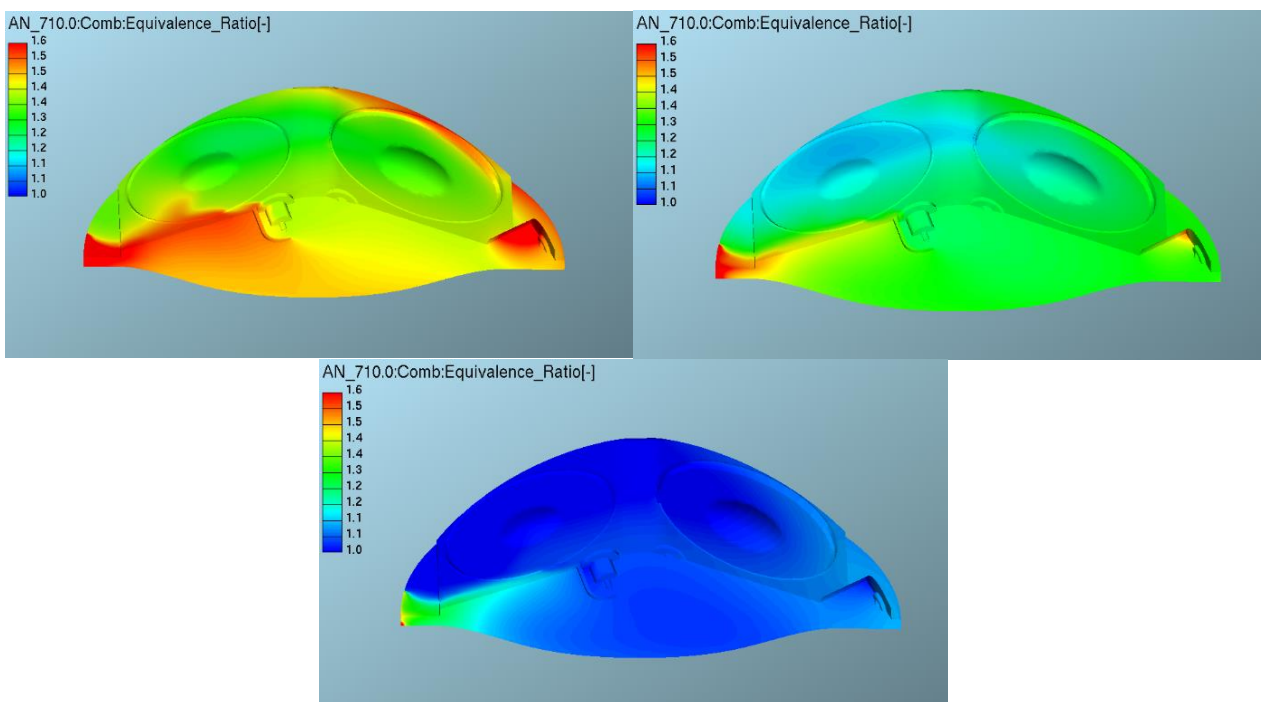


Figure 109. Equivalence ration distribution @710 CA deg.,  $\lambda$  0.75 (top left),  $\lambda$  0.85 (top right),  $\lambda$  1.0 (bottom)

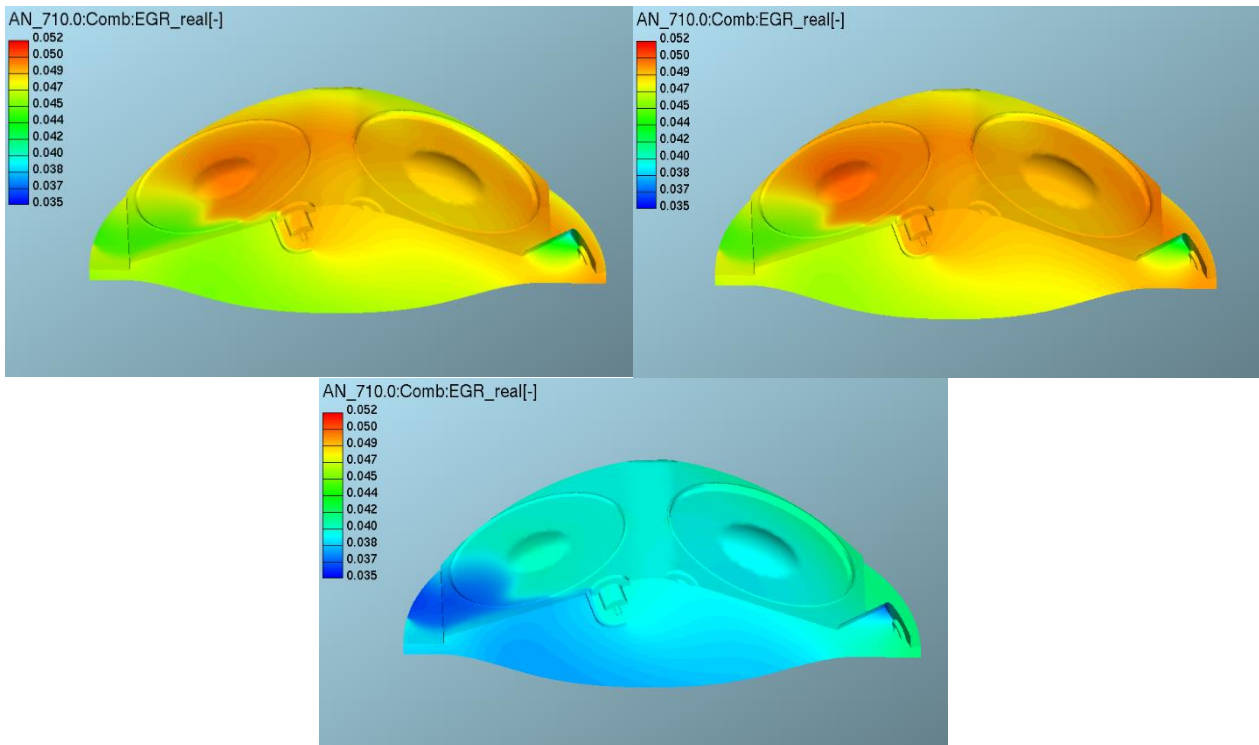


Figure 110. EGR distribution @710 CA deg.,  $\lambda$  0.75 (top left),  $\lambda$  0.85 (top right),  $\lambda$  1.0 (bottom)

Thanks to the optimized spray orientation, the wallfilm formation has been minimized, especially in the peripheral areas of the combustion chamber, where contamination of the oil may occur through the movement of the piston. Moreover, the high average cylinder and boundary temperatures, even higher than Leidenfrost's temperature for the piston, makes the residual wallfilm generated by the impact of the drops on the walls negligible, as showed in Figure 111. The pictures in Figure 114 show the dynamic of the GDI spray. Despite the great impact of the droplets on the piston near the TDC, no wallfilm formation takes place: the droplets rebound on the walls exchanging heat, and then transported by the Tumble motion created inside the cylinder. This will not only help the further drops breakup but also their distribution and evaporation inside the chamber.

Despite the stoichiometric case shows a greater evaporation rate in the first phase, it does not reach the 100% (Figure 112): some drops, formed by the less volatile components (such as n-decane) remain in the liquid state. However, these will tend to evaporate as soon as the ignition occurs due to temperature increase, without creating diffusive flames. The excess fuel strategies ( $\lambda$  0.75 and 0.85) achieve lower evaporation rates: not all the fuel is able to find the optimal thermodynamic conditions to evaporate, both for lower average temperatures in the cylinder and for the presence of local high-rich vapour fuel areas, whose liquid to gas transition tends to be inhibited for saturation reasons.

Despite the higher evaporation rate for the  $\lambda$  1.0 case, overall, the higher mass quantity of evaporated fuel for the other two mixture strategies leads to higher cooling. One of the main important difference can be seen in the average temperature profiles inside the cylinder (Figure 113), especially close to the TDC, where, thanks to the fuel evaporation, the richest mixture experiences a lower temperature of about 30 K compared to the stoichiometric case. Such temperature reduction is to be considered significant, able to preserve the turbine and/or to limit abnormal combustions.

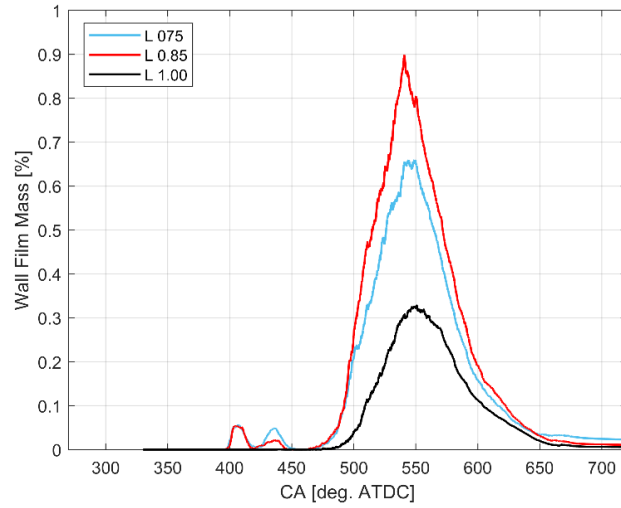


Figure 111. Wallfilm generation: percentage w.r.t the total fuel mass injected

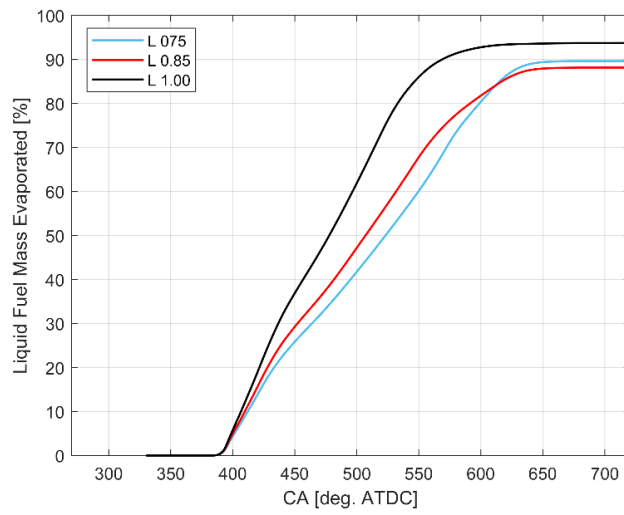


Figure 112. Fuel evaporation rate

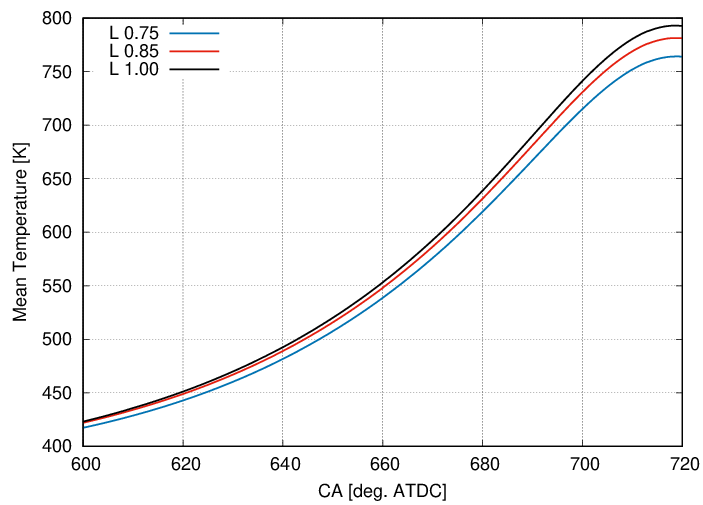


Figure 113. Mean In-cylinder temperature

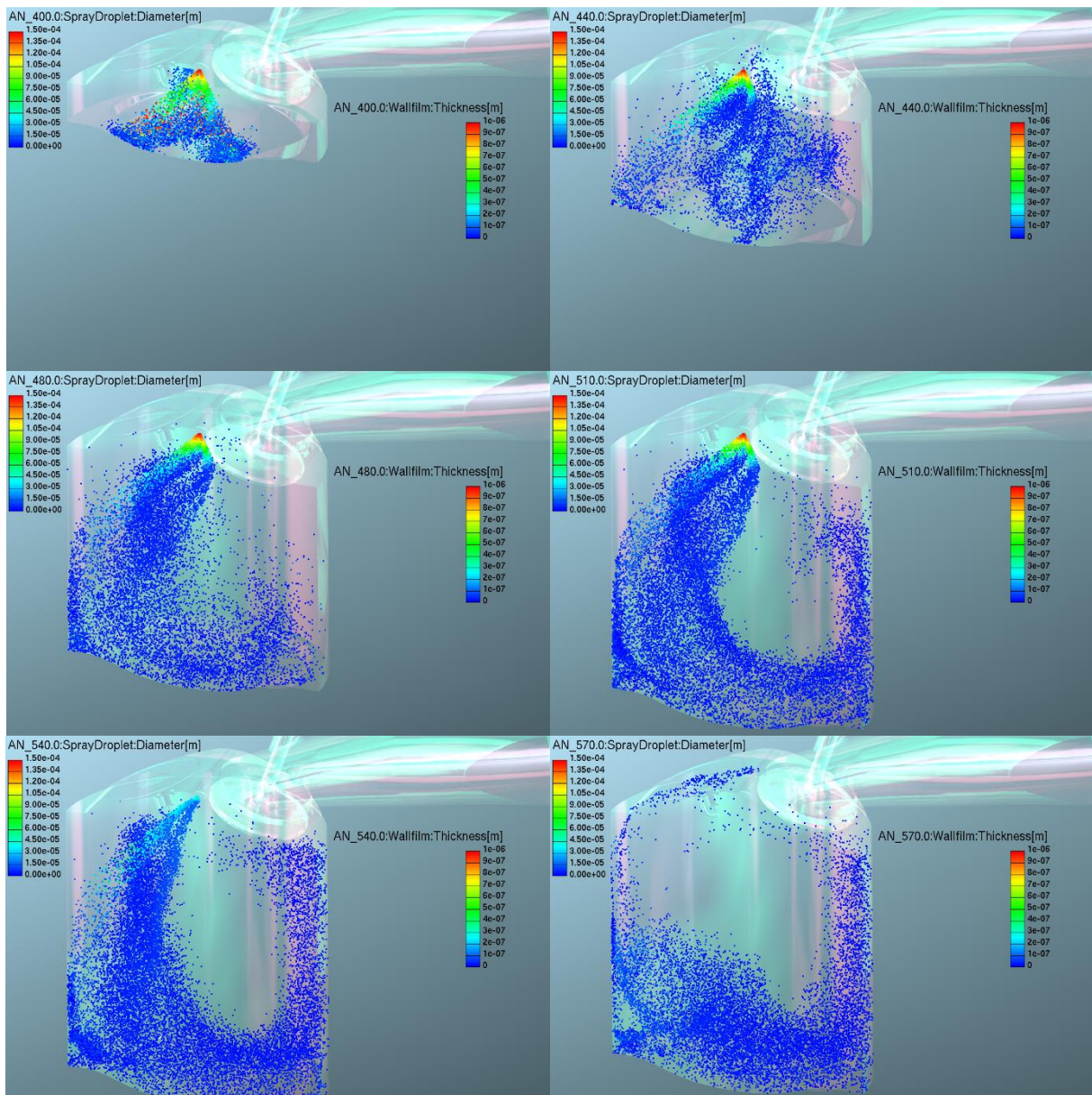


Figure 114. GDI Spray evolution

## 8.4 Summary

Through these preliminary simulations in non-reactive environment, it was possible to analyse the engine in its baseline configuration without water injection, highlighting its main characteristics in terms of mixture distribution, turbulence and mean in-cylinder temperature. This study was also essential to verify the design of the engine from a fluid-dynamic point of view and the appropriate fuel injection strategy, which would allow to consider this engine a solid starting point on which to develop the water modelling.

The analysis has highlighted the engine's excellent attitudes to turbulence generation. The intake duct, combined with the piston design, allowed to create a rather intense Tumble motion inside the combustion chamber, with an excellent breaking phase during the compression stroke. This system is therefore highly optimized under these conditions. Nevertheless, the change of some geometrical parameters could lead to a reduction or increase in this performance, as described in the following chapters.

Finally, a sufficiently homogeneous mixture distribution appears for all three strategies, especially under the ignition zone near the angles of interest for the SA. This has been made possible thanks to a careful initial phase aimed at choosing all the main parameters for the definition of the spray characteristics. In the following chapters more emphasis will be placed on the cooling effect caused by water evaporation for the different non-reacting set-ups examined, and the effects that the introduction of water can produce on the charge motion and on the mixture distribution.

# Chapter 9: Port Water Injection Simulations under Non-Reacting Flow Conditions

In this chapter the results of the water simulations performed on the previously described engine will be presented, adapted for PWI configuration.

The aim is to delineate different strategies of indirect water injection, comparing the data with those of the reference only-fuel cases from the fluid dynamic and cooling point of view. The possibility of replacing fuel enrichment with water injection is certainly one of the drivers of this study, with possible undoubted advantages in fuel consumption and fulfilment with EU AES assessment policies with particular reference to CO emissions at full power in RDE test cycle.

For this reason, the PWI simulations will be conducted under stoichiometric mixture and the results compared with the two enrichment strategies investigated in the previous chapter,  $\lambda$  0.75 and  $\lambda$  0.85.

Furthermore, two important issues have been deeply analysed and have outlined the methodology for PWI simulations:

1. looking for a PWI strategy able to replace the cooling obtained with  $\lambda$  0.75 mixture (cooling target imposed);
2. ensuring that at least 90% of the injected water mass would evaporate before TDC, limiting the formation of wallfilm and oil contamination problems. This target has never outlined in the review of the state of art: on the author's opinion is indeed one of the key points for the success of water injections since the evaporation efficiency affects water consumption. The latter, in turn, affects water tank volume and water refilling frequency.

## 9.1 Port Water Injection Features and Configurations tested

The PWI injectors, one for each intake valve, have been brought as close as possible to the cylinder and positioned at 80 mm from the combustion chamber (Figure 115). It was decided not to simulate PWI in a 'quasi-direct' layout installation in order to have a clearer view of the differences between a purely PWI and DWI technology. The spray targeting has been realized in order to orient the drops towards the inlet valve minimizing the generation of wallfilm on all the main components: valve stem, valve seat and intake port walls (Figure 116). Table 20 shows the GDI and PWI injector main features.

The plume theoretical direction, visible in Figure 116, targets the water spray droplets towards the intake valve. This has been designed to prevent the spray plumes from impacting too much on the upper part of the intake duct during valve opening, due to the air transport. The water droplets are strongly transported by the air stream into the intake duct and tend to pass through the curtain area on the exhaust side (Figure 117).

Table 20. GDI and PWI injector features

	GDI	PWI
Number of holes [-]	8.0	2.0
Injection pressure [bar]	350.0	10.0/20.0
Injection temperature [K]	313.0	313.0
HFR [cm <sup>3</sup> /s]	20.0	17.0
Hole geometric diameter [μm]	188.0	140.0

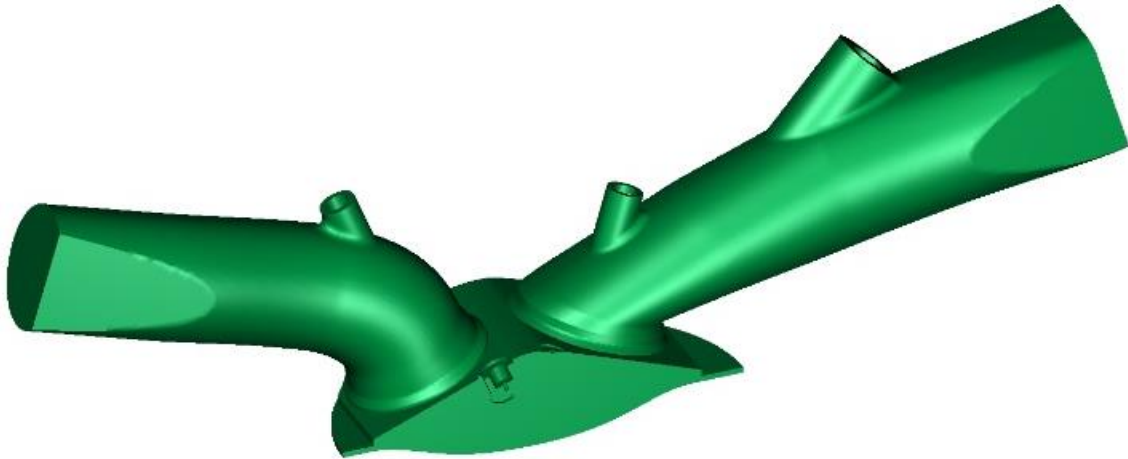


Figure 115. Virtual engine PWI configuration

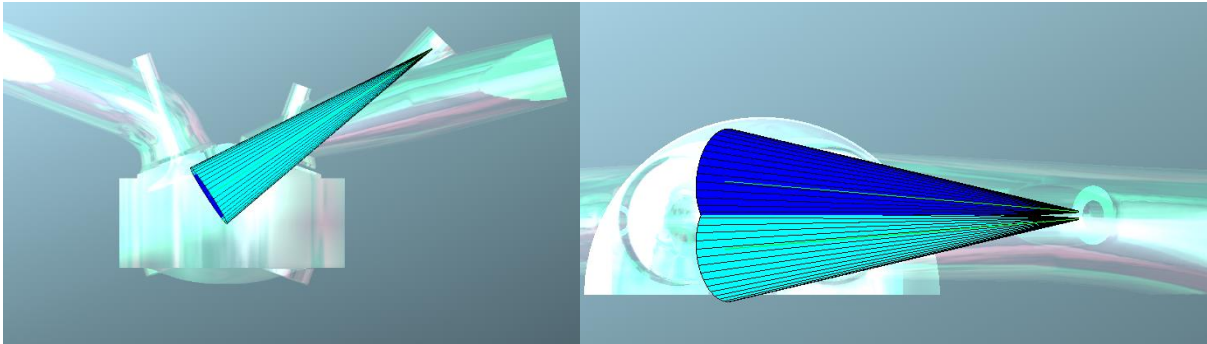


Figure 116. PWI Spray targeting

Table 21 lists the analysed cases related to the indirect water injection (PWI), divided according to the  $s$  parameter, timing and injection pressure. The  $s$  parameter is defined as:

$$s = \frac{m_{water}}{m_{fuel,s}} \quad (107)$$

where  $m_{water}$  is the injected water mass and  $m_{fuel,s}$  is the injected fuel mass in stoichiometric condition. The (relative) injection pressure ranging between 10 and 20 bar is due to two main reasons:

1. 10 bar is a level of technology widely tested and used in UREA injection systems, which can also be reused for PWI injections, keeping installation costs low;
2. increasing the pressure up to 20 bar may become interesting in order to study the effects of a lower granulometry of the water drops and their evaporation and distribution within the mixture, as well

as on the formation of liquid film on the walls. If there was a real advantage in using higher injection pressures, its cost-benefit ratio could be re-evaluated.

As far as the injection timing is concerned, it was chosen on the basis of preliminary simulations for the evaluation of the average time taken by all drops to enter inside the cylinder.

Indeed, it is important to promote the evaporation of the droplets inside the cylinder (at least 90%), maximizing the thermodynamic cooling effect. For this reason, the SOI and EOI were chosen to favour the entry of water into the cylinder still in the liquid phase before IVC (598 CA deg.). Otherwise, part of the cooling power would be lost in lowering the temperature of the intake duct walls and of the fresh air. Therefore, once the mass to be injected, the injection pressure and the need to inject all drops into the cylinder before IVC are defined, the flexibility in the choice of injection timing is greatly reduced.

Finally, Table 22 lists the fuel and water mass injected according to the cases examined. As mentioned previously, to fulfil the future international emission regulations about fuel consumption and environmental impact, the fuel will be injected under stoichiometric conditions ( $\lambda$  1.0).

The grid generation remained the same as described in the previous chapter for the pure GDI case. However, a refinement along the PWI hole axis was used, consistent with the refinement used during the water spray validation campaign (Chapters 7).

Thanks to the calibration of the break-up and interaction parameters of the water spray models, found during the validation test, it was possible to improve the PWI spray simulation setting and, thus, the result accuracy.

The analysis has been globally sorted into several sub-paragraphs, concerning:

1. *mixture quality analysis* close to spark ignition time, to assess how water addition modifies the composition of the fresh mixture especially under the spark plug;
2. *fluid-dynamics analysis*: study of the interaction between the water jet spray and the main in-cylinder motions. In this sub-paragraph the effects of the water spray on the tumble motion formation and on the final level of turbulence close to spark plug at ignition time have been reported;
3. *thermodynamic analysis*: temperature at TDC and cooling efficiency. In this sub-paragraph it has been carried out a detailed analysis of the evaporation process and the cooling efficiencies.

Table 21. PWI system: analysed cases

Parameter s [-]	SOI / EOI [CA deg. ATDC]	Injection pressure [bar]
<b>0.20</b>	293.00 / 390.00	10.00
	363.00 / 460.00	
<b>0.30</b>	293.00 / 433.00	
	320.00 / 460.00	
<b>0.40</b>	277.00 / 460.00	
<b>0.20</b>	318.00 / 390.00	
	393.00 / 465.00	
	413.00 / 485.00	
	433.00 / 505.00	

Table 22. PWI system: fuel and water mass injected

Case ( $\lambda$ 1.00)	Parameter s [-]	Fuel/Water injected mass [mg]
Fuel-only	-	84.00
Water-added	0.20	16.80
	0.30	25.20
	0.40	33.60

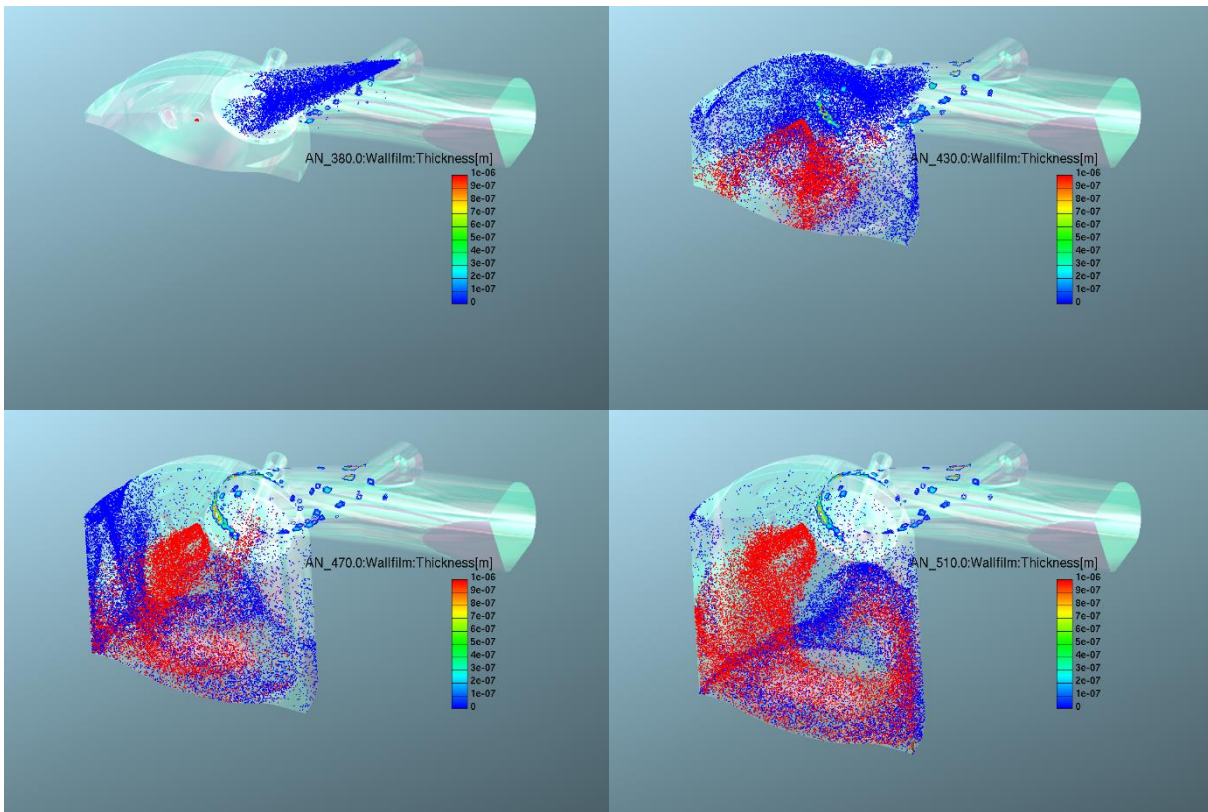


Figure 117. PWI droplets passing through the intake valve curtain area on the exhaust side

## 9.2 Simulation Results for PWI 10 bar Strategies

### 9.2.1 Mixture Quality Effects

In this section, for the non-reacting engine flow analysis, the mixture conditions and the dilution effects under the spark plug due to the presence of water are examined, leaving the chemical effects on combustion process in Chapter 11.

The in-cylinder mixture standard deviation (STD) (Figure 118), which can be used as an indicator of the cycle to cycle variability, shows a constant decrease in the range from 680 CA deg. to 720 CA deg., and the values are globally low. For more delayed starting injection angle (SOI) the STD is lower in the most interesting range for ignition timing (from 695 CA deg. to 710 CA deg.).

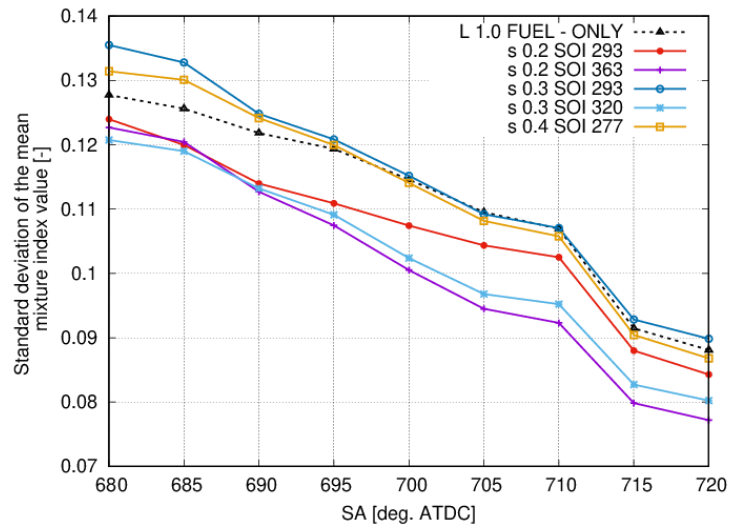


Figure 118. In-Cylinder STD mixture distribution for different PWI strategies

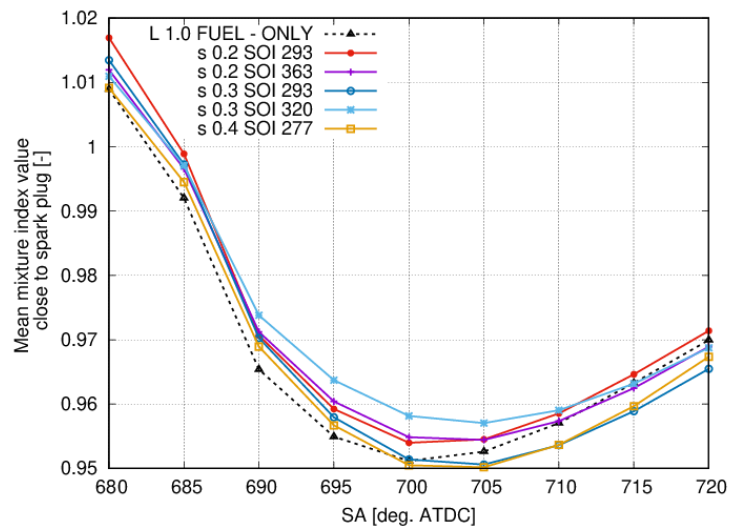


Figure 119. Spark plug mixture index distribution for different PWI strategies

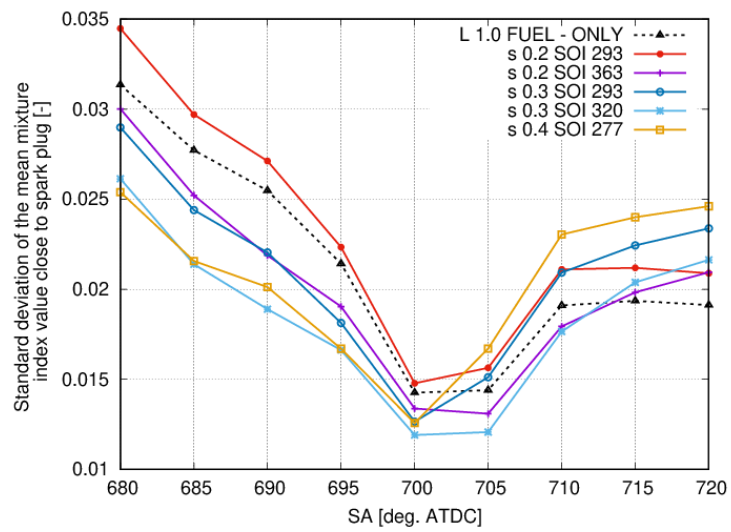


Figure 120. Spark plug STD mixture distribution for different PWI strategies

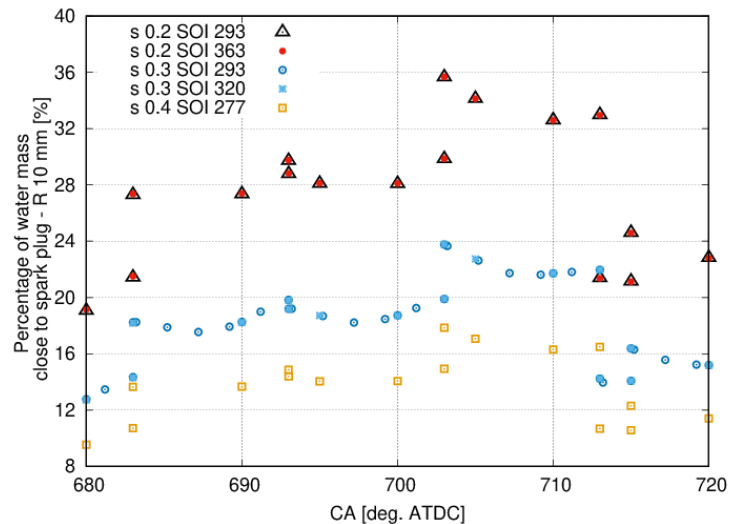


Figure 121. Percentage of water mass close to spark plug

This is one of the factors indicating that during the first combustion phases of each engine cycle, the flame may develop within a very similar cylinder mixture, limiting the cyclic variability of the engine: in order to ensure the target performance, it is of utmost importance to optimize the flame propagation in the first instants.

On the other hand, under the spark plug the dilution effect becomes more important as shown in Figure 119. The case *s 03 SOI 320* seems to have the best mixture conditions: slightly richer for a first rapid flame front propagation, and a low STD (Figure 120).

Finally, in Figure 121 the percentage of vapor water mass close to the spark plug has been reported: the presence of the water vapor near the spark plug produces thermal and dilution effects on the air-fuel mixture, affecting the development of the initial flame kernel. The presence of the water vapor close to the spark plug may have detrimental effects on the combustion process, hindering the flame propagation. This has also been deeply investigated in Chapter 5, highlighting the chemical water effect on laminar flame speed and ignition delayed time. The highest percentages of water close to the spark plug are present for all cases at *s 0.2*: the best solution seems to be *s 0.3*, almost independently by the SOI time.

### 9.2.2 Fluid-dynamic Analysis

In Figure 122 and Figure 123 the Tumble ratio and the in-cylinder mean turbulent intensity trends (evaluated as the ratio between the turbulent fluctuating energy and the mean piston velocity) have been reported. The Tumble ratio gives an indication for the formation of a coherent and structured vortex, which is the main source of the next turbulence development towards the ignition crank angle.

During the spin-up phase, from IVC to 650 CA deg., except for case *s 0.2 SOI 293*, a small interaction effect is visible between the fuel-only case and PWI cases. In this phase the Tumble motion, created inside the cylinder, tends to accelerate reaching its maximum near 650 CA deg.. The interaction between the water spray and the motion of the charge creates a variation in the flow momentum, that tends to slightly slow down the main vortex, with a greater effect as the water introduced increases. Globally, the TR (Tumble Ratio) values are quite high even with PWI system, confirming the optimized design of the intake duct and of the spray targeting.

In the next phase from 650 CA deg. to TDC, characterized by the vortex breakdown and turbulence generation, the profiles tend to converge to the only-fuel reference case, especially in the area for possible mixture ignition (from 690 CA deg. to 710 CA deg.).

The Figure 124 also reports the main phases of the interaction between Tumble motion, fuel spray and water spray during the intake stroke.

The turbulence created in the in the cylinder, (Figure 123), shows a more appreciable difference in the zone of interest between 690 CA deg. and 710 CA deg. for all the PWI cases. The turbulence intensity reductions, with regard to the *L 1.0 FUEL -ONLY*, range between -5 % and -7 %, and this is very important since the combustion speed is proportional to  $T$  (*turbulent intensity*). The case *s 0.2 SOI 293* is the only one that shows a behaviour quite similar to the reference case (only-fuel). However, the turbulent intensity levels remain high, deviating slightly from the maximum reference value of the fuel-only case, as also illustrated in Figure 125, whose values are taken in the area under the spark plug, showing even higher turbulence values than the average ones in the cylinder. From this we can expect a good corrugation of the flame front just after the ignition also for PWI architectures, with a good flame propagation speed in term of turbulence. In a similar way as seen for the fuel-only reference case, the turbulence at 700 CA deg. (crank angle where the maximum turbulence generation occurs) shows its maximum value in the area under the intake valve (Figure 126). For what concerns turbulent levels, case *s 0.3 SOI 293* is the best solution immediately after the case overlying the fuel-only case (*s 0.2 SOI 293*). Other implications due to the effect of water on combustion speed will be highlighted in the Chapter 11.

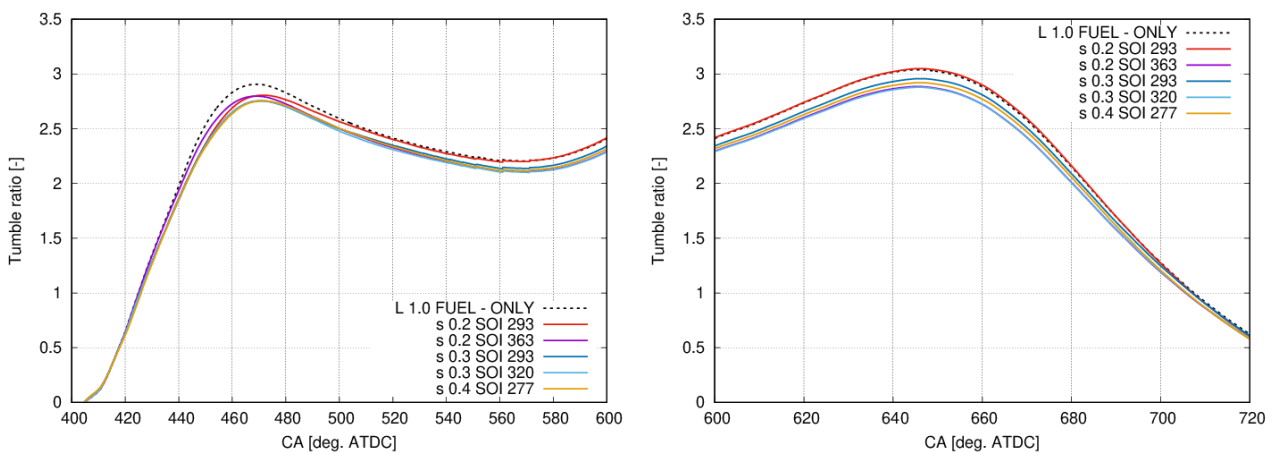


Figure 122. PWI effect on tumble ratio during intake stroke (on the left) and compression stroke (on the right)

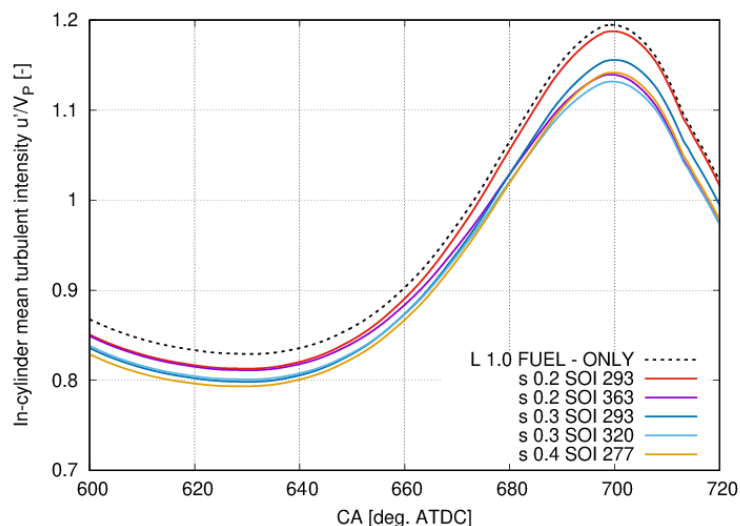


Figure 123. PWI effect on in-cylinder mean turbulent intensity

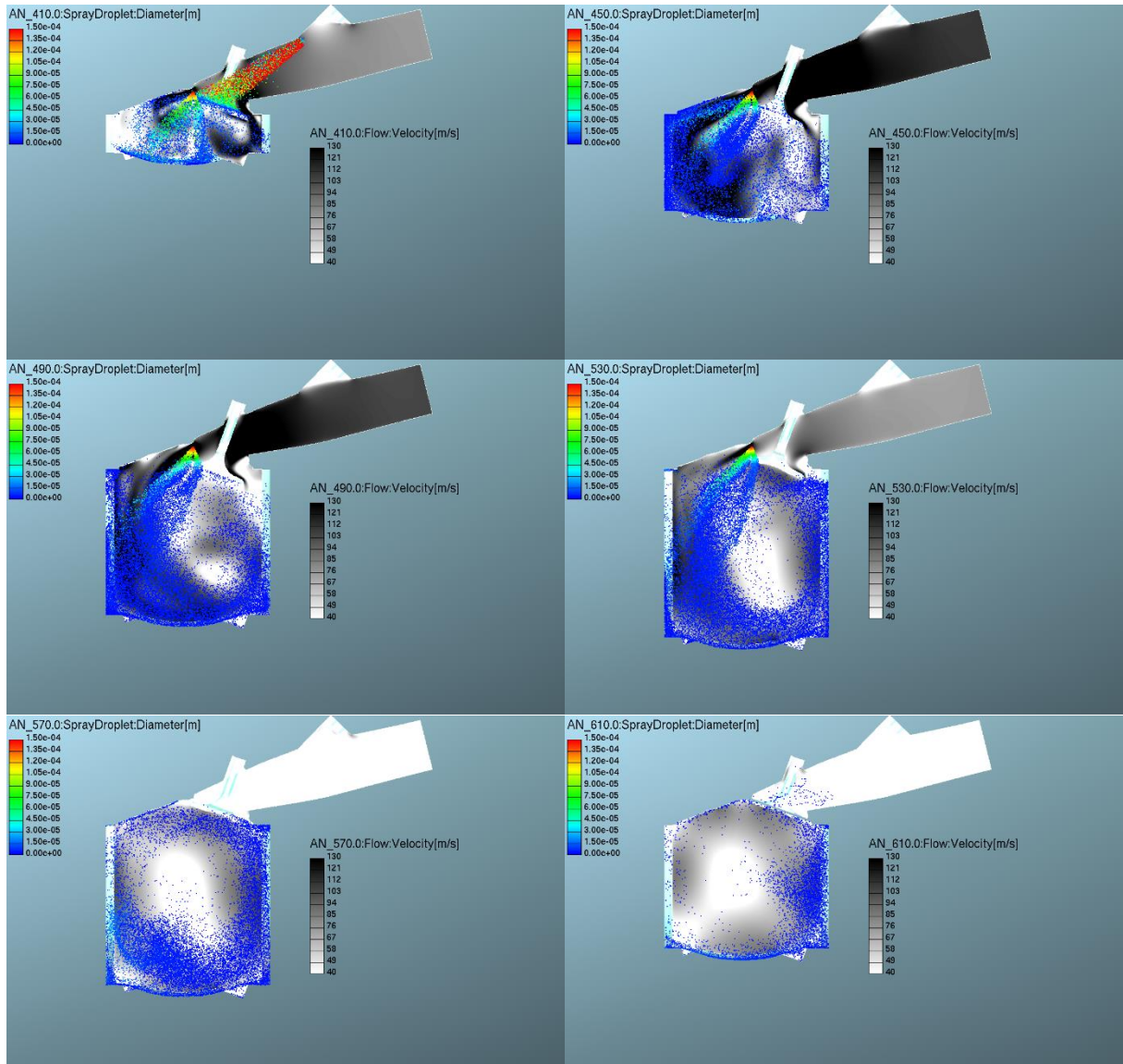


Figure 124. Tumble and Fuel-Water Spray interaction

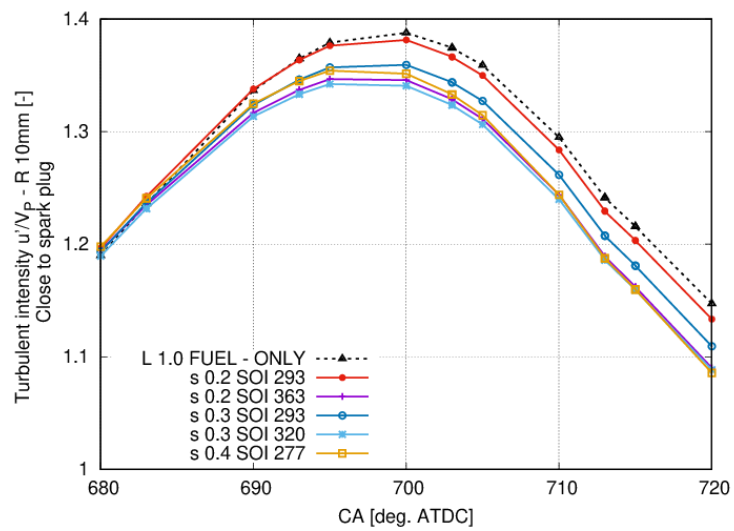


Figure 125. PWI effect on turbulent intensity close to the spark plug

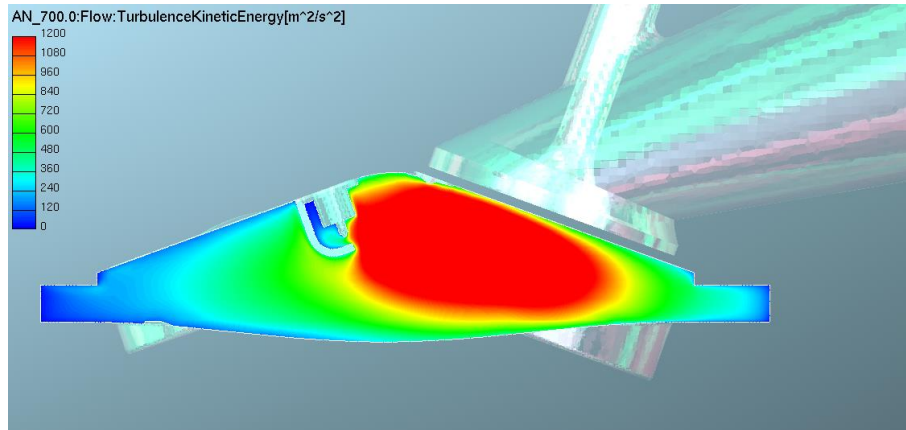


Figure 126. Turbulence field at 700 CA deg., PWI 10 bar,  $s$  0.3 SOI 293

### 9.2.3 Thermodynamic Analysis

Figure 127 shows the mean in-cylinder temperature variation ( $\Delta T$ ) at TDC between the PWI cases analysed so far and the lambda 1.0 case. In addition, values for richer mixtures have also been added ( $\lambda$  0.75 and  $\lambda$  0.85), representing modern fuel enrichment strategies for the protection of turbine components and knock mitigation. So, the  $\Delta T$  in the y-axis is defined for PWI cases as:

$$\Delta T = T_{@TDC, \lambda=1.0+PWI} - T_{@TDC, \lambda=1.0} \quad (108)$$

and for rich strategies,

$$\Delta T = T_{@TDC, \lambda=0.75 \text{ or } \lambda=0.85} - T_{@TDC, \lambda=1.0} \quad (109)$$

It is reminded that, the  $\lambda$  0.75 case represents in this analysis the minimum cooling level to achieve using a PWI architecture under stoichiometric conditions. From the analysis of Figure 127 it can be seen that:

- the minimum cooling level is reached even with the lowest amount of water in the most advanced SOI version ( $s$  0.2 SOI 293);
- by delaying the injection with the same water/fuel ratio, a slight reduction in cooling capacity occurs;
- as  $s$  increases the  $\Delta T$  increases but in a non-linear way: moving from  $s$  0.20 to  $s$  0.30 the water added is 50% more, while the further temperature decrease is 44.5%, thus some of the injected water mass is wasted.

To understand this effect, it is necessary to evaluate the water evaporation profiles of the analysed cases, the water-fuel liquid spray evolution, and the water wallfilm formation inside the intake port. First, from the Figure 128 it can be seen that all cases at 10 bar, regardless of the amount of water injected and the SOI, meet the main requirement of minimum water evaporation of at least 90% before the crank angle ignition window. This is important not only to optimize the water consumption with respect to the cooling effect, but also to limit the wallfilm generation. Moreover, by doubling the injected water,  $s$  0.40 compared to  $s$  0.20, the evaporation rate seems to be limited, thus not being able to express the full potential of a higher water quantity. The slope of the curve changes depends on both  $s$  parameter and SOI time, denoting different thermodynamic conditions in the cylinder for each case, that can be less favourable for the water evaporation process.

Figure 129 shows the trends of the percentage of water-fuel liquid phase as drops in the spray cloud, from the start of injection to TDC. Although the 90% evaporated condition is always met, only the case  $s$  0.2 SOI

293 guarantees complete evaporation of both fluids before ignition. The more the droplets of both water and fuel are able to evaporate completely inside the cylinder, the more effective is the cooling process. In addition, Figure 130 illustrates the water wall film percentage evolution formed on the intake port and valve walls. A drop impacting on walls can undergo different evolutions depending on the dynamic and thermodynamic conditions of the drop-wall system. However, these can be summarized for simplicity in two cases: the first is the rebound with heat drop-wall exchange, the second is the formation of wallfilm. In both cases the cooling capability of the system is reduced because the water subtracts heat from the walls rather than from the fresh charge. The worst-case scenario is that of wallfilm because the heat dissipation is prolonged. The water vapor created by the wallfilm acts in the cylinder only as diluent, without lowering the temperature thanks to its latent heat. The big difference of wallfilm mass between *s 02 SOI 293* and *s 02 SOI 363* is partly responsible for the lower cooling capacity of this last strategy with delayed SOI.

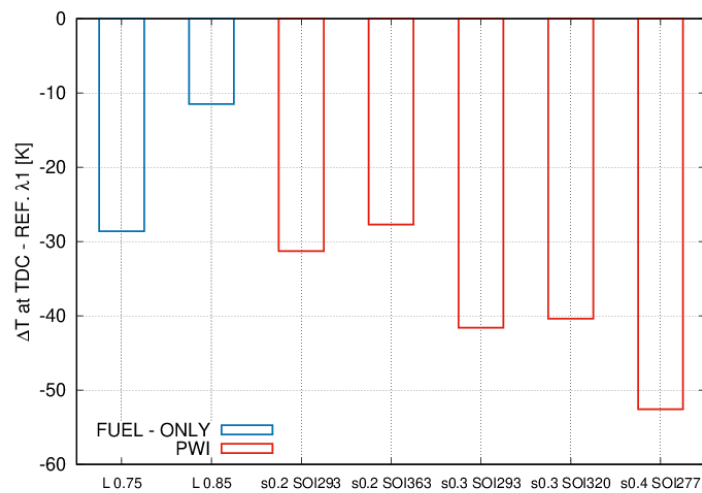


Figure 127. Temperature variation w.r.t  $\lambda 1.0$  case –  $\lambda 0.75$   $\lambda 0.85$  and PWI 10 bar strategies comparison

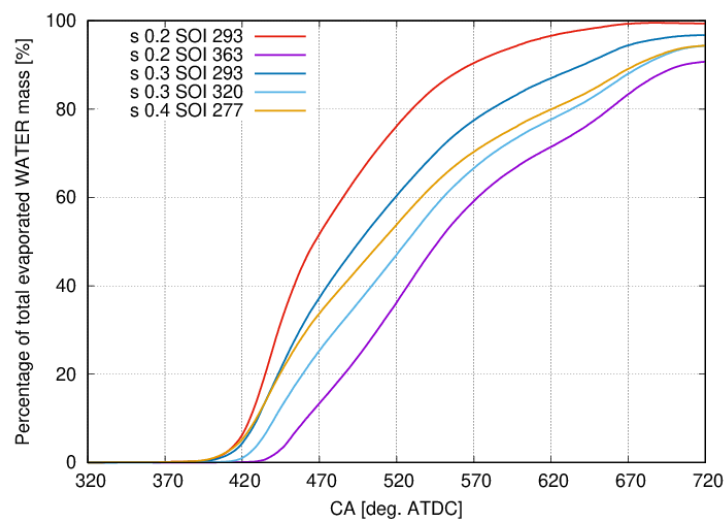


Figure 128. PWI 10 bar system: water evaporation rate

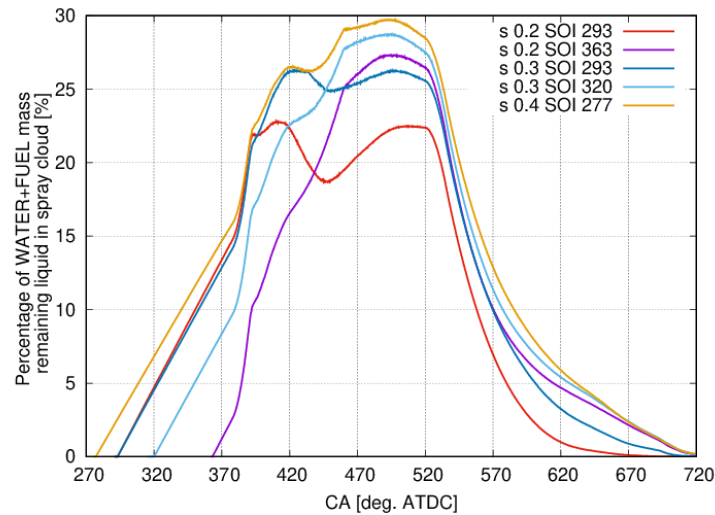


Figure 129. PWI 10 bar: Water-fuel liquid remaining in spray cloud

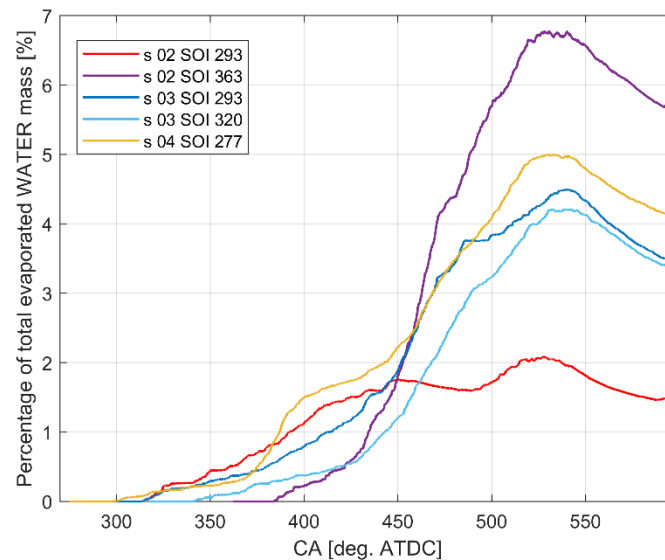


Figure 130. PWI 10 bar: Water wallfilm formation

Figure 131 contains two frames showing the extension of the wall film zone, for the two SOIs analysed at  $s$  0.2, on the intake duct walls, where it is evident the larger area covered by the wallfilm for the delayed SOI 363 especially close to inlet valve.

All these results can be summarized in the concept of the cooling efficiency, introduced in Chapter 3. The cooling efficiency  $\eta_{\text{COOLING}}$  was introduced for assessing the *quantity of wasted water*, i.e. injected but useless for the mixture cooling. The cooling efficiency  $\eta_{\text{COOLING}}$  was defined as the ratio between the effective temperature decrease reached at TDC ( $\Delta T_{\text{REAL}}$ ) and the ideal (maximum) temperature decrease ( $\Delta T_{\text{IDEAL}}$ ) reachable under the hypothesis of instantaneous (isochoric) vaporization of 100% of the injected mass of water at SOI conditions, both at the stoichiometric condition.

The cooling efficiency trend is reported in Figure 132, where the cases having the least advanced SOI have been compared. The delayed SOIs, for both  $s$  0.20 and  $s$  0.30, have shown to lower the evaporation rate because the injection takes place in an ambient whose thermodynamic characteristics are less favourable to the spray evaporation. The best cooling efficiency is for  $s$  0.20 but the case  $s$  0.30 has shown to have lower water evaporated mass under the spark plug. Moreover, its cooling temperature is greater than that of case  $s$  0.20. Concluding, the best setting seems to be  $s$  0.3 SOI 293 CA deg. ATDC at 10 bar.

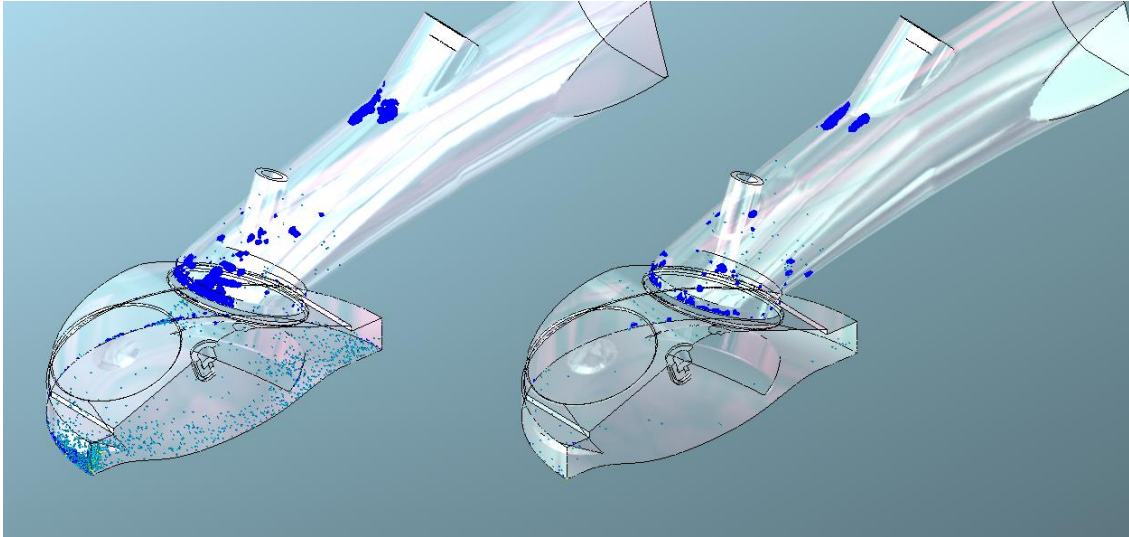


Figure 131. Wallfilm formation areas on intake walls: s 02 SOI 363 (on the left) and s 02 SOI 293 (on the right)

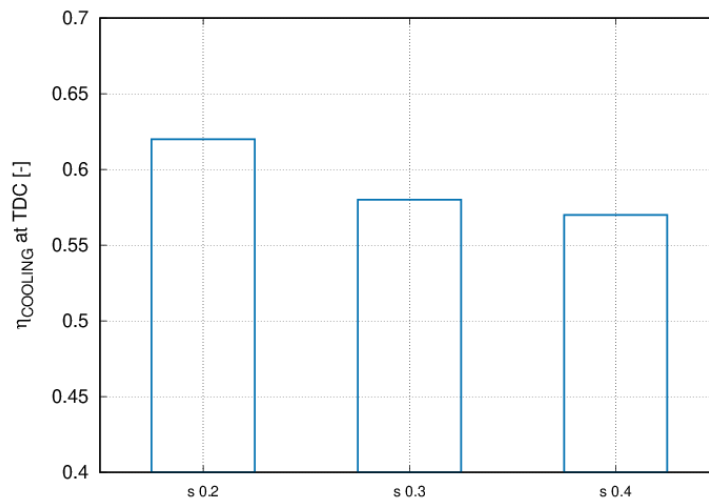


Figure 132. PWI cooling efficiency for the least advanced SOI

### 9.3 Simulation Results for PWI 20 bar Strategies

In a similar way to the 10 bar case, the same type of analysis was repeated also for the highest injection pressure of 20 bar, with s 0.2 and different SOIs. For the sake of brevity and clarity, all the graphs at 20 bar are reported without paragraph subdivision as before, because the conclusions are similar to the case at 10 bar.

Figure 133 shows that by delaying the SOI there is a constant reduction in charge cooling capacity at the TDC. Beyond SOI 393 the overall effect is too small compared to the  $\lambda$  0.75 (minimum target).

Another interesting feature concerns the evaporation rate and liquid spray evolution, as illustrated in Figure 134 and Figure 135. Unlike 10 bar case, only with the greatest advanced s SOI the 20 bar system is able to satisfy the request for 90% of evaporated mass before TDC.

The difficulty of the water evaporation for the SOI 393, 413 and 433 conditions results in a greater generation of liquid film on the walls, even inside the cylinder (Figure 136), with a greater probability of flame quenching and oil contamination.

For the worst case SOI 433, more than 20% of water introduced was not used to decrease the mixture temperature, making this strategy inefficient.

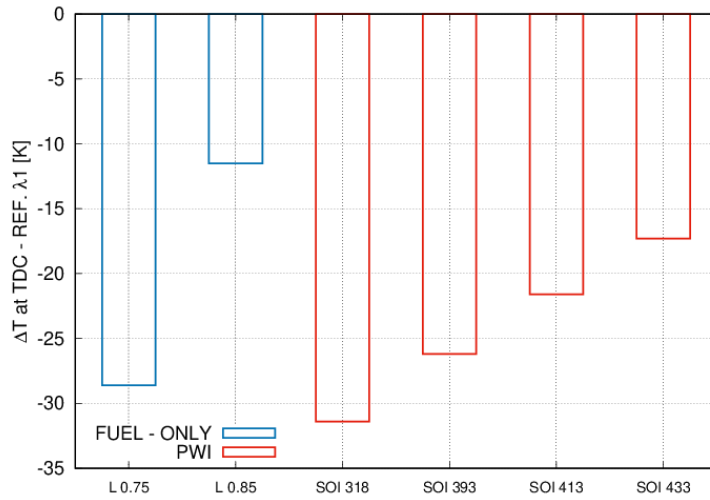


Figure 133. Temperature variation w.r.t  $\lambda 1.0$  case –  $\lambda 0.75$   $\lambda 0.85$  and PWI 20 bar strategies comparison

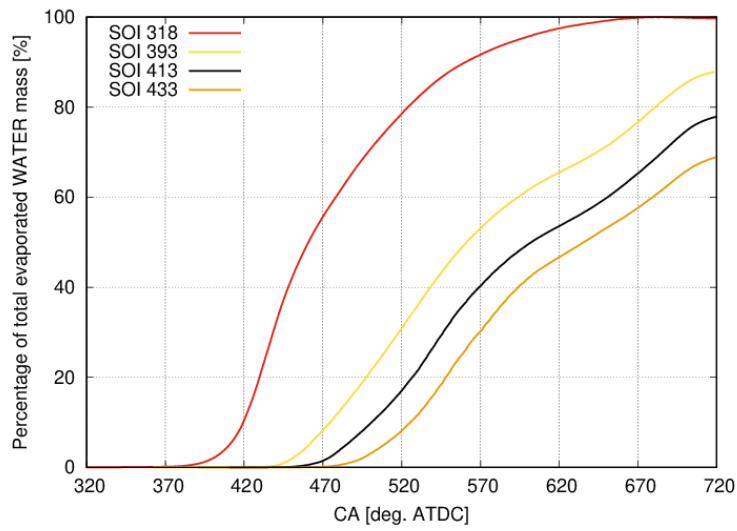


Figure 134. PWI 20 bar system: water evaporation rate

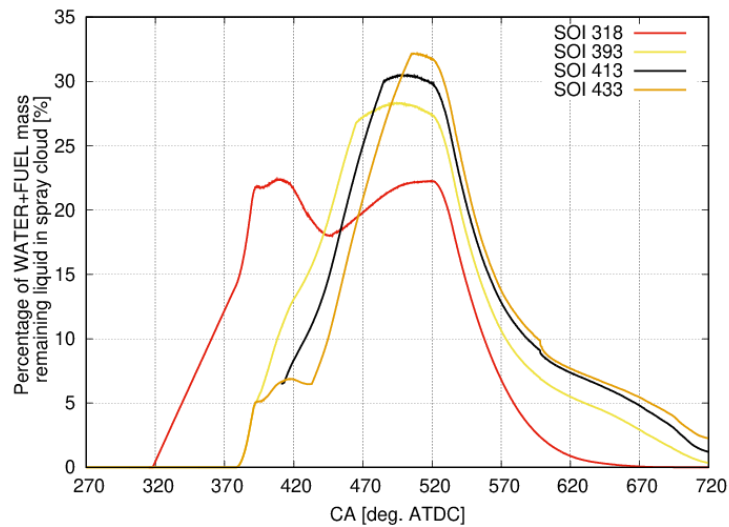


Figure 135. PWI 20 bar: water-fuel liquid reaming in spray cloud

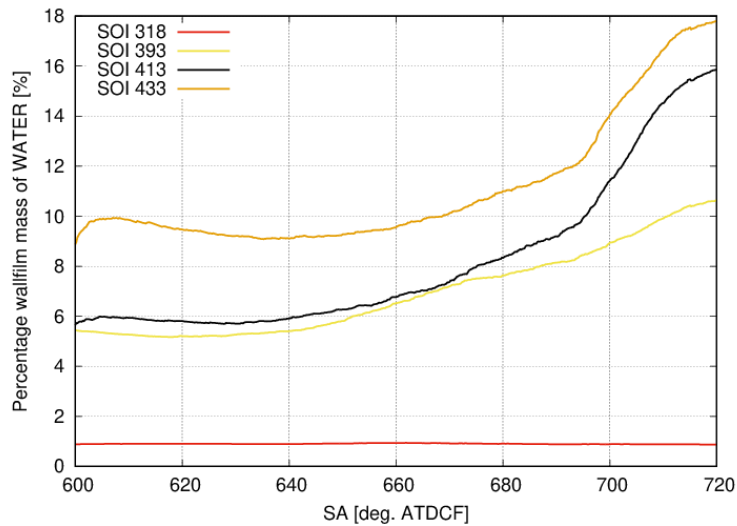


Figure 136. PWI 20 bar: In-Cylinder water wallfilm formation

The advantage of a reliable CFD simulation is to discard a priori those configurations that show to be far from the prefixed targets of cooling and evaporated percentage, concentrating the efforts and comparisons on the more promising strategies.

## 9.4 Results comparison among PWI strategies at 10 bar and 20 bar

In this section the comparison, for  $s = 0.2$ , between the case at 10 bar SOI 293 and the case at 20 bar SOI 318 is proposed. The cooling induced inside the cylinder is the same for both cases (Figure 137). The increased injection pressure has not demonstrated a remarkable cooling benefit through reduced droplet granulometry. This can be seen in part from the evaporation rate evolution in Figure 138. Although the SOI of 20 bar is delayed by 25 CA deg. compared to 10 bar, the profile rises earlier and remains slightly translated to the left throughout the spray event. The smaller characteristic diameter of the drops ( $d_{32}$ ), in fact, makes the evaporation faster when the drops are still mainly in the intake duct. However, the overall effect of this phenomenon, as seen, is negligible on final cylinder cooling at TDC.

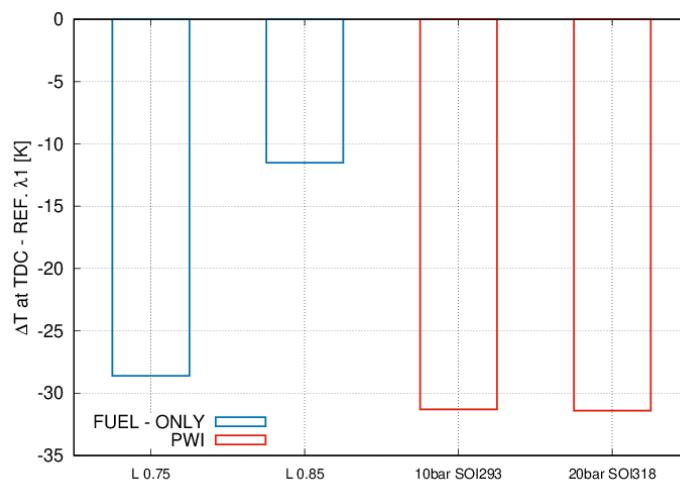


Figure 137. Temperature variation w.r.t  $\lambda = 1.0$  case –  $\lambda = 0.75$   $\lambda = 0.85$  and PWI 10 bar - 20 bar strategies,  $s = 0.2$

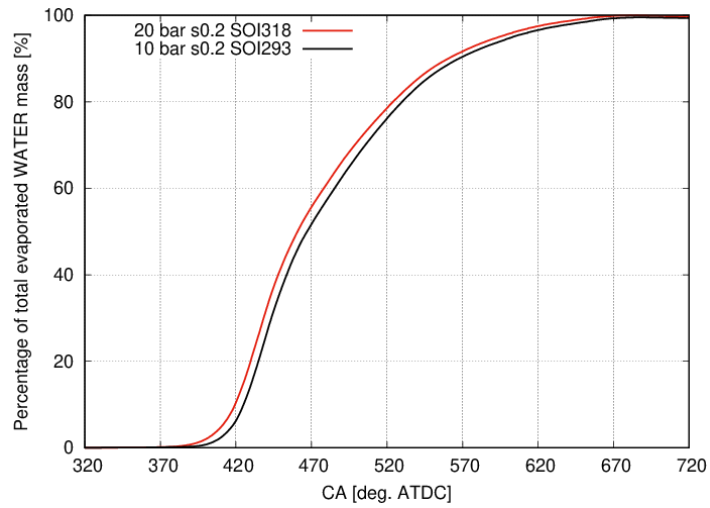


Figure 138. PWI 10 bar - 20 bar systems: water evaporation rate

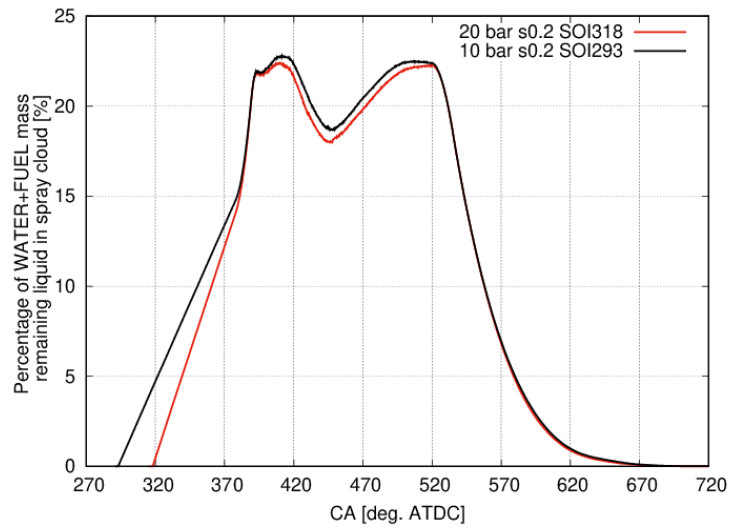


Figure 139. PWI 10 bar - 20 bar: Water-fuel liquid reaming in spray cloud

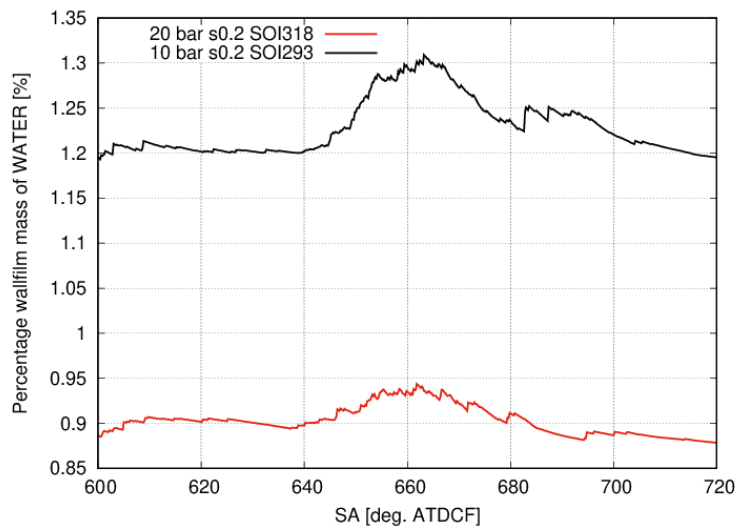


Figure 140. PWI 10 bar - 20 bar: In-Cylinder Water wallfilm formation

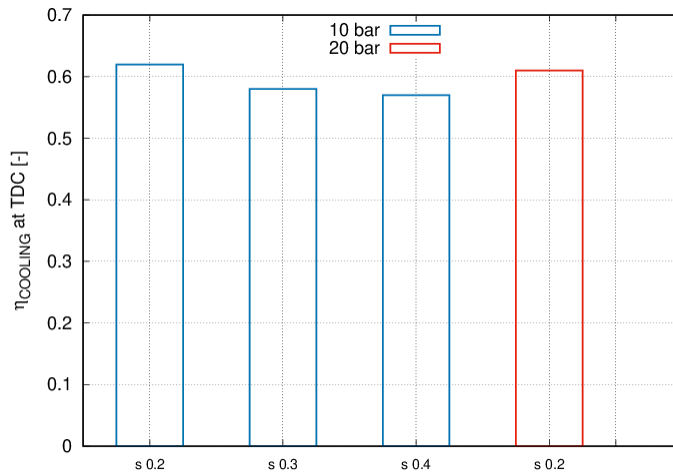


Figure 141. PWI 10 bar - 20 bar cooling efficiency

Both configurations have the best water evaporation conditions with rather similar trends, that well exceed 90% of evaporated water. Even the remaining liquid components (drops and film) do not show substantial differences (Figure 139 and Figure 140) and the in-cylinder water wallfilm still remains very low. Finally, in Figure 141, the cooling efficiency has been reported for all the cases tested at 10 bar, in their best SOI configurations, and the case *20 bar s 0.2 SOI 318*. The cases at 10 and 20 bar have almost the same cooling efficiency, confirming what has just been assessed. The maximum efficiency is just over 60%.

From this comparison it clear why other systems at 20 bar with higher *s* ratio have not been studied:

- 1) the objective is not to cool down as much as possible but to reach at least the pre-set target cooling level of the  $\lambda$  0.75 case (already satisfied with *s* 0.20). Moreover, increasing *s* the system would experience the same PWI 10 bar trend, with a reduced cooling efficiency;
- 2) the PWI 10 bar have shown a similar cooling efficiency of the higher-pressure system, it would not be convenient to further study other 20 bar strategies because of its worse cost versus performance balance.

As a conclusion of the previous non reacting flow assessment carried out at the full power point of a very high bmep GDI engine, the best setup for PWI architecture is *10 bar* and the best non-dimensional water mass to inject is *s 0.3 with SOI 293 CA deg. ATDC*.

## 9.5 Relative Humidity Effects on PWI Performance

In the present analysis, as intake air conditions, the ambient conditions of 1 bar and 20°C have been considered. Flowing through the turbocharger, despite the intercooler, the intake air temperature increases. The final value of the intake air after the turbocharger-intercooler assembly has been evaluated by the available map for a typical turbocharger equipping such a modern GDI engine. Different RHU values have been considered: 60%, 65% and 75%. The PWI system setup considered in these simulations has been chosen to be *s 0.30 and 10 bar, SOI 293 CA deg. ATDC*, which is the optimum one, as emerging by the above considerations.

Results of simulation for PWI system have been compared with the simulation performed under the hypothesis of dry air but keeping constant the other parameters, such as mass of injected water (*s* 0.30), injection pressure (10 bar) and SOI (293 CA deg. ATDC): the latter represents the reference case (named DRY AIR in figures). Figure 142 shows the in-cylinder temperature variation at the TDC compared to the lambda 1.0 fuel-only case, for the different relative humidity considered here. The results do not show appreciable differences, being all around -42 °C.

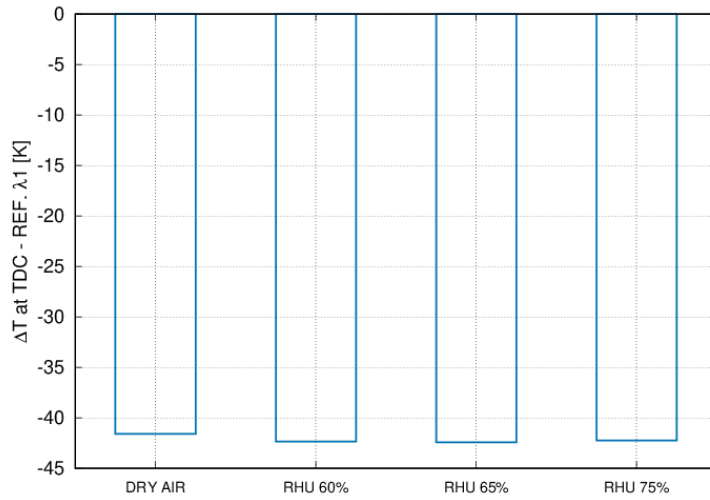


Figure 142. Temperature difference at TDC w.r.t  $\lambda$  1.0 only-fuel case, for different RHU values

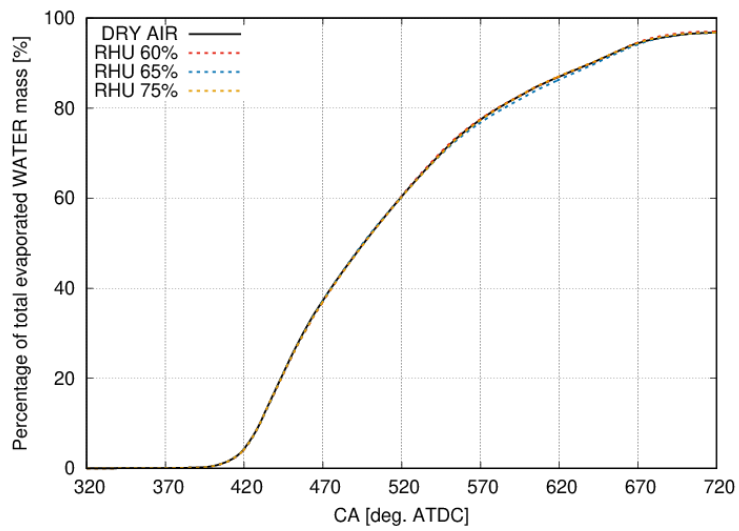


Figure 143. Percentage of evaporated water: comparison between DRY air and different RHU values

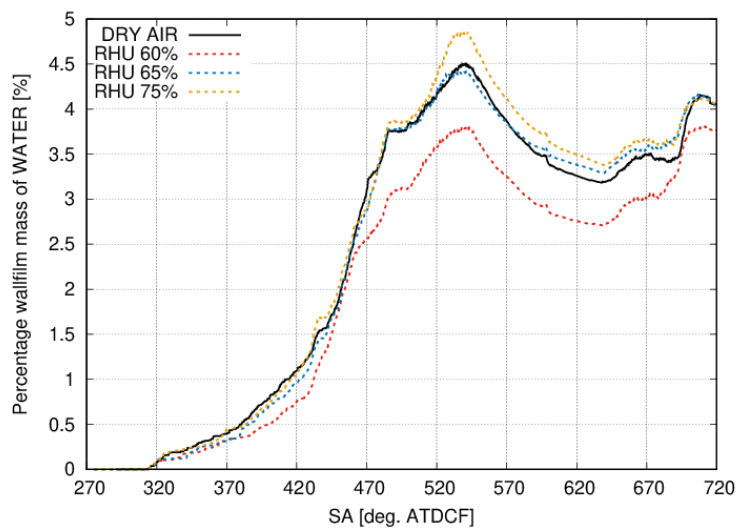


Figure 144. Percentage of water wallfilm: comparison between DRY air and different RHU values

Even the evaporation rate profiles, illustrated in Figure 143 for DRY air and different RHU values are comparable. Figure 144 shows the water wallfilm evolution inside the cylinder that is weakly affected by the RHU value at TDC. These results confirm the initial target set during the choice of the injection characteristics. The water has to enter mostly as droplets inside the cylinder, minimizing the evaporation in the intake duct. Therefore, even if the relative humidity increases inside the duct approaching the saturation condition, this has no effect on the dynamics of the spray. The evaporation, concentrated inside the cylinder, finds very favourable thermodynamic conditions that do not allow to bring the charge to saturation, independently from the RHU value imposed. So, for this injection layout, it is admissible to make the hypothesis of dry air in the engine simulations running with water injection strategy from the cooling point of view.

## 9.6 Evaluation of the Main Effects of Higher S/B Ratio on PWI Strategy

The stroke-to-bore ratio of turbocharged high-power engines is typically close to 1 as that of the investigated engine. However, the increase in the S/B ratio involves some interesting aspects which may increase the engine efficiency. In fact, it increases the Tumble ratio and the turbulent intensity, increase the flame surface available for oxidation, reduces the wall heat exchange and it may reduce the *bmep* if a rightsizing re-design concept is pursued. The decrease of *bmep* is of interest because larger compression ratio may be used and the turbocharger specification get less demanding, especially if overexpanded cycle would be used.

In general, the increase of the S/B ratio of the engine can be done following two different ways:

1. keeping the displacement constant, increasing the stroke and simultaneously decreasing the bore. However, in order not to have an impact on the intake air mass and therefore on the performance, it would be necessary to increase the intake pressure as the diameter of the valves would be reduced as well as the discharge coefficients. Furthermore, decreasing the diameter of the piston would directly decrease the power output. For this reason, with the goal of preserving the same power for this high-demanding cylinder engine, and for design issues, this first strategy has been discarded;
2. keeping the bore constant and therefore increasing the displacement by acting on the stroke length. However, it should be noted that this solution is limited by the average speed of the piston: at equal engine speed, increasing the stroke, the piston speed will increase accordingly and for constructive reasons is limited to 20-21 m/s. Although this strategy may not seem usual, it may be interesting to study its positive or negative fluid-dynamic and thermodynamic effects, through water injection as well.

Following the second strategy, some fundamental engine equations were used to identify the new S/B ratio:

$$P = \frac{bmep \cdot n \cdot v_p}{4 \cdot 60} \quad (110)$$

$$v_p = 2 \cdot S \cdot \frac{n}{60} \quad (111)$$

keeping the power target constant and a maximum piston velocity of 20 m/s, the engine stroke has been increased from 85 mm to 95 mm, shifting the rotation speed from 7000 rpm to 6250 rpm.

The comparison between the two S/B ratios was performed on the PWI and CR 10.5 architecture, with the s 0.3 -10 bar configuration, being, as already mentioned, the most promising in terms of cost and performance reduction.

The two configurations with different S/B ratios therefore share the same RC (10.5), increased by 1 point compared to the cases analysed previously (9.5). The effect of the compression ratio, moving from 9.5 to 10.5, will be discussed in the next chapter, since this analysis was also performed for the DWI architecture.

Here the objective is to highlight only the effect of the S/B ratio, considering the limits imposed on the piston speed and the new cylinder shape with a longer stroke. In order to keep the same compression ratio (10.5) with a longer stroke, it was necessary to increase the volume of the combustion chamber at the top dead centre by acting on the shape of the piston.

The PWI CR 10.5 S/B 1.01 has a flatter piston shape than case with CR 9.5, while PWI CR 10.5 S/B 1.13 has a more similar bowl shape as for CR 9.5 case (in order to recover volume at TDC to achieve CR 10.5). These are two very important features to take into account during the result analysis. An image of the two piston profiles is proposed in Figure 151, as described later.

As a result of these changes the trapped mass increased by 8.4 % due to the swept volume increase and the brake-specific fuel consumption (BSFC), evaluated in OpenWAM, has been reduced of 27.0% at stoichiometric conditions, due to the thermodynamic efficiency increase. The injected water at s 0.3 has been 28.0 mg, about 3 mg more than the previous PWI simulation with S/B 1.01, the fuel mass is indeed increased in order to have a stoichiometric mixture.

In terms of charge temperature, the increased S/B ratio results in a slightly lower cooling capacity of about 3 K at TDC as illustrated in Figure 145. The main reason was found in the heat transfer evolution illustrated in Figure 146. For the first part of the cycle the cylinder is exposed to a greater heat exchange due to the extended stroke and surface, getting more heat from the walls, which decrease the water-cooling effect. The overall effect is such that the system is unable to achieve the minimum level of temperature drop as is the case with the rich mixture (*baseline engine  $\lambda$  0.75*).

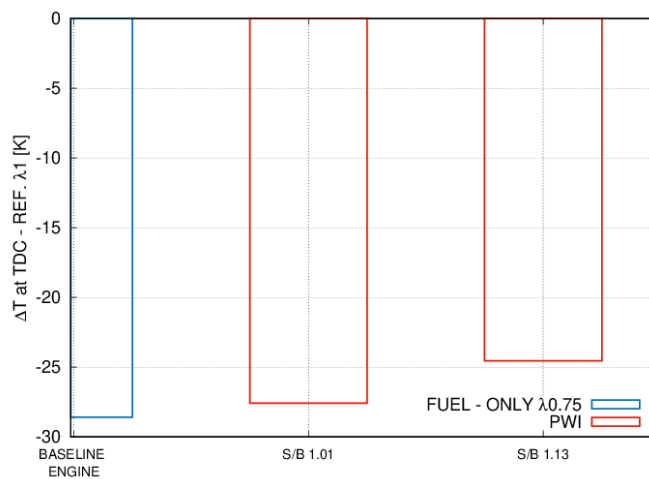


Figure 145. PWI strategy: stroke/bore ratio effect on temperature reduction

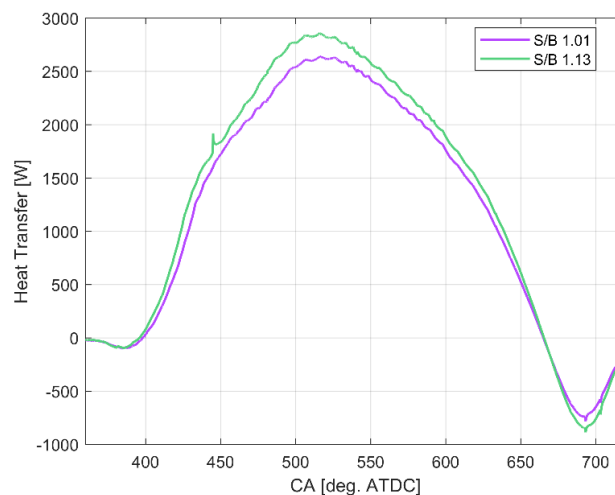


Figure 146. Heat transfer comparison between S/B 1.01 and S/B 1.13

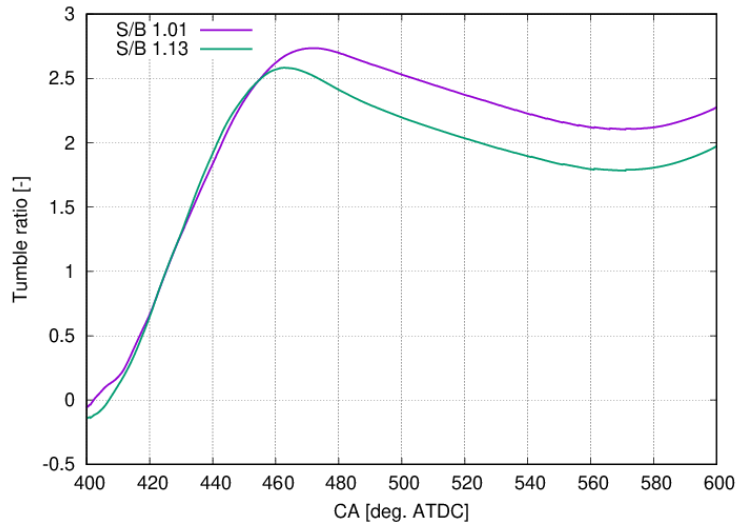


Figure 147. PWI strategy: bore/stroke ratio effects on Tumble ratio (intake stroke)

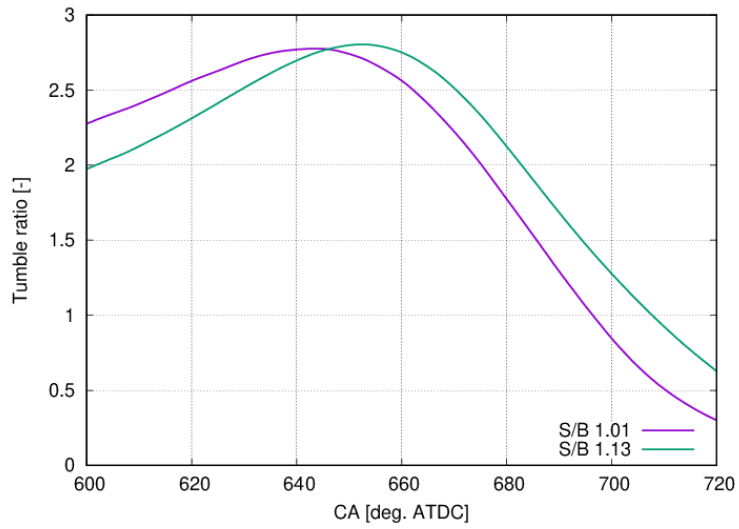


Figure 148. PWI strategy: stroke/bore ratio effects on Tumble ratio (compression stroke)

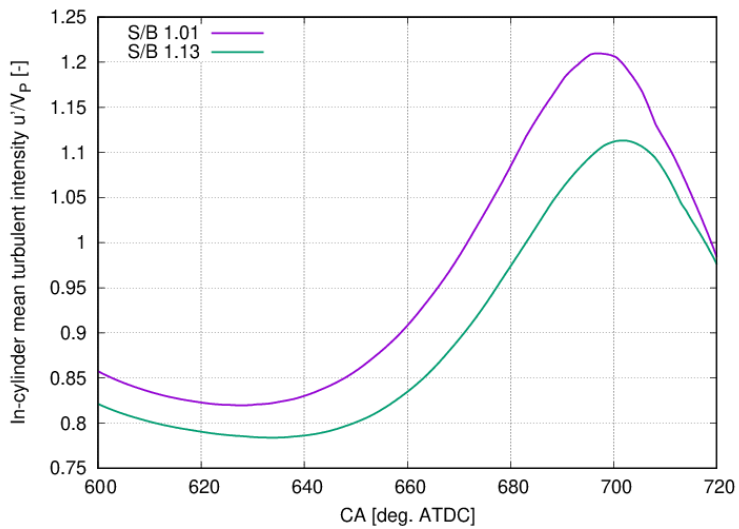


Figure 149. PWI strategy: stroke/bore ratio effects on turbulent intensity

As far as the turbulence generated inside the cylinder is concerned, this is negatively affected by the new combustion chamber shape and by the interaction between the Tumble vortex and piston shape. Case *S/B 1.13* presents a less optimized vortex spin-up phase compared to case *S/B 1.01*, with a less intense vortex breakdown, as showed in Figure 147 Figure 148, which represent the Tumble motion evolution during the intake and compression strokes. Ideally a zero RT can be considered the optimal condition, where the main vortex has been completely converted into turbulence generation. Increasing the *S/B* ratio would result in an increase of turbulence intensity. This does not occur in this case, as demonstrated by the turbulent intensity profiles in Figure 149, because the benefit due to a better geometric configuration of the combustion chamber is mitigated by the unfavourable charge motion interaction with the walls. The intake duct has not been adapted for the new cylinder shape. In addition, as will be demonstrated in the next chapter, the shape of the piston chosen to increase the compression ratio (flatter) leads to a more violent initial turbulence generation than the bowl shape, but also to a faster dissipation. The further difference about the delayed peak for the *S/B 1.13* case, is due to the increased stroke.

Figure 150 actually shows how a larger residual charge movement remained in the combustion chamber for case *S/B 1.13*, leading to different turbulence generation (Figure 151). Despite the decrease observed compared to the base case *S/B 1.01*, in general the system *S/B 1.13* can still be considered to have good turbulence level.

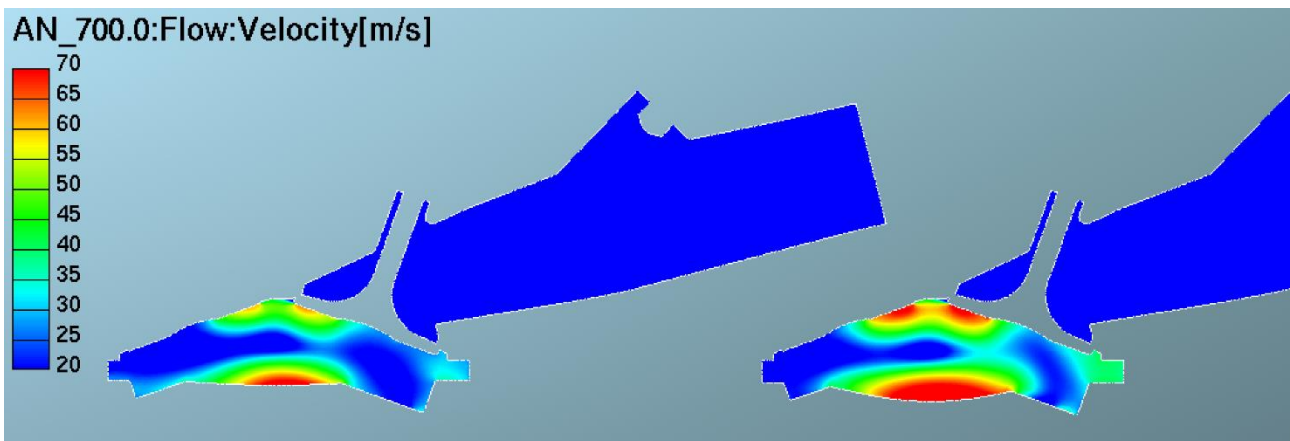


Figure 150. Tumble motion residual at 700 CA deg., *S/B 1.01* (on the left) and *S/B 1.13* (on the right)

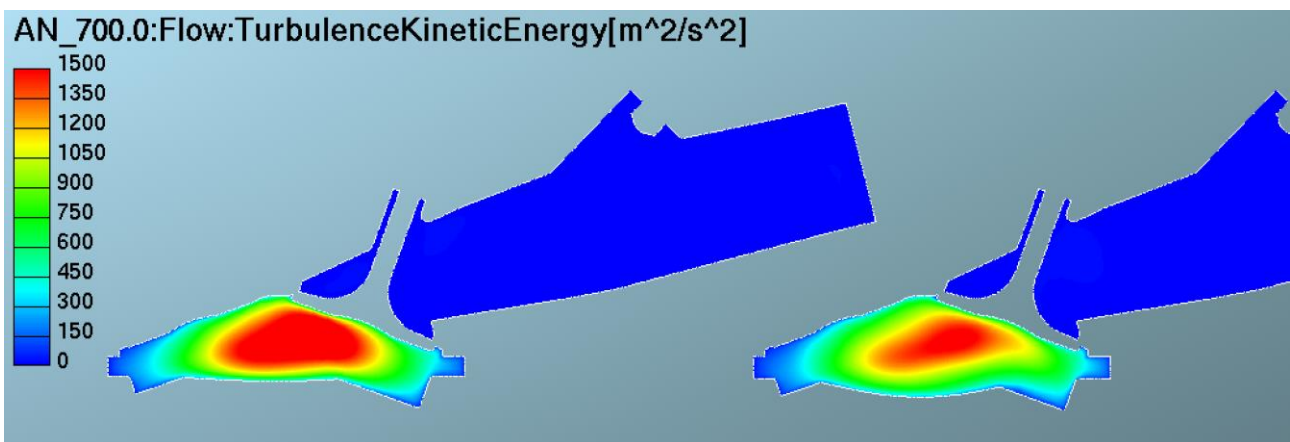


Figure 151. Turbulence kinetic energy at 700 CA deg., *S/B 1.01* (on the left) and *S/B 1.13* (on the right)

## 9.7 Summary

The PWI injector spray pattern was oriented toward the intake valve to target the cylinder properly. The objective was to minimize the impact of liquid water against intake and port walls as well as intake valve stems and seats. The injection timing was set to promote the spray entering the cylinder, taking so the water spray the advantage of the most favourable thermodynamic conditions for the evaporation process and cooling maximization. The relative injection pressure was varied in the range 10 bar – 20 bar. The SOI/EOI times and the  $s$  parameter values have been varied for both injection pressure. At 10 bar, the best cooling efficiency has been detected for case  $s 0.2$  but the case  $s 0.3$  has shown to have the best evaporated mass and the lowest wallfilm. Moreover, its cooling temperature is greater than that of case  $s 0.2$ . Concluding, the best case is to be  $s 0.3$  SOI 293 CA deg. ATDC at 10 bar.

For injection pressure 20 bar the case  $s 0.2$  only has been tested, varying the SOI time: the best one has been found to be  $s 0.2$  SOI 318 CA deg. ATDC. The whole trends at 10 and 20 bar are almost the same, without notable difference. Considering that the injection pressure level of 20 bar is more cost demanding, there aren't advantages if compared to the case at 10 bar. Thus, for PWI architecture the best solution is  $s 0.3$  at 10 bar, SOI 293 CA deg. ATDC.

Since it was not possible for this engine configuration to decrease the bore in order to increase the S/B ratio, the stroke has been increased, leaving the bore unchanged and decreasing the engine speed in order not to exceed the piston limit speed of 20 m/s and to keep the power output constant. Globally, it has been found a slightly reduced cooling effect and a decrease of the in-cylinder turbulence, because the gain due to the better geometric configuration of the combustion chamber is mitigated by the detrimental charge motion interaction with the walls.

# Chapter 10: Direct Water Injection Simulations under Non-Reacting Flow Conditions

In this chapter the effect of the water injection is studied always in non-firing conditions for a DWI architecture. While this strategy is more expensive and less attractive for a short-term application, it is important to comprehensively understand what advantages and disadvantages can arise over PWI. First, the DWI will be examined under different operating conditions, dividing the study in a similar way to that seen for the PWI. Finally, the two systems will be compared.

The objectives of the research remain to verify that at least 90% of the water mass is evaporated before the TDC and that the lowering of the temperature of the mixture is comparable to that of the strategy  $\lambda$  0.75.

## 10.1 Direct Water Injection Features

The engine is the same as seen in the previous Chapter 8, characterized by a compression ratio of 9.5 and a S/B of 1.01. The injector in the DWI case is mounted on the intake side of the engine head (Figure 152). This helps in the overall drawing of the engine head and it allows larger free spray path between the injector and the cylinder or piston surfaces. Moreover, the water spray beam orientation (Figure 153) was set in order to promote the interaction between the water plumes and the in-cylinder air-flow field, enhancing the water evaporation rate. In Table 23 are listed the main injector characteristics.

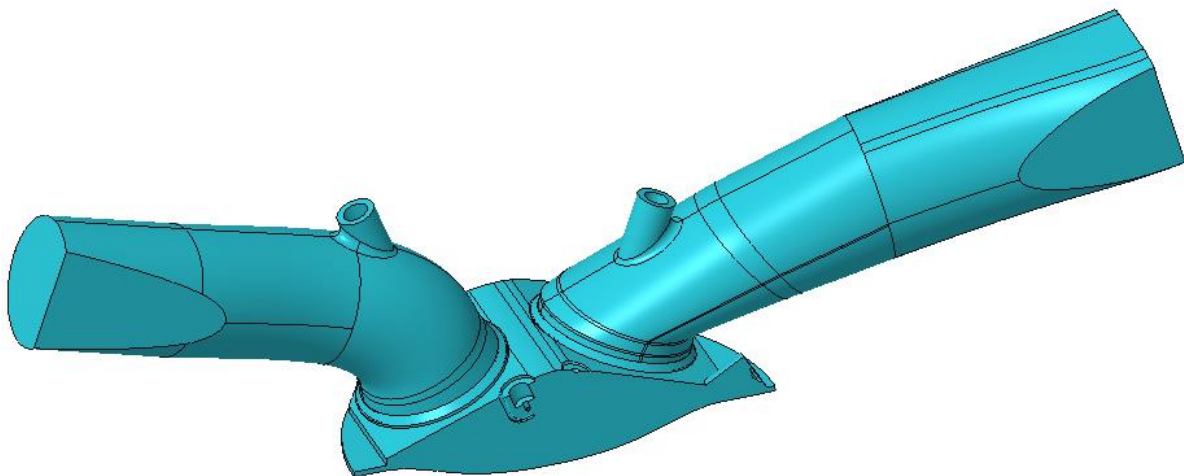


Figure 152. DWI engine design

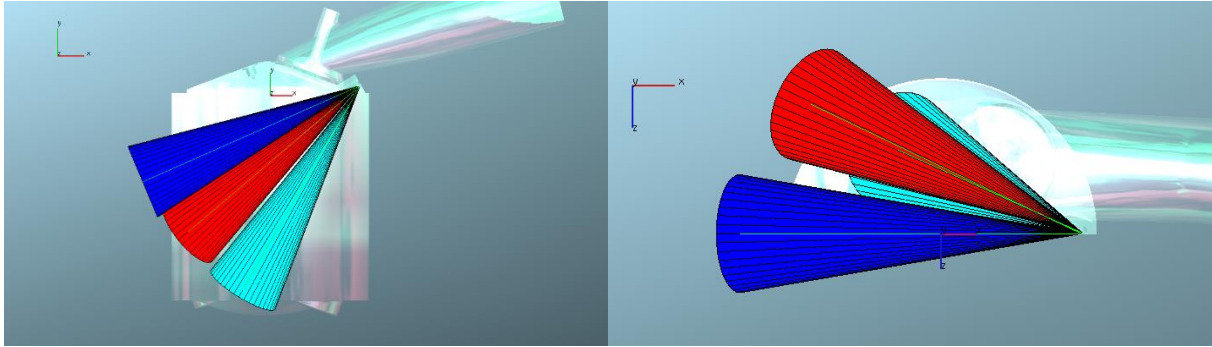


Figure 153. DWI Spray targeting

Table 23. GDI and DWI injector features

	<b>GDI</b>	<b>DWI</b>
<b>Number of holes [-]</b>	8.0	5.0
<b>Injection pressure [bar]</b>	350.0	50.0/150.0
<b>Injection temperature [K]</b>	313.0	313.0
<b>HFR [cm<sup>3</sup>/s]</b>	20.0	17.0
<b>Hole geometric diameter [μm]</b>	188.0	220.0

## 10.2 Definition of the DWI Injection Centre

Unlike injection in the intake duct, DWI allows for greater flexibility in managing the injection timing. In particular, the aim is to find the optimal phase of the injection window based on the concept of the injection centre. Once the SOI (or EOI) has been chosen, the EOI (or SOI) is calculated based on the injector design data for that engine: injection flow rate, injection pressure and mass injected.

The idea of the “injection centre” lays on the definition of an angle which represents the centre of each considered injection law, once fixed minimum and maximum injection pressure values, independently by the mass to be injected or the chosen injection pressure. For understanding the concept of “injection centre”, it is first to remind that the SOI (or even the EOI) greatly influences the engine performances [138,139]:

1. As far as the cooling effectiveness is concerned, the best choice would be to shift the EOI toward IVC;
2. In order to not penalize the turbulence inside the cylinder, the EOI should be advanced just before BDC;
3. In order to enhance the evaporation of the injected fuel mass from the spray, the EOI should be even more advanced, close to 500 CA ATDCF or just before.

Following the common procedure of fixing a priori the SOI and defining then the EOI as a function of the mass to be injected could penalize one or more of the above listed issues.

The injection centre was evaluated considering an average injection flow rate between the two extremes of injection pressure considered (50 bar and 150 bar), ie 93 bar. As regards the water / fuel ratio, it was set at 0.35, an average value within the most commonly adopted range (0.2 - 0.5). However, the injections laws calculated in this way must satisfy two main requirements:

1. the injection event must take place during the intake phase;
2. the injection event must start after 360 CA ATDCF to avoid the jet of water impacting the piston surface and the liner surface, where it would evaporate by absorbing heat from wall surfaces, which

is useless. To achieve the maximum charge cooling, the water needs to evaporate by absorbing heat from in-cylinder mixture.

Table 24 shows the cases studied in order to define the best DWI injection law for this type of engine. In this first analysis the quantity of injected water mass is not a variable.

Table 24. DWI injection law centre tested

SOI [CA deg. ATDC]	EOI [CA deg. ATDC]	INJECTION CENTER [CA deg. ATDC]
372	480	426
406	515	461
432	540	486
467	575	521

### 10.2.1 Mixture Distribution Analysis

The objective is to verify the effect of SOI/EOI on the distribution of the mixture both as an average internal cylinder value and under spark plug (10 mm radius sphere). Figure 154 shows the quality mixture values for the cases analysed in the last angular range near the ignition zone (680 CA deg. up to TDC). Overall, there is no marked effect on the average mixture index since all values are around  $\lambda$  1.0. The reason why not even the reference case L1 is exactly equal to 1, is due to the small amount of fuel (the less volatile components) that remains in liquid form, as droplets or wallfilm, up to TDC. The standard deviation of the average mixture quality in the cylinder, Figure 155, shows a decreasing trend towards the TDC with globally low values. The highest standard deviation is for injection centre (namely INJ. C. in labels pictures) 461 CA deg. ATDC and 486 CA deg. ATDC, while the least one is for injection centre 521 CA deg. ATDC.

The mean mixture index close to spark plug (Figure 156) is leaner before 695 CA deg. and it does not show substantial differences between the analysed cases. As shown in Figure 156 the mixture tends to become slightly rich, leading to an even more favourable condition for the initial flame development with a lower variability of the mixture near the spark plug close to 710 CA deg. (Figure 157). In conclusion it can be said that for this DWI architecture, the effect of SOI/EOI, and therefore the centre of the injection law, on the mixture distribution is minimal.

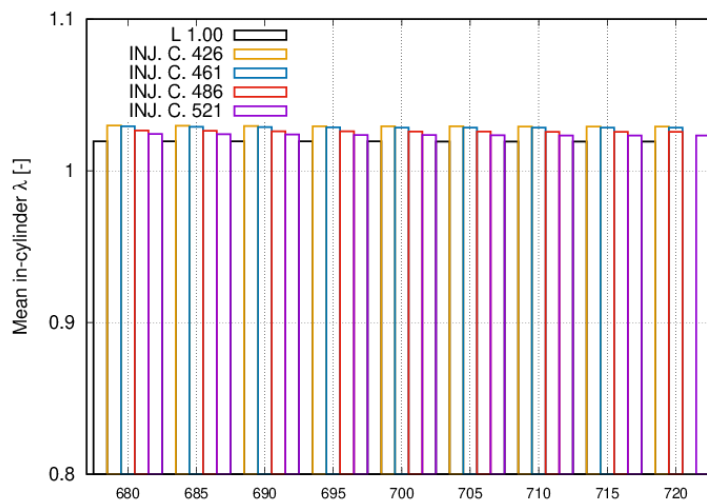


Figure 154. Mean In-Cylinder quality mixture

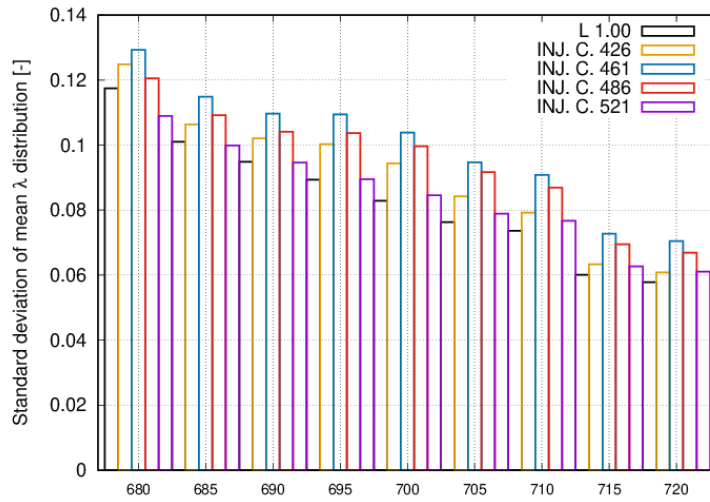


Figure 155. In-Cylinder STD mixture distribution

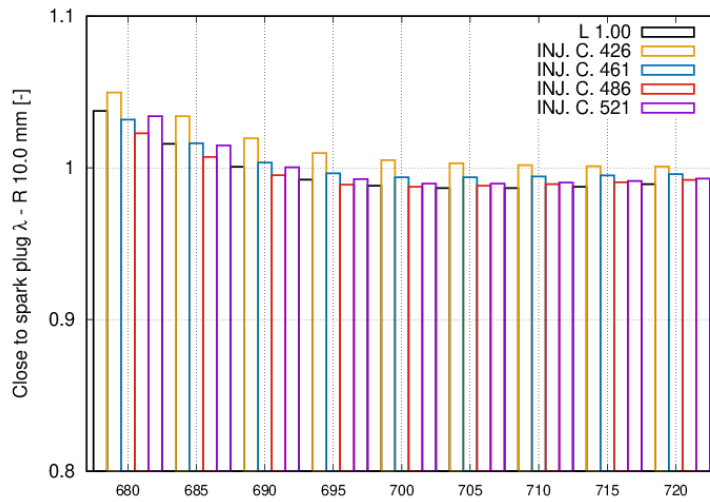


Figure 156. Mean quality mixture close to sprak plug

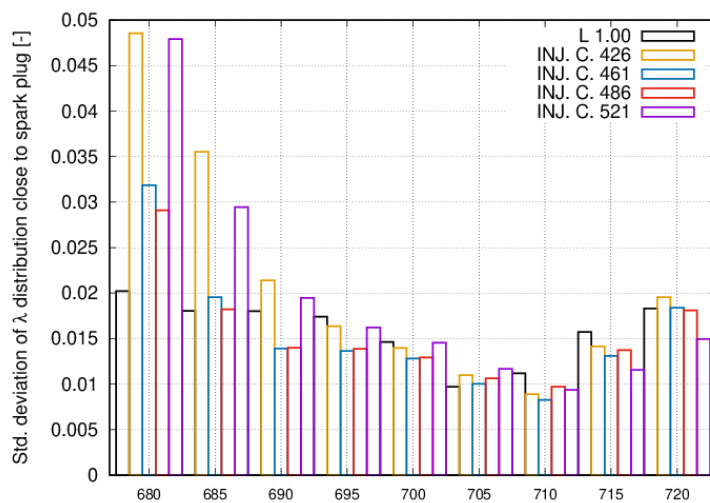


Figure 157. STD mixture distribution close to spark plug

## 10.2.2 Thermodynamic Effect

The cooling of the mixture obtained by this DWI architecture is shown in Figure 158 and compared with the two most used modern enrichment strategies ( $\lambda$  0.75 and  $\lambda$  0.85). The cooling of the charge obtained by evaporation of the water largely exceeds that experienced by the richest mixture. Unlike the PWI strategy, in this case the water, being injected directly into the cylinder, is able to better exploit its lower heating value. The evaporation rate, Figure 159, confirms that in all cases examined it is possible to reach the target of 90% evaporation and the generation of wallfilm remains below 1%, except for the most delayed case. The most advanced SOI shows the fastest evaporation rate, the lowest wallfilm mass but at the same time the lowest cooling. The reason lies in the fact that most of the drops evaporate during the intake stroke, where the increase in volume of the cylinder tends to decrease the temperature of the charge partially masking the effect of the water. By shifting the evaporation rate towards the compression stroke, a better thermodynamic effect can be achieved.

From a thermodynamic point of view, the best injection centres are 461 CA deg. ATDC and 486 CA ATDC.

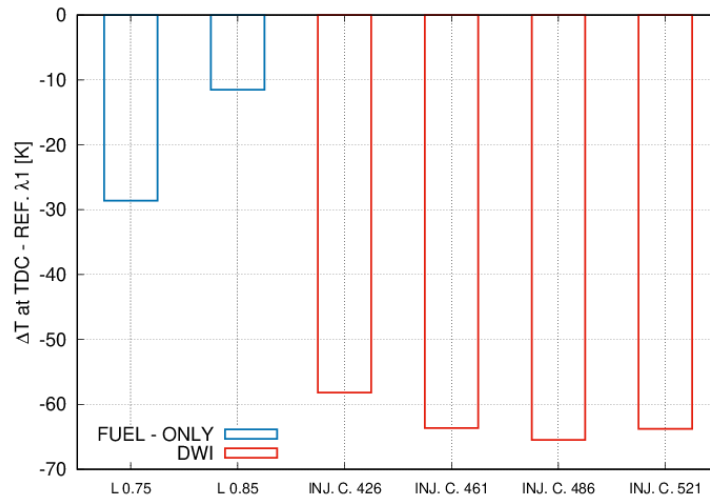


Figure 158. Cylinder temperature variation w.r.t  $\lambda$  1.0 case – Injection law centre comparison

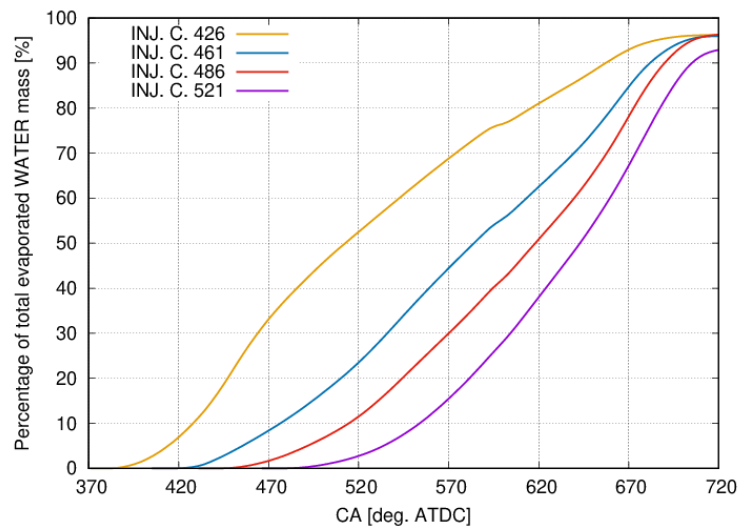


Figure 159. Evaporation rate: Injection law centre comparison

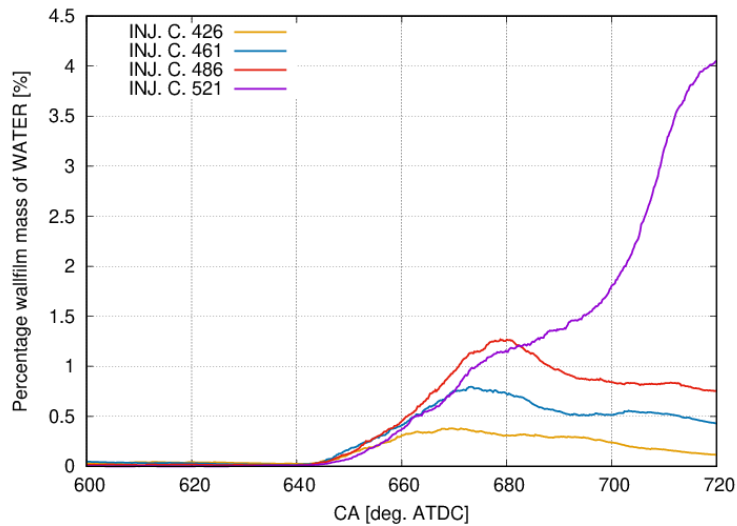


Figure 160. Water wall film: Injection law centre comparison

### 10.2.3 Fluid-dynamic Analysis

In this last section the effect of SOI on Tumble Ratio and turbulence generation inside the cylinder have been investigated (Figure 161 -Figure 162). Globally, the interaction of the water spray with the main vortex leads to a decrease of the TR and of the turbulent intensity. Initially, in the first spin-up part of the vortex, only the most advanced case (426 CA deg.) shows a considerable deviation from the reference (black curve). However, its behaviour seems to be only anticipated with respect to the other injection laws: starting from 480 CA deg. the curves tend to converge, deviating sharply from the reference in the compression phase, with a peak at about 650 CA deg. 7% lower.

The negative impact on the turbulent intensity is evident as illustrated in Figure 163, mainly in the area where the spark advance could be chosen. This, combined with the presence of water and lower temperatures, can cause serious problems in flame speed control and combustion.

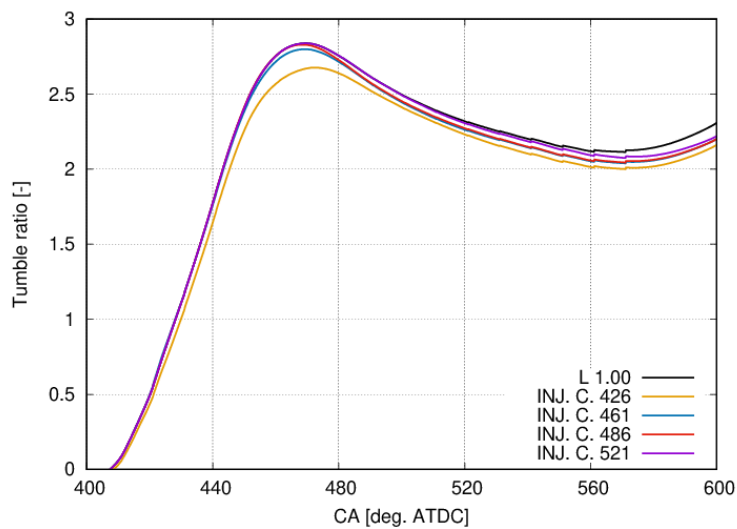


Figure 161. Effect of injection law on Tumble Ratio: Intake stroke

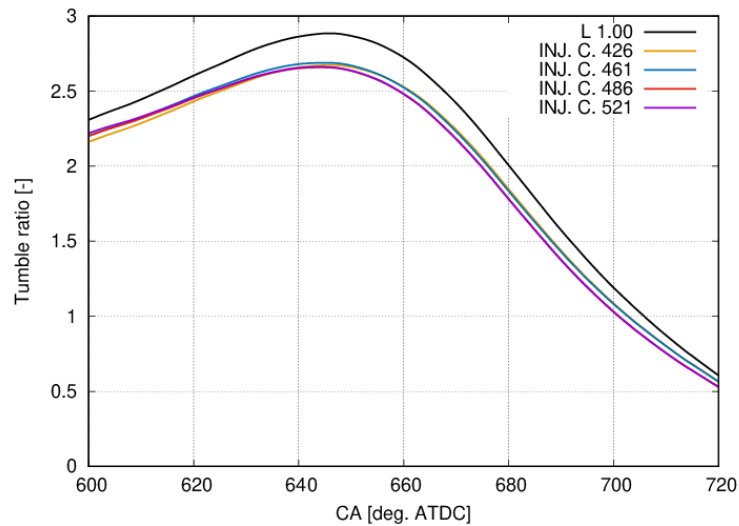


Figure 162. Effect of injection law on Tumble Ratio: Compression stroke

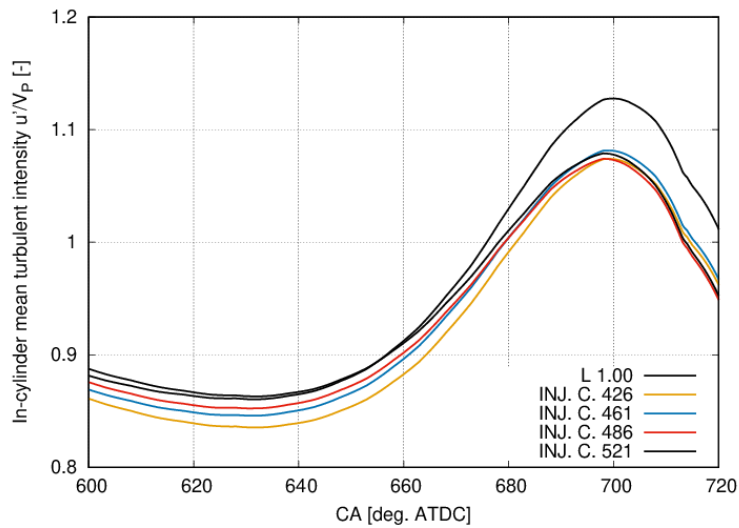


Figure 163. Effect of injection law on In-cylinder turbulent intensity

Looking for the best trade-off among all the injection centres in analysis, the optimal setting has been found to be 461 CA deg. ATDC. For this reason, it has been adopted for the next injection laws at both 50 bar and 150 bar. The results coming from these two injection pressure levels have been examined together, varying the parameter  $s$  in order to explore the effect of different amount of water.

Simulation Results of the DWI System for different Water Injection Strategies at 50 bar and 150 bar Table 25 the investigated cases for DWI systems have been reported. The injection pressure for DWI strategy has been chosen in the range between 50 bar and 150 bar, i.e. respectively the lowest and the probably highest-pressure level for the DWI solution. The lowest injection pressure (i.e. 50 bar) may be the most feasible forecast solution in a short term because of the injection system cost. In Table 26 the injected masses under stoichiometric conditions for fuel-only case and with variable parameter  $s$  are summarized. In this section a direct comparison between injection pressures 50 bar and 150 bar have been performed, splitting the study in mixture, thermodynamic and fluid-dynamic analysis.

Table 25. DWI configurations tested

Parameter s [-]	SOI / EOI [CA deg. ATDC]	Injection pressure [bar]
0.25	409 / 515	50.00
0.35	390 / 533	
0.55	377 / 595	
0.25	429 / 495	150.00
0.35	418 / 506	
0.55	396 / 527	

Table 26. Fuel and water mass introduced for the DWI strategies

Case	Parameter s [-]	Injected mass [mg]
Fuel-only		84.00
Water-added	0.25	21.00
	0.35	29.40
	0.55	46.20

#### 10.2.4 Mixture Distribution Analysis

From Figure 164 regarding the quality of the in-cylinder mixture, it can be seen that as the mass of water introduced and/or the injection pressure increases, no influence on lambda evolution is recorded. The mixture quality is close to the target for all the case between 680 CA deg. and 720 CA deg., this means that all the fuel has evaporated previously and DWI has not generated persisting fuel wallfilm that would decrease the mean in-cylinder mixture quality. In a similar way this happens also near the spark plug, where after a first phase of strong  $\lambda$  decrease, the distribution tends to stabilize after 700 CA deg. (Figure 166).

The in-cylinder STD distributions, Figure 165, show a tendency to increase the differences for higher injection pressure values while the standard deviations under spark plug indicate a high cyclic repeatability from the mixture quality point of view (Figure 167).

In Figure 168, the percentage of mass water vapor has been reported: the analysis has been limited to cases *s* 0.35 and *s* 0.55 for seeking of clarity. Being this trend the result of a mathematical expression based on cell centroid values, there are some sudden variations in the parameter in analysis: this is due to the flow motion in the cylinder, which moves away water vapor from some cell centroids inside the ideal sphere.

Only the mass of water introduced is directly related to the amount of water vapour presents under the spark plug: the injection pressure has no influence. This type of evaluation is important to get an idea of the effect of water in the first combustion phase corresponding to 10% of burned fuel (MFB10). As described in Chapter 5, water not only lowers temperatures but also acts as a diluent in a similar way to EGR, negatively impacting on laminar speed, lowering its value and increasing the cyclic dispersion of the combustion phase.

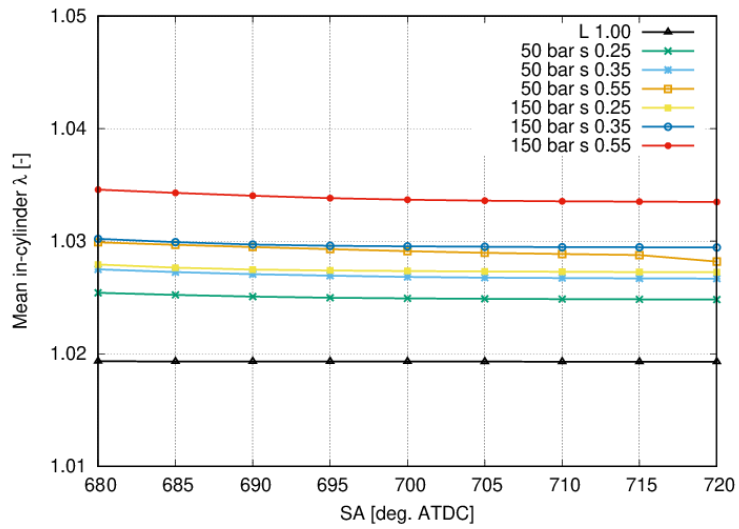


Figure 164. DWI strategy: in-cylinder mixture quality index

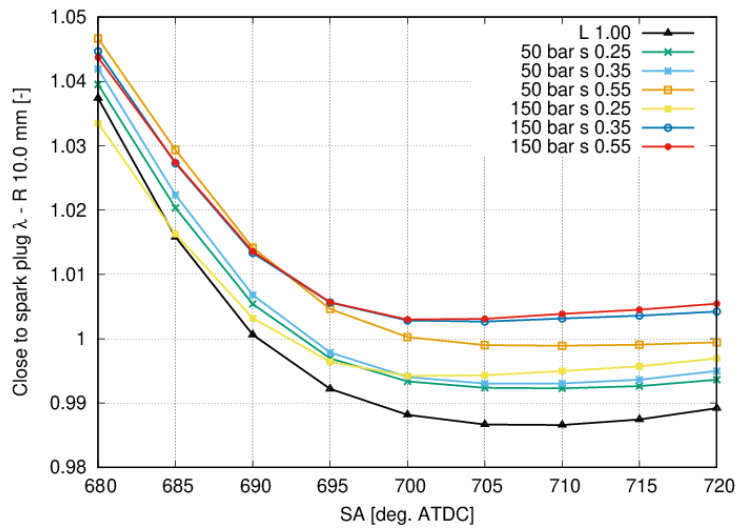


Figure 165. DWI strategy: mixture quality index close to spark plug

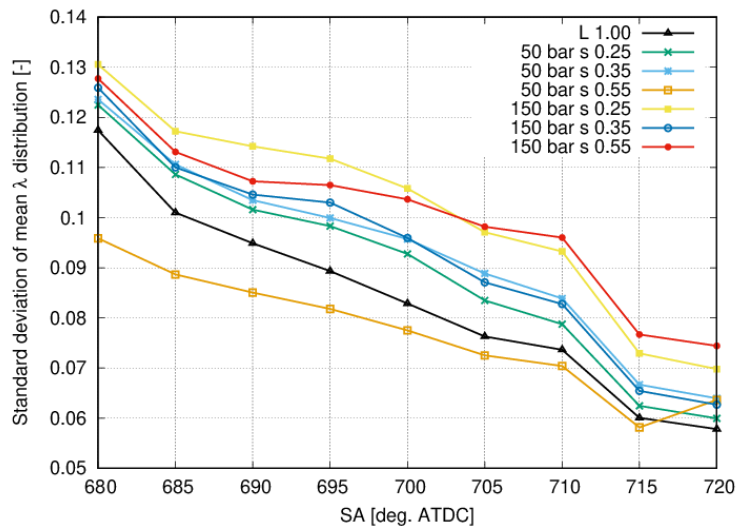


Figure 166. DWI strategy: DWI strategy: in-cylinder mixture index STD

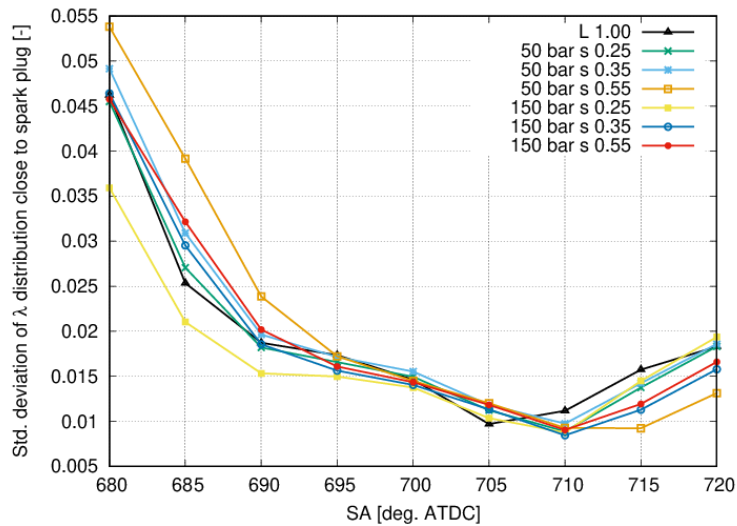


Figure 167. DWI strategy: mixture index STD close to spark plug

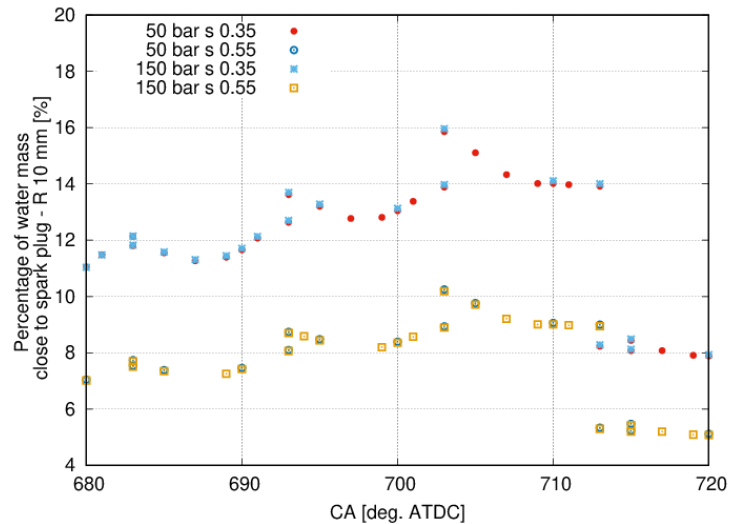


Figure 168. Percentage of water mass close to spark plug

### 10.2.5 Thermodynamic Analysis

From the thermodynamic point of view, the DWI cases shown here are able to exceed the minimum cooling level required, regardless of the ratio  $s$  and the injection pressure (Figure 169). In contrast with PWI strategy, as the quantity of water introduced increases, the cooling of the charge also increases. The best solution, focusing only on the final cooling effect, seems to be 150 bar and  $s$  0.55. Moreover, seeking for efficiency evaluation, in Figure 170, the cases running at  $s$  0.35 have been compared for both injection pressures in terms of cooling efficiency: the higher the injection pressure, the greater the cooling efficiency. This is also possible thanks to an appropriate choice of the spray pattern, which minimize direct contact with the piston and with the cylinder walls, maximizing the charge cooling effect.

The injection pressure also allows the lowering of charge temperature because of a greater breakup of the drops which therefore leads to a faster evaporation during the compression stroke, as can be seen from the Figure 171, which show the evaporation rate for all DWI configurations. The cases at 50 bar start earlier than the 150 bar but the slope of the curves slows down already in the middle of the intake stroke.

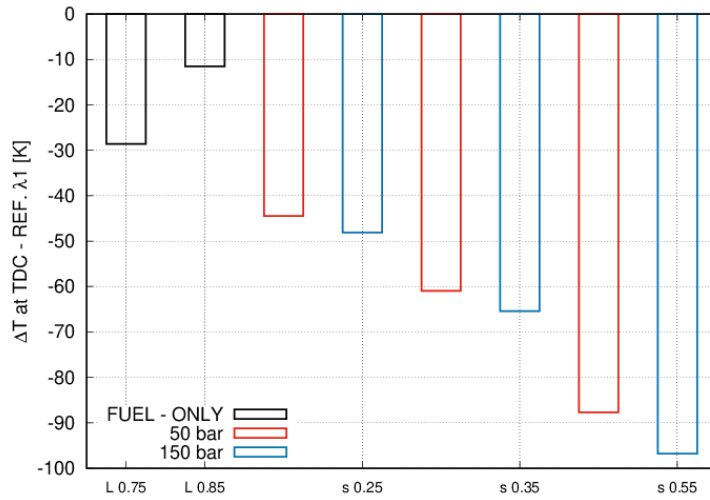


Figure 169. DWI strategies: temperature variation at TDC

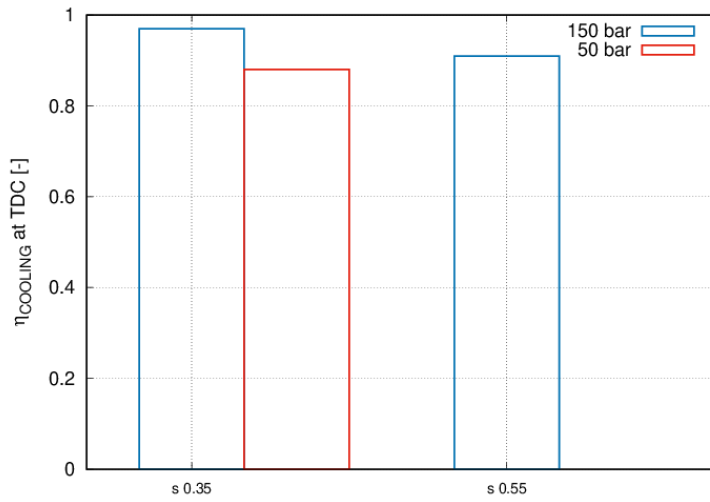


Figure 170. DWI best strategies: cooling efficiency

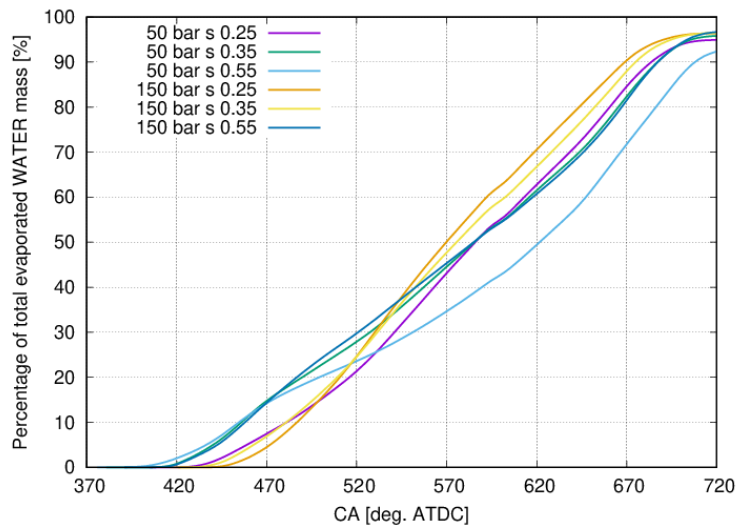


Figure 171. DWI strategies: water evaporation rates

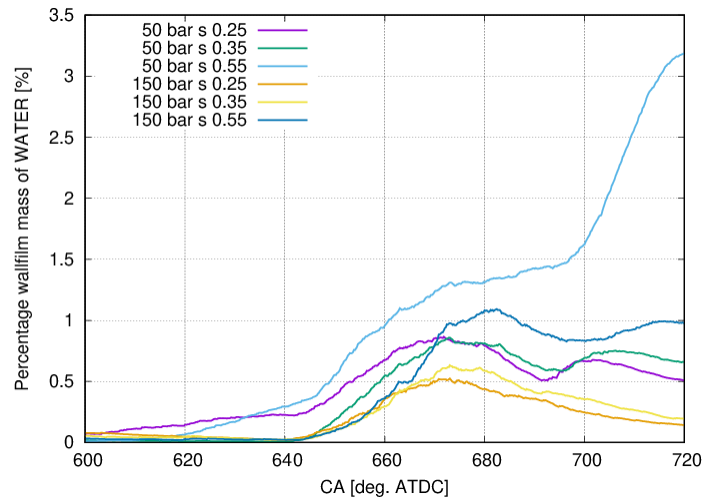


Figure 172. DWI strategies: wallfilm formation

The most critical cases, in terms of evaporation, are given by  $s = 0.55$  and in particular for injection pressure at 50 bar. In fact, in these last operating conditions, Figure 172 shows a higher residual liquid film mass inside the cylinder with also a marked effect of the injection pressure. At 150 bar and with  $s$  ratios not higher than 0.35 it is possible to limit the wallfilm generation. The greater is the amount of film deposited on the walls the greater is the decrease of the water effect, as the heat for evaporation is removed from the walls rather than from the charge.

### 10.2.6 Fluid-dynamic Analysis

In order to evaluate the effect of direct water injection on charge motion and turbulence, Figure 173 and Figure 174 show the tumble ratio profiles during the intake and compression strokes, and the average turbulence intensity in the cylinder. The reference (without water injection and stoichiometric mixture) is always above the other profiles, indicating, also in this case, a reduction in the momentum of the main vortex with DWI. The differences become more marked during the spin-up phase of the vortex. Moreover, the amount of water has a primary effect with respect to the injection pressure, decreasing the maximum turbulent intensity near 700 CA deg. as  $s$  increases.

On the other hand, the influence of the DWI on turbulence generation determines opposite effects under the spark plug. The directionality of the spray and its interaction with the charge creates a localized increase in turbulence intensity of about 7%, anticipating the maximum peak with respect to the reference (Figure 175).

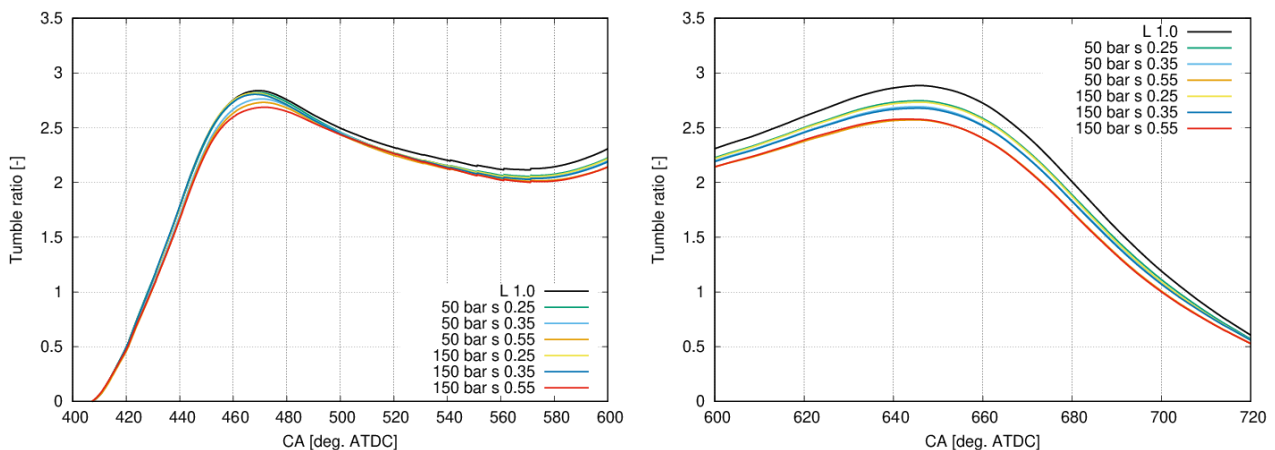


Figure 173. DWI strategies: Tumble motion, intake stroke (on the left) and compression stroke (on the right)

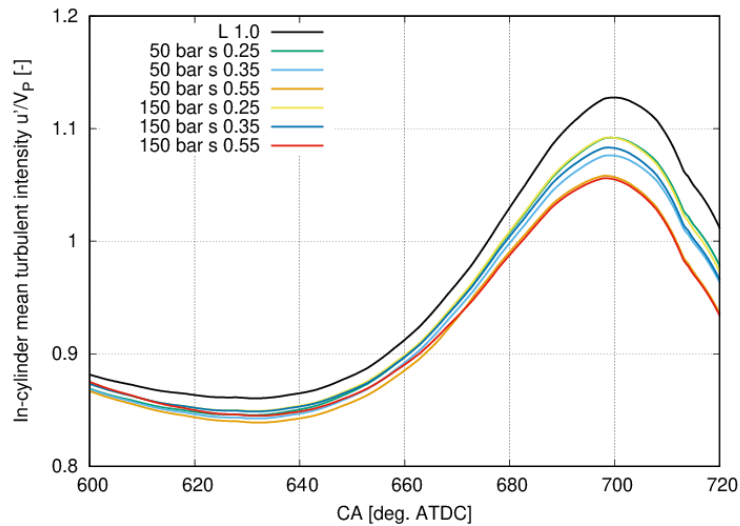


Figure 174. DWI strategies: In-cylinder mean turbulent intensity

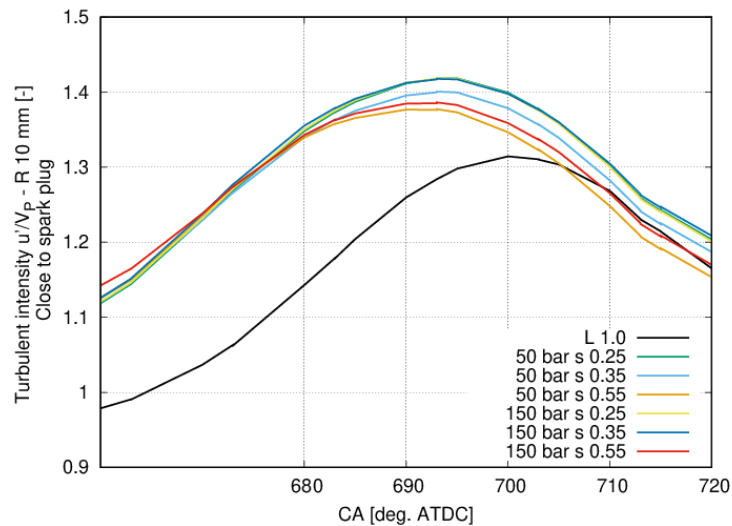


Figure 175. DWI strategies: Mean turbulent intensity close to spark plug

It is important to consider this charge motion and turbulence effects, not appeared in the PWI strategy, during reacting flow simulations. For the DWI case, in the range between 690 CA deg. and 700 CA deg. (possible ignition crank angle window) the system might experience better initial combustion speed thanks to the flame wrinkling effect.

### 10.3 Comparison between PWI and DWI best Configurations and Rich Mixture Strategies

Even if it is clear that the use of water injection in internal combustion engines is more likely to develop with PWI systems for a cost/performance reasons, it is interesting to compare PWI with the results just investigated for DWI. Based on the analyses carried out so far in terms of mixture, thermodynamic and fluid dynamic effects, the comparison is performed on the following best solutions:

1. DWI:
  - a. 150 bar: s 0.35, s 0.55;
  - b. 50 bar: s 0.35;

2. PWI:

- a. 10 bar:  $s$  0.30.

The following analyses will be focused on these parameters:

1. temperature difference with respect to the reference fuel-only stoichiometric case at TDC;
2. the cooling efficiency at TDC;
3. the evaporation rate;
4. wall film formation;
5. the standard deviation of the mixture index close to spark plug;
6. the quantity of vaporized water close to spark plug at ignition time, which affects the laminar flame speed value;
7. the tumble ratio and the mean in-cylinder turbulent intensity trends.

As mentioned above, the cooling capability of the DWI strategy results, by its nature, higher than that provided by the PWI strategy, in a similar way as for GDI systems when compared to PFI (considering the spray design optimised for both systems). From Figure 176 it can be seen that the  $s$  0.55 150 bar system involves the greatest temperature variation at TDC thanks to the high water mass injected. However, in order to understand exactly if and how much one system is better than the other in terms of cooling, it is necessary to compare them with the same water introduced or in terms of efficiency, as previously done for the individual strategies. Figure 177 confirms that a much higher efficiency is achieved for DWI (between 0.9 and 0.98). The most efficient injection condition is given by the  $s$  0.35 150 bar, while the lowest efficient is the PWI  $s$  0.3 10 bar, with a maximum value of about 0.6: this means that a considerable amount of water (40%) is not used for charge temperature reduction.

Both architectures reach a level of evaporated water mass above the target of 90% (Figure 178). The evaporation in the PWI case is also faster, thanks to better thermodynamic evaporation conditions during the intake stroke and injection timing. However, it should be reminded that the best cooling capability of the DWI also lies in the non-wallfilm generation on the cylinder walls (in PWI part of the water spray impinges walls forming wall film), trying to maximize the evaporation of the drops directly into the cylinder fresh charge.

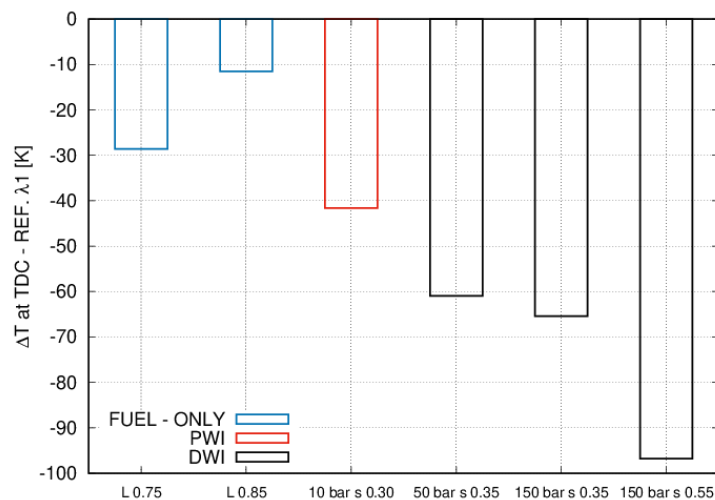


Figure 176. Temperature variation at TDC: PWI, DWI, rich mixture comparison

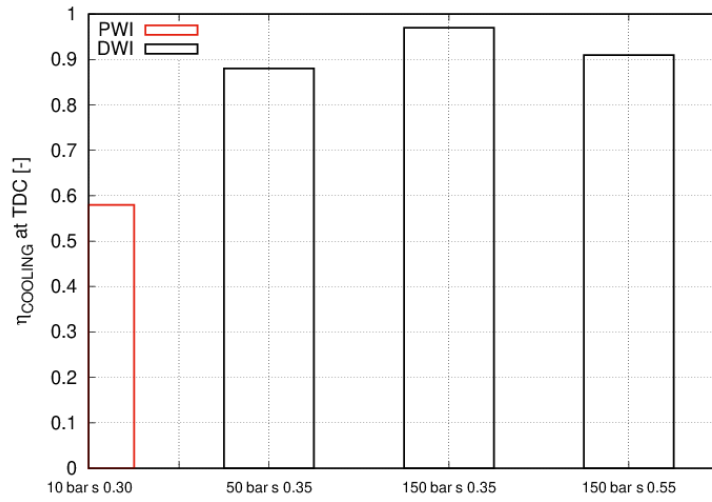


Figure 177. Cooling efficiency at TDC: PWI and DWI comparison

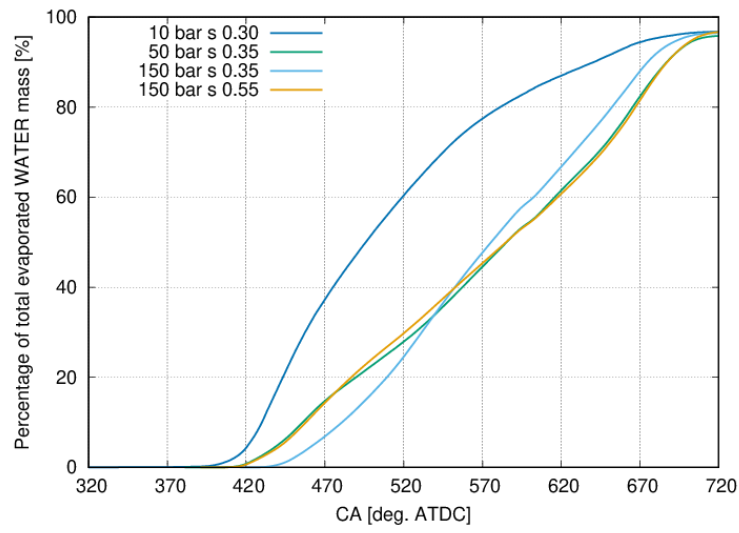


Figure 178. Evaporation rate: PWI and DWI comparison

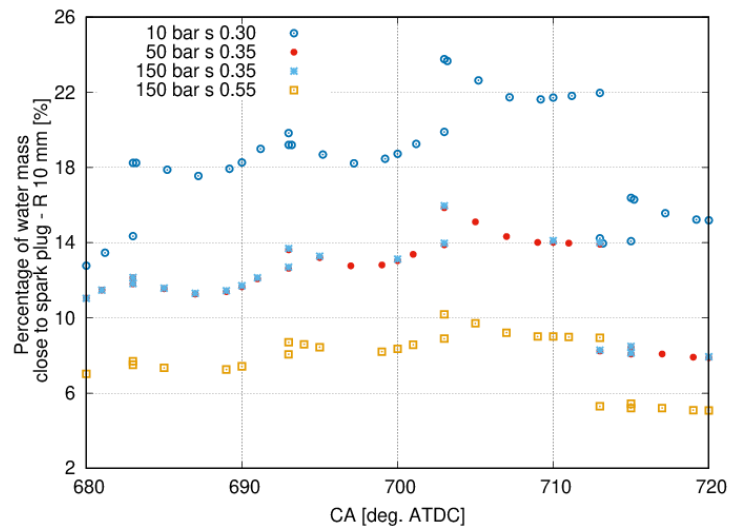


Figure 179. Percentage of water mass under the spark plug: PWI and DWI comparison

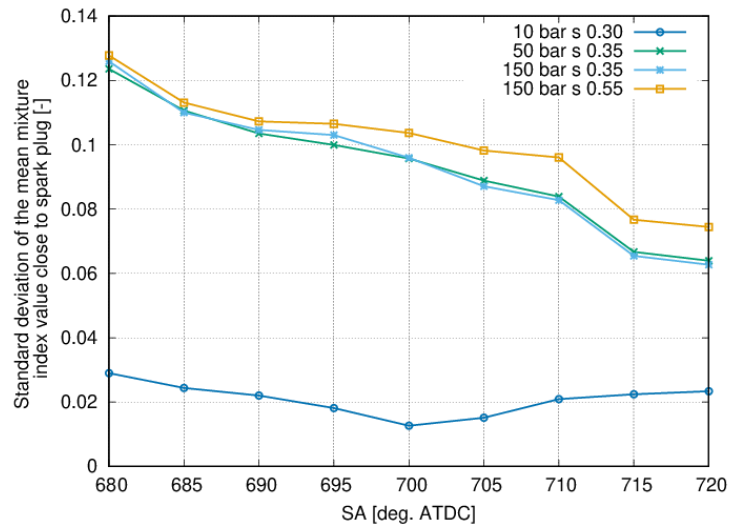


Figure 180. PWI and DWI strategies: mixture index STD close to spark plug

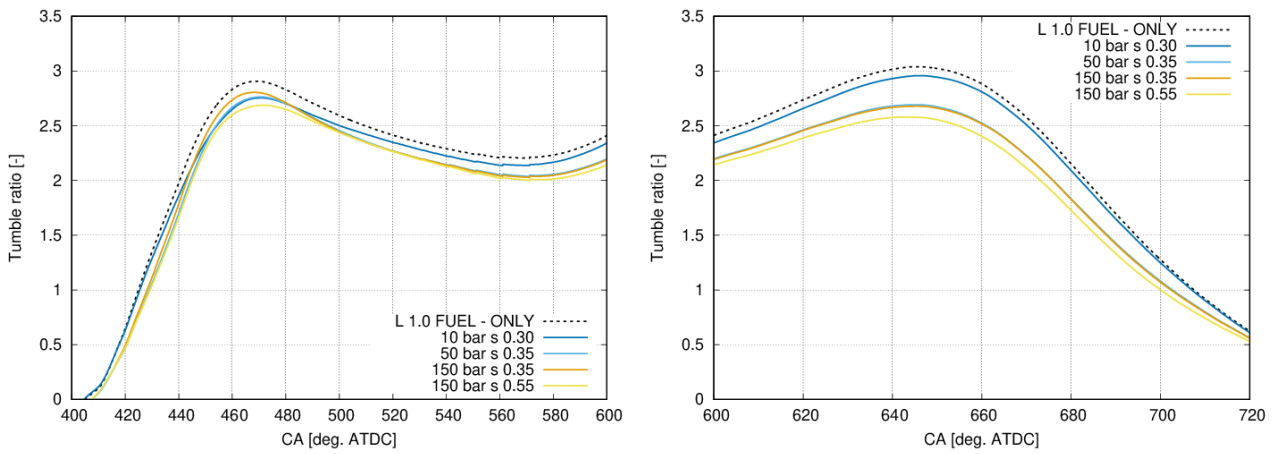


Figure 181. PWI and DWI strategies: Tumble motion comparison

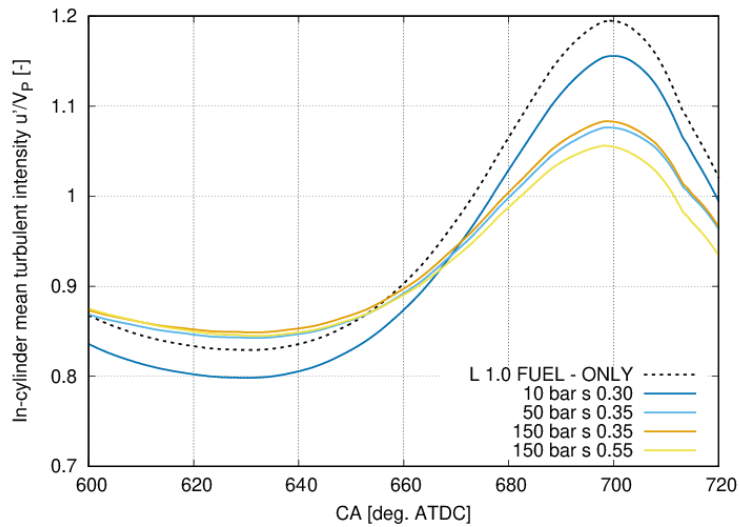


Figure 182. DWI strategy: in-cylinder turbulent intensity comparison

As stated before, the quantity of vaporized water close to the spark plug and near the possible ignition crank angle interval (from 680 CA deg. to 720 CA deg. ATDC) is one of the parameters affecting the laminar flame speed value: the more the water mass fraction, the slower the laminar flame speed is at ignition time, leading to longer combustion duration. For this reason, in Figure 179 the quantity of water under the spark plug has been reported for PWI and DWI architectures: the PWI case shows a greater mass fraction of water than that provided by DWI strategy. On the other hand, the standard deviation of the hypothetical gaussian distribution of the mean in-cylinder mixture index (Figure 180) is lower for PWI than for DWI: there is less interference between the liquid jet and the mean in-cylinder flow field, as highlighted by the tumble motion trend in Figure 181. The PWI trend is the closest to the fuel-only case: this implies a maximum level of turbulence, very close to the fuel-only case for PWI strategy (Figure 182). So, one might expect a less cyclic variability for PWI solutions.

## 10.4 Evaluation of the Main Effects of Higher Compression Ratio on PWI and DWI Strategies

The baseline engine has been modified in terms of compression ratio increasing it up to 10.5 for both PWI and DWI architecture, considering the best strategies seen so far in terms of mixture, thermodynamic and fluid dynamics effects, in order to take advantage from the water cooling and try to increase the thermodynamic efficiency of about 1.7%. For this reason, for the DWI case it was taken  $s\ 0.35\ 150\ bar$  and for PWI  $s\ 0.3\ 10\ bar$  case.

### 10.4.1 Higher Compression Ratio Geometries Design

The modification of the combustion chamber was performed for PWI and DWI architectures with two different design approaches, that must be highlighted in order to understand the non-reacting and reacting flow results. The geometries are reported in Figure 183.

For the PWI system, the increase in the compression ratio was achieved by acting on the shape of the piston, in particular by decreasing the depth of the bowl, leaving unchanged the squish high. So, in addition to the thermodynamic effect of the different compression ratio, it will be necessary to evaluate what fluid dynamics and turbulence consequences, positive or negative, the new shape of the piston involves, taking into account that no further modifications (intake duct, valve lift laws, etc.) have been made.

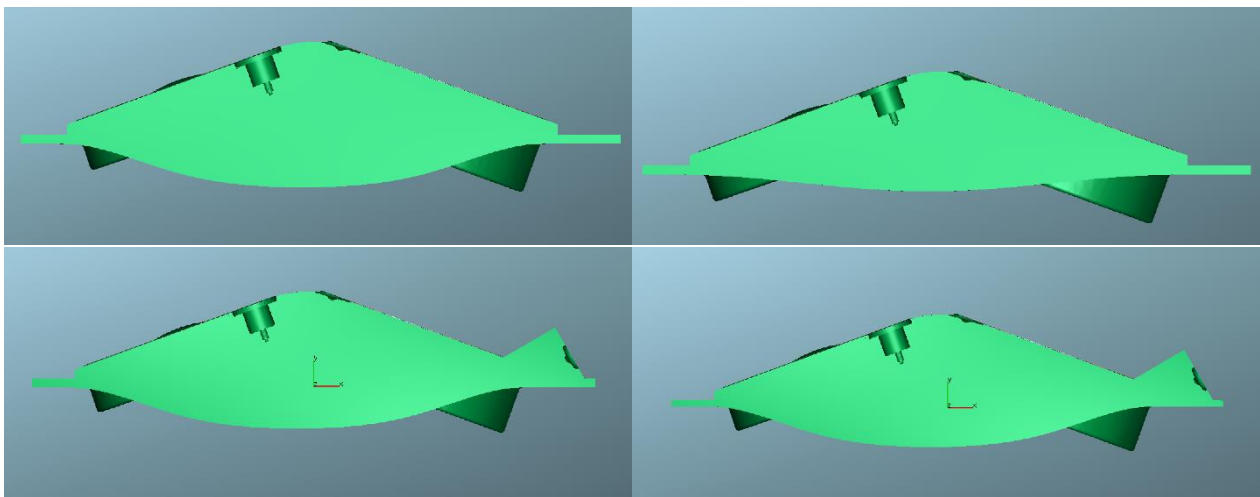


Figure 183. On the top, PWI CR 9.5 (left) PWI CR 10.5 (right), on the bottom DWI CR 9.5 (left) DWI CR 10.5 (right)

On the contrary, for the DWI system the original shape of the piston remained unmodified, and the increase in RC was achieved by decreasing the squish height. In this way the impact on the fluid dynamics could be minimal, making the thermodynamic effect more evident.

A value of CR higher than 10.5 was not feasible because of the intrinsic drawing limits in the present combustion system baseline geometry.

### 10.4.2 Simulation Results in Non-Reacting Flow Conditions for Higher Compression Ratio

The simulations were performed keeping constant the trapped air mass and leaving the fuel always in stoichiometric conditions. This leads to an increase in engine output power (as provided by OpenWAM) as a direct consequence of the increased thermodynamic efficiency (about 1.7 %). On the other hand a different strategy could be chosen, for having the same rated power of the baseline engine, it would be necessary to reduce the fuel consumption and so the trapped mass, also reducing the boost pressure of the turbocharger. The last would be another advantage in terms of losses reduction. It must be underlined that this investigation is carried out under non reacting flow conditions and that combustion calculation are mandatory to include properly the effect (and the penalty) of the water dilution on combustion reaction rate.

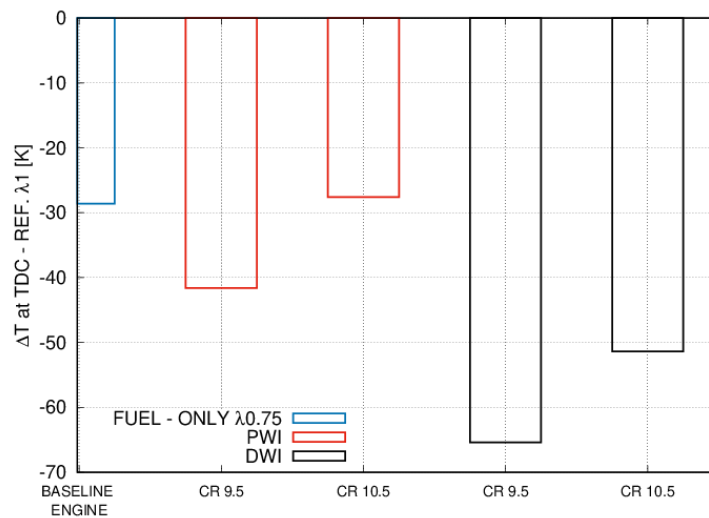


Figure 184. PWI vs DWI strategies: compression ratio effect on temperature reduction at TDC

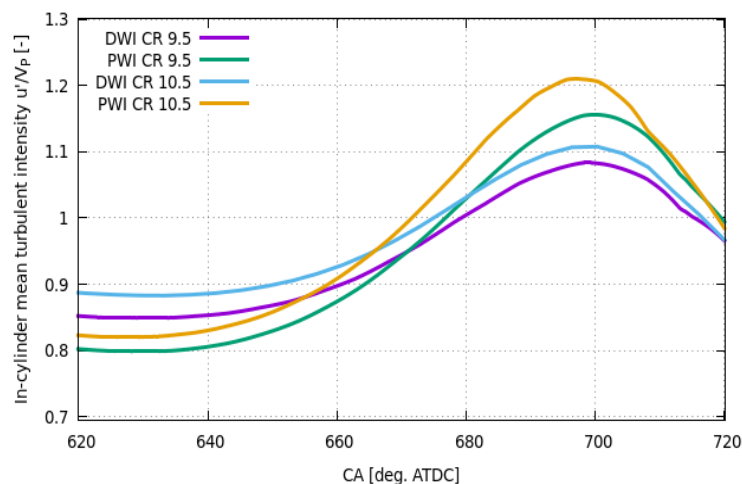


Figure 185. PWI vs DWI strategies: compression ratio effect on Tumble ratio

The compression ratio has a similar effect for both PWI and DWI. Moving from CR 9.5 to CR 10.5 results in a rise of the average internal cylinder temperature at TDC of about 14 K in both cases (Figure 184). Therefore, for these two analyzed cases, the effect of the compression ratio seems to be more marked for the PWI strategy, where the reduction is 35%.

In the latter case, with CR 10.5, the  $\Delta T$  at TDC almost equals that achievable by the rich mixture (reference cooling), making this strategy still interesting even if it appears to be borderline. On the other hand, the DWI system has a much higher temperature difference at TDC compared to the  $\lambda$  0.75 case, about -65 K, which allows it to have an optimal cooling even after the CR increase, bringing it to about -52 K (about twice as much as the  $\lambda$  0.75 case).

It is reminded that higher mass-averaged in-cylinder temperature differences  $\Delta T$  indicate a better charge cooling while lower values denote possible knocking issues, as well as the risk to overcome the TiT threshold. These mixture temperature evaluations at TDC, compared to the stoichiometric case without water injection, are thus a measure of the net performance of the water injection.

Finally, as far as the turbulence is concerned, Figure 185 shows the influence of the new designs on the intensity turbulent trend. Higher peak values have been obtained for both strategies increasing CR, especially at 700 deg., closer to possible spark angle. This is due to the elongated shape of the cylinder which allows a better compression and vortex breakdown. Furthermore, even moving towards CR 10.5 the PWI system continues to have a higher turbulence generation than the DWI, due to the fact that the indirect water injection tends to follow the tumble motion created by the intake port design rather than hinder it. So, the new piston shape for the PWI system seems to emphasize turbulence generation, while in the DWI system with CR 10.5, only a small initial turbulence increase up to 700 CA deg. was recorded.

Therefore, increasing the CR there is a worsening of the surface-to-volume ratio of the combustion chamber but there is also an increase in the maximum level of turbulence. However, a closer look at Figure 185 shows that in the case of the highest compression ratio 10.5 (both PWI and DWI) the turbulence tends to dissipate faster immediately after reaching its peak. For computational time reasons, the non-reacting simulations have been interrupted at 720 CA deg., but it is precisely from this angle that the curves (both PWI and DWI) tend to cross. It will therefore be necessary to verify what happens to the turbulence during prolonged combustion simulations up to 800 CA deg. This interesting effect has been attributed to a shape factor related to the new designs used for the RC increase. The global dynamic of the Tumble vortex might be no longer optimized, dissipating turbulence more quickly during the expansion phase. Only through a new design of the intake duct this negative final effect could be recovered.

As pointed out several times, the laminar flame speed, among others, also strongly depends on turbulence evolution inside the cylinder. So, in the reacting flows analysis, it will be necessary to evaluate the effective influence of turbulence on the laminar flame speed and combustion process.

## 10.5 Summary

A methodology for the CFD simulation of non-reacting SI GDI turbocharged engine under water injection operation has been proposed. Direct Water Injection (DWI) architecture has been tested for the same baseline engine configuration and the main results have been checked in terms of evaporation rate, cooling temperature, and efficiency. The main aim of these simulations was to maximize water injection benefits and minimize possible disadvantage, such as primarily oil dilution and incomplete water evaporation.

The DWI case has been run at full power condition, at the same rated power engine speed by varying: i) the injection pressure; ii) the injection timing; iii) the normalized water injected on the stoichiometric fuel ( $s$  parameter). Moreover, for pursuing the target of improving the engine efficiency over the whole engine map for CO<sub>2</sub> emission reduction and maintaining good performance level, the compression ratio CR of the baseline engine have been increased up to 10.5.

From these analysis, some macroscopic evaluation indexes have emerged: a) temperature difference with respect to the reference fuel-only stoichiometric case at TDC; b) cooling efficiency at TDC; c) evaporation rate; d) standard deviation of the mixture index close to spark plug, which is a measure of its distribution; e) quantity of vaporized water close to spark plug at ignition time, which affects the laminar flame speed value at ignition time; f) tumble ratio and mean in-cylinder turbulent intensity trends.

In the DWI strategy the injection pressure levels have been varied in the range 50 and 150 bar. In DWI applications there is more flexibility in choosing the SOI or EOI timing and the concept of 'injection centre' has been applied. Results obtained running the simulations at 50 bar and 150 bar have been compared, changing the mass of injected water. Pursuing the maximum efficiency, the best choice is *150 bar s 0.35*, which by far succeeds in overcoming the cooling obtained with the  $\lambda$  0.75 strategy. Instead, considering the costs, the best solution would be 50 bar. In addition, it has been showed how the DWI injection interacts with the main intake flow: the more the injected water mass, the less the turbulent intensity.

Finally, the effects of the geometrical variation of the engine in terms of compression ratio, has showed some differences on the best strategies identified, whose comparison has been reported also for the PWI configuration for clarity reason. Increasing the CR results in a decrease of cooling due to the higher thermal efficiency. Furthermore, the turbulence tends to decrease more rapidly during the expansion stroke, which might lead to combustion deceleration.

In conclusion, the *DWI s 0.35 150 bar SOI 418 CA deg. CR 9.5*, *DWI s 0.55 150 bar SOI 396 CA deg. CR 9.5* and *DWI s 0.35 50 bar SOI 390 CA deg. CR 9.5* are able to keep the charge temperature variation at TDC lower than  $\lambda$  0.75 strategy with good mixture distribution, resulting in the best DWI strategies found. Possible improvement given by the higher compression ratio must be checked under reacting flow conditions, extending the simulation up to 800 CA deg.

The comparison presented in this chapter between DWI and PWI strategy has shown that although the charge cooling capacities are much higher for DWI, PWI shows some important benefits from the turbulence point of view, so it still remains an interesting strategy to test under reacting conditions.

# Chapter 11: PWI and DWI Engine Applications under Reacting Flow Conditions

It has been pointed out that, under the pressure of rapid climate change, the European community will introduce new and increasingly stringent policies on CO<sub>2</sub> emissions, that will not allow the use of mixture enrichment for the protection of exhaust components (Turbine an TWC) and knock mitigation. This will lead to a complete overhaul of the AES systems implemented so far, forcing to operate at  $\lambda$  1.0 on the overall engine map.

For these reasons, it becomes important to investigate under reacting flow conditions in order to estimate the real potential of water evaporation and its anti-knock attitude. The water acts as a heat sink reducing the mixture temperature during the compression phase: the added water also changes the ratio of specific heats of the charge mixture and slightly dilutes the oxygen concentration.

In the previous chapters it has been examined, through CFD simulations, the application of the water injection with both PWI and DWI architecture in non-reacting flow case, highlighting the best configurations in terms of injection pressure, mass introduced, evaporation capability and cooling efficiency. In addition, the effects on the variation of some fundamental geometrical parameters, such as compression ratio and stroke to bore ratio, have been included. Despite the fact that those simulations carried out in non-reacting conditions are very effective to drive the water injection system design for ICE applications, they are not sufficient to provide a complete overview of the real effects of water. In fact, in previous chapters focused on the literature review and the detailed chemistry, it has been highlighted that the water is a diluter and it affects greatly the laminar flame speeds and the auto-ignition time of the mixture. Therefore, a detailed combustion analysis has been performed on the same engines previously analysed by using CFD.

The methodology is able to account for both physical and chemical effects of the mixture dilution due the injected vaporized water, being suited for the assessment of the water injection system architecture and operating conditions considered. The goal is to find the final trade-off between the benefits arising from the mixture cooling and the shortcomings due to combustion rate lowering. In particular, the final aim is to explore how the water injection may contribute to increase the performance of the engine (or in turn to reduce the specific fuel consumption at fixed power) while fulfilling the exhaust gas temperature limits.

The investigation is performed by using 3D CFD simulations, using the CFD code AVL Fire v2020.

## 11.1 Combustion Simulation Set-up

For a sake of completeness in the following a brief summary of the combustion simulations setup is provided. In these simulations the overall setup is the same as that used for non-reacting flow simulations, with some specific user-defined functions and sub-models activation to handle premixed reacting flow combustion. The combustion is simulated by using the ECFM – 3Z model [90]. Specific and custom models have been used to model: spark ignition, the flame laminar speed, and the knock in term of autoignition time (IDT) and knock rate. As mentioned in Chapter 5 detailed chemical simulations with machine learning was extensively used to populate look-up tables, run time called by the main CFD solver. Table 27 resumes the main set-up adopted for these combustion simulations, as described in Chapter 4.

Table 27. Combustion simulation main set-up and models

<b>Start angle</b>	270 CA deg. ATDC
<b>End angle</b>	850 CA deg. ATDC – corresponding to EVO
<b>Turbulence model</b>	K-z-f
<b>Wall heat model</b>	Hybrid wall treatment
<b>Law of the wall</b>	Standard + Han-Reitz
<b>Combustion model</b>	ECFM-3Z adopting correlations for LFS, flame thickness and auto-ignition delay time
<b>Ignition model</b>	Lagrangian ignition model
<b>Knock model</b>	Two steps autoignition model

It must be highlighted that the ECFM-3Z combustion model included a single component fuel and it is initialized by the fuel mass fraction equivalence ratio and EGR mass fraction which is expected to include the water formed from combustion. A representative fuel of commercial gasoline (named GASOLINE 1 in Fire code), was used.

As far as the water vapor mass fraction due to the liquid water injected is concerned, the ECFM-3Z model allows to initialize only as a part of the EGR mass fraction. In order to properly account for the injected water contribution to the laminar flame speed and auto-ignition, taking it separated from the water included in the combustion products (i.e, EGR), a devoted model approach has been used. An external subroutine has been created to initialize, before ignition time, a passive scalar that transport solely the water vapor from the injected water evaporation. In such a way the local gaseous mass fraction of the vaporized injected water is available to be used runtime for the evaluation of both the laminar flame speed and the autoignition delay time, keeping separated its contribution from that coming from EGR (and combustion water) dilution.

Differencing schemes are second order for mass, momentum and energy, while turbulence is resolved with a second order blended scheme. The solution is converged when the residual error for each equation is below the tolerance threshold of  $1e-4$ . No variations in terms of grid generation has been performed, being already optimized also for a combustion simulation.

## 11.2 Criteria and Aim of Combustion Simulation Analysis

The results are discussed with the aim to verify not only the possible gain in performance but also to operate the engine safely with respect to the knock and the fulfilment of the *TiT* limit.

As far as the *TiT* limit is concerned, it must be noted that CFD simulation ends close to EVO and therefore the *TiT* limit must be shifted into a limit of in-cylinder temperature at a given crank angle. Based on previous estimates made with the OpenWAM 1D code, a *TiT* limit of 1030°C reasonably corresponds to an in-cylinder exhaust gases temperature limit at 800 CA deg. ATDCF equal to 1903,15 K (1630 °C).

With regard to knock, the engine knock limit condition has been evaluated using a MAPO threshold value defined according to the BOSCH criterion, which consists in dividing the engine speed (rpm) by 1000 (7 bar). As done in experiments, a 4th order Butterworth band-pass filter between 5kHz and 20kHz has been applied to the numerical pressure trace in a crank angle window between -10 and 80 crank angle degrees after top the dead center (ATDC). The pressure trace was recorded by a virtual probe flush mounted on the cylinder head close to the location of the water injector (the probe location is the same for both configurations).

In order to have an approach closer to reality, trying to include the effect of the cycle-to-cycle variation on knock, that can not be reproduce by RANS simulations, the Knock Limit Spark Advance (KLSA) has been

evaluated as the crank angle that provides a MAPO of 7 bar minus 4 crank angle degrees. In this way the KLSA and the evaluated MFB50 crank angle provided a quite good representation with respect to the real engine operations.

Finally, the data related to the characteristic combustion angles have been extrapolated from the pressure trace, recorded from the virtual transducer using post-processing analysis methods as those used at the test bench for the indicating data analysis and base of a First Law of Thermodynamic analysis.

The reference cases are the results obtained from combustion simulations without water injection at full power with lambda equal to 0.75, 0.85 and 1.0.

The PWI and DWI architectures have been tested only under stoichiometric mixture conditions to fulfill with EU AES policy assessment and thus to cope with the reduction of emissions. Table 28 lists all the cases with water injection evaluated: in the following they are referred to as from *W1* to *W7*. They include different water injections system layouts (i.e., PWI and DWI), amount of water injected (i.e, *s* parameter), injection pressures, engine compression ratios and bore to stroke ratios. It is reminded that for the *W7* case, in order to keep the same output power and limiting the mean piston speed at 20 m/s, the rated power engine speed was reduced to 6250 rpm.

Table 29 and Table 30 report the amounts of water and fuel injected and the laws of injection, the best found during the study under non-reacting flow conditions.

Finally for the sake of clarity, the main results obtained from previous simulations under non-reacting conditions are summarized in Figure 186 Figure 188: the turbulent intensity, the temperature variation at TDC and the distribution of mixture under spark plug in a sphere with a radius of 10 mm.

Table 28. List of water injection cases examined in reacting flow conditions

CASE #	H2O INJ. SYST.	Parameter <i>s</i> [-]	Inj. Press [bar]	CR	S/B
W1	<b>DWI</b>	0.35	50.00	9.5	1.01
W2		0.35	150.0	9.5	
W3		0.55		9.5	
W4		0.35		10.5	
W5	<b>PWI</b>	0.30	10.00	9.5	
W6				10.5	
W7				1.13	

Table 29. Fuel and water mass injected

Case ( $\lambda$ 1.00)	Parameter <i>s</i> [-]	Fuel/Water injected mass [mg]
<b>Fuel-only</b>	-	84.00
<b>Water-added</b>	0.30	25.20
	0.35	29.40
	0.55	46.20

Table 30. Injection strategies

TYPE OF INJECTOR	Injection pressure [bar]	Parameter s [-]	SOI [CA deg. ATDCF]	EOI [CA deg. ATDCF]
<b>GASOLINE</b>	350.0	-	378	532
<b>DWI</b>	150.0	0.35	418	506
<b>DWI</b>	150.0	0.55	396	527
<b>DWI</b>	50.0	0.35	390	533
<b>PWI</b>	10.0	0.30	293	433

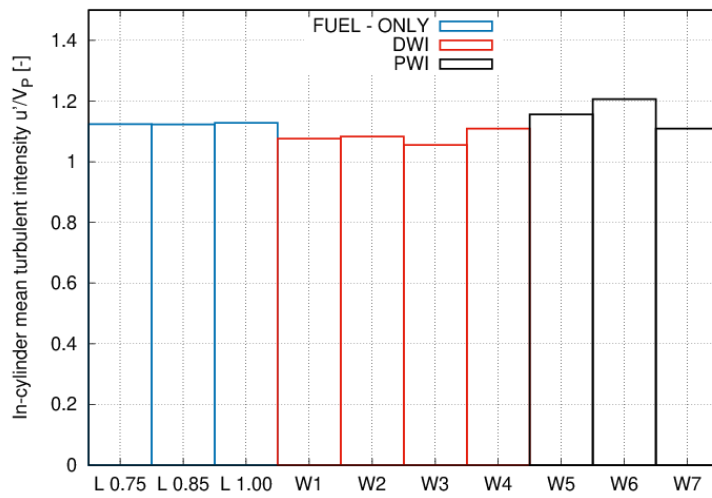


Figure 186. In-cylinder turbulent intensity of W1-W7 and rich fuel strategies in non-reacting conditions at 700 CA deg.

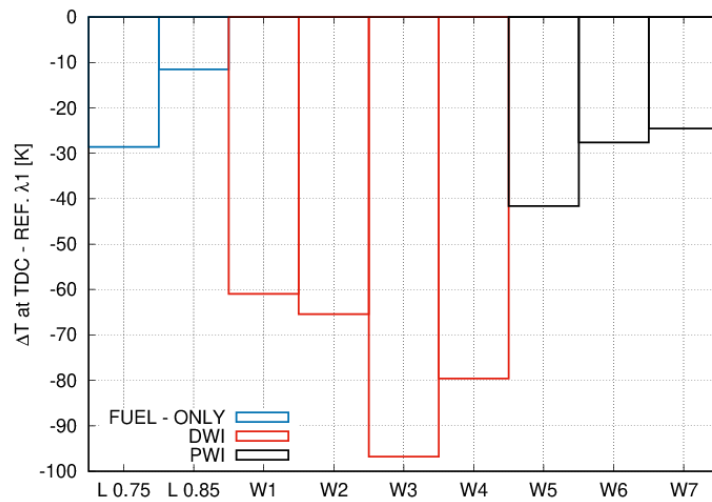


Figure 187. Temperature reduction at TDC of W1-W7 and rich fuel strategies in non-reacting conditions

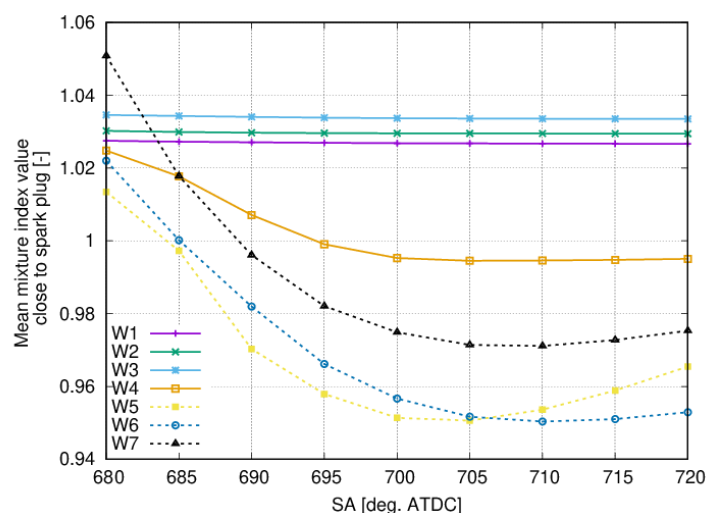


Figure 188. Mixture distribution close to spark plug of W1-W7 and rich fuel strategies in non-reacting conditions

### 11.3 Combustion Simulation without Water Injection

In this paragraph are reported the results of the combustion simulations without water injection considering the following values of  $\lambda$  0.75, 0.85 and 1.0. The results have been used as references to characterize the baseline engine with respect to the application with water injection at stoichiometric conditions.

Figure 189 and Figure 190 show the MAPO values on the y-axes, obtained from the ignition advance sweep in the various simulations, versus the MFB50 crank angle and the exhaust gas temperature at 800 CA deg., respectively. As expected, by advancing the ignition, the combustion center (MFB50), which represents the angle of 50% of burned fuel, moves toward TDC. However, below 15-18 CA deg. of MFB50, only the case with the richest mixture can maintain a MAPO value below the maximum threshold (7 bar) for greater SA. The reason is found in its greater ability to lower the fresh mixture temperatures, inhibiting the occurrence of autoignition sites thus increasing the antiknock attitude.

Figure 191 depicts the combustion heat release for the same SA crank angle at 706 CA deg. ATDC for all cases plotted (the selected SA provides the most intense knocking case at lambda 1 between those simulated), while Figure 192 shows the in-cylinder pressure recorded at the transducer location. From the latter figures one can see that the case lambda 0.75 exhibits the lowest knock attitude (no oscillations or spikes in the heat release and pressure graphs) thanks to largest fuel enrichment cooling effect and the more homogeneous mixture distribution. On the contrary, the lambda 1.0 case with SA 706 CA deg., provides at 736 CA deg. a very hot region under the exhaust valve and close to the squish area. As a consequence, the temperature of the mixture increases, rapidly accelerating the various oxidation reactions leading to the auto-ignition of the mixture before the arrival of the flame (Figure 193).

As far as the turbine inlet temperature of the exhaust gas is concerned, Figure 190 shows that for high MFB50 crank angle values (i.e., due to delayed spark advance because of knock) the combustion, for  $\lambda$  1.0 and 0.85, moves late in the expansion phase, raising the temperature of the exhaust gases at 800 CA deg. ATDCF much above the imposed limits. In the case of mixture at  $\lambda=1.0$ , values over 2000 °C at 800 CA deg. ATDCF have been achieved, while the limits imposed as a criteria in present simulation was set to 1630 °C. As a matter of fact, only the SA values that allow to remain in the lowest left part of the graph of Figure 190 are suitable for safe engine operations as far as both knock and TiT requirements are considered. Basically, at full power condition, the present high *bmep* engine can work only at  $\lambda$  0.75. Both the  $\lambda$  1.0 and the  $\lambda$  0.85 cases, at the knock safe advance points, do not respect the constraint of the prescribed average in-cylinder maximum temperature at 800 ca deg. ATDCF which has been set as representative of the TiT limit. This highlights that the TiT limits are more demanding than the knock limits at safe engine operation.

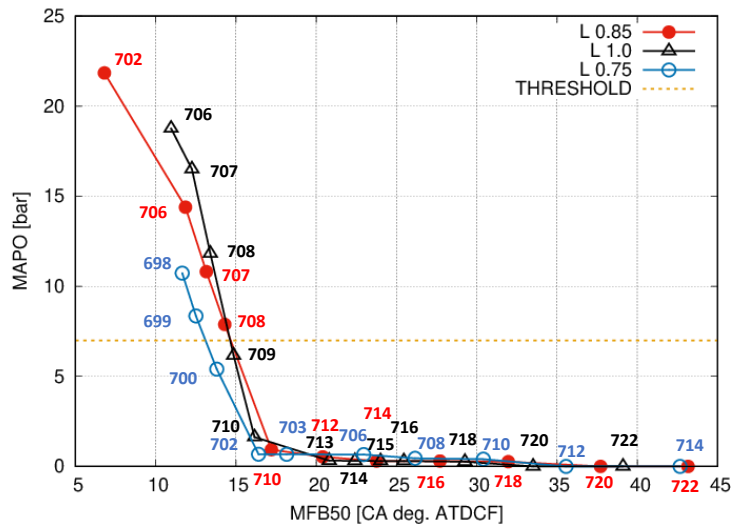


Figure 189. MAPO vs MFB50 only-fuel combustion cases

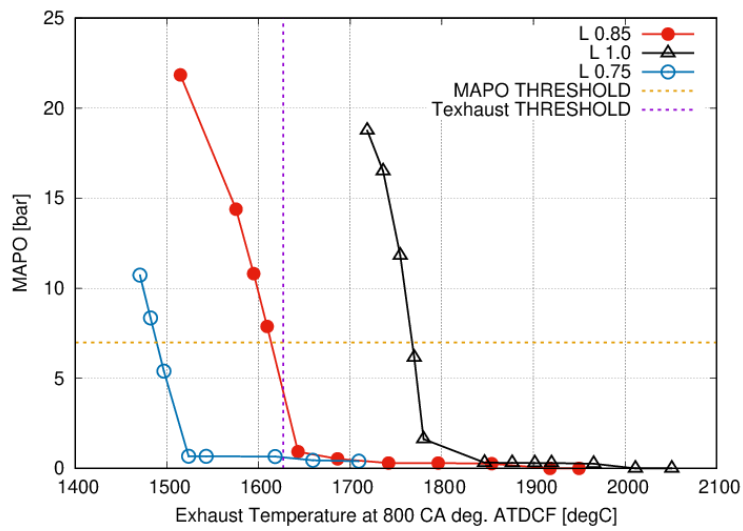


Figure 190. MAPO vs exhaust temperature only-fuel combustion cases

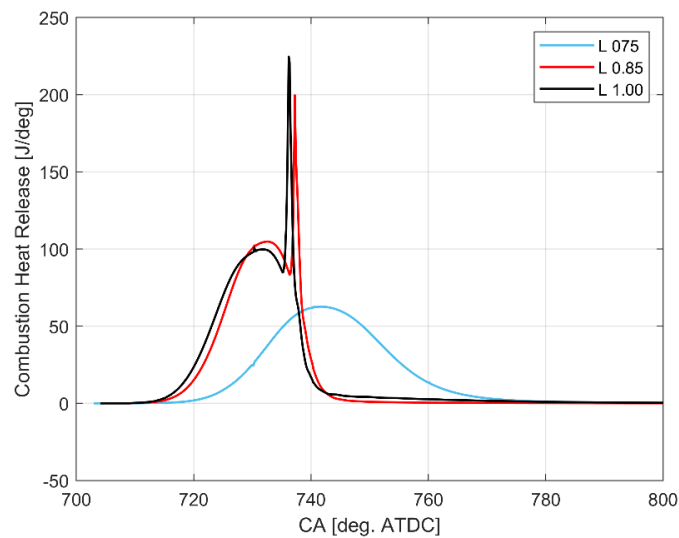


Figure 191. Combustion heat release, only-fuel combustion cases, SA 706 CA deg.

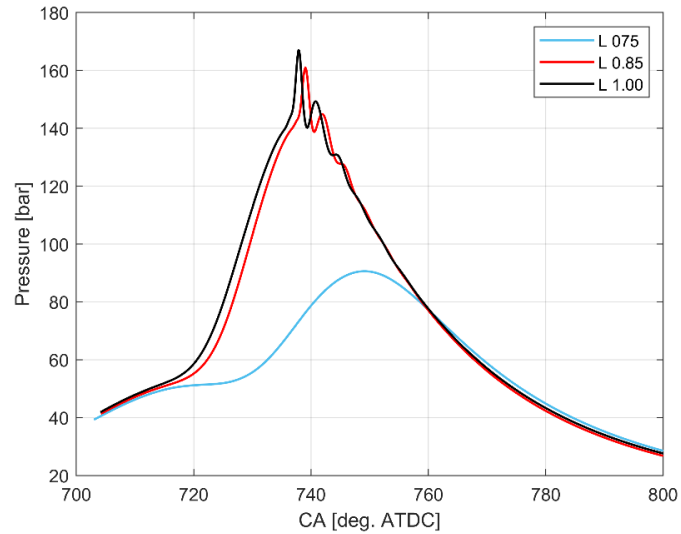


Figure 192. Pressure sensor, only-fuel combustion cases, SA 706 CA deg.

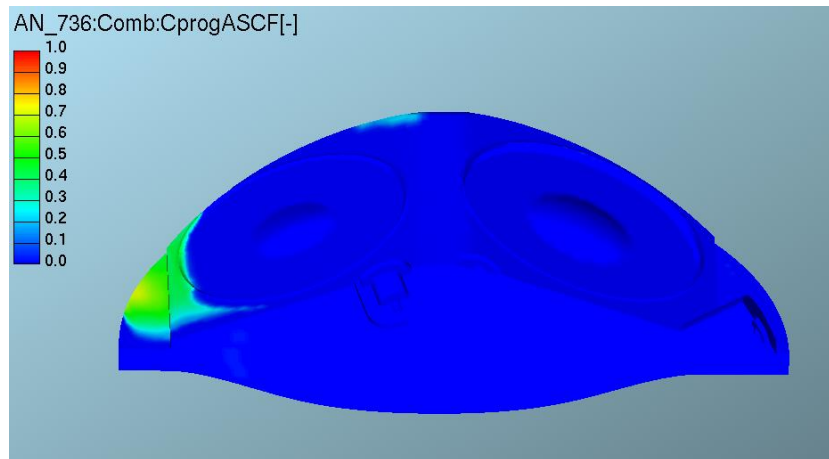


Figure 193. Mixture auto-ignition region at 736 CA deg. for the case  $\lambda$  1.0 with SA 706 CA deg.

The IMEP\_H (Indicated Mean Effective Pressure at High pressure), calculated in the symmetric angular range between 640 CA deg. and 800 CA deg., is shown in Figure 194 versus MFB50 crank angle and SA, normalized with respect to the target value ( $IMEPH_{target}$ ). The reference target IMEPH is related to the working point of full power and safe conditions from the knock (KLSA minus 4 degrees) and *TiT* point of view ( $\lambda$  0.75 with SA 703 CA deg. ATDCF). It should be noted that the reference was taken as the target IMEPH rather than the target BMEP in order to perform the comparisons based on present combustion three-dimensional simulation that rely on the high pressure and closed valve part of the engine cycle. This assumption may be taken as reasonable for the purpose of the present investigation.

Values greater than 1 indicate an increase in the *engine output indicating specific work*, while the dashed line in each individual trace indicate the region undergoing knock conditions, up to MAPO higher than the threshold value. The knock limit spark advance (KLSA, those allowing operating at limit of knock minus 4 CA deg.) for each of the mixture indices considered are those at the boundary between the dashed part and continuous part of each trace.

It is to note that at fixed target IMEPH value, the KLSA at  $\lambda$  0.75 is 703 CA deg. ATDCF, the KLSA at  $\lambda$  0.85 is 712 CA deg. ATDCF and the KLSA at  $\lambda$  1.00 is 713 CA deg. ATDCF. The in-cylinder thermal regime is higher for  $\lambda$  0.85 and  $\lambda$  1.00 than for  $\lambda$  0.75.

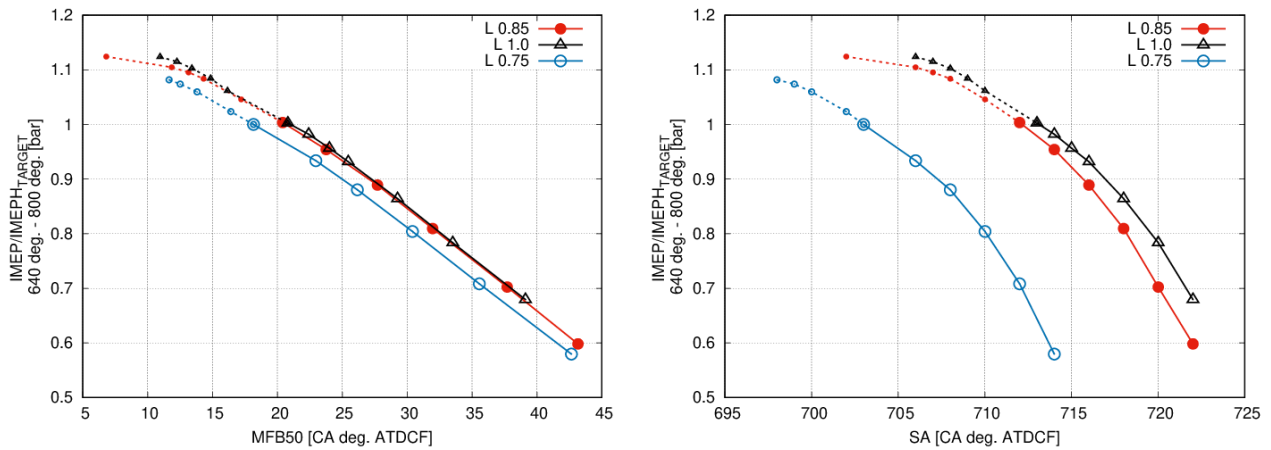


Figure 194. Normalized IMPEH vs MFB50 crank angle (on the left) and vs SA (on the right) for fuel-only simulations

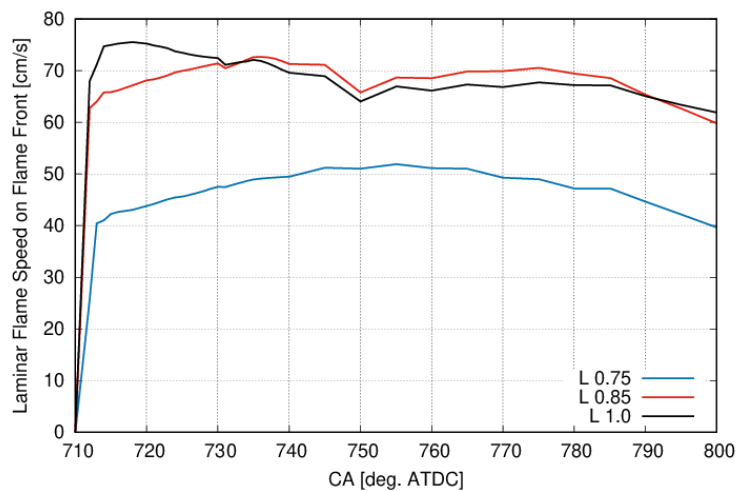


Figure 195. Laminar flame speed evolution: fuel-only simulations

As a matter of fact, the case with a slightly rich mixture ( $\lambda$  0.85) is able to reach the same IMPEH value as the stoichiometric mixture, but with a 1 CA deg. lower SA, as showed by the black and read points that separates dashed and continues lines. In addition, Figure 194 shows how, for the same MFB50 crank angle, combustion with  $\lambda$  0.85 and 1.0 are faster, with a gain in terms of IMPEH over the  $\lambda$  0.75 strategy. However, globally the performance can be considered almost the same for all configurations because no strategy can exceed the target value of 1 without increasing the knock risk. Although the combustion process of the  $\lambda$  0.75 strategy is slower, due to fuel evaporation and lower combustion chamber temperatures, it can accept lower MFB50 crank angle without facing knock, shifting the combustion closer to TDC. The evolution of combustion speeds is described by analyzing the laminar speeds (the combustion duration will be reported in the next paragraph with water injection).

Figure 195 shows the evolution of the average laminar flame speed on the flame front during the flame propagation. In the first crank angles after ignition, the laminar speed for the case at  $\lambda$  1.0 is higher than the other two cases thanks to the better mixing conditions found by the flame close to the spark plug, which strongly influence the ignition start. The  $\lambda$  0.85 case remains with greater velocity levels above 65 cm/s for longer, thanks to a more homogeneous distribution of fuel in the cylinder and close to the value that determines the maximum speeds. On the other hand, the velocity of the  $\lambda$  0.75 case is strongly affected by the richer mixture and by the lower charge temperature and it is characterized by the lowest flame speed values which almost lay below 50 cm/s. Globally, as highlighted in Chapter 9, the three GDI strategies showed a good homogeneity of the mixture distribution proved by the laminar velocity values, considering that the spray pattern has been optimized for cat-heating conditions and not for full power operating point.

Figure 196 shows a frame sequence of the flame front propagation starting from the same Spark Advance, 706 CA deg., of the three cases, where red areas mean complete burnt fuel. The differences are minor for cases  $\lambda$  1.0 and 0.85, while case  $\lambda$  0.75 shows a decelerated flame progression. From these images it is possible to notice how the flame tends to propagate primarily towards the intake valve, where most of the turbulence is concentrated in the cylinder, as described by the non-reacting simulations. The last peripheral area under the exhaust valve is not reached in time by the flame, generating a knock event both for  $\lambda$  1.0 and  $\lambda$  0.85 case as presented in Figure 193.

To summarize, the simulations carried out so far have shown that in these operating conditions only a strategy with a very rich mixture ( $\lambda$  0.75) is able to ensure safe operativity of the engine both for the knock and the exhaust gases temperature. In fact, in both other cases ( $\lambda$  0.85 and 1.0), even if there are conditions with MAPO lower than 7 bar (maximum imposed limit), under these operating conditions they do not correspond to exhaust gas temperature at 800 CA deg. lower than 1630 °C. It is therefore of primary interest to verify the possibility of using a stoichiometric mixture with the addition of water, to cope with future pollution limits and the new AES policy.

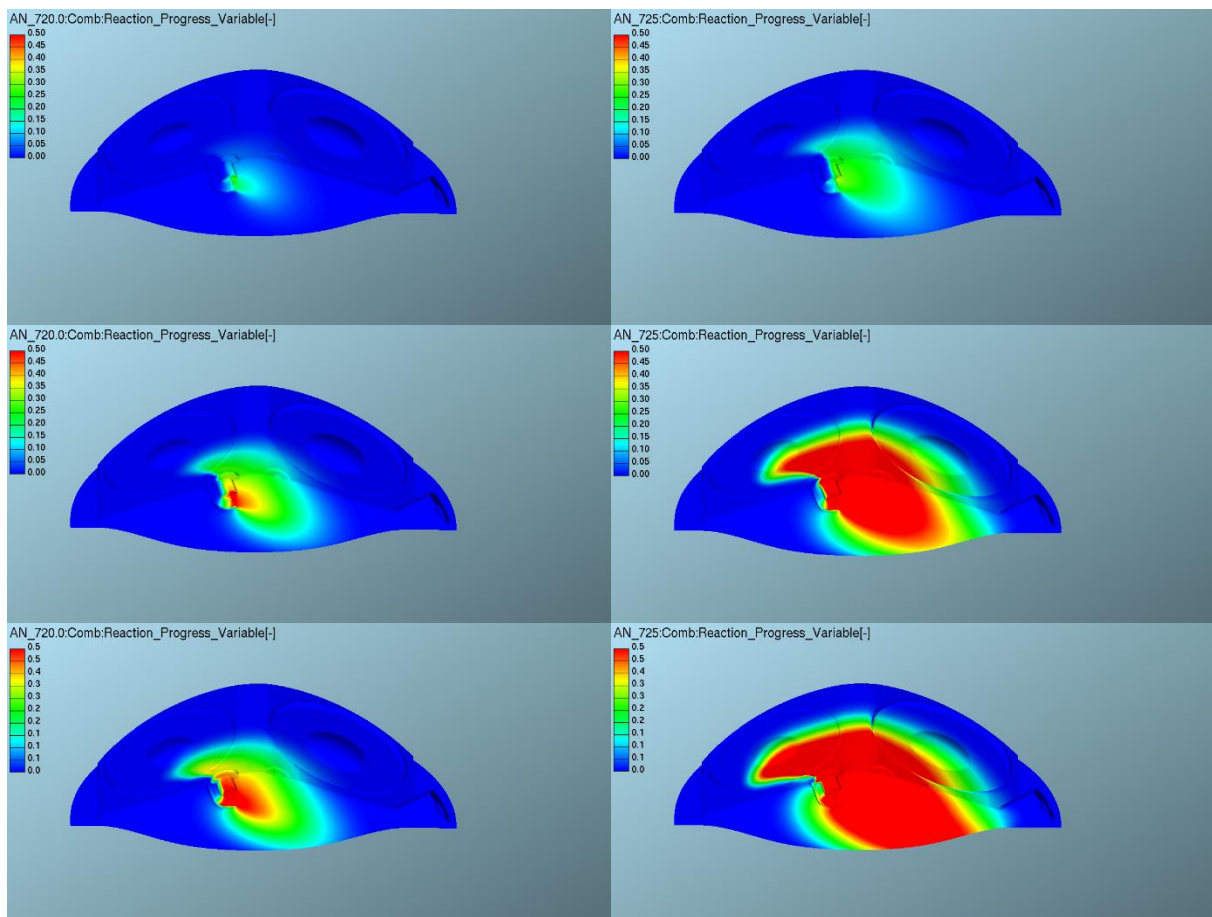


Figure 196. Combustion flame propagation at 720 CA deg. and 725 CA deg.,  $\lambda$  0.75 (top),  $\lambda$  0.85 (centre) and  $\lambda$  1.0 (bottom), SA 706 CA deg.

## 11.4 Combustion Simulation with Water Injection

Moving to the application of the water injection, a brief summary of the previous considerations on expected water effect on thermodynamics is here provided. The dilution of the mixture with water reduces its heat capacity ratio: on one hand this contributes further to reduce the fresh mixture pressure and temperature at TDC (which is good for reducing knock risk and the exhaust temperature), on the other hand this results in a

lower theoretical thermodynamic efficiency of the engine cycle. In this chapter the overall effect of water dilution on engine performance is finally provided thanks to investigations of combustion simulations, carried out by using a detailed chemistry modeling of the laminar flame speed and auto-ignition time which may account accurately for water dilution. The latter is a mandatory in order to properly evaluate the engine performance in terms of balance between performance, weaker knock risk and slowing of combustion speed, which may lead to significantly higher exhaust gas temperatures. Therefore, the results from CFD simulation have been analyzed by considering that:

1. a more suitable (advanced) setting of the spark advance is able to move the combustion towards the TDC resulting in a performance increase;
2. the limit safe condition thresholds in terms of MAPO (i.e, the threshold is set equal to 7 bar in the present case) and exhaust temperature (1630 °C) must be evaluated for each case;
3. the lowering of cylinder temperatures created by the evaporation of water increases the adiabatic efficiency of the engine, with a better energy-work conversion;
4. the lengthening of the combustion duration has a negative effect on the final temperature of the exhaust gases and on the indicating efficiency.

The combustion results for both water architectures in their best set-ups (examined under non-reacting-flow conditions), are now presented. The comparisons are divided into dedicated subparagraphs concerning:

- best PWI and DWI configurations with compression ratio of 9.5;
- main effects of higher compression ratio (10.5) on both PWI and DWI best strategies;
- main effects of higher stroke to bore ratio on PWI best strategy.

#### 11.4.1 Water Injection Combustion Results - CR 9.5

The investigation focuses on the comparison between the best PWI and DWI water injection strategies identified during the non-reacting analysis and only-fuel mixture strategies. The characteristics of the engine are those previously described in Table 17, with compression ratio 9.5.

Figure 197, Figure 198 and Figure 199 show the IMPEH profiles, normalized to the reference target, versus the MFB50 crank angle and SA, the MAPO versus MFB50 crank angle and the MAPO versus the exhaust gas temperature at 800 CA deg., respectively. The analysis of these charts shows that:

1. At fixed combustion phase (MFB50 crank angle), the *PWIs 0.30 10 bar* case provides an IMPEH higher than the target configuration ( $\lambda$  0.75 with SA in complete safe operating conditions) without facing knock. Compared to the  $\lambda$  1.0 case without water injection, the gain of IMEPH is mainly attributable to the increase of the engine adiabatic efficiency. Although the combustion speeds are lower with water, as shown shortly, due to the lowering of fresh mixture temperature, the thermal energy lost at the wall compared to the fuel energy decreases. By advancing the ignition, MAPO begins to rise because some small areas inside the combustion chamber tend to auto-ignite. Further advancing SA, MAPO value exceeds the 7 bar threshold. However, looking at the exhaust gas temperatures at 800 CA deg., there aren't any operating points that simultaneously allows temperatures and MAPO to remain below their own imposed thresholds;
2. The DWI shows, in general, a much higher detonation tolerance. In none of the tested configurations MAPO exceeds 7 bar, although for the case *DWIs 0.35 50 bar* with SA 694 CA deg., which corresponds to an MFB50 angle of 6 CA deg., the value is very close to the threshold. Moreover, also the DWI solution allows to obtain IMPEH values higher than the target for the same MFB50 thanks to the greater adiabatic efficiency. The remarkable low-knock attitude allows higher spark advance with shifted MFB50 crank angle, moving the pressure peak more towards the TDC, with an effective gain

in terms of *bfsc* without facing knock, especially for the 150 bar cases. However, due to the significant presence of water, the higher fresh mixture cooling and the negative effect played on the laminar flame velocity lead to a slowing down of the combustion (as highlighted in Chapter 5) carrying the exhaust gas temperature above the maximum threshold. In addition, in the previous chapter it has been shown that for the DWI configuration the turbulence intensity and the mixture distribution close to spark plug were found less optimized than PWI, and the water vapor close to the spark plug was lower than PWI. These phenomena explain their small performance and combustion velocities differences.

The performance gain (IMEPH), compared to the stoichiometric case without water injection, might be attributed also to the increase of the in-cylinder mass due to water injected (between 1.8% and 3.4% depending on *s*). The compression phase is less affected by the greater mass present in the system because the drops are still in the liquid phase at IVC, and the evaporation is completed along all the compression stroke [32,33].

It is interesting to point out that both water injection systems, for the same MAPO (at the same detonation index), exhibit a much earlier central combustion phase, closer to the optimal ideal value (MFB50 8 CA deg.) when compared with the reference fuel enrichment strategy. However, this is not sufficient to have a clear picture of the combustion process and further investigations are needed.

Extending the investigation to the MFB10-MFB50 and MFB50-MFB90 combustion durations (Figure 200 and Figure 201), the slowdown of the combustion development in the cylinder due to the presence of water is clearly confirmed. It is also clear that the *DWI s 0.55* case, even if it was interesting for the study in non-reacting environment, shows a combustion speed too low and not experimentally acceptable. The Figure 202 illustrates how for *s* 0.55 the unburnt temperature drops significantly compared to other strategies used, drastically decelerating the flame.

Globally the water has a detrimental effect on the flame propagation, both for thermodynamic and chemical reasons. The images in Figure 203 compare the position of the flame front for stoichiometric mixture conditions with and without the presence of water. After about 25 CA deg. from ignition (SA 706 CA deg.), the effect of water has clearly led the flame to cover a smaller area of the combustion chamber, lengthening the combustion duration.

Summarizing, the results examined so far show a strong ability to obtain higher engine loads than the target for both DWI and PWI architectures, (BMEP target 26.6 bar), highlighting the possibility to reduce the fuel and therefore the thermal load and the exhaust temperature in general, thanks to the optimized *bfsc*.

Because of the interesting results found in the non-reacting conditions, the combustion analysis are now performed with the compression ratio increased to 10.5.

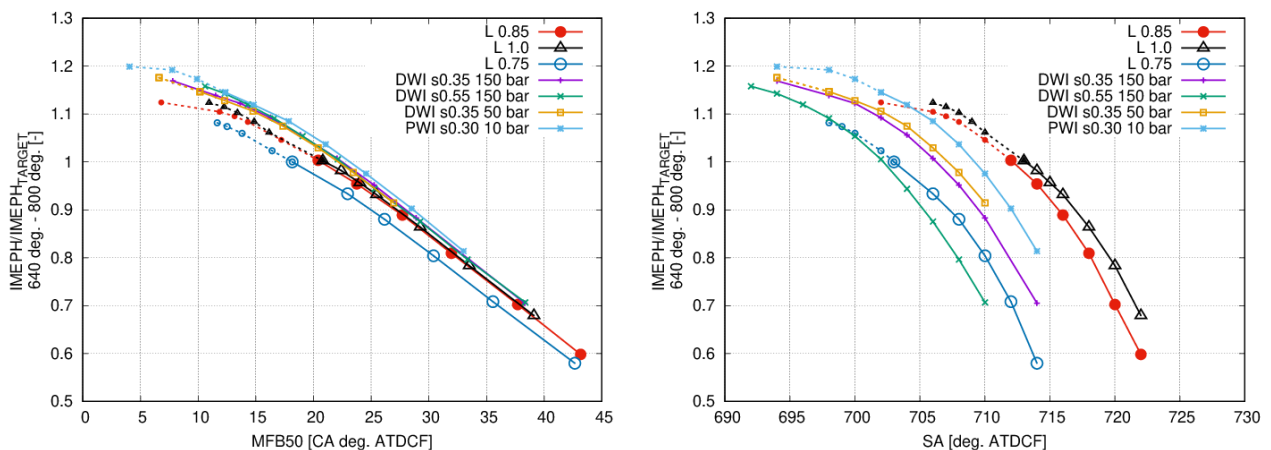


Figure 197. Normalized IMPEH vs MFB50 crank angle (on the left) and SA (on the right): PWI, DWI and fuel-only strategies

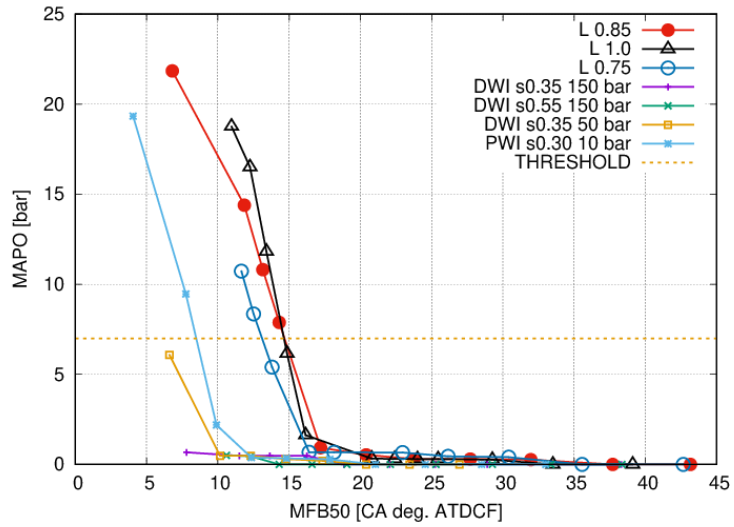


Figure 198. MAPO vs MFB50: PWI, DWI and fuel-only strategies

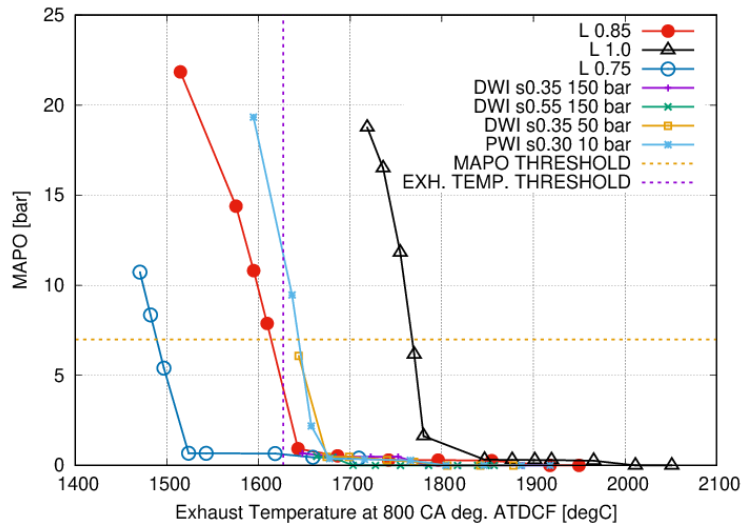


Figure 199. MAPO vs exhaust gas temperature: PWI, DWI and fuel-only strategies

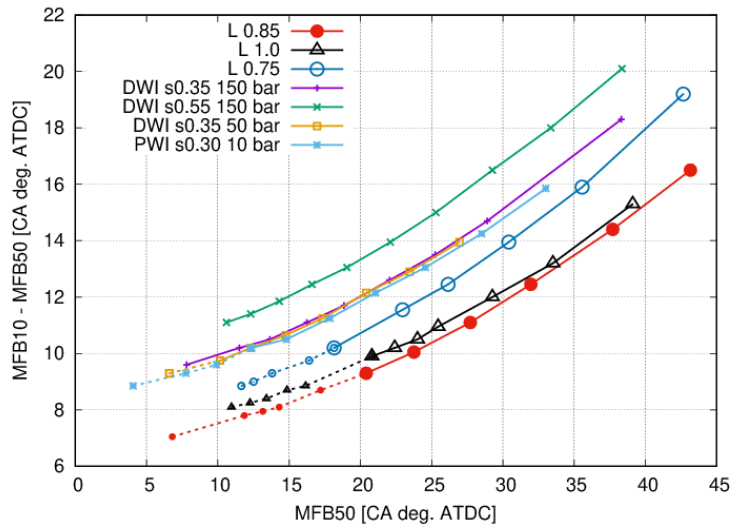


Figure 200. MFB10-MFB50 vs MFB50: PWI, DWI and fuel-only strategies

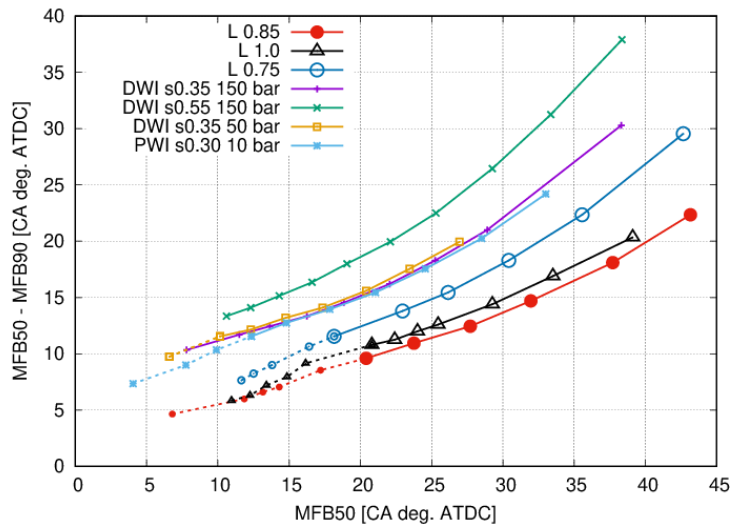


Figure 201. MFB50-MFB90 vs MFB50: PWI, DWI and fuel-only strategies

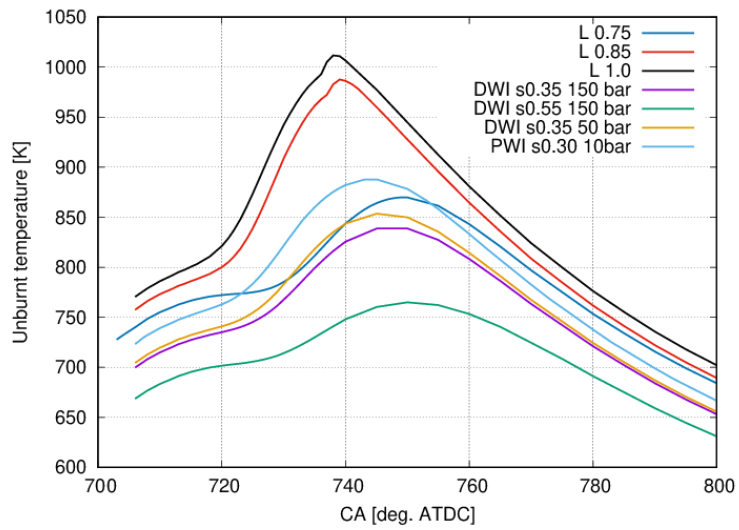


Figure 202. Unburnt temperature: PWI, DWI and fuel-only strategies

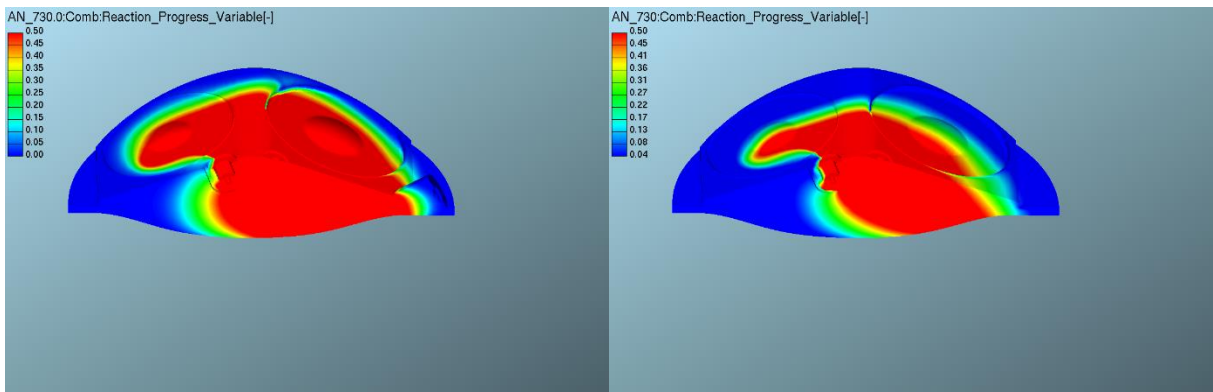


Figure 203. Flame front propagation  $\lambda$  1.0 SA 706 CA deg. without water (left), PWI s 0.3 (right)

### 11.4.2 Water Injection Combustion Results for Higher Compression Ratio

Based on previous results and considerations about the strategies investigated with a compression ratio equal to 9.5, *DWI s 0.35 150 bar* and *PWI s 0.30 10 bar* cases (best non-reacting flow cases) were operated with a larger engine compression ratio of 10.5. The simulations have been realized keeping constant the trapped mass and the stoichiometric mixture condition.

As a direct consequence of the higher compression ratio, the increase in thermodynamic efficiency has led to an increase in engine power and therefore IMPEH. For this reason, in order to keep the power target constant by reducing consumption, it would be possible to decrease the fuel introduced in the cylinder and the trapped mass (with a gain also achieved in the reduction of the boost pressure and, as a consequence, the pumping loss).

Figure 204 - Figure 205 - Figure 206 show the normalized IMEPH curve versus MFB50 crank angle and SA, the MAPO curves versus MFB50 crank angle and exhaust temperature at 800 CA deg. ATDCF, respectively.

The assessment of the compression ratio raise allows one to draw that:

1. looking at the knock safe SA, thus considering the maximum performances of the engine, the DWI system gains 6 CA deg. in the knock safe SA with regard to PWI, resulting in a 1% increment of the IMEPH value and the exhaust temperature reduces of almost 100.0 K;
2. in the DWI system with an increased CR, the higher thermodynamic load causes the KLSA to be delayed of 6 CA deg., as the MFB50 crank angle by about 4 CA deg., SA 700 CA deg. ATDCF is the knock safe SA for DWI CR 10.5. In addition, there is an exhaust temperature reduction of 77.0 K if compared to the same system having CR 9.5. The last is due to the more efficient combustion process linked to the increased thermodynamic efficiency, which reduces the combustion angles. In general, increasing the compression ratio of 1.0 point, results in the increment of the IMEPH (Figure 204). The IMEPH value, at the same SA, increases of about 2%. The configuration *s 0.35 150 bar CR 10.5* with SA at 698 CA deg., is able to meet both the MAPO and TiT maximum targets, with higher IMPEH.
3. Increasing the CR of 1.0 point in the PWI system, the knock safe SA is retarded of 4 degrees due to high thermal load (and MFB50 crank angle longer of about 6 degrees), i.e. KLSA is 706.0 CA deg. ATDCF instead of 702.0 CA deg. ATDCF: the exhaust temperature increases from 1950.0 K to 2007 K due to longer combustion duration and the normalized IMEPH reduces from 1.12 at CR 9.5 to 1.09 at CR 10.5. Although the combustion speed is reduced for the PWI case with CR 10.5, the increase in thermodynamic efficiency has resulted in a gain of IMPEH. Despite the maximum temperature increase of the fresh mixture, the smaller heat exchange surface of the piston has allowed to leave the adiabatic efficiency unchanged. The SA at target IMEPH is shifted towards TDC of 1 degree (SA 709.0 CA deg. ATDCF instead of 710.0 CA deg. ATDCF), with an exhaust temperature reduction from 2120 K to 2080 K at CR 10.5;

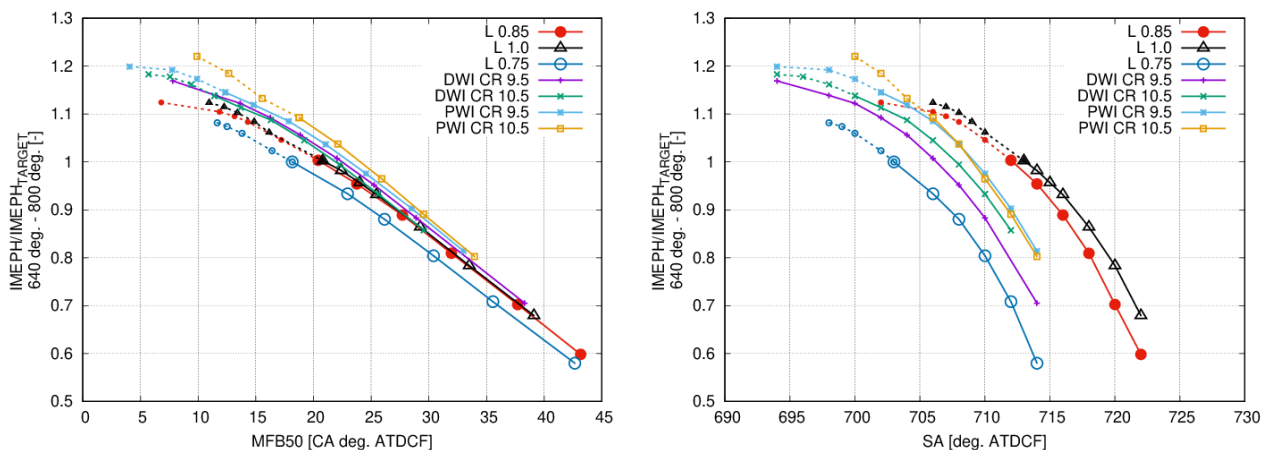


Figure 204. Normalized IMEPH vs MFB50 crank angle (on the left) and SA (on the right): CR 9.5 and 10.5

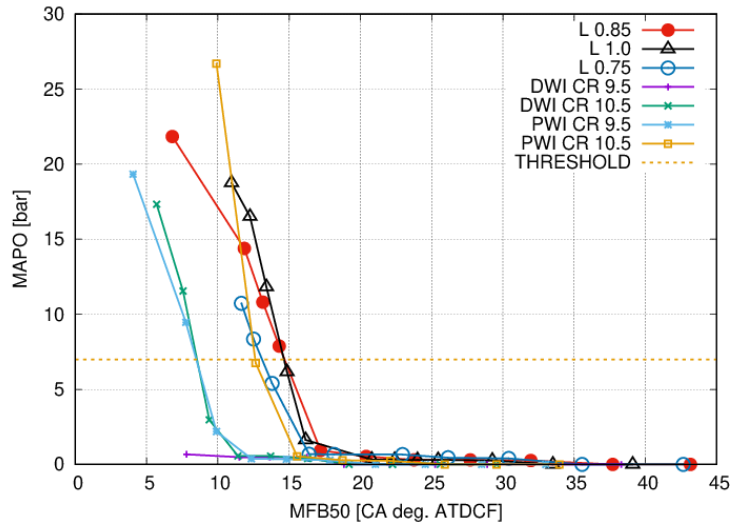


Figure 205. MAPO vs MFB50: PWI, DWI and fuel-only strategies, CR 9.5 and 10.5

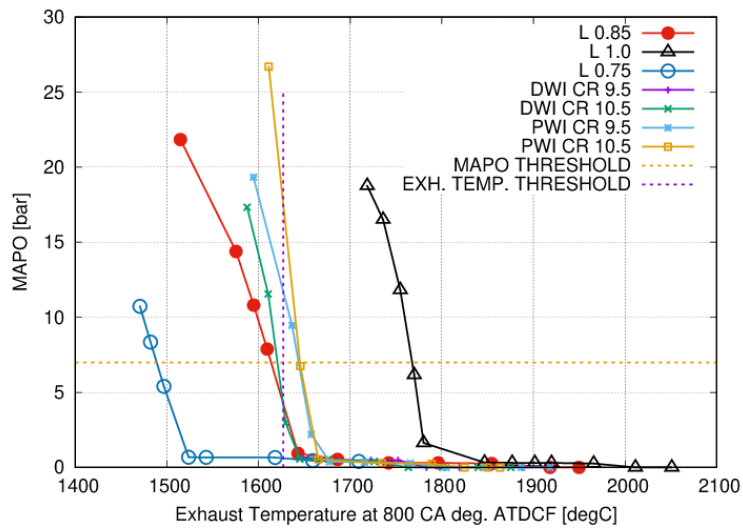


Figure 206. MAPO vs exhaust gas temperature: PWI, DWI and fuel-only strategies, CR 9.5 and 10.5

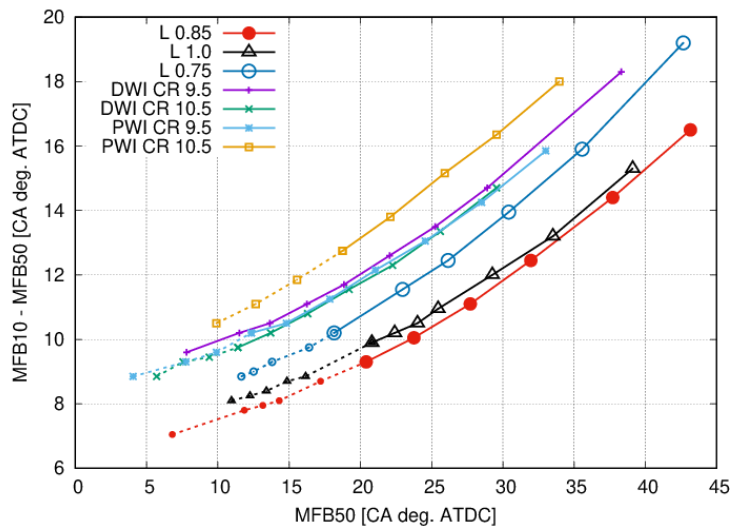


Figure 207. MFB10-MFB50 vs MFB50: PWI, DWI and fuel-only strategies, CR 9.5 and 10.5

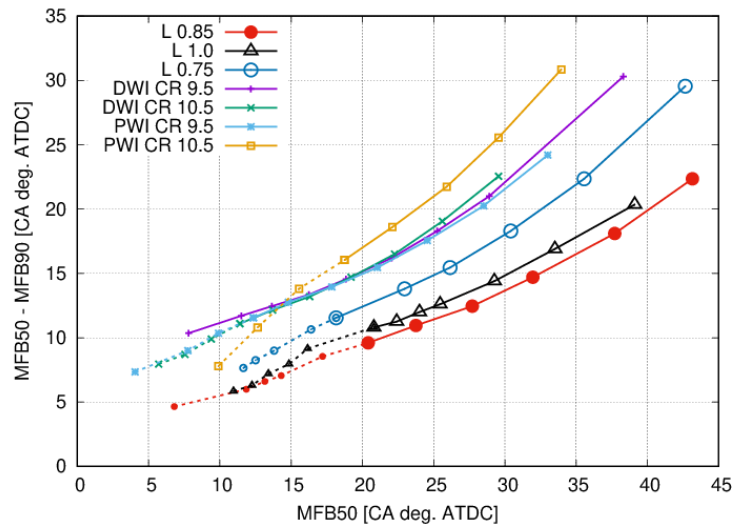


Figure 208. MFB50-MFB90 vs MFB50: PWI, DWI and fuel-only strategies, CR 9.5 and 10.5

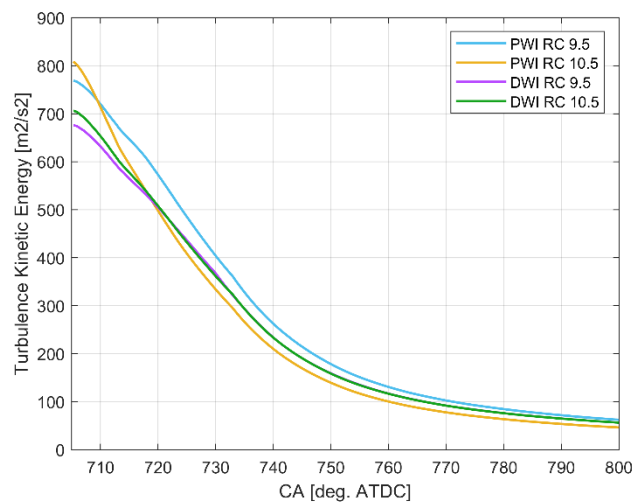


Figure 209. In-Cylinder turbulence kinetic energy at SA 706 CA deg.

The combustion angles in Figure 207 and Figure 208 show that the increase of the compression ratio has opposite effect on DWI and PWI configurations. For the latter, there is an average loss of combustion duration of about 2 degrees for the same MFB50 crank angle. This feature is due to the different evolutions of the in-cylinder turbulence. Figure 209 shows the profiles of the turbulent kinetic energy in the expansion phase. As already mentioned in the non-reacting Chapter 10, the different shape of the PWI piston with CR 10.5 has led on the one hand to a stronger production of turbulence during the compression stroke but a following violent dissipation close to TDC and during the early expansion phase, with negative consequences on combustion speed.

### 11.4.3 Effects of Stroke to Bore Ratio Increase from 1.01 to 1.13 on Best PWI CR 10.5 Strategy

For this last analysis, the PWI architecture only has been chosen because it is the most promising in terms of cost reduction. The PWI *s 0.30 10 bar* solution has been applied to the engine having S/B 1.01 and 1.13, at the same CR 10.5. The idea was to explore the difference performance of the water injection strategy applied to two different engine types but having the same CR. Increasing the S/B ratio from 1.01 to 1.13, there is an increase of the stroke from 85.0 mm to 95.0 mm, which leads to an increment of the unitary swept volume.

For working at the same target power, the engine speed has been reduced from 7000 rpm to 6250 rpm. The mean piston velocity has been kept below the maximum limit 20 m/s due to inertia issues of the crank mechanism. In order to keep the same compression ratio (10.5) with a longer stroke, it was necessary to increase the volume of the combustion chamber at the top dead centre by acting on the shape of the piston. The approach chosen, for design issues, was to preserve the cylinder power target for this high-bmep demanding engine, without reducing its bore and therefore the valve diameters due to space constraints. In the latter case, the boost pressure should have been adjusted to ensure the same trapped air mass, thus increasing pumping losses. So, the increase in the S/B stroke ratio was obtained, as described above, by increasing the stroke. However, it is interesting to verify if there are any performance gain margins thanks to the different combustion chamber shape, taking into account that already going from 7000 rpm to 6250 rpm, leaving the output power unchanged, there is an excellent reduction of engine friction and therefore of its efficiency in general.

The trapped mass has been increased of 8.4% due to the swept volume increase and the brake-specific fuel consumption (from OpenWAM) has been reduced of 27.0% at stoichiometric conditions, due to the thermodynamic efficiency increase. The injected water at  $s$  0.3 is 28.0 mg. It must be kept in mind that in general the increase of the S/B ratio would promote a lower interaction between the flame front and the walls, decreasing the wall exchange. In the case under consideration, as already mentioned, the increase of the stroke has enhanced the heat rejection through cylinder liner, reducing the adiabaticity of the combustion chamber.

Figure 210 compares the IMPEH against MFB50 crank angle and SA showing that the S/B ratio 1.13 provides a loss in performance (IMEPH) attributable to 1 degree of MFB50 for the same target IMEPH. By increasing the displacement with the same RC, the volume at TDC is greater, so the curve of the PWI S/B 1.13 case, on the normalized MPEH vs SA of Figure 210, tends to converge to that of PWI S/B 1.01 for high SA values. Moving the combustion towards the TDC, the greater volume at the top dead centre of the S/B 1.13 configuration results in a more moderate increase of pressure, and therefore IMPEH.

The S/B 1.13 case also leads to a slight decrease in the knock tendency for the same combustion phase (MFB50): for the S/B curve 1.13 the knock safe SA moves away TDC of 2 degrees reducing the MFB50 crank angle without facing knock. In addition, due to the local conditions that the fresh mixture faces with a higher accumulation of water near the knock spot, the knock for the S/B 1.13 configuration is slightly retarded as illustrated in Figure 211 which plots MAPO versus MFB50 crank angle. This behaviour is well captured thanks to the effect of water on the ignition delayed time, whose database has been generated as described in Chapter 5 through chemical kinetic simulations.

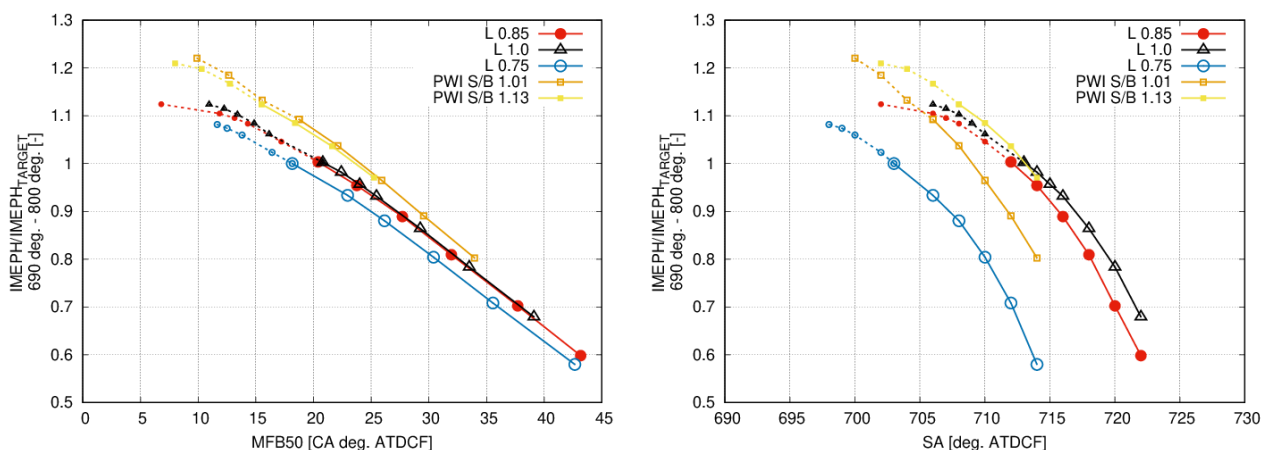


Figure 210. Normalized IMPEH vs MFB50 crank angle (on the left) and SA (on the right): PWI S/B 1.01 and 1.13

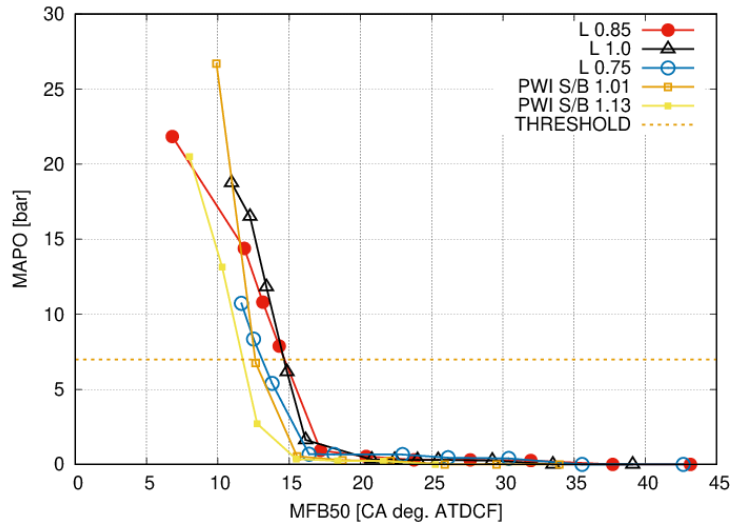


Figure 211. MAPO vs MFB50: fuel-only strategies and PWI S/B 1.01 and 1.13

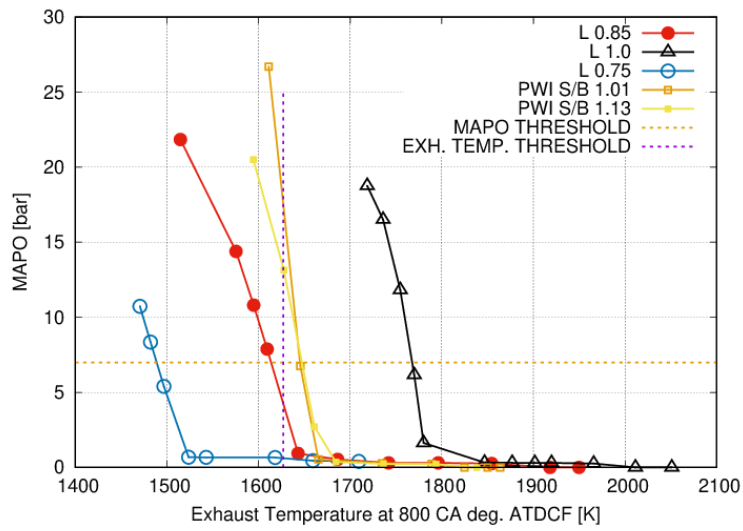


Figure 212. MAPO vs exhaust gas temperature: fuel-only strategies and PWI S/B 1.01 and 1.13

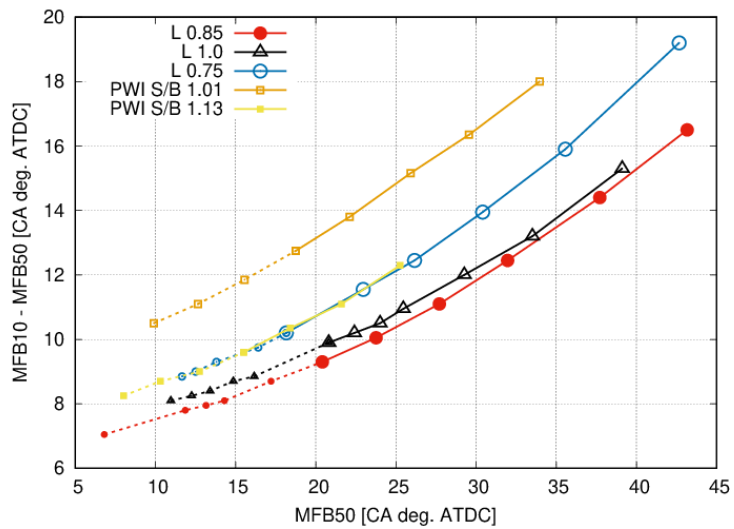


Figure 213. MFB10-MFB50 vs MFB50: fuel-only strategies and PWI S/B 1.01 and 1.13

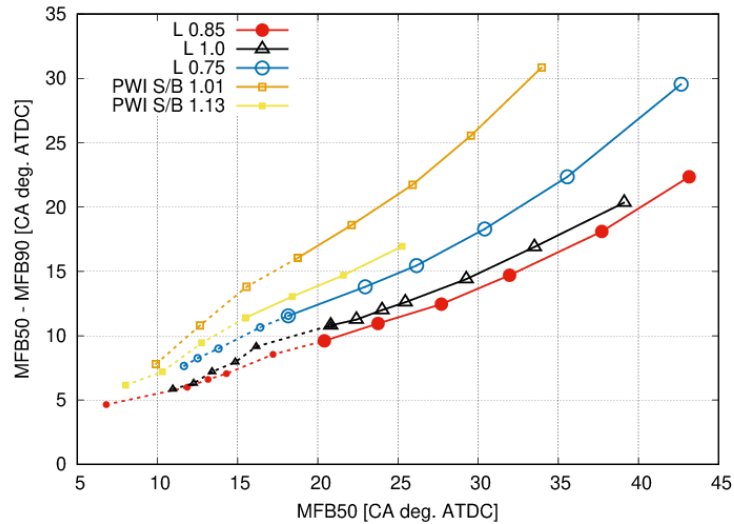


Figure 214. MFB50-MFB90 vs MFB50: fuel-only strategies and PWI S/B 1.01 and 1.13

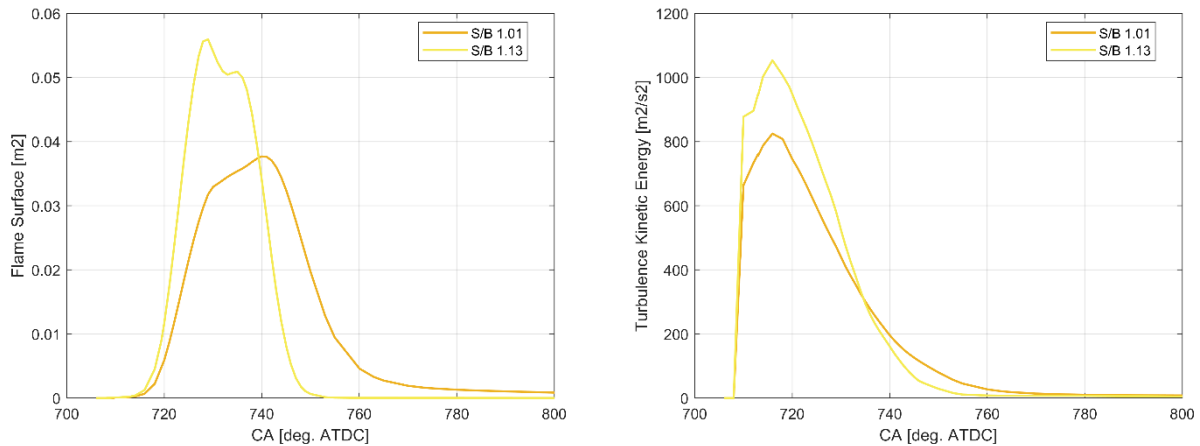


Figure 215. Flame surface and turbulence kinetic energy on the flame front: comparison between PWI S/B 1.01 and S/B 1.13 cases for SA 706 CA deg.

As far as the exhaust gas temperature is concerned, the gain for the case S/B 1.13 was not evident (Figure 212), because as shown in Chapter 9, due to a higher accumulation of water wallfilm the cooling capacity at the TDC is lower, even lower than that provided by the  $\lambda$  0.75 strategy (cooling target).

Figure 213 and Figure 214 report the combustion duration (MFB50-MFB10 and MFB90-MFB50), respectively, versus the MFB50 crank angle. The increase in the bore to stroke ratio leads to an improvement in the S/V ratio of the combustion chamber which, despite the lower average turbulent intensity levels, allows faster combustion especially in the intermediate stage (MFB50-MFB10) thanks to the larger flame surface.

For the case S/B 1.13, a higher turbulence concentration was found in the propagation zone of the flame front despite a lower average level in the cylinder. Figure 215 shows the evolution of the turbulence extracted on the flame front and the flame surface available for the combustion reaction. The localized turbulence is able to approach and overcome that of case S/B 1.01 with a greater flame front extension. This condition lasts up to about 740 CA deg. which for this SA examined (706 CA deg.) corresponds to about 80% of burned mixture. However, much of the gain obtained in term of combustion duration is lost due to a lower adiabatic efficiency, caused by the increased stroke. Figure 216 shows how the case S/B 1.13 with 95 mm stroke exchanges more energy towards the cylinder wall, reducing the IMPEH.

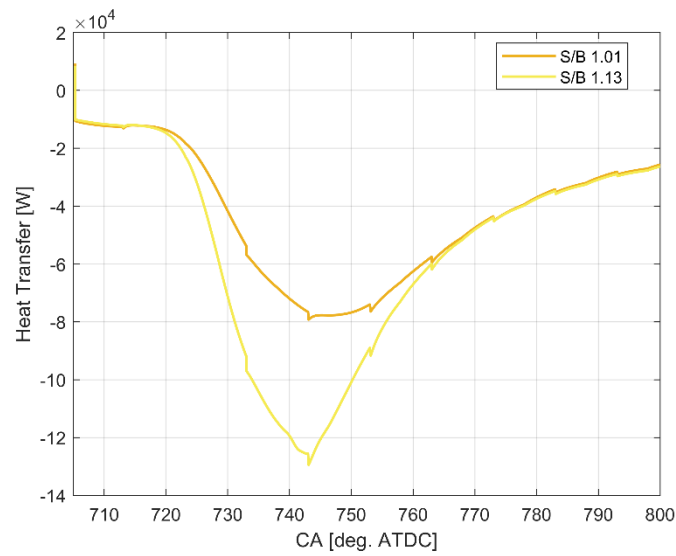


Figure 216. Heat transfer comparison between PWI S/B 1.01 and S/B 1.13 cases for SA 706 CA deg.

## 11.5 Summary

The main results seen so far are now summarized in Figure 217 -Figure 220 by comparing the different cases on the basis of specific quantities, in order to have a clearer overall picture. The quantities considered are: the SA for operation in knock-safe condition, the normalized IMEPH, the exhaust gas temperature at 800 CA deg. At KSSA, and MFB50 crank angle at KLSA. The reference case is  $\lambda$  0.75, which has KLSA at 703 CA deg. ATDC., an IMEPH equal to the target one and an exhaust temperature below the threshold value of 1630 °C. Therefore, it fulfills both knock safe operation and TiT limit constrains.

The cases without water injection running at  $\lambda$  0.85 and  $\lambda$  1.0 present faster combustion thanks to higher thermal condition and better in-cylinder mixture distribution. On the other hand, they are characterized by a more delayed KLSA (Knock Limit Spark Advance) of about 6 and 7 crank angle degrees, respectively, with IMEPH values close to the target one. This denotes a shift towards the expansion and a longer combustion phase, causing the MFB50 to be about 2.0 – 2.5 degree longer and the in-cylinder exhaust temperatures to exceed 1800 °C at knock safe SA conditions.

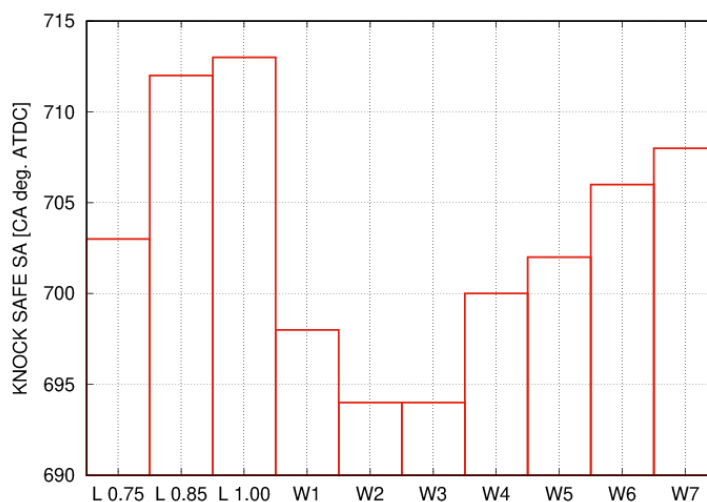


Figure 217. Knock Safe SA for all the cases tested

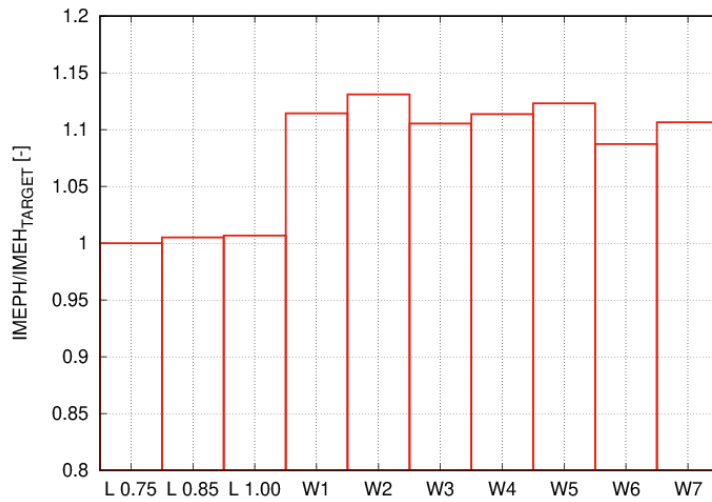


Figure 218. Normalized IMPEH at Knock Safe SA for all the cases tested

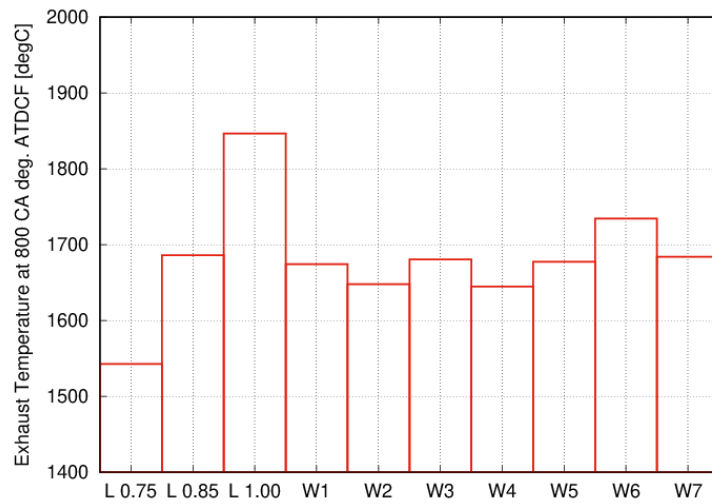


Figure 219. Exhaust gas temperature at 800 CA deg. ATDCF, at Knock Safe SA, for all case tested

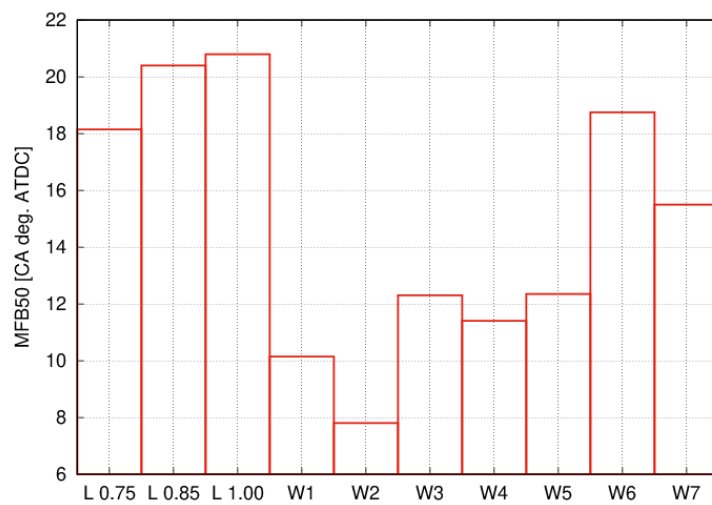


Figure 220. MFB50 at Knock Safe SA for all the cases tested

The results of combustion simulations have shown that the flame front propagation and knock, are two phenomena strongly dependent on the water dilution, mainly related to the lowering of temperatures and the change of mixture quality. The use of chemical kinetics for a correct evaluation of these phenomena and the right representation of the mixture distribution were essential to provide accurate solutions for such simulations.

As far as the application of the water injection is concerned, cases W1 to W4 (DWI) and W5 – W7 (PWI) show the possibility to run the engine with more advanced KLSA and MFB50 crank angle at safe condition, gaining a substantial increase in IMEPH. However, running the engine with a compression ratio equal 9.5, no strategy of water injection was found to accomplish with the exhaust gas temperature at 800 CA deg. limit of 1630 °C, at fixed IMEPH. This issue can be solved by exploiting the optimization of the *bsfc* by increasing the compression ratio and by reducing the fuel introduced and bringing the performance back to the target value (IMEPH<sub>target</sub>). This would decrease the engine thermal load with a consequent reduction of the TiT.

To summarize it is possible to say that:

1. the  $\lambda$  cases 0.85 and 1.0 have been demonstrated, in the fuel-only configurations, to be the most prone to knock and to exceed the TiT threshold. This is the reason why the  $\lambda$  0.75 SA 703 CA case was taken as reference to ensure safe engine operation (MAPO under 7 bar and exhaust gas temperature under 1630 °C);
2. the PWI architecture showed a higher laminar flame speed thanks to the lower amount of water introduced and an improvement in performance (IMEPH) compared to the reference, because of the reduced MFB50 crank angle (greater SA). The test achieved at higher bore to stroke ratio showed a higher combustion speed thanks also to the better S/V ratio of the combustion chamber and the flame;
3. the DWI strategy is the one with the lowest knock attitude thanks to a more intense charge cooling. All cases recorded a MAPO lower than 7 bar. For DWI s 0.35 p 150 bar, IMEPH lies between  $\lambda$  1.0 -  $\lambda$  0.85 cases and  $\lambda$  0.75;
4. the increase in the compression ratio from 9.5 to 10.5 seems to be more effective for the PWI than the DWI. Apparently, even for *DWI CR 10.5* at KLSA is not possible to drop the temperature below the threshold, because of the limited evaporation rate which strongly affects the cooling effect. On the other hand, the configuration *s 0.35 150 bar CR 10.5* with SA at 698 CA deg., is able to meet both the MAPO and TiT targets. Moreover, the two different approaches with which the increases in RC in the PWI and DWI strategy have been realized, also showed different turbulence characteristics and combustion speeds. This explained why the PWI system with CR 10.5 was characterized by higher combustion angles;
5. The increase of the bore to stroke ratio up to 1.13, by lengthening the stroke, has been carried out only on the PWI strategy. Overall, the system was able to slightly reduce both the exhaust gas temperature and the knock tendency due to a faster combustion development. However, part of the IMEPH gain has been lost due to adiabatic efficiency reduction because of the specific geometrical configuration adopted.

To conclude, based on the architectures and strategies analyzed in this thesis, both PWI and DWI, applied to this specific high-bmep virtual engine, the best configurations considering performance, knock attitude and exhaust temperature are:

- DWI: s 0.35 p 150 bar SOI 418 deg. ATDC, CR 10.5
- PWI: s 0.3 p 10 bar SOI 293 deg. ATDC, CR 9.5, S/B 1.13

Although DWI technology has proven to be in some aspects better than PWI, the latter can be exploited and optimized to achieve an improvement in terms of *bsfc*, reducing the injected fuel with respect to the 'no water' injection case, as well as the temperature and abnormal combustion conditions. In addition, this architecture remains more feasible in a series production view with lower costs. For this reason, it is very likely that in the near future the use of water injection on a large scale is going to be used and studied together with other technologies that make internal combustion engines more and more efficient and performing.

# Chapter 12: Conclusion and Future Direction

In this thesis the topic of the water injection in GDI engines has been deeply investigated through the use of fluid-dynamic computational simulations and detailed chemical kinetics calculations.

Among the different solutions that could currently be implemented, those related to PWI (Port Water Injection) and DWI (Direct Water Injection) have been examined, with specific injection strategies based on fluid dynamics, thermal and chemical aspects. The strategies have been tested on a high-*bmep* and high-power S.I. GDI turbo-charged engine virtually designed, with different geometry configurations.

One of the main driving factors that have determined the development of this research, and that differentiates it from many scientific articles providing the first scientific contribution, is the analysis carried out considering the real applicability of these strategies (injection pressures, injected mass, etc.), trying to minimize the real engine problems related to water evaporation, combustion process and lubricant oil contamination.

In literature there are many experimental examples showing how the water injection can decrease the engine knock attitude and TiT. The problem is that there is a lack of detailed analysis leading to the definition of an efficient (with less water consumption), functional and cost-effective system. Therefore, the analyses reported in this doctoral thesis have always been evaluated considering an evaporation constraint of at least 90% of water mass.

Many configurations studied here were in fact discarded because even if they had apparent better cooling potentials, these could not be realized in practice for the reasons mentioned above.

The second important scientific contribution is related to the characterization of the spray for PWI systems. This allowed to highlight some physical aspects in the dynamics of the spray that differ from those with fuel (PFI). In literature there is a strong lack of experimental characterization of water spray under engine like operating conditions. For this reason, the numerical validation of spray models is certainly an important methodological step to obtain reliable results in term of water distribution during the simulations. It has been seen that a correct evaluation of the presence of water vapor under the spark plug is of fundamental importance to characterize the combustion.

The third scientific contribution is related to this last aspect. The chemical effect of water has a primary importance role to accurately simulate the combustion process. Thanks to the use of detailed chemical kinetics mechanisms, several simulations have been performed under several thermodynamic and mixing conditions typical of high-*bmep* GDI engines, to extract new databases of the laminar flame speed, the flame thickness and the auto-ignition times. The effects of the injected water were separated from the water included in the EGR during CFD simulations, through an appropriate developed methodology.

This research has allowed to reliably highlight some very important aspects related to the introduction of water and the lowering of the charge temperature. On the one hand it is possible to obtain an excellent advantage in terms of MAPO, decreasing the engine knock attitude, on the other hand the slowing down of combustion due to water leads to excessively high exhaust gas temperatures. This is only partially recovered thanks to higher spark advance, allowed without detonation. However, the real advantage is the higher *bsfc*

achievable thanks to the water introduction. The relevant performance gain can be exploited to reduce the fuel mass injected, keeping the engine at the same target output power as for the rich fuel strategy used for component and knock protection working conditions.

Future research activities related to water injection can be many, since this technology can be combined with other strategies already widely used in modern engines.

Among the first activities there is certainly that of PWI and DWI technologies combined with Miller or Atkinson cycles to understand how these two systems can be optimized to work together. In addition, a new engine design with proper stroke to bore ratio would be necessary to better assess the possible turbulence benefit on WI (Water Injection) engines. Both projects have already been started.

A second research theme could be the one focused on pollutant emissions. The improvement of the *bsfc* is a factor that already indicates an improvement of the engine efficiency and therefore of the pollutant emissions. However, an in-depth analysis of the local dynamics of pollutant formation with injected water could lead to new considerations.

Finally, to conclude the spray characterization activity, interrupted because of the pandemic emergency, it would be necessary to carry out a dedicated experimental campaign also for a DWI system.

Internal combustion engines are still far from being replaced by other systems and their development is still long, taking into consideration hybrid-powertrain with the use of renewable synthetic fuels. Water injection is certainly one of the many strategies that can be studied and optimized to meet the demand of tomorrow's engines, starting from PWI system, in order to reduce CO<sub>2</sub> tailpipe concentration and increase performance.

## Acknowledgements

*The list of people to thank is undoubtedly very long and it is certainly not my intention to list them by importance, as all of them were necessary to complete this three-year journey.*

*I would like to start by thanking NAIS S.r.l, and in particular Claudio Forte, who directly funded my doctorate and allowed me to develop my knowledge of fluid dynamics in different areas. As well as Marco Costa, mentor for all technical aspects related to fluid dynamics and engineering in general. A big thank you to Professor Gian Marco Bianchi, supervisor of my PhD, who managed to transmit me the passion for engines since university, with a willingness and care for a successful outcome of my PhD really admirable.*

*Thanks also to the research group of the University of Bologna, in particular to Ing. Stefania Falfari and Ing. Giulio Cazzoli, for their continuous scientific activity.*

*One of the most important opportunities was certainly that of dedicating myself to a work experience abroad, thanks to the availability of Professor Raul Payri of the CMT department in Valencia. That experience, although short due to the pandemic, allowed me to approach the world of experimental activities with different working methods and to understand the important contribution in the diversity of people. For this reason, a big thank you is dedicated to the whole research group and in particular to two colleagues and friends, Armando Moreno and Vincenzo Pagano, who welcomed me from the beginning in an extraordinary way, making me feel an integral part of the group, and despite the short time spent together I will never forget.*

*The last and most important part of the acknowledgements is dedicated to the people closest to me. First of all, my girlfriend Francesca, who has contributed to the realization of this thesis with her character and love, always leaving me the necessary space for my activities, sacrificing much of our time.*

*Finally, the most important thought and thanks is dedicated to my parents. They have put all their efforts and sacrifices to help me in my personal realization never leaving me alone. From primary school to doctorate, they have always believed in me and supported me not only financially but also morally in all difficult time. Being able to concentrate my energies mainly on studying, during my educational path, is undoubtedly an immense help and for this reason I consider myself very lucky.*

*Well, perhaps a thank you must also be given to myself, for my passion and perseverance in the life projects I pursue.*

## References

- [1] <https://www.eea.europa.eu/publications/air-quality-in-europe-2019>
- [2] Nils Hooftman, Maarten Messagie, Joeri Van Mierlo, Thierry Coosemans, "A review of the European passenger car regulations – Real driving emissions vs local air quality, Renewable and Sustainable Energy Reviews", Volume 86, 2018, Pages 1-21, ISSN 1364-0321, <https://doi.org/10.1016/j.rser.2018.01.012>
- [3] [https://theicct.org/sites/default/files/publications/Post\\_Euro6\\_standards\\_report\\_20191003.pdf](https://theicct.org/sites/default/files/publications/Post_Euro6_standards_report_20191003.pdf)
- [4] "Emission legislation trend", Emission Test System, 2018, AVL conference
- [5] Jerzy, M., Piotr, L., Pawel F., "Measurement of Exhaust Emissions under Actual Operating Conditions with the Use of PEMS: Review of Selected Vehicles". Improvement trends for ICE, DOI:10.57772/intechopen.70442
- [6] "Guidance on the evaluation of Auxiliary Emission Strategies and the presence of Defeat Devices with regard to the application of Regulation (EC) No 715/2007",
- [7] Gian Marco Bianchi, Dispense del corso "Fluidodinamica dei motori a combustione interna M" 2015
- [8] Reitz, R. D., Ogawa, H., Payri, R., Fansler, T., Kokjohn, S., Moriyoshi, Y., ... Zhao, H. (2020). IJER editorial: The future of the internal combustion engine. International Journal of Engine Research, 21(1), 3–10. <https://doi.org/10.1177/1468087419877990>
- [9] De Cesare, M., Cavina, N., and Paiano, L., "Technology Comparison for Spark Ignition Engines of New Generation," SAE Int. J. Engines 10(5):2513-2534, 2017, <https://doi.org/10.4271/2017-24-0151>.
- [10] John B. Heywood, "Internal Combustion Engine Fundamentals", McGraw-Hill, 2011
- [11] Andersson, J., Keenan, M., Osborne, R., Rouaud, C., "Development of lean stratified turbocharged gasoline engines for 2018 SOP", SIA Technical paper, R-2013-06-22.
- [12] Brooker, A., Gonder, J., Wang, L., Wood, E. et al., "FASTSim: A Model to Estimate Vehicle Efficiency, Cost and Performance," SAE Technical Paper 2015-01-0973, 2015, doi:10.4271/2015-01-0973.
- [13] Niizato, T., Yasui, Y., Urata, Y., Wada, Y., Jono, M., Nakano, K., Taguchi, M. "Honda's New Turbo-GDI Engine Series for global application", International Vienna Motor Symposium 2016.
- [14] Boggs, D., Dorobantu, M., German, J., Isenstadt A., Watson, T., "Downsized, boosted gasoline engines", ICCT Working Paper 2016-21
- [15] Kyoung-Pyo Ha, Woo Tae Kim, In Sang Ryu, You Sang Son, "Development of Continuously Variable Valve Duration (CVVD) Engine", 25th Aachen Colloquium Automobile and Engine Technology 2016.
- [16] A Study of a Multiple-link Variable Compression Ratio System for Improving Engine Performance
- [17] Ihlemann A., Nitz N., Cylinder Deactivation - A technology with a future or a niche application?, 11th Schaeffler Symposium, 2014.
- [18] Kapus P.E., Spanner C., Graf B., Fraidl G.K. "Cylinder Deactivation with 4 Cylinder Engines - An Alternative to 2 Cylinders?", International Vienna Motor Symposium 2011

- [19] Lu, H., Deng, J., Hu, Z., Wu, Z. et al., "Study on Fuel Economy Improvement by Low Pressure Water-Cooled EGR System on a Downsized Boosted Gasoline Engine," SAE Technical Paper 2016-01-0678, 2016, doi:10.4271/2016-01-0678.
- [20] Wei, H., Zhu, T., Shu, G., Tan, L., and Wang, Y. (2012). Gasoline engine exhaust gas recirculation-a review. *Applied Energy*, 99, 534-544.
- [21] Wei H et al. Gasoline engine exhaust gas recirculation – A review. *Appl Energy* (2012), <http://dx.doi.org/10.1016/j.apenergy.2012.05.011>
- [22] Lenga, H., Hartmann, R., Hyouk Min, B., Grimm, J., Winkler, M., "Low Pressure EGR for Downsized Gasoline Engines, 23rd Aachen Colloquium Automobile and Engine Technology 2014
- [23] Bevilacqua, V., Jacobs, E., Grauli, G., Wüst J. Future of Downsizing: Fuel Consumption Improvement in NEDC as well as in Customer Operating Conditions, SIA Technical paper 2013, R-2013-06-30
- [24] Rowe MR, Ladd GT. Water injection for aircraft engines. SAE Technical Paper 460192; 1946.
- [25] Eaton DC. Cruising economy by use of water injection. SAE Technical Paper 460198; 1946.
- [26] Obert EF. Detonation and internal coolants. SAE Technical Paper 480173; 1948.
- [27] Nicholls J, El-Messiri I, Newhali H. Inlet manifold water injection for control of nitrogen oxides-theory and experiment. SAE Technical Paper 690018; 1969.
- [28] Lestz SS, Meyer WE, Colony CM. Emissions from a direct-cylinder water-injected spark-ignition engine. SAE Technical Paper 720113; 1972.
- [29] Lestz SJ, Melton RB, Rambie EJ. Feasibility of cooling diesel engines by introducing water into the combustion chamber. SAE Technical Paper 750129; 1975.
- [30] Harrington JA. Water addition to gasoline-effect on combustion, emissions, performance, and knock. SAE Technical Paper 820314; 1982.
- [31] Citation: Christensen, M. and Johansson, B., "Homogeneous Charge Compression Ignition with Water Injection," SAE Technical Paper 1999-01-0182, 1999, <https://doi.org/10.4271/1999-01-0182>.
- [32] Lanzafame, R., "Water Injection Effects In A Single-Cylinder CFR Engine," SAE Technical Paper 1999-01-0568, 1999, <https://doi.org/10.4271/1999-01-0568>
- [33] Citation: Brusca, S. and Lanzafame, R., "Water Injection in IC - SI Engines to Control Detonation and to Reduce Pollutant Emissions," SAE Technical Paper 2003-01-1912, 2003, <https://doi.org/10.4271/2003-01-1912>.
- [34] Nande, A., Wallner, T., and Naber, J., "Influence of Water Injection on Performance and Emissions of a Direct-Injection Hydrogen Research Engine," SAE Technical Paper 2008-01-2377, 2008, <https://doi.org/10.4271/2008-01-2377>.
- [35] Younkings, M., Wooldridge, M., and Boyer, B., "Direct In-cylinder Injection of Water into a PI Hydrogen Engine," SAE Technical Paper 2013-01-0227, 2013, <https://doi.org/10.4271/2013-01-0227>.
- [36] Iacobacci, A., Marchitto, L., and Valentino, G., "Water Injection to Enhance Performance and Emissions of a Turbocharged Gasoline Engine under High Load Condition," *SAE Int. J. Engines* 10(3):928-937, 2017, <https://doi.org/10.4271/2017-01-0660>.

- [37] Battistoni, M., Grimaldi, C., Cruccolini, V., Discepoli, G. et al., "Assessment of Port Water Injection Strategies to Control Knock in a GDI Engine through Multi-Cycle CFD Simulations," SAE Technical Paper 2017-24-0034, 2017, doi:10.4271/2017-24-0034.
- [38] Hoppe, F., Thewes, M., Seibel, J., Balazs, A. et al., "Evaluation of the Potential of Water Injection for Gasoline Engines," SAE Int. J. Engines 10(5):2017, doi:10.4271/2017-24-0149.
- [39] Sebastiano Breda, Fabio Berni, Alessandro d'Adamo, Francesco Testa, Elena Severi, Giuseppe Cantore, Effects on Knock Intensity and Specific Fuel Consumption of Port Water/Methanol Injection in a Turbocharged GDI Engine: Comparative Analysis, Energy Procedia, Volume 82, 2015, Pages 96-102, ISSN 1876-6102, <https://doi.org/10.1016/j.egypro.2015.11.888>.
- [40] Cordier, M., Lecompte, M., Malbec, L.-M., Reveille, B. et al., "Water Injection to Improve Direct Injection Spark Ignition Engine Efficiency," SAE Technical Paper 2019-01-1139, 2019, doi:10.4271/2019-01-1139.
- [41] Citation: d'Adamo, A., Berni, F., Breda, S., Lugli, M. et al., "A Numerical Investigation on the Potentials of Water Injection as a Fuel Efficiency Enhancer in Highly Downsized GDI Engines," SAE Technical Paper 2015-01-0393, 2015, <https://doi.org/10.4271/2015-01-0393>.
- [42] Netzer, C., Franken, T., Mauss, F., Seidel, L. et al., "Numerical Analysis of the Impact of Water Injection on Combustion and Thermodynamics in a Gasoline Engine Using Detailed Chemistry," SAE Int. J. Engines 11(6):1151-1166, 2018, doi:10.4271/2018-01-0200.
- [43] Teodosio, L., De Bellis, V., and Bozza, F., "Combined Effects of Valve Strategies, Compression Ratio, Water Injection, and Cooled EGR on the Fuel Consumption of a Small Turbocharged VVA Spark-Ignition Engine," SAE Int. J. Engines 11(6):643-656, 2018, doi:10.4271/2018-01-0854.
- [44] Citation: Raut, A.A. and Mallikarjuna, J.M., "Effect of Water Injection and Spatial Distribution on Combustion, Emission and Performance GDI Engine-A CFD Analysis," SAE Technical Paper 2018-01-1725, 2018, doi:10.4271/2018-01-1725.
- [45] Hoppe F, Thewes M, Seibel J, Balazs A, Scharf J. Evaluation of the potential of water injection for gasoline Engines. SAE Technical Paper 2017-24-0149; 2017
- [46] Citation: Vacca, A., Bargende, M., Chiodi, M., Franken, T. et al., "Analysis of Water Injection Strategies to Exploit the Thermodynamic Effects of Water in Gasoline Engines by Means of a 3D-CFD Virtual Test Bench," SAE Technical Paper 2019-24-0102, 2019, doi:10.4271/2019-24-0102.
- [47] Citation: Lif, A., Skoglundh, M., Gjirja, S., and Denbratt, I., "Reduction of Soot Emissions from a Direct Injection Diesel Engine using Water-in-Diesel Emulsion and Microemulsion Fuels," SAE Technical Paper 2007-01-1076, 2007, <https://doi.org/10.4271/2007-01-1076>.
- [48] Citation: Shah, S., Maiboom, A., Tautzia, X., and Hétet, J., "Experimental Study of Inlet Manifold Water Injection on a Common Rail HSDI Automobile Diesel Engine, Compared to EGR with Respect to PM and Nox Emissions and Specific Consumption," SAE Technical Paper 2009-01-1439,
- [49] Wirbeleit F, Enderle C, Lehner W, Raab A, Binder K. Stratified diesel fuel-waterdiesel fuel injection combined with EGR-the most efficient in-cylinder NOx and PM reduction technology. SAE Technical Paper 972962; 1997.
- [50] Tanner FX, Brunner M, Weisser G. A computational investigation of water injection strategies for nitric oxide reduction in large-bore DI diesel engines. SAE Technical Paper 2001-01-1069; 2001.
- [51] Kegl B, Pehan S. Reduction of diesel engine emissions by water injection. SAE Technical Paper 2001-01-3259; 2001
- [52] Sipeng Z., Sam A., Colin C. Andrew, L., "A review of water injection applied on the internal combustion engine", Energy conversion and Management, Volume 184, 139-158, 2019, <https://doi.org/10.1016/j.enconman.2019.01.042>

- [53] Park H-K, Ghal S-H, Park H-C, Choi S-W, Kim S-H. A study on NO<sub>x</sub> reduction of marine 4-stroke diesel engine using charge air humidification. SAE Technical Paper 2011-24-0172; 2011.
- [54] Turner JWG, Pearson RJ, Holland B, Peck R. Alcohol-based fuels in high performance engines. SAE Technical Paper 2007-01-0056; 2007.
- [55] Turner J, Pearson R. High Output Supercharging Without intercooling: Theory and Results ATA High Performance Engines Seminar. University of BATH; 2001.
- [56] Worm J, Naber J, Duncan J, Barros S, Atkinson W. Water injection as an enabler for increased efficiency at high-load in a direct injected, boosted, SI engine. SAE Technical Paper 2017-01-0663; 2017.
- [57] Bhagat M, Cung K, Johnson J, Lee S-Y, Naber J, Barros S. Experimental and numerical study of water spray injection at engine-relevant conditions. SAE Technical Paper 2013-01-0250; 2013.
- [58] Psota M, Easley W, Fort T, Mellor A. Water injection effects on NO<sub>x</sub> emissions for engines utilizing diffusion flame combustion. SAE Technical Paper 971657; 1997.
- [59] Chadwell CJ, Dingle PJ. Effect of diesel and water co-injection with real-time control on diesel engine performance and emissions. SAE Technical Paper 2008-01-1190; 2008.
- [60] Kadota T, Yamasaki H. Recent advances in the combustion of water fuel emulsion. Prog Energy Combust Sci 2002;28:385–404.
- [61] Vellaiyan S, Amirthagadeswaran K. The role of water-in-diesel emulsion and its additives on diesel engine performance and emission levels: a retrospective review. Alexandria Eng J 2016;55:2463–72.
- [62] Ithnin AM, Noge H, Kadir HA, Jazair W. An overview of utilizing water-in-diesel emulsion fuel in diesel engine and its potential research study. J Energy Inst 2014;87:273–88.
- [63] Selim MY, Ghannam MT. Performance and engine roughness of a diesel engine running on stabilized water diesel emulsion. SAE Technical Paper 2007-24-0132; 2007
- [64] Heinrich C, Dörksen H, Esch A, Krämer K. Gasoline Water Direct Injection (GWDI) as a Key Feature for Future Gasoline Engines. Gasoline Engines. Springer; 2017. p.322–37.
- [65] Hermann I, Glahn C, Kluin M, Paroll M, Gumprich W. Water Injection for Gasoline Engines-Quo Vadis? International Conference on Knocking in Gasoline Engines:Springer; 2017. p. 299–321.
- [66] Hoppe F, Thewes M, Baumgarten H, Dohmen J. Water injection for gasoline engines: potentials, challenges, and solutions. Int J Engine Res 2016;17:86–96.
- [67] Nour, Mohamed & kosaka, H. & Abdel-Rahman, Ali Kamel & Bady, Mahmoud. (2016). Effect of Water Injection into Exhaust Manifold on Diesel Engine Combustion and Emissions. Energy Procedia. 100. 178-187. 10.1016/j.egypro.2016.10.162.
- [68] Martin, B., Werner, M., Hans, B., Sthephan, R., “Functional Integration of Water Injection into Gasoline engine”
- [69] Martin, B., Werner, M., Hans, B., Sthephan, R., “Approaches for On-board Water Provision for water injection”
- [70] Sun, Y., Fischer, M., Bradford, M., Kotrba, A. et al., “Water Recovery from Gasoline Engine Exhaust for Water Injection,” SAE Technical Paper 2018-01-0369, 2018, doi:10.4271/2018-01-0369.
- [71] Falfari, S., Bianchi, G.M., Cazzoli, G., Ricci, M. et al., “Water Injection Applicability to Gasoline Engines: Thermodynamic Analysis,” SAE Technical Paper 2019-01-0266, 2019, doi:10.4271/2019-01-0266.

- [72] Hoppe F, Thewes M, Baumgarten H, Dohmen J. Water injection for gasoline engines: Potentials, challenges, and solutions. *International Journal of Engine Research*. 2016;17(1):86-96. doi:10.1177/1468087415599867
- [73] Arthur H. Lefebvre, Vincent G. McDonell "Atomization and Sprays"
- [74] Ohnesorge, W., Formation of drops by nozzles and the breakup of liquid jets, *Z. Angew. Math. Mech.*, Vol. 16, 1936, pp. 355–358.
- [75] Reitz, R. D., Atomization and Other Breakup Regimes of a Liquid Jet, Ph.D. thesis, Princeton University, Princeton, NJ, 1978.
- [76] Grant, R. P., and Middleman, S., Newtonian jet stability, *AIChE J.*, Vol. 12, No. 4, 1966, pp. 669–678.
- [77] Baron, T., Technical report No. 4, University of Illinois, 1949.
- [78] Miesse, C. C, Correlation of experimental data on the disintegration of liquid jets, *Ind. Eng. Chem.*, Vol. 47, No. 9, 1955, pp. 1690–1701.
- [79] Hinze, J. O., Fundamentals of the hydrodynamic mechanism of splitting in dispersion processes, *AIChE J.*, Vol. 1, No. 3, 1955, pp. 289–295.
- [80] Hsiang, L. P., and Faeth, G. M., Drop deformation and breakup due to shock wave and steady disturbances, *Int. J. Multiphase Flow*, Vol. 21, 1995, pp. 545–560.
- [81] Pilch, M., and Erdman, C. A., Use of breakup time data and velocity history data to predict the maximum size of stable fragments of acceleration-induced breakup of a liquid drop, *Int. J. Multiphase Flow*, Vol. 13, 1987, pp. 741–757.
- [82] Spalding, D. B., The combustion of liquid fuels, in: 4<sup>th</sup> Symposium (International) on Combustion, Williams & Wilkins, Baltimore, 1953, pp. 847–864.
- [83] Hubbard, G. L., Denny, V. E., and Mills, A. F., Droplet evaporation: Effects of transients and variable properties, *Int. J. Heat Mass Transfer.*, Vol. 18, 1975, pp. 1003–1008
- [84] Sparrow, E. M., and Gregg, J. L., Similar solutions for free convection from a non-isothermal vertical plate, *Trans ASME*, Vol. 80, 1958, pp. 379–386.
- [85] Ranz, W. E., and Marshall, W. R., Evaporation from drops, *Chem. Eng. Prog.*, Vol. 48, 1952, Part I, pp. 141–146; Part II, pp. 173–180.
- [86] Vacca, A., Bargende, M., Chiodi, M., Franken, T. et al., "Analysis of Water Injection Strategies to Exploit the Thermodynamic Effects of Water in Gasoline Engines by Means of a 3D-CFD Virtual Test Bench," *SAE Technical Paper 2019-24-0102*, 2019, doi:10.4271/2019-24-0102.
- [87] Arden L. Buck. "New Equations for Computing Vapor Pressure and Enhancement Factor". National Center for Atmospheric Research, 11 May and 15 August 1981.
- [88] Netzer, C., Franken, T., Mauss, F., Seidel, L. et al., "Numerical Analysis of the Impact of Water Injection on Combustion and Thermodynamics in a Gasoline Engine Using Detailed Chemistry," *SAE Int. J. Engines* 11(6):1151-1166, 2018, doi:10.4271/2018-01-0200.
- [89] Paltrinieri, S., Mortellaro, F., Silvestri, N., Rolando, L. et al., "Water Injection Contribution to Enabling Stoichiometric Air-to-Fuel Ratio Operation at Rated Power Conditions of a High-Performance DISI Single Cylinder Engine," *SAE Technical Paper 2019-24-0173*, 2019, doi:10.4271/2019-24-0173.
- [90] AVL-Fire manual, "Fire Spray Module"

- [91] Dukowicz, J.K. "Quasi-steady droplet change in the presence of convection, informal report Los Alamos Scientific Laboratory", LA7997-MS.
- [92] Amsden, A. A., O'Rourke, P. J. and Butler, T. D. "KIVA-II: A Computer Program for Chemically Reactive Flows with Sprays", LA-11560-MS, Los Alamos Laboratory, 1989.
- [93] Brusiani, F., Bianchi, G., and Tiberi, A., "Primary Breakup Model for Turbulent Liquid Jet Based on Ligament Evolution," SAE Technical Paper 2012-01-0460, 2012, <https://doi.org/10.4271/2012-01-0460>.
- [94] K.Y. Huh and A.D. Gosman: Phenomenological Model of Diesel spray atomisation. Proceedings of the International Conference on Multiphase Flows, Sept. 24-27, Tsukuba, Japan, 1999
- [95] Reitz, R.D., "Modeling Atomization Processes in High-Pressure Vaporizing Sprays", Atomization and Spray Technology, Vol. 3, pages 309-337, 1987.
- [96] Hsiang, L.-P. and Faeth, G.M., "Near-Limit Drop Deformation and Secondary Breakup", J. Multiphase and Flow, Vol. 18, No. 5, pp. 635-652, 1992.
- [97] Pilch, M. and Erdam, C.A., "Use of breakup time data and velocity history data to predict the maximum size of stable fragments for acceleration – induced breakup of a liquid drop", Int. J. Multiphase Flow, Vol. 13, No. 6, pp. 741-757, 1987.
- [98] O'Rourke, P.J. and Bracco, F.V. "Modeling of Drop Interactions in Thick Sprays and a Comparison With Experiments", IMECHE, 1980.
- [99] Kuhnke D., Spray Wall Interaction Modeling by Dimensionless Data Analysis, PhD thesis, Technische Universität Darmstadt (2004).
- [100] Falfari S., Bianchi G.M.; "Development of an Ignition Model for S.I. Engines Simulation", presented at SAE World Congress, 2007-01-0148, 2007
- [101] Forte, C., Bianchi, G. M., Corti, E. "Validation of a Lagrangian Ignition Model in SI Engine Simulations" SAE Technical Paper, 2010-12-15, ICEF2010-35159
- [102] . Stone R., Pashley N., Graham R. "Ignition System Measurement Techniques and Correlations for Breakdown and Arc Voltages and Currents", SAE paper 2000-01- 0245, 2000
- [103] Song J., Sunwoo M. "A Modeling and Experimental Study of Initial Flame Kernel Development and Propagation in SI Engines", SAE paper 2000-01-0960, 2000
- [104] Kravchik T., Sher E., Heywood J.B., "From spark ignition to flame initiation", Comb Sci. Technol., 108:1-20, 1995
- [105] Herweg R., Maly R.R. "A Fundamental Model for Flame Kernel Formation in SI Engines", SAE paper 922243, 1992
- [106] Han, Z., and Reitz, R. D., "A temperature wall function formulation for variable-density turbulent flows with application to engine convective heat transfer modeling," International Journal of Heat and Mass Transfer, 40(3):613-625, 1997, doi:[https://doi.org/10.1016/0017-9310\(96\)00117-2](https://doi.org/10.1016/0017-9310(96)00117-2).
- [107] Reitz, R., "Assessment of Wall Heat Transfer Models for Premixed-Charge Engine Combustion Computations," SAE Technical Paper 910267, 1991, doi:10.4271/910267.
- [108] Ricci, M., Pulga, L., Bianchi, G., Falfari, S. et al., "Numerical Aspects Affecting Heat Transfer in ICE Applications and Definition of a Temperature Wall Function Accounting for the Boundary Layer Compressibility," SAE Int. J. Engines 12(5):525-541, 2019, <https://doi-org.ezproxy.unibo.it/10.4271/03-12-05-0034>.

- [109] Sarić, S., Basara, B., Zunic, Z., "Advanced near-wall modeling for engine heat transfer," *International Journal of Heat and Fluid Flow* 63:205–211, 2017, doi: <https://doi.org/10.1016/j.ijheatfluidflow.2016.06.019>.
- [110] Mehl, M., Pitz, W.J., Westbrook, C.K., and Curran, H.J., "Kinetic Modeling of Gasoline Surrogate Components and Mixtures under Engine Conditions," *Proceedings of the Combustion Institute* 33:193-200, 2011.
- [111] Pitz, W. J., Cernansky, N. P., Dryer, F. L., Egolfopoulos, F. N. et al., "Development of an Experimental Database and Chemical Kinetic Models for Surrogate Gasoline Fuels". In *SAE Technical Paper Series*," SAE International., doi:10.4271/2007-01-0175.
- [112] Dirrenberger, P., Glaude, P.A., Bounaceur, R., Le Gall, H. et al., "Laminar Burning Velocity of Gasolines with Addition of Ethanol," *Fuel* 115:162-169, 2014, doi:10.1016/j.fuel.2013.07.015.
- [113] Poinso, T. and Veynante, D., *Theoretical and Numerical Combustion* (Edwards, 2001). ISBN:9781930217058.
- [114] Deka, M. and Peters, N., "Combustion Modeling with the G-Equation," *Oil Gas Sci. Technol.* 54:265-270, 1999.
- [115] Cazzoli, G., Forte, C., Bianchi, G., Falfari, S. et al., "A Chemical-Kinetic Approach to the Definition of the Laminar Flame Speed for the Simulation of the Combustion of Spark-Ignition Engines," *SAE Technical Paper* 2017-24-0035, 2017, doi:10.4271/2017-24-0035.
- [116] Del Pecchia, M., Breda, S., D'Adamo, A., Fontanesi, S. et al., "Development of Chemistry-Based Laminar Flame Speed Correlation for Part-Load SI Conditions and Validation in a GDI Research Engine," *SAE Int. J. Engines* 11(6):715-741, 2018, doi:10.4271/2018-01-0174.
- [117] Heywood, J.B., *Internal Combustion Engine Fundamentals* (New York: McGraw-Hill, 1988).
- [118] Metghalchi, M. and Keck, J., "Burning Velocities of Mixtures of Air with Methanol, Isooctane, and Indolene at High Pressure and Temperature," *Combustion and Flame* 48(C):191-210, 1982.
- [119] Gulder, O., "Laminar Burning Velocities of Methanol, Ethanol and Isooctane-Air Mixtures," *Symposium (International) on Combustion* 19(1):275-281, 1982.
- [120] Blint, R.J., "The Relationship of the Laminar Flame Width to Flame Speed," *Combustion Science and Technology* 49(1-2):79-92, doi:10.1080/00102208608923903.
- [121] Ranzi, E., Frassoldati, A., Stagni, A., Pelucchi, M. et al., "Reduced Kinetic Schemes of Complex Reaction Systems: Fossil and Biomass-Derived Transportation Fuels," *International Journal of Chemical Kinetics* 46(9):512-542, 2014, doi:10.1002/kin.20867.
- [122] Ranzi, E., Frassoldati, A., Grana, R., Cuoci, A. et al., "Hierarchical and Comparative Kinetic Modelling of Laminar Flame Speeds of Hydrocarbon and Oxygenated Fuels," *Progress in Energy and Combustion Science* 38(4):468-501, 2012, doi:10.1016/j.peccs.2012.03.004.
- [123] Mehl, M., Pitz, W.J., Westbrook, C.K., and Curran, H.J., "Kinetic Modeling of Gasoline Surrogate Components and Mixtures under Engine Conditions," *Proceedings of the Combustion Institute* 33:193-200, 2011.
- [124] Blint, R.J., "The Relationship of the Laminar Flame Width to Flame Speed," *Combustion Science and Technology* 49(1-2):79-92, doi:10.1080/00102208608923903.
- [125] Mehl, M., Chen, J. Y., Pitz, W. J., Sarathy, S. M., and Westbrook, C. K., "An Approach for Formulating Surrogates for Gasoline with Application toward a Reduced Surrogate Mechanism for CFD Engine Modeling," *Energy & Fuels* 25(11):5215-5223, doi:10.1021/ef201099y.

- [126] Bradley, D. and Kalghatgi, G. T., "Influence of Autoignition Delay Time Characteristics of Different Fuels on Pressure Waves and Knock in Reciprocating Engines," *Combustion and Flame* 156(12):2307-2318, doi:10.1016/j.combustflame.2009.08.003.
- [127] Cazzoli, G., Bianchi, G.M., Falfari, S., Ricci, M. et al., "Evaluation of Water and EGR Effects on Combustion Characteristics of GDI Engines Using a Chemical Kinetics Approach," SAE Technical Paper 2019-24-0019, 2019, doi:10.4271/2019-24-0019.
- [128] DelVescovo, D., Kokjohn, S., and Reitz, R., "The Development of an Ignition Delay Correlation for PRF Fuel Blends from PRF0 (n-Heptane) to PRF100 (iso-Octane)," *SAE Int. J. Engines* 9(1):520-535, 2016, <https://doi.org/10.4271/2016-01-0551>.
- [129] B.M. Gauthier, D.F. Davidson, R.K. Hanson, Shock tube determination of ignition delay times in full-blend and surrogate fuel mixtures, *Combustion and Flame*, Volume 139, Issue 4, 2004, Pages 300-311, ISSN 0010-2180
- [130] Gauthier, B. M., Davidson, D. F., and Hanson, R. K., "Shock Tube Determination of Ignition Delay Times in Full-Blend and Surrogate Fuel Mixtures," *Combustion and Flame* 139(4):300-311, doi:10.1016/j.combustflame.2004.08.015.
- [131] Pulga, L., Ricci, M., Falfari, S., Bianchi, G.M., "Advanced combustion modelling of high BMEP engines under water injection conditions with chemical correlations generated with detailed kinetics and machine learning algorithms. SAE Technical Paper 2020-01-2008 ISSN:0148-7191.
- [132] L. Postrioti, G. Caponeri, G. Buitoni, and N. Van Vuuren, "Experimental Assessment of a Novel Instrument for the Injection Rate Measurement of Port Fuel Injectors in Realistic Operating Conditions," *SAE International Journal of Fuels and Lubricants*, vol. 10, no. 2, pp. 1–8, 2017.
- [133] R. Payri, F. J. Salvador, J. Gimeno, and G. Bracho, "A new methodology for correcting the signal cumulative phenomenon on injection rate measurements," *Experimental Techniques*, vol. 32, no. 1, pp. 46–49, 2008.
- [134] J. M. Desantes, R. Payri, F. J. Salvador, and J. Gimeno, "Prediction of Spray Penetration by Means of Spray Momentum Flux," SAE Technical Paper 2006-01-1387, 2006.
- [135] J. Gimeno, Desarrollo y aplicación de la medida de flujo de cantidad de movimiento de un chorro Diesel. PhD thesis, E.T.S. Ingenieros Industriales, Universidad Politécnica de Valencia, 2008.
- [136] Park, J.; Lee, K.-H.; Park, S. Comprehensive Spray Characteristics of Water in Port Fuel Injection Injector. *Energies* 2020, 13, 396
- [137] Forte, C., Bianchi, G., and Corti, E., "Multicycle Simulation of the Mixture Formation Process of a PFI Gasoline Engine," SAE Technical Paper 2011-01-2463, 2012, <https://doi.org/10.4271/2011-01-2463>.
- [138] Stefania Falfari, Gian Marco Bianchi, Giulio Cazzoli, Claudio Forte, Sergio Negro, "Basics on Water Injection Process for Gasoline Engines", *Energy Procedia* (2018) pp. 50-57 DOI information: 10.1016/j.egypro.2018.08.018.
- [139] Falfari, S., Bianchi, G.M., Cazzoli, G., Ricci, M. et al., "Water Injection Applicability to Gasoline Engines: Thermodynamic Analysis," SAE Technical Paper 2019-01-0266, 2019, doi:10.4271/2019-01-0266.